EXPERIMENTAL AND THEORETICAL STUDY OF THE VISCOUS SHEAR PNEUMATIC TORQUE MOTOR

Colin D. Stewart

Ph.D

University of Edinburgh

1989

CONTENTS

ACKNOWLEDGEMENTS

I would like to thank my supervisor, Dr. George Alder, for his valuable advice both on the work itself and during the preparation of the thesis. Thanks are due also to the Department's Technical Staff, particularly Mr. Douglas Anderson, for the patience and care taken in the construction of the test equipment used.

Most of all, I must thank my wife, Alexa, for her constant support throughout the course of this work.

ABSTRACT

This work describes a feasibility study of a new concept in pneumatic turbomachinery. The concept has its origins in the Tesla turbine with a set of closely spaced, flat discs on a shaft. Fluid flows through the gaps between the discs and exerts a force on the disc faces by viscous shear. In this new concept, plates are positioned in the disc spaces to restrict the flow in one direction round the rotor. It is explained that this design offers certain advantages over conventional pneumatic drives for position control applications such as robotics and the feasibility study has focussed on this application.

A theoretical analysis is presented which indicated that the disc spaces need to be very small to limit the flowrate and a consequence of this is that the restrictor plates are flexible due to their thin size. A multiple disc motor and a single disc motor which were built are described and their performance compared with theoretical predictions.

The plates in the multiple disc motor experienced instability and an experimental and theoretical investigation of this problem is presented. The development of the theoretical analysis is described, beginning with static and quasi-steady models. The final formulation of the problem considers an unsteady, compressible, laminar flow through a straight, high aspect ratio rectangular duct containing a perfectly flexible membrane. The governing equations are solved by numerical methods. A two-step Lax-Wendroff method was employed but proved to be numerically unstable. The method of characteristics proved to be successful and is the solution method used in a computed

survey of membrane stability in a thin duct.

The implication of the theoretical and experimental results on the feasibility of the viscous shear torque motor for use in position control is discussed.

NOMENCLATURE

b - Width of duct

c - Speed of sound

c_m - Membrane wavespeed

C - Length of annulus in motor ($C = 2\pi\bar{r}$)

D - Hydraulic diameter
(D = 4 x (cross-sectional area)/(perimeter))

e - Spacer thickness

E - Modulus of elasticity

f - Friction factor in Chapter 2; frequency in Chapter 5

F - Force in Chapter 2; Function of U in Chapter 6

G - Function of U

h - Distance of membrane from lower wall unless subscript denotes otherwise

h_C - Disc clearance in single-disc motor

h_D - Shaft clearance in single-disc motor

H - Height of duct

k - Iteration step

l - Length of duct

L - Half wavelength of membrane

$\dot{m}$ - Mass flowrate

m - $\Delta t/\Delta x$

N - Number of elements

p - Pressure

p_1 - Inlet pressure

p_2 - Outlet pressure

Q - Volumetric flowrate

r_o - Outer radius

r_i - Inner radius

r_s - Shaft radius

$\bar{r}$ - Mean radius ($\bar{r} = (r_1 + r_2)/2$)

R - Gas constant

Re - Reynolds number

s - Thickness of restrictor plate

t - Time

T - Tension per unit width

u - Fluid velocity in x-direction

U - Vector of variable quantities in Chapter 6; Wall speed in Fig. 2.1

v - Fluid velocity in y-direction

x - Coordinate

X - Conserved mass per unit width ($X = ph$)

y - Coordinate

Y - Conserved momentum per unit width ($Y = p\bar{u}h$)

γ - Ideal gas specific heat ratio

λ - Wavelength

μ - Viscosity

ν - Poisson's ratio

θ - Temperature

ρ - Density of membrane per unit area

ρ_f - Density of fluid

ϕ - Membrane velocity ($\phi = \partial h/\partial t$)

ψ - Membrane slope ($\psi = \partial h/\partial x$)

τ - Shear stress

T - Torque

ω - Rotational speed

SUBSCRIPTS

a - Lower channel

b - Upper channel

u - Unrestricted duct

i - Node position in *x*-direction

I - Interpolation point

j - Node position in time

CHAPTER 1

INTRODUCTION

1.1 The Application of Pneumatics

Compressed air is widespread as a power source. Applications are found, for example, in industry, prosthetics and aircraft and missiles. In industry, pneumatic power is used for applying a force or for moving a load; a major application being "pick and place" devices on automated production lines. In prosthetics the movement of artificial limbs is often achieved with pneumatic actuators and applications are also found in the flight control of aircraft and missiles.

In selecting a device for a particular task a choice is made between pneumatic, hydraulic and electrical power. Each has its advantages and disadvantages in a given situation and the main advantages of pneumatic systems are:

1. The cost is generally less than comparable electrical or hydraulic systems.
2. Pneumatic systems are very reliable. Physical damage due to load vibration or shock are resisted and life expectancy is high. Contamination by dust or moisture from the environment is prevented since pneumatic devices are pressurised.
3. Maintenance is less complex and generally requires a lower degree of specialised training.
4. Air compressibility allows energy storage in a receiver.
5. Pneumatic devices can operate at full load consistently and can sustain stall indefinitely without overheating.

6. A high power to weight ratio and power to size ratio can be achieved across a broad range of force.
7. A broad range of operating temperatures is possible.
8. There is no spark or electrical shock hazard and so benefits are to be gained in flammable or explosive environments.

The ability to store high pressure air and a good power to weight ratio make the use of pneumatics attractive in prosthetics. In aircraft and missile flight control high pressure pneumatic systems are used. The high power to weight ratio and high power to size ratio are significant benefits in this application. The large number of pneumatic pick and place devices in industry is due to the low cost, good reliability and easy maintenance. It is also common, even for small factories, to have a compressed air ring main and the installation of new pneumatic devices is straightforward and clean.

Despite the advantages of pneumatic devices, they suffer some disadvantages in the area of position control due to the low natural damping and the compressibility of air. Allied to this are the inherent non-linearities due to viscous and static friction. In prosthetic applications the advantages of air storage and small size outweigh these disadvantages and pneumatics are the most common choice. The control loop in this instance can be closed by the human operator but the low stiffness and slow response time can cause problems.

In industrial applications where control of speed and acceleration and accurate positioning are necessary, as in robotics, the present generation of pneumatic actuators cannot provide the quality of control to compete with well developed electrical and hydraulic servomotors. As a consequence, there are no pneumatically

driven continuous path industrial robots available today. However, many industrial applications require movement to a new position without continuous control and these simple movements can be achieved by actuators working between two pre-set extremes. Pneumatics is often the best choice in these cases and does in fact dominate this sector of the market. The most common actuator to be found is the linear type which is composed of a piston in a cylinder operating between end-stops. Less common, but the most common rotary actuator, is the rotary vane operating between fixed end-stops in a quarter or half turn.

To overcome some of the problems posed for position control by compressibility, work has proceeded on both linear and rotary pneumatic actuators to reduce friction. Smith (1987) describes a linear actuator in which low friction seals were used and reports that an accurate, fast pneumatic control system was developed which was superior to previous systems. Work on reducing the friction in a rotary piston air motor is reported by Dunlop (1988). This motor is under microprocessor control and is now challenging the electric drives in the low power robotics market.

1.2 Rotary Pneumatic Drives

The purpose of any fluid machine is to convert energy contained in a fluid into useful mechanical energy or vice versa. A machine which converts fluid energy into mechanical energy is called a turbine or a motor and a machine which converts mechanical energy into fluid energy is called a pump if the fluid is incompressible and a compressor or a fan if the fluid is compressible. Here we shall confine our attention to pneumatic drives - i.e. turbines and motors.

A rotary drive basically operates as either a torque generator or as a power driver and, in general, the former run at zero to low speed and the latter run at high speed. Efficiency (i.e. the ratio of useful mechanical power output to fluid power supplied) is an important parameter for a power driver but it is not relevant to a torque generator. The important consideration for a torque generator is the torque characteristic at low speeds. The flowrate (or power) required to achieve the torque is important but is not used in efficiency calculations. Some machinery is capable of either mode of operation while others are best suited to one or other due to their design.

Energy transfer in a fluid machine is governed by inertial, pressure and viscous forces in the fluid. The relative importance of each is dependent on the working principle of a particular machine and there are basically two categories: the positive displacement group and the rotodynamic group. Transfer of energy in a positive displacement machine depends on hydrostatic principles in which pressure in an enclosed space causes the movement of a machine element. In a rotodynamic machine the operation is dependent on the motion of the fluid relative to the moving element (the rotor); the fluid possesses momentum in a direction tangential to the rotor and the rate at which this decreases corresponds to a tangential force on the rotor.

Several pneumatic positive displacement drives will be described in Section 1.2.1 and three types of pneumatic rotodynamic drive will be described in Section 1.2.2.

1.2.1 Positive Displacement Drives

There are a number of different types of positive displacement drive and each type can have a number of variations. Here we shall confine our attention to the main types and the general operating principles of each will be described. The most common are the piston and rotary vane and these are described first.

Power in a piston motor is developed from the force exerted on a piston in a cylinder by high pressure gas. In a radial piston motor the cylinders are distributed radially about a common crank and in an axial piston motor they run in the same direction as the output shaft. Radial piston motors commonly have anything between three to six cylinders attached to the crank by connecting rods; a sketch of a four cylinder type is shown in Fig. 1.1. Axial motors normally have four, five or six cylinders attached by connecting rods to a plate which transmits the force exerted on it via a series of gears to the output shaft. The radial motor is most common and has the highest starting torque of any air motor while the axial piston motor is more compact and is smoother running. These motors are found in applications where high power, good starting and stopping characteristics and accurate low speed control are required.

Rotary vane motors have longitudinal vanes fitted in radial slots along the length of a rotor mounted eccentrically in the motor body (see Fig. 1.2). The vanes are spring-loaded against the housing wall for sealing and torque is developed by the pressure difference across the vanes which can vary in number between 3 and 10. A larger number of vanes reduces blowby and produces a more uniform torque at low speeds but this is at the expense of increased friction and reduced efficiency. Vane motors are simple and compact and are used

in many applications where high speed coupled with low to medium power output are required such as portable power tools and hoists and winches.

A less common pneumatic motor is the diaphragm motor which consists of a reciprocating diaphragm driving a ratchet wheel as shown in Fig. 1.3. The speed of working is low (20 rpm is a typical maximum) but very high torques can be developed and it is essentially a torque generator. There is no leakage and the flowrate is directly related to the speed. Although very high initial torque is available, this falls off rapidly with speed. This characteristic leads to their use in valve actuation where a high initial torque is needed to crack open a valve and the falling load then allows the motor to build up speed.

The gerotor motor is a development of the gear motor with specially shaped lobes on the gears as shown in Fig. 1.4. It is composed of an inner and outer gear set which both revolve and an output shaft at the centre. The inner set has one less tooth than the outer set and the shape of each is such that all teeth of both gears are in contact at all times. The air enters the motor through the inlet port into a space between meshing teeth and exhausts through the outlet port further round the periphery of the motor. Torque is developed by the pressure difference across the teeth. A high torque can be produced at low speed which is ripple free down to approximately 15 rpm. It is considered to be a torque generator but the applications are very limited and few are commercially available.

1.2.2 Rotodynamic Drives

Rotodynamic drives (or turbines) are not at all common in

pneumatic applications but are more commonly found in applications where other sources of fluid power are available. Examples include gas turbines in which pressure is produced by the combustion of fuel and air; steam turbines in which pressure is produced by the addition of heat in a boiler; and Francis and Kaplan turbines used in hydro-electric power plants which have a reservoir of water as a pressure source. Pneumatic turbines suffer from disadvantages which limit their applicability and in this section we shall consider three different types, starting with the impulse turbine.

The rotor in the impulse turbine is composed of a set of discs with specially shaped blades on the periphery of each. A set of nozzles convert the pressure of the air supply into kinetic energy and direct a high speed stream of air onto the blades at a specific angle (a sketch of the principle is shown in Fig. 1.5). The design of the blades is such that, although the air leaves them at a large relative velocity, its absolute velocity leaving the turbine is small. Little kinetic energy is therefore wasted but efficient operation is dependent on the rotor rotating over a limited, high speed range. An impulse turbine can produce a torque comparable to that of a piston motor but the complexity of the design and the limited speed range limit the applications.

A smaller pneumatic turbine is also available which is essentially a propeller in a duct, powered by an air flow in the axial direction. It is a very high speed motor (50,000-80,000 rpm being typical) and is capable of generating only minimal torque. Torque multiplication by reduction gearing is not a viable proposition, because the load involved would be of the same order as the torque available. Small pneumatic turbine motors are therefore

strictly limited to applications where high speeds can be used with direct drive against light loads. One such application is the dentist's drill.

The potential of the Tesla steam turbine for use as an air turbine was investigated by Rice (1965). The rotor is composed of a set of flat discs on a shaft with the fluid entry round the periphery of the discs and the outlet near the centre. The flow follows a spiral path to the centre as shown in Fig. 1.7 and is governed by pressure, inertial, viscous and centrifugal forces. As the tangential momentum of the flow reduces towards the centre, transfer of energy from the fluid to the rotor is achieved by viscous drag on the discs. This turbine has not met with success as an air turbine and has only found very limited use as a steam turbine. Torque production and efficiency are very low but an advantage is that it can be run on untreated steam such as that produced by a geothermal source.

1.2.3 Summary

A fundamental difference between positive displacement machinery and rotodynamic machinery is that the positive displacement type relies on efficient sealing between stationary and moving parts to maintain pressure differences across components. Such careful sealing is not required in rotodynamic machines since fluid inertia provides the driving force and much lower pressure gradients exist. A further difference is that rotodynamic machinery generally consists of one moving part - the rotor - whereas positive displacement machines have a number of moving parts. These moving parts are susceptible to wear and require more maintenance than the rotor of a

rotodynamic machine.

These differences in construction also lead to a general difference in the maximum operating speed of each group. The low friction and steady flow nature of rotodynamic machinery allows high speeds to be attained. The frictional sealing in positive displacement machinery and, in some cases, the inertia of reciprocating parts, limits their speed range.

1.3 A New Concept in Rotodynamic Machinery

A new concept in turbomachinery is proposed here and we have called it the viscous shear pneumatic torque motor. It is based on the concept of the Tesla turbine with a set of flat discs positioned on a shaft. In order to reduce flowrate through the device, the discs are spaced much closer together and viscous forces will dominate inertial forces as the gap size is reduced. With negligible inertial force in the fluid, the flow would be controlled only by pressure and viscous forces. The flow through the Tesla turbine design would then follow paths similar to those shown in Fig. 1.8. There is no overall tangential component to the flow and hence no torque could be produced.

A diagram of the concept proposed to overcome this problem is shown in Fig. 1.9. The rotor in this case has disc spacers between the actuator discs and this results in a set of thin annuli around the periphery of the rotor. Attached to the casing are thin plates which are positioned in the annuli between the inlet and outlet ports to restrict the flow in one direction round the discs. The pressure difference across the ends of each duct is therefore only balanced by the viscous shear exerted on the walls. Since the force is shared

between the discs and the plates in the restricted region, and the cross sectional area of the flow is smaller, there is a resultant torque in the direction of flow through the unrestricted region.

With air bearings used to support the shaft there would be no surfaces in contact and the only retardation to motion would be due to the very small viscous drag between parts in relative motion. Mechanical friction could therefore be very low and, if a clean air supply is used, wear should be negligible. Also, if the viscous drag is negligible in comparison with the torque production then the torque output of such a device would be insensitive to speed transients.

This motor is a departure from conventional rotodynamic machinery since it relies on the pressure difference along ducts in a rotor rather than on momentum transfer as the fluid flows through it. Torque production is directly dependent on the pressure difference in the same manner as in positive displacement machinery. It therefore combines some of the advantages of both positive displacement and rotodynamic machinery. It offers the smooth torque output, low friction and low wear rate of a rotodynamic device whilst also offering the good starting torque characteristics of a positive displacement device. It also has the potential of a lower flowrate than other rotodynamic machines and, with the added advantages of torque insensitivity to speed transients and symmetrical, two-way continuous rotation, this motor possesses the correct attributes for positional control.

Conventional pneumatic motors all face limitations for use in accurate position control. The low torque of the small turbine makes it an impractical proposition as does the poor low speed performance

of the vane motor. The impulse turbine produces a high torque but, in its present form, it cannot be used for low speed stop/start applications. The high starting torque and good low speed capability of the gerotor, diaphragm and piston motors make them feasible propositions but all three suffer from the disadvantages of friction and wear due to the contact of moving surfaces. The problem of friction has been successfully tackled by Dunlop for a radial piston motor with the use of new plastics for seals, but the problem of wear still exists and the torque ripple is 9%.

1.4 Defining the Area of Research

The potential advantages offered by the viscous shear torque motor indicated that it would be expedient to investigate the feasibility of the concept. Attention was directed towards possible use as a position control device and thus the important considerations were related to its use as a torque generator rather than a power producer. Torque production and low air consumption were therefore primary considerations in the feasibility study.

It was clear from the outset that there were some areas of concern which could prove disadvantageous. An initial analysis of the problem showed that the gaps between the discs would have to be very small to limit the flow. The restrictor plates positioned in the disc spaces then have to be so thin that they would be flexible. There are therefore possible difficulties in manufacture and the motor could prove costly to make. Also, with small gaps in relation to disc thickness, the rotor inertia could be relatively high in relation to the torque output, thus limiting the potential applications.

It was considered that the most immediate problem which should be investigated was the feasibility of the concept itself in view of the need for flexible plates in thin spaces between discs. If the air flow were to cause the plates to contact the discs due to buckling or vibration then the design with flexible plates would not be feasible. In contrast, the flow may stabilise the plates due to the viscous and pressure fluid forces.

The first priority was to review work on similar devices working on the principle of drag on discs. Work on plate and wall vibration in ducts was also relevant in view of the flexible restrictor plates.

1.5 Survey of Relevant Work

The first step in the investigation of the feasibility of the viscous shear torque motor was to survey the literature for work on similar devices. This is described in Section 1.5.1. A potential problem for this concept is the stability of the plates in the disc spaces, so the survey also encompasses plate and wall vibration in ducts and this is described in Section 1.5.2.

1.5.1 Work Related to Disc Rotors

The review of work on similar devices revealed that no device had been investigated which used only the force of viscous shear to drive a rotor as is the case in the viscous shear motor concept. Various related devices were found and a review of the work in this area is described here.

A number of devices with single and multiple disc rotors have been investigated for use as turbines, pumps, compressors and fans. The concept of multiple disc turbomachinery is credited to Nikola

Tesla who took out a U.S. patent in 1913 on the multiple disc turbine which, since that time, has been known as the Tesla turbine, the friction turbine or the shear torque turbine. There have also been investigations into the shear-force pump which is essentially the multiple disc turbine working in reverse. With dimensional alterations the pump has also been tested as a compressor and a fan. A class of turbines and pumps with a single disc rotor which has vanes on the periphery have also attracted some attention. These have generally been called the drag turbine and the periphery pump although the pump has also been known as the friction, tangential, turbine-vane, regenerative, or turbulence pump.

Although there was no published engineering investigation of Tesla's turbine at the time of his patent, it was reported along with a description of a multiple disc pump in the semi-technical press of the time e.g. the *Scientific American* (1911). The turbine rotor consisted of a set of flat discs mounted on a shaft with the inlet at the periphery and the outlet at the centre of the discs as shown in Fig. 1.7. The fluid enters the spaces between the discs tangentially at high speed and flows in a spiral path to the exit at the centre. As the fluid flows through the gaps the inertial force of the fluid is transferred to the discs by viscous shear. In the case of the pump, the shaft is driven and the inlet is at the centre. As the discs rotate, the fluid flows in a spiral path to the outlet at the periphery due to the combined action of the tangential shear force exerted by the moving discs and the centrifugal force produced by the rotation.

Tesla never exploited these ideas and no further interest was expressed until the early 1960's when there was a revival of interest

in multiple disc rotors due to some advantages they had over conventional turbomachinery as new applications arose. Apart from the obvious benefits of ease of manufacture and consequential lower cost, a major advantage of the multiple disc turbine is that it can run on untreated steam and can therefore be powered directly by a geothermal source. The possibility also exists for a low noise pump for use in spacecraft since the design would be less prone to separation or cavitation than conventional pumps.

The revival of interest in multiple disc pumps started with Brieter and Polhausen (1962) who analysed the laminar outflow of an incompressible fluid using the Navier-Stokes equations. A simpler theoretical model was presented by Rice (1963) along with experimental results from a pump, a compressor and a fan. The model assumes a constant friction factor over the radius of the discs but this was not compared with the experimental results. He argues that his simple theory was only to be used as a design aid and was not intended to give accurate results.

A more complex pump design is described by Hasinger and Khert (1963) who published an experimental and theoretical investigation of a pump for use in spacecraft. The 125 μm thick discs were conical in shape to increase rigidity and the gaps between the discs were 135 μm. Tests were successfully performed on this pump with water as the test fluid and a maximum efficiency of 54% was obtained. A theoretical analysis based on incompressible laminar flow was used to predict the performance of pumps with various dimensions.

A theoretical investigation of the performance of conventional and shear force pumps by Balje (1965) showed that although the

efficiency of the shear pump was lower than that of a conventional pump, its suction specific speed potential was much greater (about 20 times) and hence only a small cavitation suppression head is required and higher fluid temperatures can be tolerated. He argued that the shear pump would therefore be useful as a condensate pump in a Rankine cycle power plant in spacecraft since a smaller sub cooler could be used and the efficiency of the pump is of little importance in this application.

The most recent investigation of a shear force pump was reported by Roddy et al (1987). The performance of a commercially available pump was tested experimentally and compared with theoretical predictions. A local friction factor which encompasses both laminar and turbulent flow was used in the theory and good agreement was obtained.

Work on multiple disc turbines commenced with Rice (1965) and Beans (1966) who both published results of tests on experimental turbines driven by compressed air. Beans reported problems of vibration with his 660 μm thick discs but this was solved by placing thin plastic pads between them. Both Rice and Beans described theoretical analyses based on incompressible flow with Beans also considering compressible turbulent flow. Rice defined a constant friction factor over the radius of the discs while Beans used the integral form of the equations by assuming a parabolic velocity profile for laminar flow and by using an empirically obtained friction factor for turbulent flow. Beans reported an efficiency of 24% and that although the qualitative agreement was good the quantitative agreement was far from satisfactory. Rice did not compare theoretical and experimental results.

Matsch and Rice (1967a,b,1968) initially analysed the two limiting cases of potential flow and creeping flow and then took the analysis further by using order of magnitude arguments to simplify the Navier Stokes equations of incompressible laminar flow. Boyd and Rice (1968) developed a numerical method to solve the resulting equations and Boyack and Rice (1971) subsequently developed an improved numerical procedure which reduced computer time. Lawn and Rice (1974) used the computer program of Boyack and Rice to produce performance maps for the use of designers. An experimental investigation by Adams and Rice (1970) involving a pair of driven discs substantiated the adequacy of the problem statement and of the numerical solution given by Boyd and Rice. Pater et al (1974) endeavoured to define the transition point from laminar to turbulent flow but did not meet with much success although their flow visualisation tests confirmed earlier assumptions regarding the flow structure.

Bassett (1975) and Garrison et al (1976) independently published theoretical analyses of compressible laminar flow through a turbine which were in close agreement. By modelling a low Mach number flow Garrison et al checked their theoretical results against existing experimental results involving incompressible flow and obtained good agreement.

Parodi (1981) reported results from tests on turbines for use in geothermal power plants using raw untreated steam. Since the announcement of Tesla's turbine in 1911 it would appear that this is the first report of a turbine being used in a practical application.

Shortly before the revival of interest in the multiple disc concept there was a period of interest in the 1950's in the single

disc drag turbine and the periphery pump. A diagram of the turbine is shown in Fig. 1.6. The disc in these devices has vanes on the periphery and the casing contains the fluid passage. The casing clearance is reduced between the inlet and outlet ports to block the high pressure port from the low pressure port and the disc is dragged round by the fluid as it flows round the periphery of the turbine. As with their multiple disc counterparts, the pump has the same construction as the turbine and operates as a turbine in reverse.

Experimental periphery pumps were built by Senoo (1948) and by Iversen (1955) and the results compared with analytic predictions of incompressible flow. Both these investigators assumed that the vanes produce turbulence in the flow passage which transfers momentum from the disc to the fluid but Wilson et al (1955) explained that the momentum transfer is due to vortices which are set up by the centrifugal force exerted on the fluid by the disc.

Balje (1956) argued that although the momentum transfer was by vortices, the analysis of Iversen was sufficient to predict performance and he extended Iversen's analysis to include compressible flow. Balje (1957) extended his earlier investigation to look at various aspects of drag turbine performance and predicted that peak efficiencies would occur at low speeds. He suggested that even though the efficiency is expected to be low, the simplicity of design and the inherent reliability would be advantageous for certain applications such as small accessory power units in aircraft and missiles.

Finally, the multiple disc fan described by Charters et al (1973) is the design closest in concept to the viscous shear torque motor. It consists of a set of discs on a shaft separated by

smaller discs. The inlet and outlet are separated by metal/felt finger seals and as the shaft is rotated the flow is dragged through the gaps between the discs. Two theoretical models were developed assuming compressible turbulent flow. One was a simple friction factor model and the other was a more complex boundary layer model. The results of both are very similar and agree very well with experimental results of the fan head. Flow visualisation tests confirmed the distinct turbulent nature of the flow.

1.5.2 Plate and Wall Vibration in Ducts

Bland et al (1967) undertook an experimental and analytical study of the stability of a plate in a rectangular channel containing an airflow. This was instigated by the failure of a nuclear rocket engine reported by Spence (1968) in which control rods failed due to fatigue. The plate in Bland's investigation was held at its upstream end by springs which allowed pitching and translation perpendicular to the flow and the height of the duct normal to the plate was variable. It was found both experimentally and analytically that a critical fluid velocity could be defined above which the plate would oscillate. Experimentally, this velocity decreased with duct height until a duct height to plate length ratio of 0.1, below which the critical velocity increased as the height was reduced. The theory, based on a two-dimensional inviscid potential flow analysis, predicted a continuous decrease in velocity and it was concluded, therefore, that the inviscid analysis broke down at smaller duct heights.

Dodge and Muller (1969) improved on Bland's model with a one-dimensional, viscous, incompressible flow analysis in which

viscosity was approximated by a friction factor and energy dissipation by a loss coefficient, but this model also predicted a drop in critical velocity at small duct heights. They also attempted a quasi-steady analysis in which the instantaneous position of the plate determined the flow distribution but this did not predict plate vibrations with the elastic axis at the upstream edge although it did predict a divergent condition with the axis placed downstream of the plate mid-point.

Thorpe (1963) analysed turbulent air flow through unequal parallel channels in a duct, separated by a flat plate spanning the width. The analysis consisted of an isothermal, one-dimensional, incompressible flow and the stagnation streamline was used to define fictitious channels upstream and downstream of the plate. Good agreement was found between theory and experiment and it was shown that the static pressure was higher in the narrow channel. Thorpe (1964) extended this analysis to apply to flow past an inclined plate in a duct. The plate does not span the channel so transverse flow may occur and a discharge coefficient was used in its computation. Good agreement was found between theory and experiment regarding the pressure distributions along both sides of the plate; the pressure in the convergent channel always being higher than that in the divergent channel.

Thorpe et al (1971) analysed the stability of long slender plates in a flow channel with the downstream edge of the plate supported by a torsion bar which permitted rotational but not translational motion. Although the method of fixing the plate was quite different from that described by Bland, Thorpe also suggested that his system modelled the fuel rods in a nuclear core. The

instability in this system was found both experimentally and theoretically to be a divergent motion of the plate from the initial equilibrium position in the centre. The critical flow velocity at which this occurred was determined as a function of the torsional spring constant. Experimentally, the critical velocity was found to increase with the spring constant and the theoretical model, which assumed the flow was one-dimensional and incompressible, predicted a qualitatively similar increase but with half the velocity. No vibration of the plate was encountered, the only motion being a wandering motion just prior to divergence which was attributed to turbulent fluctuations. A test was also undertaken with the plate one third distance across the duct and it was found that the plate always diverged (at approximately the same critical velocity) towards the larger duct which they concluded was due to the higher static pressure on the smaller side. Hwang and Thorpe (1973) investigated the same problem as Thorpe but with a different analysis of the crossflow between the channels and a significant improvement was obtained in predicting plate instability.

Work which stands somewhat on its own in this area is that of Desai (1974) in which he investigated the phenomenon which he called the "fluffing of cards". This had been observed with a stack of thin, rigid, parallel, rectangular cards in a subsonic wind tunnel, where, under certain conditions, the flow would separate the cards and maintain them in a stable configuration. In the analysis of this phenomenon he assumed that the plates were rigid and parallel to the flow and that a viscous, incompressible flow existed between the plates which was fully developed except at the entrance. With the application of Bernoulli's equation at the entrance to each gap the

resulting forces tend to equalise the gaps.

Flow of a compressible fluid over one side of a single flexible surface has been examined by Dowell (1967) with regard to aeronautical applications of plate flutter. Dowell's work was the culmination of previous investigators' work, incorporating the best features, namely, full linearized inviscid potential flow and von Karman's non-linear large deflection plate equation applied to a three-dimensional simply supported plate. He found that a static divergence would occur in subsonic flow and predicted flutter of the plate in supersonic flow.

The flow of both gases and liquids have been studied in flexible tubes with applications in oil pipelines, fuel lines in liquid propellant rockets and in physiological applications such as air flow in the passageways of the lungs. Weaver and Paidoussis (1977) announced the first experimental observation of classical mode flutter of a flexible tube containing an air flow. It was found that as the flow was increased from zero the tube would eventually buckle and this is referred to as static divergence. Increasing the flow further results in flapping flutter which is akin to two adjacent parallel walls flapping and further increase results in classical shell mode flutter. The flow velocity at which instability first occurs is called the critical velocity and Weaver and others have attempted to predict this value as well as the type of instability.

Weaver included damping in his model of the flexible walls and employed an incompressible, inviscid flow but this predicted static divergence and not flutter. Matsuzaki and Fung (1977,1979) included wall damping along with spring supports providing "elastance" and initially assumed an incompressible, inviscid flow with subsequent

work applying linearized compressible potential flow theory but these also predicted static divergence. Grotberg and Davis (1980) excluded wall damping from their model, assumed an incompressible, inviscid flow and found that flutter was the unstable mode. Both Grotberg and Reiss (1984) and Grotberg and Shee (1985) included wall damping in their models and predicted flutter; the former employing an incompressible viscous flow and the latter a compressible viscous flow. Thus it would appear that damping in this system plays an important role in determining the type of instability which results.

1.5.3 Summary

The review of devices with disc rotors has shown that the Tesla turbine and the related pump have received a fair amount of attention. Neither device, however, has provided any useful information for the development of the viscous shear torque motor with the turbine requiring excessive quantities of air for the required torque. The pump described by Hasinger and Khert (1963) with conical discs for rigidity is an interesting concept but it would involve some very complicated manufacturing techniques to position restrictor plates in the disc spaces and is outwith the scope of this research. The fan described by Charters et al (1973) is closest in concept to the motor but used felt finger seals rather than restrictor plates. Their simple approach to analysing the flow through the disc spaces was found to be useful in analysing the flow through the shear torque motor but the use of finger seals was not applicable to the motor since the pressure differences involved in the motor are much higher.

The review of plate and wall vibration in ducts has shown that two modes of instability are found and that both occur above a

critical fluid velocity. The first mode is divergence (or buckling) and the second is flutter. The investigations on plate stability, in particular, have shown that that there is a good possibility that the plates in the motor will be stable. The experimental finding of Bland et al (1967) that the critical fluid velocity increased markedly at thinner duct sizes is particularly promising and Thorpe et al (1971) found that the critical velocity was approximately the same for a plate off-centre as for one in the centre of the duct. Also, for a laminar flow, Desai (1974) theoretically predicted that the tendency is for a set of plates to space out equally in a duct.

1.6 Objectives

The literature review revealed that no device had previously been investigated which operated on the same principle as the proposed viscous shear torque motor. The review also indicated that the restrictor plates would have the tendency to stabalise in the centre of the disc spaces with fluid flow present. The first objective was therefore to build an experimental motor and investigate any problems which arose. The motor was constructed with very small gaps and had flexible restrictor plates. This is described in Chapter 2 along with a second, simpler motor which was built.

The experimental motor experienced problems due to the flexibility of the plates and this was identified as the area in most need of investigation. The second objective was therefore defined as the investigation of the stability of a flexible plate in a thin duct. The experimental work undertaken on this is described in Chapter 3 and the theoretical work occupies Chapters 4 to 7.

Chapter 4 describes the first two simpler approaches to the problem and Chapter 5 describes the more in-depth theoretical model which was finally developed. Chapter 6 describes the numerical methods which were employed in the solution of the equations derived in Chapter 5, the first being a Lax-Wendroff finite difference method and the second being the method of characteristics on a rectangular grid. Difficulty was encountered obtaining numerically stable solutions from the computer program which was written specially for the purpose and a great deal of time was devoted to this. The instability problem with the Lax-Wendroff method was never solved but the characteristics method eventually provided stable results which are discussed in Chapter 7. The relevance of the results on plate stability to the feasibility of the shear torque motor is finally discussed in Chapter 8.

CHAPTER 2

INITIAL SHEAR TORQUE MOTOR STUDY

The initial investigation of the shear torque motor is described in this chapter. Two motors were built to assess the feasibility of the design and to investigate the performance. The first motor had 17 discs spaced very closely on a shaft and the second motor was built with a single disc. The majority of experimental results were obtained from the single-disc motor.

The equations used in the prediction of torque and flowrate for the two motors are described in Section 2.1. The multiple-disc motor is described in Section 2.2 and the single-disc motor in Section 2.3. The discussion in Section 2.4 focusses on experimental results from both motors and on operational difficulties encountered during testing.

2.1 Theoretical Analysis

In this section we shall consider a steady isothermal compressible flow through the disc spaces in the design of the multiple-disc motor shown in Fig. 1.9. The resulting equations are also applicable to the single-disc motor. In the analysis, flow between a single pair of discs will be considered on the assumption that the flow in all disc spaces is similar and that there is no cross-flow between the channels. The rotor is assumed to be contained within a housing which does not exert a restraining torque and which does not allow any leakage out through the bearings. Expressions for torque and flowrate will be derived for a generalised duct in which one wall is stationary and one is moving. The

unrestricted duct is the special case in which there is no relative wall motion.

To facilitate the calculation of the overall performance without requiring a knowledge of the internal flow structure we shall follow a similar treatment to that of Charters et al (1973) who found good agreement between theory and experiment for a multiple-disc fan of similar design. The following simplifying assumptions will be made:

1. The pressure and tangential velocity distribution at the inlet and outlet of each duct are uniform.
2. The effective velocity, $\omega\bar{r}$, is based on the rotational speed of the discs, ω, at the radial mid-point of the annular section, $\bar{r}$.
3. The circumferential flow in the ducts is equivalent to flow through a straight, high aspect ratio, rectangular duct.

The duct which will therefore be analysed is shown in Fig. 2.1 and is of height H, width b, and length l. H is small compared to the other dimensions and the lower wall is moving at a velocity $\omega\bar{r}$ relative to the upper wall which is stationary.

The analysis of laminar flow through the duct follows similar lines to the analysis of flow through gas lubricated bearings (e.g. Gross 1962) which also involves compressible flow in thin channels. Since $H << l$ the pressure gradient across the film (i.e. in the y-direction) is assumed to be insignificant compared to the gradients in the flow direction and if side-leakage is neglected we have one remaining Navier-Stokes equation of motion in the x-direction represented by equation 5.14. Owing to the minute thickness of the fluid film the inertia terms are negligible and, following the same order of magnitude argument presented in Chapter 5, only a single

viscous term remains. We are therefore left with the following simplified form of equation 5.14:

$$\frac{dp}{dx} = \mu\frac{\partial^2 u}{\partial y^2} \tag{2.1}$$

where x and y are the coordinates parallel and normal to the channel axis; p is the pressure; u is the velocity component in the x direction; and μ is the viscosity. By integrating u with respect to y and by substituting the limits $u = \omega\bar{r}$ at $y = 0$ and $u = 0$ at $y = H$, the equation for the velocity distribution is:

$$u = \frac{1}{2\mu}\left(\frac{dp}{dx}\right)\left(y^2 - Hy\right) + \omega\bar{r}\left(1 - \frac{y}{H}\right) \tag{2.2}$$

To calculate the force exerted on the moving wall by the flow we first define the shear force, δF, acting on an elemental area of length δx and width b on the lower plane:

$$\delta F = \tau_0 b\delta x \tag{2.3}$$

where τ_0 is the shear stress at $y = 0$. By Newton's law of viscous flow $\tau = \mu\frac{\partial u}{\partial y}$ and, with $\delta x \to 0$, equation 2.3 becomes:

$$dF = \mu\left(\frac{\partial u}{\partial y}\right)_0 b dx \tag{2.4}$$

Substitution of equation 2.2 in equation 2.4 and differentiating the expression for u then leads to:

$$dF = \left\{-\frac{H}{2}\left(\frac{dp}{dx}\right) - \frac{\mu\omega\bar{r}}{H}\right\} b dx \tag{2.5}$$

If we now integrate equation 2.5 with respect to x and substitute the limits $p = p_1$ at $x = 0$ and $p = p_2$ at $x = l$, we arrive at the following expression for the force exerted over the length l:

$$F = b\left\{\frac{H}{2}\left(p_1 - p_2\right) - \frac{\mu\omega\bar{r}l}{H}\right\} \tag{2.6}$$

To calculate the torque, T, exerted on a single disc face, we define:

$$T = \bar{r}F \tag{2.7}$$

and since $\bar{r} = (r_o + r_i)/2$ and $b = r_o - r_i$ then substitution of equation 2.6 in equation 2.7 gives:

$$T = \frac{r_o^2 - r_i^2}{2}\left\{\frac{H}{2}\left(p_1 - p_2\right) - \frac{\mu\omega\bar{r}l}{H}\right\} \tag{2.8}$$

which is the general expression for torque exerted on a single disc face in both motors. The ratio between the two terms on the right hand side of equation 2.8 can now give an indication of the effect of rotational velocity on torque. This ratio is equal to unity when:

$$\omega = \frac{H^2}{2\mu\bar{r}l}\left(p_1 - p_2\right) \tag{2.9}$$

If the rotational velocity is much less than this critical velocity then the last term in equation 2.8 can be considered negligible and the torque will be independent of velocity.

The total torque output of each duct in the multiple disc motor is equal to $2T_u - T_a - T_b$ where subscripts *a* and *b* denote the channels either side of the restrictor plate; and *u* denotes the unrestricted duct. Thus, with the help of equation 2.8, the total torque output of a single duct is:

$$T = \frac{r_o^2 - r_i^2}{2}\left\{\left(H_u - \frac{H_a + H_b}{2}\right)\left(p_1 - p_2\right) - \mu\omega\bar{r}l_a\left(\frac{1}{H_a} + \frac{1}{H_b}\right)\right\} \tag{2.10}$$

With a restrictor plate thickness *s*, then $H_b = H_u - H_a - s$ and we can

rewrite equation 2.10 as follows:

$$T = \frac{r_o^2 - r_i^2}{2}\left\{\left(H_u + s\right)\left(p_1 - p_2\right) - \mu\omega\bar{r}l_a\left(\frac{1}{H_a} + \frac{1}{H_b}\right)\right\} \qquad (2.11)$$

If ω is much less than the critical velocity defined by equation 2.9, for both channels a and b, then equation 2.11 becomes:

$$T = \frac{r_o^2 - r_i^2}{2}\left(H_u + s\right)\left(p_1 - p_2\right) \qquad (2.12)$$

which shows that the torque is independent of the position of the restrictor plate in the duct and that it is linearly dependent on the duct height, the plate thickness and the pressure drop. For both the experimental motors, the last term in equation 2.11 will be shown to be negligible and equation 2.12 therefore applies. Since the viscous term is negligible in laminar flow it is reasonable to assume that this is also the case in turbulent flow and equation 2.12 will therefore be used when the flow is turbulent.

To calculate the mass flowrate of laminar flow through the duct shown in Fig. 2.1 we consider the flow through a small elemental strip of width b and height δy and if b is sufficiently large and δy is sufficiently small then the velocity u may be taken as the average velocity through the element. Assuming that the fluid density ρ_f is constant over the short length δx, the mass flow, $\dot{m}$, through the strip $b\delta x\delta y$ is therefore $\rho_f ub\delta y$ and the total mass flow through $bH\delta x$ is:

$$\dot{m} = \int_0^H \rho_f ub \, dy \qquad (2.13)$$

If we now substitute equation 2.2 in equation 2.13 and substitute the perfect gas law $\rho_f = p/R\theta$ (where R is the gas constant and θ is the

temperature) we get:

$$\dot{m} = \frac{pb}{R\theta}\int_0^H \left\{\frac{1}{2\mu}\left(\frac{dp}{dx}\right)\left(y^2 - Hy\right) + \omega\bar{r}\left(1 - \frac{y}{H}\right)\right\}dy \qquad (2.14)$$

Evaluation of the integral then results in:

$$\dot{m} = \frac{pb}{R\theta}\left(- \frac{H^3}{12\mu}\frac{dp}{dx} + \frac{\omega\bar{r}H}{2}\right) \qquad (2.15)$$

If we now integrate equation 2.15 with respect to x and substitute the limits $p = p_1$ at $x = 0$ and $p = p_2$ at $x = l$, we arrive at the following expression for the mass flow through a duct length l:

$$\dot{m} = \frac{bH^3}{24\mu R\theta l}\left(p_1^2 - p_2^2\right) + \frac{bH\omega\bar{r}}{2R\theta l}\int_0^1 p\, dx \qquad (2.16)$$

If it is assumed, as a first approximation, that the pressure variation in the x direction is linear then equation 2.16 becomes:

$$\dot{m} = \frac{bH^3}{24\mu R\theta l}\left(p_1^2 - p_2^2\right) + \frac{bH\omega\bar{r}}{4R\theta}\left(p_1 + p_2\right) \qquad (2.17)$$

The ratio between the two terms on the right hand side of equation 2.17 can now give an indication of the effect of rotational velocity on the flowrate. This ratio is equal to unity when:

$$\omega = \frac{H^2}{6\mu\bar{r}l}\left(p_1 - p_2\right) \qquad (2.18)$$

If the rotational velocity is much less than this critical velocity then the flowrate can be considered to be independent of velocity.

For the calculation of turbulent mass flowrate we shall introduce a dimensionless friction factor f in the following equation as defined, for example, by Schlichting (1968):

$$\frac{dp}{dx} = - \frac{f}{D}\frac{\rho_f \bar{u}^2}{2} \qquad (2.19)$$

where D is the hydraulic diameter and $\bar{u}$ is the mean fluid velocity across the duct. f is defined empirically and is a function of the relative roughness of the channel wall and of the Reynolds number. Equation 2.19 is customarily used for incompressible flow but it has been shown by Egli (1937) that it can also be applied to compressible flow. He also claims that f is independent of the compressibility of the fluid.

The hydraulic diameter is defined as four times the ratio of the cross sectional area of the flow to the perimeter in contact with the fluid. Thus, for a rectangular duct $D = 4bH/(2b + 2H)$ and since $b >> H$ then $D = 2H$ and equation 2.19 becomes:

$$\frac{dp}{dx} = - \frac{f}{H} \frac{\rho_f \bar{u}^2}{4} \tag{2.20}$$

A number of empirical formulae are available for the friction factor and the Blasius equation was found by Beavers et al (1971) to agree well with results from a high aspect ratio rectangular duct up to a Reynolds number, Re, of 2.8×10^4. When written in terms of equation 2.20, the Blasius relation is:

$$f = 0.316 \, \mathrm{Re}^{-1/4} \tag{2.21}$$

where

$$\mathrm{Re} = \frac{2\rho_f \bar{u} H}{\mu} \tag{2.22}$$

Substitution of equation 2.21 in equation 2.20 then gives us:

$$\frac{dp}{dx} = - 0.079 \frac{\rho_f \bar{u}^2}{H} \left(\frac{\mu}{2\rho_f \bar{u} H} \right)^{1/4} \tag{2.23}$$

By continuity, $\dot{m} = \rho_f \bar{u} b H$, and equation 2.23 becomes:

$$\frac{dp}{dx} = - 0.079 \frac{1}{\rho_f H^3} \left(\frac{\mu \dot{m}^7}{2b^7} \right)^{1/4} \tag{2.24}$$

which for a perfect gas results in:

$$\frac{dp}{dx} = - 0.079 \frac{R\theta}{pH^3} \left(\frac{\mu \dot{m}^7}{2b^7} \right)^{1/4} \tag{2.25}$$

If we now integrate equation 2.25 with respect to x and substitute the limits $p = p_1$ at $x = 0$ and $p = p_2$ at $x = l$, we arrive at the following expression for the turbulent mass flow through a duct length l:

$$\dot{m} = b \left(\frac{H^3}{0.079 R\theta l} \left(\frac{2}{\mu} \right)^{1/4} \left(p_1^2 - p_2^2 \right) \right)^{4/7} \tag{2.26}$$

2.2 The Multiple-Disc Motor

As the first machine constructed to determine the feasibility of this concept, the motor was crude with respect to mechanical design. The aim was to investigate its operating characteristics and to obtain experimental torque and flowrate measurements which could be compared with theoretical predictions. Sections 2.2.1 and 2.2.2 describe the design and the construction of the prototype motor and Section 2.2.3 explains the difficulties which were encountered. Section 2.2.4 describes the experimental rig used for flowrate measurement and the tests which were undertaken.

2.2.1 Design

Study of the theoretical equations shows that the gap between the discs has to be very small in order to keep the flowrate

reasonably low which leads to the requirement for very thin, and therefore flexible, restrictor plates. 50 μm thick steel shim is flexible but still workable and so was chosen for the plates and a disc spacing of 250 μm was chosen to allow for clearance. Dimensions of 130 mm and 90 mm were chosen for the outer and inner diameters of the ducts respectively. These dimensions lead to the requirement for 16 ducts to produce an estimated torque of 1.5 Nm (which is equivalent to a small DC motor) at an inlet pressure of 6 bar gauge.

It was necessary to amend the design of the motor proposed in Section 1.3 (see Fig. 1.9) because flexible plates of that design would most likely be prone to unstable behaviour such as flutter and/or buckling. In the amended design which is shown in Fig. 2.2, the plate has no unsupported edges which, it was hoped, would reduce the likelihood of instability.

The discs were designed to be rigid but light. They were manufactured from aluminium alloy for low inertia and workability and the 2.5 mm thickness was considered to be the thinnest the discs could be while remaining flat. The ducts were formed by a step change in thickness of each disc round the periphery and the 17 discs result in a rotor width of 42.5 mm.

Since the predicted torque was low, the motor was designed without seals between the shaft and the housing in order to minimise friction. It was therefore necessary to keep the clearance between the rotor and the casing as small as possible to ensure that the bulk of the flow would pass through the ducts and not out through the bearings. This allowed a comparison of the theoretical and experimental results. Initially the design had a clearance of 50 μm

between the rotor and the casing but the axial clearance had to be increased to 150 μm to prevent contact.

2.2.2 Construction

The discs were first machined to the correct thickness with the duct cut out of the periphery and the outer diameter was left slightly oversize. They were then clamped together on the shaft and the outer diameter was turned down to size. Location on the shaft was by a spigot at one end and a nut and washer at the other. This was satisfactory while the discs were perfectly flat immediately after manufacture but over a period of two weeks they buckled due to ageing. The shaft was then re-designed with a fixed steel disc at one end and a threaded one at the other. The latter could be torqued up to flatten the discs to within the required tolerance. The completed rotor assembly is shown in Plates 1 and 2.

On mounting the rotor in the housing it was found that although the radial clearance of 50 μm was satisfactory, the axial clearance had to be increased to 150 μm on both sides since the discs were slightly buckled. With no perceptible evidence of contact the static friction was 4.9×10^{-4} Nm.

The restrictor plates and the spacers which are located between the plates were made on a CNC mill which produced a set of perfectly matching location holes on each part. The thin steel plates were machined as a stack, clamped between steel plates 5 mm thick. Since the machining tolerance was 25 μm and clearance between the restrictor plate and the discs was 100 μm in each of 16 ducts, it was necessary to match each spacer with a disc on the rotor before assembly by measuring the distance between each gap in the rotor and

the thickness of every spacer. The assembly of the plates in preparation for insertion in the motor is shown in Plates 3 and 4 and the location in the motor is shown in Plate 5.

With the plate assembly positioned in the motor, the shaft would not rotate until all the nuts on the housing were torqued up tightly and some friction could still be felt in certain regions of each revolution which was due to slight buckling of the discs. The static friction at the position of minimum friction was 8.1×10^{-3}Nm.

2.2.3 Operational Difficulties

With the air supply turned on, the rotor would not rotate and above 0.25 bar gauge a high pitched noise could be heard from within the motor. The retarding force increased as the pressure was increased and a dial gauge showed that the shaft moved a distance of 75 μm axially towards the fixed bearing. The movement was initiated with the slightest pressure and was completed by approximately 0.2 bar gauge, the shaft remaining stationary at each pressure.

Limited rotation over a third of a revolution was achieved with air flowing through the motor by altering the position of the fixed bearing with various thicknesses of steel shim placed between the bearing housing and the motor housing. Rotation became increasingly difficult with and without an air flow, so the motor was dismantled to assess the damage. The damage to the restrictor plates was immediately obvious. Four plates were fractured at the downstream edge and an example of one is shown in Plate 6. All plates were either dented or scored by the outer edge of the discs.

Close inspection of the damage to the plates revealed that a block of six spacers and plates had to be moved approximately 50 μm

axially to reduce contact. This was achieved by reducing the thickness of the spacer at one end by 50 μm and inserting a 50 μm thick shim, the shape of a spacer, at the other. Any badly damaged plates were replaced and the motor was reassembled.

During the second trial the rotor could be rotated more freely by hand throughout a full revolution than on the first trial but the problem of the rotor locking up with any amount of air flow through it still remained. Pneumatically powered rotation was eventually achieved by pushing the nib of a ball point pen into the end of the shaft which forced it towards the centre and on two occasions the rotor revolved at approximately 20-30 rev/s. After these tests the motor would not turn under its own power. On dismantling the motor, many plates were again found to be badly damaged from fracture and denting.

2.2.4 Experimental Rig and Description of Tests

Flowrate was the only aspect of performance to be measured since the lack of rotation precluded torque measurement. The rig used in the measurement of the flowrate is shown in Fig. 2.3. A settling tank was attached to the inlet of the motor and a laminar flowmeter was positioned upstream of this with a length of pipe attached to the entry containing a wire wool baffle to ensure a uniform flow to the flowmeter. A gate valve attached to the air supply controlled the flowrate through the rig. To calculate the mass flowrate, the temperature and the static pressure downstream of the flowmeter were measured along with the differential pressure across the meter. The instrumentation was as follows:

i) Static pressure : Mercury filled U-tube manometer.

ii) Differential pressure : Vernier type water micromanometer.

iii) Temperature : Thermocouple.

iv) Atmospheric pressure : Mercury barometer.

Measurements were taken with the rotor stationary over an inlet pressure range of 0-1 bar gauge rather than the originally planned 0-6 bar gauge since some rotation was achieved below 1 bar gauge while proving impossible above. One set of results was taken on each assembly of the motor; named Test M1 on the first assembly and Test M2 on the second. Plots of mass flowrate against pressure drop for the two tests are shown in Fig. 2.4 along with various theoretical predictions which are discussed in Section 2.4.

2.3 The Single-Disc Motor

The objectives in building the single-disc motor were to measure the torque output and to investigate the effect of rotational speed on the torque and flowrate. The primary aim was therefore to design a motor which would rotate and not lock up as the multiple-disc motor had done. Since it was considered that the problem with the first motor was due to buckling of the flexible restrictor plates, the single-disc motor was therefore designed without flexible components. The motor is described in Section 2.3.1 and problems encountered obtaining rotation with this motor and the means whereby these problems were overcome are discussed in Section 2.3.2. The experimental work is described in Section 2.3.3.

2.3.1 Design

A diagram of the single-disc motor is shown in Fig. 2.5. The principle of operation is the same as that of the multiple-disc motor with flow passing through two unequal sized channels on the periphery of the disc. Force is transmitted by viscous shear from the fluid to the disc and the resultant torque is in the direction of the flow through the larger passage.

The rotor is composed of a single flat disc which was manufactured from Tufnol. This material is light and is not prone to weathering as the aluminium alloy was found to be in the original motor. The casing is in two halves, one made of aluminium alloy and the other of perspex. The disc is situated in the aluminium half of the casing in a recess slightly larger than itself and the flow channels are machined into the casing, around the periphery of the disc. The shaft runs on small roller bearings with one adjustable axially and the other radially.

The ducts in the casing were machined on a CNC mill which enabled easy alteration of the duct depth between tests by running the same program with the depth setting changed. It was also a simple matter to reduce the clearance between the disc and the casing by using a lathe to take a cut off the face of the aluminium half of the casing.

2.3.2 Preliminary Tests

When the motor was first assembled the bearing housings were positioned so that the disc could rotate freely without touching the casing and the bearings were preloaded to remove end-float. With the air supply turned on it was found that the disc rotated freely up to

an inlet pressure of approximately 0.09 bar gauge whereupon it jammed against the casing. Rotation was subsequently found to be possible up to a pressure of 1 bar gauge by removing the preloading nuts and continually adjusting the screwed housing as the pressure was varied. A further point of note is that of the two discs which were manufactured only one would rotate with an air flow. It was found that the disc which worked had a slight buckle and the one which failed was perfectly flat.

Each time the rotor locked up, the disc could be observed through the perspex wall jumping across to the aluminium wall and the effect of adjusting the screwed bearing was to pull the disc back towards the centre of the duct. It was ascertained that the disc always moved to the side through which there was most leakage out by the shaft.

2.3.3 Experimental Rig and Description of Tests

Flowrate through the single-disc motor was measured on the same rig that had been used for the multiple-disc motor and is described in Section 2.2.4. Torque output was measured on the apparatus shown in Fig. 2.6 by taking the product of the radius of the pulley and the difference in tension in the band (i.e. $T_1 - T_2$). The rotational speed of the rotor could be varied by altering the mass of the counterweight and the rate of rotation was measured by timing a number of revolutions with a stop watch.

The tests have been divided into six series, each with a different duct height H. In Tests S1 to S4 the clearance h_c was held constant while the duct height was varied and in Tests S5 and S6 both H and h_c were decreased by the same amount by taking a thin cut off

the aluminium half of the casing. Details are given in Table 2.1.

In each series of tests the rotational speed was varied from zero up to about 5 rev/s at each inlet pressure up to a maximum of 0.6 bar gauge. A mercury filled U-tube manometer was used to measure pressures up to 0.6 bar gauge and, in Test S6, a water filled U-tube was used up to 0.055 bar gauge.

Torque and flowrate results from each series of tests are shown in Figs. 2.7 to 2.12. Figs. 2.13a and 2.13b show the results at zero or near zero speed compared with theoretical predictions - the experimental points and the theoretical prediction for each test are shown in the same colour; the red theoretical line in Fig. 2.13a representing the torque prediction for both tests S4 and S5. The theoretical equations derived in Section 2.1 are used to calculate the flow through Regions *A* and *B* (see Fig. 2.5) and to calculate the torque exerted on the disc by the flow through Regions *A* and *B*. The flowrate prediction includes an estimation of leakage which is described in Appendix A.

2.4 Discussion

Theoretical predictions of torque and flowrate for the viscous shear torque motor have shown that the gap between the discs has to be very small to limit air consumption. 250 μm disc spacing and 50 μm thick steel plates were used in the multiple-disc motor and these were considered to be the minimum sizes that could be used, with the available materials and workshop facilities, while maintaining some clearance. Even this gap size resulted in a flowrate of 17.5 l/s at a pressure of 0.87 bar gauge for an estimated 0.2 Nm. A practical working motor will therefore need even smaller

disc spaces and the restrictor plates will consequently be flexible.

On building the multiple-disc motor with flexible restrictor plates it was found that the rotor locked up when air flowed through it. Although it was originally assumed that the thin plates had buckled and pressed against the discs, thus producing a braking action, it was also found to be a problem with the single disc motor which had no flexible parts. It was subsequently found that the rotor in both motors moved axially in the casing due to air leakage through the bearings and this caused the rotor to rub against the casing which prevented rotation. This was remedied by incorporating adjustable bearing housings in the single-disc motor which allowed the shaft to be adjusted as required. This worked for the slightly buckled disc but not the perfectly flat one. An explanation for this may lie in the work of Taylor and Saffman (1957) who found a rise in pressure in the airspace between two flat discs when they are very close together and one of them rotates. The rise in pressure occurred if the plates were closer than 20 μm and this is the same order of magnitude as rotor to casing clearance in the shear motors. Taylor shows theoretically that the rise in pressure can be explained by the effects of compressibility which make the air layer exert a pressure when two wavy or rough surfaces move relative to each other. He concludes that the experimental discs could never be perfectly flat or perfectly parallel and hence the pressure will rise as the two surfaces are brought together. Such a mechanism may be present in the single-disc motor keeping the slightly buckled disc away from the casing while the force with the flat disc may not be large enough to counteract the force due to leakage.

Two potential problems with the flexible restrictor plates were

flutter and buckling. Early work with the multiple-disc motor indicated that a problem did exist when the downstream edge of some plates broke up during testing and it appeared to be due to vibration fatigue. Buckling may not have been involved in the rotor locking up and since the rotor rotated rapidly when pushed back to the centre of the casing it is unlikely that the plates were buckled under those conditions.

The single-disc motor was built primarily to measure torque and to investigate the effect of rotational speed on torque and flowrate. Results from this motor are shown in Figs. 2.7 to 2.14 with the experimental results in Fig. 2.13a and Fig. 2.14a showing the expected linear increase in torque with pressure drop. Figs. 2.7 to 2.12 show that torque and flowrate are independent of rotational speed up to 5 rev/s (The scatter in the results of the torque measurements was due to difficulty in operating the pulley apparatus rather than due to measurement error or hydrodynamic effects). Theoretical analysis also shows that the effect of speed is negligible. Taking the "worst case" of the smallest duct (i.e. h_c in Test S1) at its lowest inlet pressure and highest velocity, we find from equations 2.9 and 2.18 that the critical velocities are 147 rev/s for torque and 49 rev/s for flowrate. The maximum speed of 4 rev/s at the lowest pressure in Test S1 is well below both these values.

Using the multiple-disc motor dimensions in equation 2.9, gives the result that, at 4 rev/s, the torque exerted on the disc in the restricted section is sensitive to the velocity up to 0.004 bar. Above this, the sensitivity decreases linearly with pressure; thus at 0.04 bar the viscous term in equation 2.8 is one tenth the magnitude

of the pressure term. Similarly, using equation 2.18, the flowrate is sensitive to speed up to 0.013 bar.

Flowrate was measured through both motors and compared with theoretical predictions. The prediction of flowrate through the single-disc motor agrees particularly well with experimental results in Fig. 2.14b although theory and experiment diverge at higher pressures in Fig. 2.13b. The flow model used for the central region is probably the reason for the discrepancy because a direct radial route from the perimeter to the centre was assumed and in reality it will consist of a spiraling inflow due to the tangential component of the incoming flow, as in the Tesla turbine. The spiral flow paths effectively increase the distance the fluid travels and the path length increases as the tangential component increases. This increases the resistance to flow and reduces the rate of increase in flowrate. Further confirmation of the effect of the central region on the over-estimation of the flowrate can be seen in the result of Test S5 in Fig. 2.13b. The depth of the central region was reduced in this test and closer agreement was found between theory and experiment.

Fig. 2.4 shows experimental flowrates through the multiple-disc motor compared to various theoretical predictions. All four predictions assume that the unrestricted duct occupies three quarters of the circumference and two assume that the restricted section occupies a full quarter (i.e. $l/C = 0.25$). Since the restrictor plate did not occupy the complete area of the restricted section, predictions with the restricted section equal to one eighth of the circumference ($l/C = 0.125$) are also included. Although the rotor was found to move axially and it could therefore be assumed that the

discs were pushed against the plates it is seen that the theoretical curves with the plate against the disc (i.e. $h/(H-s) = 1.0$) do not agree with the experimental results. The best agreement is found with a restricted section one eighth the circumference and the plate in the centre of the duct (i.e. $h/(H-s) = 0.5$).

In obtaining the theoretical predictions of flowrate a critical Reynolds number of 2000 was used. Not only is this the usual value for flow through circular section pipes but it was also found by Egli (1937) to apply to high aspect ratio rectangular ducts when $Re = 2\rho uH/\mu$. The change of slope in the theoretical flowrate line for the single-disc motor in Fig. 2.14b is due to the transition from laminar to turbulent flow in the main duct and the experimental points can be seen to undergo a similar change of slope. The experimental results from the multiple-disc motor shown in Fig. 2.4 undergo a transition at 0.4 bar which is similar to that seen on the theoretical line closest to the experimental points; the transition in the theory is again in the main duct. It is therefore not unreasonable to assume that transition from laminar to turbulent flow in the main duct has been successfully predicted by the theory.

2.5 Conclusions

Two experimental motors have been constructed to investigate the feasibility of the viscous shear torque motor concept and to corroborate theoretical predictions of performance. The multiple-disc motor provided flowrate measurements and the single-disc motor provided torque and flowrate measurements over a range of pressures, rotational speeds and duct sizes. These results have confirmed that the theoretical predictions are of the correct

order of magnitude and that the disc spaces need to be very small to limit air consumption.

The need for small disc spaces has introduced the need for very thin restrictor plates which are inherently flexible but the behaviour of flexible plates in thin ducts is an unresearched area. The flexible plates in the multiple-disc motor appear to have suffered breakage due to flow induced flutter and they may have played a role in the locking up of the rotor by buckling. The requirement of flexible plates in thin ducts is therefore an important factor in the consideration of the feasibility of the viscous shear torque motor design and warrants further investigation. The remaining chapters are devoted to this topic.

Table 2.1

Duct Heights in the Single-Disc Motor

Test No	Duct Height H (μm)	Clearance h_c (μm)
S1	360	150
S2	440	150
S3	550	150
S4	670	150
S5	645	125
S6	620	100

CHAPTER 3

EXPERIMENTAL STUDY OF FLEXIBLE PLATE BEHAVIOUR IN A THIN DUCT

Two separate experiments were undertaken to investigate the behaviour of a flexible plate in a thin duct. The first experiment involved a plate in a duct identical to those found in the motor and the walls were made of perspex so that the plate behaviour could be observed. The second experiment involved a flexible plate in a straight duct. This allowed a more general study of plate stability to be undertaken and the analysis in subsequent chapters is based on this model. The perspex duct experiment is described in Section 3.1 and the straight duct is described in Section 3.2. A discussion of the results obtained from both experiments is given in Section 3.3.

3.1 Perspex Model of a Disc Space

The aim of this experiment was to observe the behaviour of the flexible plate in conditions as close to those in the multiple-disc motor as possible. A model of a single disc space was therefore made with walls of perspex which allowed visual observation of the plate. The apparatus is described in Section 3.1.1 and the tests are described in Section 3.1.2. Section 3.1.3 discusses the results from this first experiment.

3.1.1 Description of Apparatus

The walls of the model were 13 mm thick perspex plates, machined flat on a lathe and polished to a smooth, transparent finish. The shape and height of the duct was formed by 250 μm thick steel shim

positioned between the two walls as shown in Fig. 3.1. The restrictor plate was made from the same 50 μm thick steel shim used in the multiple-disc motor and the lateral position of the plate was achieved with various thicknesses of steel spacer placed either side of it. To achieve similar entrance and exit conditions to those in the motor, channels were cut in the perspex walls coincident with the inlet and outlet ducts. All dimensions were the same as those in the motor.

A proximity sensor was fitted in wall *A* (see Fig. 3.1) to measure the position of the plate in the middle of the restricted section of the duct. It had to be recessed about 100 μm into the wall to obtain results. The output was displayed on an oscilloscope. A pressure tapping was drilled in the wall next to the sensor and a second tapping was drilled in the facing wall (wall *B*), directly opposite it. The pressure difference across these taps was measured with a water manometer and the upstream pressure was measured with a mercury manometer.

3.1.2 Description of Tests

In the tests performed with this apparatus the position of the plate and the pressure difference across it were measured over a range of inlet pressures up to 0.5 bar gauge. The variables in the tests were the plate curvature (which was due to the steel shim having been stored in a roll) and the thickness of the spacers positioning the plate edge. The tests are numbered P1 to P8 and are summarised in Table 3.1 where the wall towards which the plate was initially curved is listed as the ratio h/H (0 denoting wall *A* and 1 denoting wall *B*). The support position is given by $e/(H-s)$, where e

is the thickness of the spacer nearest to wall *A*.

The results of Tests P1 to P4 with the plate edge supported in the centre of the duct are shown in Figs. 3.2a and 3.2b. Fig. 3.2a shows the position against inlet pressure and Fig. 3.2b shows the pressure difference across the plate against inlet pressure. The same information from Tests P5 to P8 in which the plate edge was supported off-centre is shown in Figs. 3.3a and 3.3b

3.1.3 Discussion of Results

During many of the tests a high pitched noise could be heard which was very similar to that heard in the motor. The noise started above a pressure of approximately 0.25 bar gauge which was the same pressure at which the noise started in the motor. While the noise lasted, fracture lines developed at the downstream edge of the plate and small pieces broke off. The resulting damage was the same as that found on the plates removed from the motor (see Plate 6). The frequency of the vibration which caused this breakage was measured on the oscilloscope and found to be 1.4 kHz at 0.26 bar gauge.

In Fig. 3.2a it can be seen that the plate moved over to wall *A* ($h = 0$) as the pressure was increased in Tests P1 and P2 and at higher pressures it moved back towards the centre. The pressure imbalance across the plate in those tests can be seen in Fig. 3.2b and in an attempt to reduce this imbalance a hole was drilled in the plate next to the proximity sensor. This plate was used in Tests P3 and P4 but a pressure imbalance still existed and the same movement occurred as can be seen in Figs. 3.2b and 3.2a respectively.

Fig. 3.2a shows that the plate curvature had an effect at low pressure with the plate moving in the opposite direction to the curve

in all four tests. Since the only imbalance in the system, other than the plate curvature, was the sensor recess, it was concluded that the recess caused the plate motion towards wall *A*.

The results of Tests P5 to P8 with the plate initially positioned off-centre are shown in Figs. 3.3a and 3.3b. In Fig. 3.3a it can be seen that there is a threshold pressure in each test at which the plate diverged to the far wall. Similar behaviour was found by Thorpe et al (1971) with a rigid plate supported at its downstream end in a parallel walled duct with an incompressible turbulent flow of air. With the plate initially parallel to the walls and supported in the centre, Thorpe found that it diverged towards either wall but when held off-centre it always diverged to the farthest wall. Referring to the work of Thorpe (1964), he concludes that this is due to a larger static pressure in the smaller channel. With an estimated Reynolds number of 540 in the large channel of the restricted section in Test P5, for example, the buckling in the present test was probably due to the manner in which the flow negotiates the bending duct rather than due to any static pressure effects.

3.2 A Flexible Plate in a Straight Duct

The aim of this experiment was to initiate a more in depth study of flexible plate behaviour in a thin duct. The geometry of the single duct model described in the previous section leads to a complex flow pattern and is specific to this particular design of shear torque motor. A simpler configuration was therefore used as the starting point for a general study of flexible plate behaviour in a duct and the theory described in subsequent chapters is based on

this. The configuration consists of a straight, high-aspect ratio, parallel walled duct with a plate positioned between the walls and clamped at the upstream and downstream ends. This experiment was simply a qualitative visual study of the plate behaviour and no measurements were taken. The apparatus is described in Section 3.2.1 and the observations which were made are described in Section 3.2.2.

3.2.1 Description of Apparatus

The construction of the duct is shown in Fig. 3.4. The side walls were made of aluminium alloy, the upper and lower walls of perspex and the plate was manufactured from 50 μm thick steel shim. The duct formed by these walls was 23 cm long by 2.2 cm wide and the clearance between the plate and the perspex walls was 50 μm. The height of the duct (perpendicular to the plate plane) was 250 μm along the central 20 cm of the duct length and 3mm over a distance of 15 mm at the inlet and outlet. The plate was supported at its upstream and downstream edges between spacers whose thickness could be varied.

A light was placed below the duct and a travelling microscope positioned above so that the plate's position and behaviour could be observed along its length. The light from a stroboscope was also directed onto the duct from above and proved a valuable aid in detecting vibration.

A series of tests were undertaken with the plate supports at various heights and some tests were run with no support at the downstream end. The upstream pressure was varied from 0 to 1 bar gauge and observations were made through the microscope before and after the airflow was turned on. Notes of these observations

were taken and a summary of these is given below.

3.2.2 Description of Observations

When viewed in the duct with no airflow, the plate was slightly wavy even when tensioned by the supports. With air flowing through the duct the plate flattened out into a straight line between the end-points. This occurred with the end-points in the centre of the duct and about three quarters of the way across the duct. This straightening of the plate also occurred with no downstream support and it remained stable in this case up to approximately 0.25 bar gauge. Above this pressure the unsupported plate fluttered violently. Other tests also had a pressure threshold above which flutter appeared and the threshold increased as the tension placed on the supports was increased.

3.3 Discussion and Conclusions

The two experiments described in this chapter have given some indication of the behaviour of a flexible plate in a thin duct. Two types of instability were found. Both the experiments showed flutter instability but only the perspex duct model showed divergent buckling behaviour.

Although the plate in the perspex duct had a tendency to divergent behaviour, it returned to the centre at flowrates higher than those which caused the divergence. With the plate in this model not having any form of support along its leading edge, any imbalance such as that caused by the proximity sensor recess would probably act to destabilise it. The fact that the membrane in the straight duct remained stable in a position three quarters of the way across the

duct, while in the perspex duct the plate diverged when positioned off-centre, is an indication that the divergence was more due to the geometry rather than an inherent stability problem for flexible plates in thin ducts.

Flutter occurred at approximately the same pressure in the perspex duct as it did in the straight duct test which had no downstream support. This would indicate that the same mechanism is responsible for the flutter in both experiments. Also, since the fracture damage to the plates in the motor was the same as the damage to the plate in the perspex duct due to flutter, the same mechanism would account for the damage in the motor. The flutter in the straight duct was stopped by tensioning the plate, so it is not unreasonable to assume that the damage to the plates in the motor could be prevented with tension.

Table 3.1

Details of Perspex Duct Experiment

Test No	Plate Support Position $e/(H-s)$	Curvature Direction h/H
P1	0.5	0
P2	0.5	1
P3*	0.5	0
P4**	0.5	1
P5	0.25	0
P6	0.25	1
P7	0.75	1
P8	1.0	1

* A 3 mm hole was drilled in the plate, upstream of the proximity sensor.

** A 3 mm hole was drilled in the plate, downstream of the proximity sensor.

CHAPTER 4

INITIAL ANALYSIS OF MEMBRANE MOTION IN A THIN DUCT

The initial investigation of the viscous shear torque motor has shown the need for flexible plates in thin ducts. Work on the experimental motor has shown that this leads to problems with plate fracture and that buckling of the plates is possibly the cause of rotor lockage. A theoretical analysis of the dynamics of a flexible plate in a thin duct was undertaken to study this problem and complements the experimental work described in Chapter 3. The analysis starts in this chapter and is finalised in Chapter 5. Since the plate is very thin and the changes in slope are small due to the small height of the duct, the plate is assumed to be without bending rigidity and will henceforth be referred to as a membrane.

A typical qualitative stability analysis of the problem is described in Section 4.2 in which the membrane is held rigidly in a position displaced from equilibrium and the force distribution along it is calculated. The aim of this approach was to see if the force distribution would tend to return the membrane to the equilibrium position if it were free to move. The results from this model proved inconclusive and so a quasi-steady model was developed to provide a quantitative stability analysis. This is described in Section 4.3. In this model the membrane is free to move due to the forces acting on it and the instantaneous position of the membrane determines the flow. We shall start in Section 4.1 with a description of the system which is to be modelled.

4.1 Description of Problem

The problem to be considered is the stability of a membrane in a thin duct. We shall consider a straight, high-aspect ratio, parallel walled duct with stationary walls. The membrane occupies the full width of the duct and is pin-jointed in the entrance and exit planes. This configuration is shown in Fig. 4.1 and is very similar to the straight duct experiment described in Chapter 3.

It will be assumed that a motor can be built to the accuracy required so that the plate supports are in the centre of the disc spaces. The membrane end-points are therefore positioned at the mid-height of the duct and the stability analysis focusses on the effect of perturbing the membrane from its equilibrium position along the centre of the duct. For the purpose of the theoretical model it will be assumed that although the membrane possesses mass, it is infinitely thin so that the combined height of the upper and lower channels at any point equals the duct height H.

Fluid flows through both channels from a common reservoir at the inlet and exhausts to the atmosphere at the outlet. The flow is compressible and since $H << l$ it is assumed to be laminar. Entrance and exit losses will be neglected and a fully developed flow will be assumed to exist in both channels. Side leakage will be neglected and since $H << l$ then, as is common in the analysis of air bearings (e.g. Gross 1962), the pressure gradient in the y-direction is considered negligible in comparison with the gradient in the x-direction. The flow problem therefore reduces to only the x-direction. It is also assumed that isothermal conditions exist since the height of the duct is so small that perfect heat conduction can be assumed. On the assumption that the fluid is Newtonian, the

flow is therefore also isoviscous.

4.2 Static Model

In the static model the membrane is held rigidly in a predefined shape and the flow is steady in both channels. The aim of this approach is to ascertain the force distribution along the membrane and to see if any conclusions can be drawn regarding the possibility of the membrane returning to the centre of the duct if it were allowed to move.

4.2.1 Steady Flow Analysis

The mass flowrate of a compressible laminar flow through a rectangular duct is given by equation 2.15 which, with $\omega = 0$, gives:

$$\dot{m} = - \frac{pbh^3}{12\mu R\theta} \frac{dp}{dx} \tag{4.1}$$

where h is the height of the membrane from the wall. Rearrangement of equation 4.1 gives:

$$\frac{dp^2}{dx} = - \frac{24\mu R\theta \dot{m}}{bh^3} \tag{4.2}$$

If we now integrate equation 4.2 with respect to x and substitute the limits $p = p_1$ at $x = 0$ and $p = p_2$ at $x = l$, we arrive at:

$$\dot{m} = \frac{b\left(p_1^2 - p_2^2\right)}{24\mu R\theta \; F(l)} \tag{4.3}$$

where:

$$F(l) = \int_0^l \frac{dx}{h(x)^3} \tag{4.4}$$

Substitution of equation 4.3 into equation 4.2 now gives us:

$$\frac{dp^2}{dx} = \frac{p_1^2 - p_2^2}{F(l)h^3} \tag{4.5}$$

If we now integrate equation 4.5 with respect to x and substitute the limits $p = p_1$ at $x = 0$ and $p = p(x)$ at x, we arrive at the following expression for the pressure distribution along a duct of varying height:

$$p(x)^2 = p_1^2 - \frac{F(x)}{F(l)}\left(p_1^2 - p_2^2\right) \tag{4.6}$$

where:

$$F(x) = \int_0^x \frac{dx}{h(x)^3} \tag{4.7}$$

From equation 4.6 we can see that if the membrane is parallel to the walls (i.e. if $h(x)$ = constant) then the pressure distribution is given by:

$$p(x)^2 = p_1^2 - \frac{x}{l}\left(p_1^2 - p_2^2\right) \tag{4.8}$$

This distribution is the same in any parallel walled duct regardless of the height. There is therefore no force across the membrane when it is parallel to the walls at any height in the duct and it is then in stable equilibrium.

4.2.2 Description of Tests

The force distribution was calculated with the membrane in various parabolic shapes. With $h = h_1$ at $x = 0$, $h = h_2$ at $x = l$ and $h = h_3$ at $x = l/2$ then the function defining h is:

$$h(x) = h_1 + \left(4h_3 - 3h_1 - h_2\right)\frac{x}{l} + 2\left(h_2 - 2h_3 + h_1\right)\left(\frac{x}{l}\right)^2 \tag{4.9}$$

The integrals resulting from the substitution of equation 4.9 in equations 4.4 and 4.7 were evaluated numerically using the trapezoidal rule in a FORTRAN77 computer program. This program calculated the pressure distribution in channels *a* and *b* and, from this, calculated the force across the membrane at a number of points along its length.

The dimensions of the duct modelled in the tests were based on the straight duct experiment described in Chapter 3. The length l was 0.18 m and the height H was 200 μm. The inlet pressure was arbitrarily set at 0.6 bar gauge for all the tests. No other pressures were tested since, by equation 4.6, the pressure difference across the membrane will always be in the same direction for a given membrane shape, if $p_1 > p_2$.

The pressure distribution was determined with the membrane in many positions in the duct. For this set of tests the end-points were positioned at unequal heights as well as at equal heights with the membrane in a parabolic shape or a straight line. It was found in all cases, that if $dh/dx < 0$ then $p_a - p_b > 0$ and if $dh/dx > 0$ then $p_a - p_b < 0$. A typical example of a result with a parabolic shape is shown in Fig. 4.2 which is the force distribution for the case shown in Fig. 4.1 (i.e. with $h/H = 0.5$ at $x = 0$ and $x = l$; and $h/H = 0.4$ at $x/l = 0.5$).

4.2.3 Discussion and Conclusions

The purpose of this static membrane, steady flow analysis, was to see if the stability of the membrane could be predicted from a knowledge of the force distribution along its length. Stability could be said to be achieved if the direction of the force at each

point was towards the position of equilibrium.

From the result shown in Fig. 4.2, it is not possible to predict if the membrane would return to the centre if it were allowed to move from that position. The force at the left hand end certainly acts towards the centre, but the force at the right hand end is pushing that portion further away from the centre. The situation is further complicated by the fact that the pressure distribution will change as the membrane moves and it is impossible to predict what will happen at the downstream end of this example.

The static model therefore did not permit an assessment of the membrane stability since the nature of the force distributions which were found did not allow the movement of the membrane to be predicted with any certainty.

4.3 Quasi-Steady Analysis

In the quasi-steady analysis the membrane moves under the action of the forces acting upon it and the instantaneous position of the membrane determines the pressure distribution in both channels. A full description of the derivation of the membrane equation of motion and all the assumptions made is given in Section 5.1. The equation of motion is shown to be:

$$\frac{\partial^2 h}{\partial t^2} = \frac{T}{\rho}\frac{\partial^2 h}{\partial x^2} + \frac{1}{\rho}\left(p_a - p_b\right) \qquad (5.4)$$

where T is the membrane tension per unit width; ρ is the membrane density per unit area; and t is time. The flow conditions assumed to exist in this model are the same as in the static model and so equation 4.6 for the pressure distribution also applies to each channel in this model.

The membrane equation of motion was solved using a finite difference technique which is described in Section 4.3.1 and the pressure difference at each point was calculated by the same method used in the static model. A FORTRAN77 program was written specially for the purpose of this solution and Section 4.3.2 discusses the results from this model.

4.3.1 Numerical Solution Method

The space-time domain was split up into a grid with equal intervals in x and t and the hyperbolic equation of motion for the membrane was solved using a second order explicit finite difference method as described by Ames (1977). We take the Taylor series of equation 5.4, ignore second order small quantities and express it in finite difference form at node i, j as follows:

$$\left(\frac{h_{i,j+1} - 2h_{i,j} + h_{i,j-1}}{\Delta t^2}\right) = \frac{T}{\rho}\left(\frac{h_{i+1,j} - 2h_{i,j} + h_{i-1,j}}{\Delta x^2}\right) + \frac{1}{\rho}\left(p_a - p_b\right)_{i,j} \tag{4.10}$$

After some rearrangement we obtain h at the next time step :

$$h_{i,j+1} = \frac{Tm^2}{\rho}\left(h_{i+1,j} + h_{i-1,j}\right) + 2\left(1 - \frac{Tm^2}{\rho}\right)h_{i,j} - h_{i,j-1} + \frac{\Delta t^2}{\rho}\left(p_a - p_b\right)_{i,j} \tag{4.11}$$

where $m = \Delta t/\Delta x$. Since $h_{i,-1}$ does not exist, a false boundary has to be employed on the first time step by defining the velocity of the membrane, ϕ, at j = 0:

$$\phi_{i,0} = \frac{h_{i,1} - h_{i,-1}}{2\Delta t} \tag{4.12}$$

From equation 4.11 and equation 4.12 we then obtain the following

expression for use on the first time step:

$$h_{1,1} = \frac{Tm^2}{2\rho}\left(h_{i+1,0} + h_{i-1,0}\right) + \left(1 - \frac{Tm^2}{\rho}\right)h_{1,0} - \Delta t\left(\phi_{1,0}\right) + \frac{\Delta t^2}{\rho}\left(p_a - p_b\right)_{1,0} \tag{4.13}$$

To ensure numerical stability when using this solution method Ames explains that the Courant-Friedrichs-Lewy (CFL) condition must apply. Discussion of this condition is given in Chapter 8. For this problem the condition is:

$$\frac{Tm^2}{\rho} \leq 1 \tag{4.14}$$

The solution will then converge to the differential problem, equation 5.4, as Δx and $\Delta t \rightarrow 0$.

4.3.2 Description of Tests

The dimensions of the duct modelled in the tests were again based on the straight duct experiment as in the static model described in the preceding section. Here, we have the addition of membrane density which was based on 50 μm thick steel shim (as used in the experimental work) with a value of 400 g/m^2. The perturbation from equilibrium was achieved by defining a shape for the membrane at $t = 0$ with an initial velocity of zero. The steady state pressure distribution in both channels was calculated according to the shape. A range of shapes, inlet pressures and tensions were tested.

4.3.3 Discussion and Conclusions

A typical result from this model was gained from a test with an inlet pressure of 0.1 bar gauge, a tension of 200 N/m and a gently curved initial membrane shape with $h/H = 0.4$ at $x/l = 0.25$ and

h/H = 0.6 at x/l = 0.75. The whole membrane, excluding the end-points, was found to oscillate with increasing amplitude until it touched each wall alternately. The velocity of the membrane in this test could reach approximately 2 m/s.

Now, the speed of sound in ambient air is approximately 340 m/s. Thus, in the time it took the membrane to move from one wall to the other a pressure transient would only have travelled 0.03 m. Since the length of the duct is 0.18 m and the wave would need to travel a number of lengths before a transient decays, the assumption of steady state flow at each instantaneous membrane position is erroneous. The quasi-steady approach therefore does not apply and a full unsteady analysis is necessary. This is the subject of the next chapter.

CHAPTER 5

ANALYSIS OF MEMBRANE MOTION IN A THIN DUCT

This chapter is concerned with the derivation of the equations which describe the motion of a flexible membrane in a thin parallel walled duct containing a viscous compressible flow. The duct geometry is the same as that in Chapter 4 and a diagram is shown in Fig. 4.1. The membrane is again pin-jointed at its ends and the supports are in the same plane as the duct inlet and outlet. In this chapter, the time dependent conservative form is used for both the continuity equation and the Navier-Stokes fluid equations. These are reduced to one space dimension by assuming no side leakage and by integrating across the channel perpendicular to the axis.

The equations relating to the membrane dynamics and to the fluid dynamics are derived in Sections 5.1 and 5.2 respectively and the dimensionless form of these equations is described in Section 5.3. The conservative form of the fluid equations which was used in the numerical solution is derived in Section 5.4 and a natural frequency of the system is described in Section 5.5.

5.1 Membrane Equation of Motion

In the derivation of the membrane equation of motion we can draw on theoretical work relating to the foil bearing. The foil bearing is composed of a flexible foil wrapped U-shaped round a shaft with a lubricating film of oil between. The first published account of the bearing was that of Blok and van Rossum (1953) in which a 75 μm thick cellulose foil was used and subsequent work by Patel and Cameron (1957) involved the use of 50 μm thick steel foil.

Theoretical analyses of the foil shape were published by Wildmann and Wright (1964) and Eshel and Elrod (1965) in which the equilibrium equation for the foil accounted for the pressure and tension forces but neglected bending force. Wildmann (1965) extended these analyses to include a term for bending. In the analysis of the membrane we shall assume perfect flexibility and the resulting equation is the unsteady form of Wildmann and Wright's equation.

The derivation of the equation of motion follows the conventional lines for a vibrating string (e.g. Kreyszig 1979) except that here an additional term for the pressure difference across the membrane is included. We shall consider the small element of the membrane shown in Fig. 5.1 and apply the following assumptions:

1. There is no resistance to bending.
2. The mass per unit area is constant.
3. The pressure on the upper and lower surfaces of an element is evenly distributed.
4. The slope at any point is small.
5. Tension due to the shearing action of the fluid flow is negligible compared to the tension exerted by the end points.
6. Gravitational forces are negligible in comparison to those due to tension or pressure.
7. Each element moves strictly perpendicular to the channel axis.
8. Stretching is negligible due to the small slope.

With the membrane offering no resistance to bending, the force due to the tension exerted at its end points is everywhere tangential to the curve of the membrane. Also, since the slope is small, the force due to the pressure difference in the horizontal direction is

negligible and, with no horizontal motion, the force balance is:

$$T = T_1 \cos\alpha = T_2 \cos\beta \tag{5.1}$$

The force in the vertical direction is composed of the force due to the pressure difference across the membrane and a force at each end of the element from the vertical component of the tensioning force. By Newton's second law the resultant of these forces is equal to the product of the mass of the element and its acceleration:

$$\rho\delta x \frac{\partial^2 h}{\partial t^2} = T_2 \sin\beta - T_1 \sin\alpha + p_a \delta x - p_b \delta x \tag{5.2}$$

Substitution of equation 5.1 into equation 5.2 gives:

$$\delta x \frac{\rho}{T} \frac{\partial^2 h}{\partial t^2} = \tan\beta - \tan\alpha + \frac{\delta x}{T}\left(p_a - p_b\right)$$

$$= \left(\frac{\partial h}{\partial x}\right)_2 - \left(\frac{\partial h}{\partial x}\right)_1 + \frac{\delta x}{T}\left(p_a - p_b\right) \tag{5.3}$$

Taking equation 5.3 in the limit $\delta x \rightarrow 0$ and rearranging results in:

$$\frac{\partial^2 h}{\partial t^2} = \frac{T}{\rho} \frac{\partial^2 h}{\partial x^2} + \frac{1}{\rho}\left(p_a - p_b\right) \tag{5.4}$$

The numerical methods used in the solution of the equations derived in this chapter are for use with first order partial differential equations. To make equation 5.4 compatible, we first define the membrane velocity, ϕ, and slope, ψ, as follows:

$$\phi = \frac{\partial h}{\partial t} \tag{5.5a}$$

$$\psi = \frac{\partial h}{\partial x} \tag{5.5b}$$

Inserting equations 5.5 in equation 5.4 leads to following membrane

equation of motion:

$$\frac{\partial \phi}{\partial t} = \frac{T}{\rho}\frac{\partial \psi}{\partial x} + \frac{1}{\rho}\left(p_a - p_b\right) \tag{5.6}$$

and we also have:

$$\frac{\partial \psi}{\partial t} = \frac{\partial \phi}{\partial x} \tag{5.7}$$

5.2 Fluid Equations

The equations relating to the flow in the lower channel will be derived here and since the same conditions are assumed to exist in both channels, the equations may also be applied to the flow in the upper channel with the relevant substitution of variables. Side leakage will be neglected and the problem is therefore limited to two dimensions. A fully developed laminar flow with no entrance or exit losses is assumed to exist in the channels and the fluid is assumed to be a perfect gas. Since $H << l$, then, as is common in the analysis of thin film air bearings, the pressure gradient in the y-direction is considered to be negligible in comparison with the gradient in the x-direction. It is also assumed that isothermal conditions exist since the flow velocities are low and the height of the duct is so small that perfect heat conduction can be assumed. Isothermal conditions and the assumption of a Newtonian fluid results in an isoviscous flow.

The continuity equation for unsteady two-dimensional compressible flow is given by Schlichting (1968):

$$\frac{\partial \rho_f}{\partial t} + \frac{\partial}{\partial x}\left(\rho_f u\right) + \frac{\partial}{\partial y}\left(\rho_f v\right) = 0 \tag{5.8}$$

where v is the velocity component in the y-direction. For a perfect

gas we may substitute $\rho_f = p/R\theta$ into equation 5.8 and since the flow is isothermal we then obtain:

$$\frac{\partial p}{\partial t} + \frac{\partial}{\partial x}(pu) + \frac{\partial}{\partial y}(pv) = 0 \qquad (5.9)$$

Since it is possible to estimate or assume the variation of the variables in the y-direction we may now integrate this equation with respect to y and arrive at an equation involving differential terms in only x and t. The first step is to assume that the variation of u in the y-direction follows the well known parabolic profile for a laminar flow and that any distortion in this due to the motion of the membrane is negligible. With the no-slip boundary condition at the wall, $u = 0$ at $y=0$ and at $y = h$. We may then define u as follows:

$$u = 6\bar{u}\left(\frac{y}{h} - \frac{y^2}{h^2}\right) \qquad (5.10)$$

If we now substitute equation 5.10 into equation 5.9 and differentiate with respect to x we obtain:

$$\frac{\partial p}{\partial t} + 6\left(\frac{y}{h} - \frac{y^2}{h^2}\right)\frac{\partial}{\partial x}(p\bar{u}) + 6p\bar{u}\left(\frac{2y^2}{h^3} - \frac{y}{h^2}\right)\frac{\partial h}{\partial x} + \frac{\partial}{\partial y}(pv) = 0 \qquad (5.11)$$

With constant pressure in the y-direction we may now integrate equation 5.11 with respect to y and substitute the limits $v = 0$ at $y = 0$ and $v = \partial h/\partial t$ at $y = h$, to obtain:

$$h\frac{\partial p}{\partial t} + h\frac{\partial}{\partial x}(p\bar{u}) + p\bar{u}\frac{\partial h}{\partial x} + p\frac{\partial h}{\partial t} = 0 \qquad (5.12)$$

With some reorganisation this becomes:

$$\frac{\partial}{\partial t}(ph) + \frac{\partial}{\partial x}(p\bar{u}h) = 0 \qquad (5.13)$$

With no side leakage and with a negligible pressure gradient in

the y-direction the Navier-Stokes equations given by Schlichting reduce to the single x-direction momentum equation. For unsteady viscous flow this is shown to be (on omitting the z differential terms):

$$\rho_f\left(\frac{\partial u}{\partial t} + u\frac{\partial u}{\partial x} + v\frac{\partial u}{\partial y}\right) = -\frac{\partial p}{\partial x} + \mu\left(\frac{\partial^2 u}{\partial y^2} + \frac{4}{3}\frac{\partial^2 u}{\partial x^2} + \frac{1}{3}\frac{\partial^2 v}{\partial x \partial y}\right) \qquad (5.14)$$

It is commonly agreed (e.g. Ames 1977) that conservative systems generally give more accurate results. The conservative form of equation 5.14 is obtained from the addition of u times equation 5.8 to the left hand side of equation 5.14:

$$\frac{\partial}{\partial t}(\rho_f u) + \frac{\partial}{\partial x}(\rho_f u^2) + \frac{\partial}{\partial y}(\rho_f uv) = -\frac{\partial p}{\partial x} + \mu\left(\frac{\partial^2 u}{\partial y^2} + \frac{4}{3}\frac{\partial^2 u}{\partial x^2} + \frac{1}{3}\frac{\partial^2 v}{\partial x \partial y}\right) \qquad (5.15)$$

Following the same argument as in air bearing theory, we now assume that velocities, x distances and time fluctuations are of order one compared with y distances of order h, which is a representative film thickness. Equation 5.15 then reduces to the conservative momentum equation for this system:

$$\frac{\partial}{\partial t}(\rho_f u) + \frac{\partial}{\partial x}(\rho_f u^2) + \frac{\partial}{\partial y}(\rho_f uv) = -\frac{\partial p}{\partial x} + \mu\frac{\partial^2 u}{\partial y^2} \qquad (5.16)$$

For isothermal flow, we may now substitute the perfect gas relationship $\rho_f = p/R\theta$ into equation 5.16, and obtain, after some reorganisation:

$$\frac{\partial}{\partial t}(pu) + \frac{\partial}{\partial x}(pu^2) + \frac{\partial}{\partial y}(puv) = -R\theta\frac{\partial p}{\partial x} + \mu R\theta\left(\frac{\partial^2 u}{\partial y^2}\right) \qquad (5.17)$$

Substitution of equation 5.10, representing the parabolic profile,

into equation 5.17 now leads to:

$$\frac{\partial}{\partial t}\left\{6p\bar{u}\left(\frac{y}{h}-\frac{y^2}{h^2}\right)\right\}+\frac{\partial}{\partial x}\left\{36p\bar{u}^2\left(\frac{y}{h}-\frac{y^2}{h^2}\right)^2\right\}+\frac{\partial}{\partial y}(puv)=$$

$$-R\theta\frac{\partial p}{\partial x}+\mu R\theta\frac{\partial^2}{\partial y^2}\left\{6\bar{u}\left(\frac{y}{h}-\frac{y^2}{h^2}\right)\right\} \qquad (5.18)$$

which when differentiated with respect to x and t becomes:

$$6\left(\frac{y}{h}-\frac{y^2}{h^2}\right)\frac{\partial}{\partial t}(p\bar{u})+6p\bar{u}\left(-\frac{y}{h^2}+\frac{2y^2}{h^3}\right)\frac{\partial h}{\partial t}+36\left(\frac{y}{h}-\frac{y^2}{h^2}\right)^2\frac{\partial}{\partial x}(p\bar{u}^2)$$

$$+36p\bar{u}^2\left(-\frac{2y^2}{h^3}+\frac{6y^3}{h^4}-\frac{4y^4}{h^5}\right)\frac{\partial h}{\partial x}+\frac{\partial}{\partial y}(puv)=-R\theta\frac{\partial p}{\partial x}-12\mu R\theta\frac{\bar{u}}{h^2} \qquad (5.19)$$

With constant pressure in the y-direction, we may now integrate equation 5.19 with respect to y and since $u = 0$ at $y = 0$ and $u = 0$ at $y = h$, we obtain:

$$h\frac{\partial}{\partial t}(p\bar{u})+p\bar{u}\frac{\partial h}{\partial t}+\frac{6}{5}h\frac{\partial}{\partial x}(p\bar{u}^2)+\frac{6}{5}p\bar{u}^2\frac{\partial h}{\partial x}=-R\theta h\frac{\partial p}{\partial x}-12\mu R\theta\frac{\bar{u}}{h} \qquad (5.20)$$

Gathering the differential terms together then results in:

$$\frac{\partial}{\partial t}(p\bar{u}h)+\frac{6}{5}\frac{\partial}{\partial x}(p\bar{u}^2h)=-R\theta h\frac{\partial p}{\partial x}-12\mu R\theta\frac{\bar{u}}{h} \qquad (5.21)$$

5.3 Dimensionless Form of the Equations

A dimensional analysis may be performed on the variables which influence the behaviour of the membrane. The appropriate dimensionless groups which govern the system may then be determined and these can be used to generalise the relationships or to scale the data. However, the differential equations themselves can occasionally provide a deeper insight into the laws of similarity than a mere knowledge of the variables that enter a problem. In the

present case an analysis of equations 5.6, 5.13 and 5.21 shows that the following three non-dimensional groups govern the system:

$$\left.\begin{aligned} \Pi_1 &= \frac{\mu c l}{p_1 H^2} \\ \Pi_2 &= \frac{T}{\rho c^2} \\ \Pi_3 &= \frac{p_1 L^2}{\rho H c^2} \end{aligned}\right\} \qquad (5.22)$$

where c is the speed of sound. Rearrangement of these groups allows the definition of non-dimensional pressure, tension and density. Along with the remaining system variables we can now define the following dimensionless variables:

$$\left.\begin{aligned} p' &= p\,\frac{H^2}{\mu c l} \\ \bar{u}' &= \frac{\bar{u}}{c} \\ h' &= \frac{h}{H} \\ T' &= T\,\frac{H^3}{\mu c l^3} \\ \rho' &= \rho\,\frac{cH^3}{\mu l^3} \\ x' &= \frac{x}{l} \\ t' &= t\,\frac{c}{l} \end{aligned}\right\} \qquad (5.23)$$

where the primed values are dimensionless.

On substituting these values in equation 5.13, the dimensionless

continuity equation becomes:

$$\frac{\partial}{\partial t'}\left(p'h'\right) + \frac{\partial}{\partial x'}\left(p'\bar{u}'h'\right) = 0 \qquad (5.24)$$

Noting that $R\theta = c^2$ in idealised isothermal flow due to the assumption of infinite heat transfer (further discussion of this is given in Section 7.3.5), substitution of equations 5.23 in equation 5.21 results in the dimensionless momentum equation:

$$\frac{\partial}{\partial t'}\left(p'\bar{u}'h'\right) + \frac{6}{5}\frac{\partial}{\partial x'}\left(p'\bar{u}'^2h'\right) = -h'\frac{\partial p'}{\partial x'} - 12\frac{\bar{u}'}{h'} \qquad (5.25)$$

Substitution of equations 5.23 in equations 5.5a, 5.6 and 5.7 results in the following equations relating to the membrane motion :

$$\frac{\partial \phi'}{\partial t'} = \frac{T'}{\rho'}\frac{\partial \psi'}{\partial x'} + \frac{1}{\rho'}\left(p'_a - p'_b\right) \qquad (5.26)$$

$$\frac{\partial \psi'}{\partial t'} = \frac{\partial \phi'}{\partial x'} \qquad (5.27)$$

$$\frac{\partial h'}{\partial t'} = \phi' \qquad (5.28)$$

Henceforth the primes will be dropped and it will be assumed that we are dealing with the dimensionless values of p, $\bar{u}$, h, ϕ, ψ, T, ρ, x and t.

5.4 Conservative Form of the Fluid Equations

For accurate numerical solution of the equations relating to the fluid flow it is necessary to express the equations in terms of the conserved quantities, mass X and momentum Y:

$$\left.\begin{aligned} X &= ph \\ Y &= p\bar{u}h \end{aligned}\right\} \qquad (5.29)$$

Inserting equations 5.29 in equation 5.24 then results in the

following expression for the continuity equation:

$$\frac{\partial X}{\partial t} + \frac{\partial Y}{\partial x} = 0 \qquad (5.30)$$

To obtain the momentum equation in terms of X and Y it is first necessary to rearrange equation 5.25 as follows:

$$\frac{\partial}{\partial t}(p\bar{u}h) + \frac{6}{5}\frac{\partial}{\partial x}(p\bar{u}^2h) = -\left(\frac{\partial}{\partial x}(ph) - p\frac{\partial h}{\partial x}\right) - 12\frac{\bar{u}}{h} \qquad (5.31)$$

Inserting equations 5.29 into equation 5.31 and noting that $\partial h/\partial x = \psi$ now gives:

$$\frac{\partial Y}{\partial t} + \frac{6}{5}\frac{\partial}{\partial x}\left(\frac{Y^2}{X}\right) = -\left(\frac{\partial X}{\partial x} - \frac{X}{h}\psi\right) - 12\frac{Y}{Xh} \qquad (5.32)$$

After some rearrangement the final form of the momentum equation is:

$$\frac{\partial Y}{\partial t} + \frac{12}{5}\frac{Y}{X}\frac{\partial Y}{\partial x} + \left(1 - \frac{6}{5}\frac{Y^2}{X^2}\right)\frac{\partial X}{\partial x} = \frac{X}{h}\psi - 12\frac{Y}{Xh} \qquad (5.33)$$

The membrane equation of motion (equation 5.26) in terms of conserved quantities is:

$$\frac{\partial \phi}{\partial t} = \frac{T}{\rho}\frac{\partial \psi}{\partial x} + \frac{1}{\rho}\left(\frac{X_a}{h_a} - \frac{X_b}{h_b}\right) \qquad (5.34)$$

5.5 A Natural Frequency of the System

It is possible to predict a natural frequency of the system which is due to the squeeze film effect. The membrane is assumed to be oscillating near its equilibrium position in the centre of the duct and we start by reorganising the dimensionless continuity equation (equation 5.24):

$$h\frac{\partial p}{\partial t} = -p\frac{\partial h}{\partial t} - \frac{\partial}{\partial x}(p\bar{u}h) \qquad (5.35)$$

and since $\partial h/\partial t = \phi$ then:

$$h\frac{\partial p}{\partial t} = - p\phi - \frac{\partial}{\partial x}(p\bar{u}h) \tag{5.36}$$

If the oscillation amplitude is small then we may consider the last term to be negligible and rewrite equation 5.36 as follows:

$$\frac{\partial p}{\partial t} = - \frac{p}{h}\phi \tag{5.37}$$

The first term on the right hand side of equation 5.26 for the membrane equation of motion may also be considered negligible since the slope is small and it can be rewritten as:

$$\frac{\partial \phi}{\partial t} = \frac{1}{\rho}\left(p_a - p_b\right) \tag{5.38}$$

We now differentiate equation 5.38 with respect to t and obtain:

$$\frac{\partial^2 \phi}{\partial t^2} = \frac{1}{\rho}\left(\frac{\partial p_a}{\partial t} - \frac{\partial p_b}{\partial t} \right) \tag{5.39}$$

Application of equation 5.37 to channels a and b and substitution of these in equation 5.39 now gives us:

$$\frac{\partial^2 \phi}{\partial t^2} = \frac{1}{\rho}\left(- \frac{p_a}{h_a}\phi_a + \frac{p_b}{h_b}\phi_b \right) \tag{5.40}$$

and since $p_b \simeq p_a$, $h_b \simeq h_a$ and $\phi_b = -\phi_a = -\phi$, equation 5.40 becomes:

$$\frac{\partial^2 \phi}{\partial t^2} = - \frac{2p_a}{\rho h_a}\phi \tag{5.41}$$

This is an equation of harmonic motion for the membrane with the natural frequency f as follows:

$$f = \frac{1}{2\pi}\left(\frac{2p_a}{\rho h_a}\right)^{1/2} \tag{5.42}$$

CHAPTER 6

NUMERICAL METHODS

Details of the two numerical methods which were employed in the solution of the equations derived in Chapter 5 are presented in this chapter. Initially a Lax-Wendroff finite difference scheme was used at the interior nodes. Solution at the boundaries in this scheme was attempted by linear extrapolation, second order extrapolation and the method of characteristics but numerical instability always occurred at the boundaries. The method of characteristics was then employed on the rectangular grid at interior and boundary nodes in a Hartree type method. This proved to be numerically stable and supplied the results presented in Chapter 7.

The Lax-Wendroff method and the method of characteristics are described in Sections 6.2 and 6.3 respectively and the accuracy of the numerical solution is discussed in Section 6.4. We shall start in Section 6.1 with a summary of the equations to be solved.

6.1 The Equations to be Solved

The dynamic behaviour of the system has been shown to be dependent on seven equations - three relating to the membrane and two to the gas flow in each channel. The equations governing the membrane motion are:

$$\frac{\partial \phi}{\partial t} = \frac{T}{\rho}\frac{\partial \psi}{\partial x} + \frac{1}{\rho}\left(\frac{X_a}{\bar{h}_a} - \frac{X_b}{\bar{h}_b}\right) \tag{5.34}$$

$$\frac{\partial \psi}{\partial t} = \frac{\partial \phi}{\partial x} \tag{5.27}$$

$$\frac{\partial h}{\partial t} = \phi \tag{5.28}$$

and the equations of continuity and momentum governing the gas flow in each channel are:

$$\frac{\partial X}{\partial t} + \frac{\partial Y}{\partial x} = 0 \tag{5.30}$$

$$\frac{\partial Y}{\partial t} + \frac{12}{5}\frac{Y}{X}\frac{\partial Y}{\partial x} + \left(1 - \frac{6}{5}\frac{Y^2}{X^2}\right)\frac{\partial X}{\partial x} = \frac{X}{h}\psi - 12\frac{Y}{Xh} \tag{5.33}$$

6.2 The Lax-Wendroff Method

The two-step Lax-Wendroff scheme employed here is based on the method described by Ames (1977). It is an explicit finite difference scheme of second order accuracy and is commonly referred to as a hop-scotch or leap-frog method. The solution space, which is shown in Fig. 6.1, is composed of a rectangular grid of nodes equidistant in space and time with intermediate nodes positioned at the mesh mid-points. The finite difference equations used in the solution procedure are described below.

The equations shown in Section 6.1 are of the general form:

$$\frac{\partial U}{\partial t} = \frac{\partial F}{\partial x} + G \tag{6.1}$$

where U is the vector of variables to be solved and F and G are functions of U. The first step involves the solution of U at the intermediate mesh points and is given by the following finite difference approximation:

$$U_{i+1/2,\,j+1/2} = \frac{1}{2}\left(U_{i+1,\,j} + U_{i,\,j}\right) + \frac{\Delta t}{2\Delta x}\left(F_{i+1,\,j} - F_{i,\,j}\right) + \frac{\Delta t}{4}\left(G_{i+1,\,j} + G_{i,\,j}\right) \tag{6.2}$$

The second step to j+1 is approximated by:

$$U_{i,j+1} = U_{i,j} + \frac{\Delta t}{\Delta x}\left(F_{i+1/2,\,j+1/2} - F_{i-1/2,\,j+1/2}\right) + \frac{\Delta t}{2}\left(G_{i+1/2,\,j+1/2} + G_{i-1/2,\,j+1/2}\right) \qquad (6.3)$$

The values at step j+1 are now employed in the same manner as those at j to arrive at a solution for the values at j+2 and the solution proceeds in this manner until the final time step is reached.

An alternative procedure has to be applied at the boundaries since this method would require a knowledge of values outwith the computational domain. Various methods are available and several were tested by Chu and Sereny (1974) with the inviscid version of equations 6.2 and 6.3 applied to flow with expansion waves in a duct. Among the methods tested, the method of characteristics was found to be the most accurate and first and second order extrapolations were next. Higher order one sided difference schemes were found to be less accurate. For the present problem first and second order extrapolations and the method of characteristics were each employed but numerical stability was never achieved in the simultaneous solution of the complete set of equations. The solution of the characteristics at the boundaries is described in Section 6.3.2.

When applied independently to the membrane equations or the fluid equations the Lax-Wendroff method with characteristic solution at the boundaries was found to give near identical results to the method of characteristics which was subsequently used over the whole grid. The only discrepancy occurred when modelling a step increase in pressure at the inlet to a rigid walled duct of varying area.

Once the pressure transient had decayed and a steady flow remained in the duct there was a discontinuity of approximately 1 % in the mass flow at the boundaries of the Lax-Wendroff method. It is interesting to note that both methods gave an identical incorrect result with the fluid equations in non-conservative form. A transient was again allowed to decay and once in a steady state the mass flow was found to vary by up to 20 % from the inlet to the outlet.

The instability of the Lax-Wendroff method may have been due to the viscous terms in the fluid equations. Roach (1972) warns that explicit finite difference schemes which are stable when applied to the inviscid equations will not generally be successful when applied to the viscous terms. This is due to time centering of the viscous terms at the same point as the space differences. Rubin and Burstein (1967) found that an identical scheme, save for an additional calculation for the viscous term at i, j+1/2, was unstable when modelling shocks in ducts.

It is unlikely that the numerical instability was caused by the combination of the method of characteristics at the boundaries and the Lax-Wendroff method at the interior because it is a common procedure which has been used with success, for example, by Martin et al (1977) and Chu and Sereny (1974).

6.3 The Method of Characteristics

The governing equations of both the membrane and fluid dynamics are hyperbolic and can therefore be solved by the method of characteristics and basic details are given in Shapiro (1953). This method has become a widely accepted technique in the analysis of fluid transients in closed conduit systems; typical examples are the

simulation of a gas pipeline rupture by Cronje et al (1980) and the simulation of transient flows in a train tunnel complex by Henson and Fox (1974). The popularity of the method stems from two of its attributes. First, the partial differential equations become ordinary differential equations and second, the mathematics underlines the essential physical wave behaviour since the characteristic directions are time-space paths of information flow in the physical system.

We may examine the characteristics of the equations in the usual way (e.g. Ames 1977) by considering the conditions under which the derivatives of the equations are indeterminate. Such conditions apply when the determinants of the system are zero and the first step is to express the equations of Section 6.1 in matrix form:

$$\begin{pmatrix} 0 & \left(1 - \frac{6}{5}\frac{Y^2}{X^2}\right) & 1 & \frac{12}{5}\frac{Y}{X} \\ 1 & 0 & 0 & 1 \\ dt & dx & 0 & 0 \\ 0 & 0 & dt & dx \end{pmatrix} \begin{pmatrix} X_t \\ X_x \\ Y_t \\ Y_x \end{pmatrix} = \begin{pmatrix} \frac{X}{h}\psi - 12\frac{Y}{Xh} \\ 0 \\ dX \\ dY \end{pmatrix} \qquad (6.4a)$$

$$\begin{pmatrix} 1 & 0 \\ dt & dx \end{pmatrix} \begin{pmatrix} h_t \\ h_x \end{pmatrix} = \begin{pmatrix} \phi \\ dh \end{pmatrix} \qquad (6.4b)$$

$$\begin{pmatrix} 1 & 0 & 0 & -\frac{T}{\rho} \\ 0 & -1 & 1 & 0 \\ dt & dx & 0 & 0 \\ 0 & 0 & dt & dx \end{pmatrix} \begin{pmatrix} \phi_t \\ \phi_x \\ \psi_t \\ \psi_x \end{pmatrix} = \begin{pmatrix} \frac{1}{\rho}\left(\frac{X_a}{h_a} - \frac{X_b}{h_b}\right) \\ 0 \\ d\phi \\ d\psi \end{pmatrix} \qquad (6.4c)$$

Dealing with system 6.4a first, we equate the determinants to zero:

$$\begin{vmatrix} 0 & \left(1 - \frac{6}{5}\frac{Y^2}{X^2}\right) & 1 & \frac{12}{5}\frac{Y}{X} \\ 1 & 0 & 0 & 1 \\ dt & dx & 0 & 0 \\ 0 & 0 & dt & dx \end{vmatrix} = \begin{vmatrix} 0 & \left(\frac{X}{h}\psi - 12\frac{Y}{Xh}\right) & 1 & \frac{12}{5}\frac{Y}{X} \\ 1 & 0 & 0 & 1 \\ dt & dX & 0 & 0 \\ 0 & dY & dt & dx \end{vmatrix} = 0 \tag{6.5}$$

When these determinants are evaluated we obtain the following equations:

$$\frac{dx}{dt} = \frac{6}{5}\frac{Y}{X} \pm \left(1 + \frac{6}{25}\frac{Y^2}{X^2}\right)^{1/2} \tag{6.6a}$$

$$dY\left(\frac{dx}{dt}\right) + \left(\left(\frac{dx}{dt}\right)^2 - \frac{12}{5}\frac{Y}{X}\frac{dx}{dt}\right)dX - \frac{X}{h}\psi dx + 12\frac{Y}{Xh}dx = 0 \tag{6.6b}$$

Once equation 6.6b was written in finite difference form it was found that the approximation for ψ introduced truncation errors which amplified as the solution progressed through time. This could be remedied by reducing the mesh size but a better option was to substitute $\psi dx = dh - \phi dt$ and along with the substitution of equation 6.6a we obtain the following:

$$\left(\frac{6}{5}\frac{Y}{X} \pm \left(1 + \frac{6}{25}\frac{Y^2}{X^2}\right)^{1/2}\right)dY + \left(1 - \frac{6}{5}\frac{Y^2}{X^2}\right)dX + 12\frac{Y}{Xh}dx - \frac{X}{h}(dh - \phi dt) = 0 \tag{6.7}$$

We may now identify two families of characteristics defined by equations 6.6a and 6.7 depending on whether the upper or lower signs

are used:

$$\alpha\text{-Family}\begin{cases} \dfrac{dx}{dt} = \dfrac{6}{5}\dfrac{Y}{X} + \left(1 + \dfrac{6}{25}\dfrac{Y^2}{X^2}\right)^{1/2} & (6.8a) \\ \left(\dfrac{6}{5}\dfrac{Y}{X} + \left(1 + \dfrac{6}{25}\dfrac{Y^2}{X^2}\right)^{1/2}\right)dY + \left(1 - \dfrac{6}{5}\dfrac{Y^2}{X^2}\right)dX & \\ \qquad + 12\dfrac{Y}{Xh}dx - \dfrac{X}{h}(dh - \phi dt) = 0 & (6.8b) \end{cases}$$

$$\beta\text{-Family}\begin{cases} \dfrac{dx}{dt} = \dfrac{6}{5}\dfrac{Y}{X} - \left(1 + \dfrac{6}{25}\dfrac{Y^2}{X^2}\right)^{1/2} & (6.9a) \\ \left(\dfrac{6}{5}\dfrac{Y}{X} - \left(1 + \dfrac{6}{25}\dfrac{Y^2}{X^2}\right)^{1/2}\right)dY + \left(1 - \dfrac{6}{5}\dfrac{Y^2}{X^2}\right)dX & \\ \qquad + 12\dfrac{Y}{Xh}dx - \dfrac{X}{h}(dh - \phi dt) = 0 & (6.9b) \end{cases}$$

We now equate the determinants of system 6.4b to zero:

$$\begin{vmatrix} 1 & 0 \\ dt & dx \end{vmatrix} = \begin{vmatrix} 1 & \phi \\ dt & dh \end{vmatrix} = 0 \qquad (6.10)$$

and obtain the following equations which identify a single family:

$$\varepsilon \text{ characteristic}\begin{cases} \dfrac{dx}{dt} = 0 & (6.11a) \\ dh - \phi dt = 0 & (6.11b) \end{cases}$$

Finally, equating the determinants of system 6.4c to zero we

obtain:

$$\begin{vmatrix} 1 & 0 & 0 & -\frac{T}{\rho} \\ 0 & -1 & 1 & 0 \\ dt & dx & 0 & 0 \\ 0 & 0 & dt & dx \end{vmatrix} = \begin{vmatrix} 1 & 0 & 0 & \frac{1}{\rho}\left(\frac{X_a}{h_a} - \frac{X_b}{h_b}\right) \\ 0 & -1 & 1 & 0 \\ dt & dx & 0 & d\phi \\ 0 & 0 & dt & d\psi \end{vmatrix} = 0 \qquad (6.12)$$

which leads to:

$$\frac{dx}{dt} = \pm\left(\frac{T}{\rho}\right)^{1/2} \qquad (6.13a)$$

$$d\phi - \frac{dx}{dt}d\psi - \frac{1}{\rho}\left(\frac{X_a}{h_a} - \frac{X_b}{h_b}\right)dt = 0 \qquad (6.13b)$$

We now substitute equation 6.13a into 6.13b to get:

$$d\phi \mp \left(\frac{T}{\rho}\right)^{1/2} d\psi - \frac{1}{\rho}\left(\frac{X_a}{h_a} - \frac{X_b}{h_b}\right)dt = 0 \qquad (6.14)$$

Two families of characteristics are defined by equations 6.13a and 6.14 depending on the signs and these are:

γ-Family

$$\frac{dx}{dt} = + \left(\frac{T}{\rho}\right)^{1/2} \qquad (6.15a)$$

$$d\phi - \left(\frac{T}{\rho}\right)^{1/2} d\psi - \frac{1}{\rho}\left(\frac{X_a}{h_a} - \frac{X_b}{h_b}\right)dt = 0 \qquad (6.15b)$$

η-Family

$$\frac{dx}{dt} = - \left(\frac{T}{\rho}\right)^{1/2} \qquad (6.16a)$$

$$d\phi + \left(\frac{T}{\rho}\right)^{1/2} d\psi - \frac{1}{\rho}\left(\frac{X_a}{h_a} - \frac{X_b}{h_b}\right)dt = 0 \qquad (6.16b)$$

6.3.1 Solution of the Characteristics at an Interior Node

Fig. 6.2 shows a typical characteristic network in which two families of characteristics originate from a starting line at $t = 0$. Since the characteristics generally depend on the solution, the calculation at each point consists of the simultaneous solution of the (x, t) coordinates of a point A which lies at the intersection of characteristics from L and R and integration of the characteristic equations along LA and RA to determine the unknown quantities at A. If the spatial distribution of the dependent variables are required at a fixed time, two-dimensional interpolation in the characteristic net is required. This difficulty can be overcome by using the method attributable to Hartree (1953) which employs a rectangular space-time grid as shown in Fig. 6.3. Integration takes place along the characteristics as before but the position of A is known in advance and one-dimensional interpolation is required along BCD to determine the variable values at L and R respectively.

Fig 6.4a shows the characteristic lines of this problem intersecting at the interior node A and, for clarity, the characteristics of the flow in only one channel are shown. Due to the variation in wavespeed, the X-Y characteristics, α and β, are curved. They are approximated by straight lines in this solution method as shown by the dotted lines in the diagram. The ϕ-ψ characteristics, γ and η, are straight since the membrane wavespeed is constant and the single characteristic, ε, is the line joining C to A.

The values of U at A are found by the iterative solution of equations 6.18a to 6.21b and equation 6.23 which are derived below. The iteration is started by assuming that the value of the variables

in the vector U at L equal those at B and the values at R equal those at D. Once the iteration is started, the values at L and R are calculated by second order interpolation using the known values at B, C and D as follows:

$$U_I = U_C + \frac{1}{2}\left(U_D - U_B\right)\left(x_I - x_C\right) + \frac{1}{2}\left(U_D - 2U_C + U_B\right)\left(x_I - x_C\right)^2 \qquad (6.17)$$

where the subscript I denotes the interpolative point. Typically, 8 to 13 iteration cycles were required at each node for convergence.

Throughout this chapter the X-Y characteristics which are considered represent those of channel a (the lower channel) and the resulting equations may be extended to channel b by noting that $h_b = H - h_a$, $\psi_b = -\psi_a$ and $\phi_b = -\phi_a$. The values of X and Y at position A are found from the solution of the following equations which are the finite difference form of equations 6.8b and 6.9b:

$$\left\{\frac{6}{5}\frac{\overline{Y}_{LA}}{\overline{X}_{LA}} + \left(1 + \frac{6}{25}\frac{\overline{Y}^2_{LA}}{\overline{X}^2_{LA}}\right)^{1/2}\right\}\left(Y_A - Y_L\right) + \left(1 - \frac{6}{5}\frac{\overline{Y}^2_{LA}}{\overline{X}^2_{LA}}\right)\left(X_A - X_L\right)$$

$$+ 12\,\frac{\overline{Y}_{LA}}{\overline{X}_{LA}\,\overline{h}_{LA}}\left(x_A - x_L\right) - \frac{\overline{X}_{LA}}{\overline{h}_{LA}}\left\{\left(h_A - h_L\right) - \overline{\phi}_{LA}\Delta t\right\} = 0 \qquad (6.18a)$$

$$\left\{\frac{6}{5}\frac{\overline{Y}_{RA}}{\overline{X}_{RA}} - \left(1 + \frac{6}{25}\frac{\overline{Y}^2_{RA}}{\overline{X}^2_{RA}}\right)^{1/2}\right\}\left(Y_A - Y_R\right) + \left(1 - \frac{6}{5}\frac{\overline{Y}^2_{RA}}{\overline{X}^2_{RA}}\right)\left(X_A - X_R\right)$$

$$+ 12\,\frac{\overline{Y}_{RA}}{\overline{X}_{RA}\,\overline{h}_{RA}}\left(x_A - x_R\right) - \frac{\overline{X}_{RA}}{\overline{h}_{RA}}\left\{\left(h_A - h_R\right) - \overline{\phi}_{RA}\Delta t\right\} = 0 \qquad (6.18b)$$

where $\overline{X}$, $\overline{Y}$, $\overline{\phi}$ and $\overline{h}$ are average values of X, Y, ϕ and h along the segment denoted by the subscript; LA and RA refer to segments L to A

and R to A respectively. A simple arithmetic mean was calculated with the values at A taken from the previous iteration cycle. For example $\overline{X}_{RA}$ becomes:

$$\overline{X}_{RA} = \frac{1}{2}\left(X_R + X_{A,k-1}\right) \tag{6.19}$$

where k-1 denotes the last iterative step. The positions of points L and R are obtained from equations 6.8a and 6.9a which, in finite difference form, are:

$$\frac{x_A - x_L}{\Delta t} = \frac{6}{5}\frac{\overline{Y}_{LA}}{\overline{X}_{LA}} + \left(1 + \frac{6}{25}\frac{\overline{Y}^2_{LA}}{\overline{X}^2_{LA}}\right)^{1/2} \tag{6.20a}$$

$$\frac{x_A - x_R}{\Delta t} = \frac{6}{5}\frac{\overline{Y}_{RA}}{\overline{X}_{RA}} - \left(1 + \frac{6}{25}\frac{\overline{Y}^2_{RA}}{\overline{X}^2_{RA}}\right)^{1/2} \tag{6.20b}$$

Equations 6.20 are each solved iteratively for x_L and x_R.

The values of ϕ and ψ at A are found from the solution of the following equations which are derived from equations 6.15b and 6.16b:

$$\left(\phi_A - \phi_E\right) - \left(\frac{T}{\rho}\right)^{1/2}\left(\psi_A - \psi_E\right) - \frac{1}{\rho}\left\{\left(\frac{\overline{X}_a}{\overline{h}_a}\right)_{EA} - \left(\frac{\overline{X}_b}{\overline{h}_b}\right)_{EA}\right\}\Delta t = 0 \tag{6.21a}$$

$$\left(\phi_A - \phi_F\right) + \left(\frac{T}{\rho}\right)^{1/2}\left(\psi_A - \psi_F\right) - \frac{1}{\rho}\left\{\left(\frac{\overline{X}_a}{\overline{h}_a}\right)_{FA} - \left(\frac{\overline{X}_b}{\overline{h}_b}\right)_{FA}\right\}\Delta t = 0 \tag{6.21b}$$

The location of points E and F are obtained from equations 6.15a and 6.16a which, in finite difference form, are:

$$\frac{x_A - x_E}{\Delta t} = \left(\frac{T}{\rho}\right)^{1/2} \tag{6.22a}$$

$$\frac{x_A - x_F}{\Delta t} = - \left(\frac{T}{\rho}\right)^{1/2} \qquad (6.22b)$$

The remaining variable to be solved is h which is obtained from the following equation derived from equation 6.11b:

$$\left(h_A - h_C\right) - \overline{\phi}_{CA} \Delta t = 0 \qquad (6.23)$$

To summarise, each iteration cycle consists of the following steps :

1. Positions of E and F calculated using equations 6.22.
2. Values at E and F calculated by interpolation using equation 6.17.
3. New values of ϕ and ψ at A calculated by simultaneous solution of equations 6.21.
4. New value of h at A calculated using equation 6.23.
5. Positions L and R assumed to be coincident with B and D respectively. Variables at L made equal to those at B; variables at R made equal to those at D.
6. Positions of L and R found by iterative solution of equations 6.20a and 6.20b respectively. On each loop of the iteration the variable values at the new L and R positions are calculated by interpolation using equation 6.17.
7. New values of Y and X at A are calculated by simultaneous solution of equations 6.18.
8. If all the new values have not converged to solutions then the cycle returns to step 3.

All mean values are calculated using values at A taken from the previous iteration cycle (see equation 6.19); on the first cycle the

values are taken from the previous time step.

6.3.2 Solution of the Characteristics at the Boundaries

Hartree's method was also applied to the solution of the characteristic equations at the boundaries. Figs. 6.4b and 6.4c show the grid at the left and right hand ends respectively. The solution is simpler than for an interior node since $X = ph$ = constant and $\phi = 0$ at the boundaries and we are left with Y and ψ as unknowns.

The value of Y at 0 is found by the solution of equation 6.9b from which we derive the following finite difference equation:

$$\left\{\frac{6}{5}\frac{\bar{Y}_{RO}}{\bar{X}_{RO}} - \left[1 + \frac{6}{25}\frac{\bar{Y}^2_{RO}}{\bar{X}^2_{RO}}\right]^{1/2}\right\}\left(Y_0 - Y_R\right) + \left[1 - \frac{6}{5}\frac{\bar{Y}^2_{RO}}{\bar{X}^2_{RO}}\right]\left(X_0 - X_R\right)$$

$$- 12\,\frac{\bar{Y}_{RO}}{\bar{X}_{RO}\bar{h}_R}\,x_R - \frac{\bar{X}_{RO}}{\bar{h}_{RO}}\left\{\left(h_0 - h_R\right) - \bar{\phi}_{RO}\Delta t\right\} = 0 \qquad (6.24)$$

and the location of R is found from equation 6.9a from which we obtain:

$$-\frac{x_R}{\Delta t} = \frac{6}{5}\frac{\bar{Y}_{RO}}{\bar{X}_{RO}} - \left[1 + \frac{6}{25}\frac{\bar{Y}^2_{RO}}{\bar{X}^2_{RO}}\right]^{1/2} \qquad (6.25)$$

Equation 6.25 is solved iteratively for x_R and equations 6.24 and 6.25 are solved iteratively for Y at 0. The iteration of equation 6.25 is started by assuming that the values in U at R equal those at D. On subsequent iteration cycles the values at R are calculated by second order interpolation using the known values at C,

D and J in the following equation:

$$U_R = U_C + \frac{1}{2}\left(4U_D - 3U_C - U_J\right)x_R + \frac{1}{2}\left(U_C - 2U_D + U_J\right)x_R^2 \qquad (6.26)$$

The value of ψ at 0 is found directly from the solution of equation 6.16b which in finite difference form is:

$$-\phi_F + \left(\frac{T}{\rho}\right)^{1/2}\left(\psi_0 - \psi_F\right) - \frac{1}{\rho}\left\{\left(\frac{\overline{X}_a}{\overline{h}_a}\right)_{FO} - \left(\frac{\overline{X}_b}{\overline{h}_b}\right)_{FO}\right\}\Delta t = 0 \qquad (6.27)$$

and the location of point F is found from equation 6.16a which becomes:

$$\frac{x_F}{\Delta t} = \left(\frac{T}{\rho}\right)^{1/2} \qquad (6.28)$$

The values in U at F are found by second order interpolation as at point R.

The values of Y and ψ at N are found in exactly the same manner as those at 0. Y is found from equation 6.8b which becomes:

$$\left\{\frac{6}{5}\frac{\overline{Y}_{LN}}{\overline{X}_{LN}} + \left(1 + \frac{6}{25}\frac{\overline{Y}^2_{LN}}{\overline{X}^2_{LN}}\right)^{1/2}\right\}\left(Y_N - Y_L\right) + \left(1 - \frac{6}{5}\frac{\overline{Y}^2_{LN}}{\overline{X}^2_{LN}}\right)\left(X_N - X_L\right)$$

$$+ 12\,\frac{\overline{Y}_{LN}}{\overline{X}_{LN}\,\overline{h}_{LN}}\left(x_N - x_L\right) - \frac{\overline{X}_{LN}}{\overline{h}_{LN}}\left\{\left(h_N - h_L\right) - \overline{\phi}_{LN}\Delta t\right\} = 0 \qquad (6.29)$$

and the location of L is found from equation 6.8a which becomes:

$$\frac{x_N - x_L}{\Delta t} = \frac{6}{5}\frac{\overline{Y}_{LN}}{\overline{X}_{LN}} + \left(1 + \frac{6}{25}\frac{\overline{Y}^2_{LN}}{\overline{X}^2_{LN}}\right)^{1/2} \qquad (6.30)$$

Equation 6.30 is solved iteratively for x_L and equations 6.29 and 6.30 are solved iteratively for Y at N. The iteration of

equation 6.30 is started by assuming that the values in U at L equal those at B. On subsequent iteration cycles the values at R are calculated by second order interpolation using the known values at K, B and C in the following equation:

$$U_L = U_C + \frac{1}{2}\left(4U_B - 3U_C - U_K\right)\left(x_L - x_N\right) + \frac{1}{2}\left(U_C - 2U_B + U_K\right)\left(x_L - x_N\right)^2 \qquad (6.31)$$

The value of ψ is calculated from equation 6.15b:

$$\left(\phi_N - \phi_E\right) - \left(\frac{T}{\rho}\right)^{1/2}\left(\psi_N - \psi_E\right) - \frac{1}{\rho}\left\{\left(\frac{\overline{X}_a}{\overline{h}_a}\right)_{EN} - \left(\frac{\overline{X}_b}{\overline{h}_b}\right)_{EN}\right\}\Delta t = 0 \qquad (6.32)$$

and the location of E is calculated from equation 6.15a from which we obtain:

$$\frac{x_N - x_E}{\Delta t} = \left(\frac{T}{\rho}\right)^{1/2} \qquad (6.33)$$

The values in U at E are found by second order interpolation as at point L.

6.4 Stability and Accuracy of Solution

How close a solution approaches the "true" solution is dependent on both the stability and the accuracy of the solution method. The accuracy is dependent on the spatial grid size and the stability on the time step size. For the present problem we are considering cases where the duct and membrane have been divided into N equal sized elements and it is assumed that the numerical solution approaches the "true" solution as $N \rightarrow \infty$. Unfortunately, the limitations posed by computer storage and execution time mean that it is impractical to use very large values of N and a compromise has to be found between accuracy and the time taken for a solution.

For an explicit finite difference scheme such as the Lax-Wendroff method the time step size is restricted by the well known Courant-Freidrichs-Lewy (CFL) stability condition as described, for example, by Smith (1978). This condition stipulates that the characteristic lines through a solution point must intersect the previous time step within the numerical domain of dependence and is, in fact, the situation shown in Fig. 6.3. Thus, for stability we must have:

$$\frac{\Delta t}{\Delta x} c \leq 1$$

The CFL condition is also commonly applied to the characteristic method on a rectangular grid with the stipulation that the interpolation on the previous time step must occur between the two neighbouring grid points. Vardy (1976), however, explains that the important consideration for the characteristic method is that the grid points used in the interpolation procedure should be as close as possible to the interpolative point and that each characteristic line can, in fact, reach over several spatial grid points as long as the two nearest points are used in the interpolation. Although this method allows a time step size to be used in excess of the CFL condition there is still a limitation in the case of curved characteristics since they are approximated by straight lines.

Goldberg and Wylie (1983) proposed schemes utilizing time-line interpolations which include a reachback method and an implicit method. They claim that the reachback method reduces the numerical error encountered in spatial interpolations and the implicit method has the advantage that it is not constrained by maximum time step limitations. Although Vardy's method and Goldberg's implicit

time-line method clearly contravene the CFL condition each author claims that numerical stability and increased accuracy were achieved. However, the Hartree method, with the characteristics crossing the previous time step within the neighbouring grid points, is a well proven technique and was therefore used here. In the event, it was found that the time step size was greatly restricted by the squeeze film oscillation predicted in Section 5.5, resulting in a $(\Delta t/\Delta x)c$ ratio of approximately 0.05.

The major source of error when applying the Hartree method is due to the interpolations introducing truncation errors which do not exist in the natural characteristic grid. Zucrow and Hoffman (1976) also explain that since the interpolation is based on properties outwith the domain of dependence the accuracy is further reduced. This effect of data from a solution point entering the solution of neighbouring points outwith its zone of influence is termed numerical damping by Wylie and Streeter (1978) since it attenuates and smears steep gradients. Other terminology includes false and numerical diffusion and dissipation. Wylie claims that the damping can be reduced for smooth transients by using higher order interpolations and so second order interpolations were employed in the present scheme for both the interior and boundary nodes.

Finally, since the maximum time step size varies in proportion to the element size, the time for a test would be expected to vary as N^2. In fact, it was found that the time taken for tests run with 80, 160 and 320 elements was approximately 5, 14 and 54 minutes of computer time per simulated millisecond. While the expected factor of 4 relates the time taken for tests with 160 and 320 elements, the time taken for 80 elements is longer than expected. This is due to

the greater number of iterations needed to solve the longer curved characteristics.

CHAPTER 7

THEORETICAL STABILITY ANALYSIS

The equations for a perfectly flexible membrane in a thin duct containing a compressible flow have been described in Chapter 5 and the numerical methods employed in solving these equations have been described in Chapter 6. This chapter is devoted to a theoretical study of the membrane stability. The results presented here were obtained from a computer program written for the purpose. Details of the program itself will not be discussed, except to say that it amounted to some 1700 statements in FORTRAN77.

We shall start in Section 7.1 with a discussion of general concepts in stability and the definition of instability with regard to this system. Section 7.2 describes the tests which were run on the computer and Section 7.3 discusses the results obtained.

7.1 Concepts in Stability

The study of the stability of a membrane in a duct containing a compressible flow falls into the area of self-excited hydro-elastic vibrations. An eloquent definition of aerodynamic stability in a hydro-elastic system is given by Blevins (1977). He explains that a vibrating structure in a steady flow produces oscillations within the flow which in turn induce oscillating aerodynamic forces on the structure. If the oscillating forces act to reduce the vibrations of the structure then the structure is said to be aerodynamically stable and if the vibrations increase then it is aerodynamically unstable.

Blevins' definition of stability involves the motion of the system in the neighbourhood of an equilibrium point in the phase

space. More general texts on vibration analysis such as that of Meirovitch (1975) discuss two forms of equilibrium. The first is an equilibrium point and the second is a limit cycle. An equilibrium point is the point in the phase space which represents zero motion and if the motion of the system approaches it as $t \rightarrow \infty$ then the system is said to be asymptotically stable. A limit cycle is essentially an equilibrium motion in which the system oscillates in a closed trajectory in the phase space. This condition may only exist in a non-conservative system since it involves the inflow and outflow of energy from the system, the net energy change in any one cycle being zero. A system is said to be asymptotically orbitally stable if the motion approaches a limit cycle as $t \rightarrow \infty$.

Although the limit cycle is considered to be a stable condition in the general field of vibration analysis, in most aerodynamic applications any permanent oscillations are considered undesirable and hence unstable. Examples are aerofoil flutter as described by Den Hartog (1956), plate flutter in aeronautical applications as described by Dowell (1967) and air hammer in air bearings as described by Licht et al (1958). In the tests to be performed here a limit cycle will be considered to be an unstable state since the steel shim used in the experiments was found to fracture while vibrating. Thus, in our application as with other aerodynamic applications we shall employ Blevins' definition of stability with the addition that a vibration must decrease to an equilibrium point and not a limit cycle.

A form of instability which may occur in the neighbourhood of an equilibrium point is divergence to another stationary position. Such a condition is described by Thorpe et al (1971) with regard to a

rigid plate held in the centre of a duct containing an incompressible flow. The plate is held by a torsion bar at its downstream end and above a critical fluid velocity it is found to flip across to one side and rest against the duct wall. They called this hydro-rotational instability. A further example of divergence is the buckling of a panel on an aircraft at subsonic speeds as analysed by Dowell (1967).

Stability analysis can be approached either by qualitative or quantitative techniques. The qualitative method provides an indication of the system behaviour whereas the quantitative method provides an explicit time history of the motion of the system. The quantitative method is generally applied to systems in which the non-linear terms are small and can therefore be considered negligible. The system is then said to be quasi-linear and analytic solutions to the equations can be found. In the analytic technique the small non-linear terms are referred to as perturbations and hence it is called the perturbation method.

An alternative approach to the perturbation method is to solve the equations of motion numerically, retaining the non-linear terms. This approach was applied by Dowell to the non-linear integral-differential equations describing the motion of a fluttering plate and allowed an analysis of limit cycle amplitude and frequency to be made. The numerical approach gives by far the most reliable prediction of system behaviour for a continuous non-linear system such as that to be solved here and was therefore the method used. The numerical solution of the equations of motion was described in Chapter 6.

A final point regarding stability analysis is that the stability

of a system may be dependent on the initial conditions as well as on the system parameters. The initial condition may be close to or far away from equilibrium i.e. the motion may be "in the large" or "in the small". Thus, it may be found that a system is unstable with large perturbations from equilibrium while being stable with small perturbations.

7.2 Description of Tests

The system which has been modelled is shown in Fig. 4.1 and assumptions regarding the membrane and the fluid flow are discussed in Sections 5.1 and 5.2 respectively. The membrane is pin jointed at both ends of the duct at $h/H = 0.5$ and the gas constant R and viscosity μ have been based on ambient air.

The variables of interest in a study of the system stability are :

i) Duct height, H.

ii) Duct length, l.

iii) Upstream pressure, p_1.

iv) Tension exerted on the membrane, T.

v) Membrane density, ρ.

In Section 5.3 it was shown that a comprehensive study of the system behaviour can be undertaken by investigating the influence of three dimensionless groups which may be redefined as dimensionless pressure, membrane density and tension. Thus, the five variables are reduced to three and the height and length of the duct were held constant at 200 μm and 0.052 m respectively. These dimensions are close to those of the restricted section in the multiple-disc experimental motor.

The position of equilibrium from which the system was perturbed in order to study its behaviour was the configuration with the membrane straight along the centre of the duct with a constant fluid flow on both sides. Two types of perturbation were employed in the stability tests - a perturbed membrane shape and an impulse function applied to the membrane. The perturbed shape was arrived at by defining the height of the central node of the membrane and fitting a parabolic curve through that point and the two end points. To ensure that the initial values of all the variables were consistent with the mathematical model, the steady state fluid velocity and pressure distributions were calculated along each duct in accordance with the new shape of each. All the tests except two were performed with this type of perturbation. These two remaining tests were performed with an impulse function applied along the membrane. The membrane velocity at the central node was defined and, with the end-points set at zero, a parabolic variation in velocity could be calculated.

The results from each test consist of a time history plot of the displacement of the membrane mid-point from the equilibrium position (i.e. the duct centre line) and a plot of the shape of the membrane on the final time step and at various other steps throughout a test run. The plot of the membrane shape was useful in determining the numerical stability of the results as well as ensuring that the time plot of the central node displacement was representative of the overall behaviour of the membrane.

7.2.1 Series A to D

It was convenient to divide the tests into four series, each with a constant inlet pressure and membrane density. The density in

Series A, B and C was equivalent to the 50 μm thick steel shim which was used in the experimental motor and the density in Series D was a tenth of that. Tension was the only parameter varied within a series. The details of each series are given in Table 7.1 and each test in each series is detailed in Tables 7.2 to 7.5. A selection of the graphical output from Series A to D is given in Figs. 7.2a to 7.14b.

The mid-point of the initial parabolic shape of the membrane in these tests was at $h/H = 0.5125$ and each series of tests was initiated by finding a tension at which the system was stable and a tension at which it was unstable. By running successive tests with the tension half way between the stable and unstable tensions it was possible to "home in" on the transition region.

7.2.2 Alternative Initial Conditions

To ensure that the transition point was not dependent on the initial conditions, extra test runs were undertaken with the same inlet pressure and membrane density as Series A but with different initial conditions. These tests have been grouped together in Series F and are detailed in Table 7.6.

Tests F1 to F11 were undertaken with alterations in the initial parabolic curve of the membrane. It was varied by shifting the central node position to $h/H = 0.94$ in Tests F1 to F9 and to $h/H = 0.63$ in Tests F10 and F11. The end points were kept at $h/H = 0.5$. The results of Tests F10 and F11 are shown in Figs. 7.15 and 7.16 and the results of Tests F4 to F9 are shown in Fig. 7.17 with the shape variation of the membrane in Test F5a shown in Fig. 7.18.

The initial conditions in Tests F12 and F13 consisted of a parabolic impulse function along the membrane which started on the duct centre line. The velocity was zero at the ends with a maximum velocity of 0.005 m/s at the centre. The results of these tests are shown in Figs. 7.19 and 7.20. The double curves at the beginning of each time plot show the vibration envelope of the squeeze film oscillation which was predicted in Section 5.5.

Tests F14 and F15 were effectively reruns of Tests C1 and C7 with alternative initial conditions. Problems had been encountered with numerical stability after approximately 5000 time steps in Series C which limited the length of time the tests could be run. On the assumption that a more gently curved membrane shape would be less prone to numerical instability, these extra tests were undertaken with h/H = 0.5013 at the centre of the membrane in place of h/H = 0.5125. The results of these tests are shown in Figs. 7.21 and 7.22.

7.2.3 Verification of the Computer Model

Verification that the computer model was successfully modelling the system involved two areas. The first was to confirm that the numerical solution of the differential equations was correct and the second was to check that some assumptions made during the derivation of the equations were correct.

To ensure that the equations were solved correctly involved a check on the numerical accuracy of the results and a check for numerical stability. Numerical accuracy was checked by undertaking tests for which there are known analytic solutions. These tests consisted of the membrane vibrating in a vacuum and a steady-state

flow through the duct with the membrane in an arbitrary rigid shape. The steady state flow was arrived at by introducing a step increase in pressure at the inlet and allowing the pressure transients to decay. These checks showed that the arithmetic calculations in the program were correct but could not provide proof that the calculation of the pressure transients was correct since, if any numerical interference was present, it must have decayed with the real transients.

Confirmation that the solution of the combined equations was numerically stable was achieved by checking that the solution of tests with different numbers of elements and/or different time step size produced the same results. Although optimum settings were found in the initial tests it was necessary to vary the number of elements during subsequent tests since the system parameters were found to have an effect on the number required to maintain numerical stability. The results of some of the tests run to investigate the numerical stability are shown in Figs. 7.4, 7.8a and 7.11c. The discussion of these results is presented in Section 7.3.1.

In the derivation of the equations of motion various assumptions were made, one being that the flow is laminar. This was ensured during testing by checking that the Reynolds number of the flow did not exceed 2000 which, as discussed in Chapter 2, is not an unreasonable number to assume for transition to turbulent flow. The inlet pressure used in Series C was the highest possible with this limitation.

It was also assumed that tension exerted on the membrane by viscous shear is negligible in comparison with the tension exerted by the end-points. To check this, the tension due to shear was

calculated with the help of equation 2.6. This equation was derived for the shear force exerted on a disc face in the motor but it is equally applicable to the shear force exerted on the membrane. Since the force is exerted on both sides of the membrane and since $\omega = 0$ in this case, the tension due to shear per unit width, T_s, is:

$$T_s = h\left(p_1 - p_2\right) \tag{7.1}$$

Table 7.8 lists the minimum dimensionless tension in each test series against the tension exerted due to shear, calculated from the above expression. It will be seen that only the Series A shear tension is of comparable magnitude to the minimum test tension. This was the tension used in Test A1 which is well below the region of interest (i.e. the transition region). Test A2 has the next lowest tension in this series and it is forty times the magnitude of the shear tension. It is therefore concluded that the shear tension is negligible throughout the tests performed here.

A further assumption was that bending forces in the plate are negligible and that it can therefore be modelled as a membrane. To check on the validity of this assumption an analysis of the relative magnitudes of the tension and bending terms was undertaken and is described in Appendix B. A characteristic length, L, is defined by equation B2 which defines the half-wavelength beyond which the tension force is greater than the bending force. For the thickness of steel modelled in Series A to C we have $L/l = 0.01/\sqrt{T}$ and in Series D we have $L/l = 0.0035/\sqrt{T}$. At the lowest tension in Series C (Test C1) we have $L/l = 0.04$ which is less than any half-wavelength seen in the result of that test in Fig. 7.11b. Taking Test B3 as an example of a test near the transition point in Series B, we find that

L/l = 0.07 which is less than any half-wavelength seen in the result of that test in Fig. 7.6b. At tensions greater than those used in these two tests in each series, the same conclusions may be drawn and it is considered that this validates the negligible bending force assumption near and above the transition point in these two series. Near the transition point in Series A and D we find that L/l = 0.25 and L/l = 0.23 in Tests A4 and D3 respectively. These lengths are of the same order of magnitude as those seen in the results of these tests in Figs. 7.2b and 7.13b. The addition of bending in the membrane equation of motion may therefore affect the results of Series A and D but not those of Series B and C. It is not unreasonable to assume that it would act to reduce the critical tension required to maintain stability in Series A and D.

7.3 Discussion of Results

We shall start, in Section 7.3.1, with a discussion of the tests which were run to check the numerical stability of the results and various factors which affected this. Sections 7.3.2 and 7.3.3 then discuss the effects of inlet pressure and membrane density on membrane stability. Finally, Section 7.3.4 discusses the effect of different initial conditions and Section 7.3.5 discusses the various vibration frequencies seen in the results.

7.3.1 Numerical Stability

Evidence that the numerical method was stable was achieved by altering the number of elements and the time step size and comparing the resulting membrane shape after the same length of time. An example of such a check is seen in Fig. 7.4 in which the membrane

shape at 2.2 ms in Tests A1, A1a and A1b is shown. The agreement can be seen to be very good. Similar checks were run on Tests A6, A9, C1 and C5.

Numerical instability in the tests showed up as a "sawtooth" waveform at the downstream end of the membrane and the amplitude increased very rapidly with time. A particularly severe example of this waveform development is shown in Fig. 7.16b and evidence of it can be seen in many other plots. In the sawtooth region, it was found that whereas the variation of h shows alternating positive and negative values of slope, the value of ψ $(\partial h/\partial x)$ at each node was the average value of the slope in that area. The fluid speed on both sides of the membrane was consistent with the shape of the membrane. Thus, an inconsistency exists between the height h and the slope ψ in the sawtooth region.

It was possible to suppress the sawtooth waveform by increasing the number of elements. Figs. 7.13c and 7.13d show the results of Tests D10 and D10a which were run with 320 and 80 nodes respectively. It can be seen that the sawtooth waveform present in Test D10a with 80 elements is not present in Test D10 with 320 elements. This example also shows that the behaviour of the system can still be ascertained even though the instability is present. Any test, if run for long enough, would develop the numerical instability but tests run with more elements could be run for longer before the instability intruded on the result. Thus, the choice of the number of nodes was a compromise between computer time and obtaining a sufficiently long run time to discern the system behaviour.

A condition was included in the program to stop execution if the characteristics did not obey the CFL stability condition at any node

at any point in time. It was found that, in tests where the membrane vibration amplitude was increasing due to physically unstable behaviour, failure to obey this condition would eventually stop program execution. An example of this is shown in Fig. 7.8a which shows the time plot of Tests B1 and B1a with 320 and 80 elements respectively, plotted up to the time at which the program halted. It can be seen that the test with 320 elements proceeded for longer than the test with 80 and the fact that the result was numerically stable when the program execution was halted in Test B1 can be seen in Fig. 7.8b. Reducing the time step by half did not greatly alter this situation and the program was obviously reaching the limit of its ability to model the system.

Both the number of elements and the time step size required to maintain numerical stability varied with test conditions. The basic criterion was that conditions which led to a more curved membrane shape required a greater number of elements. These conditions were lower tensions, higher inlet pressures and larger initial perturbations of the membrane shape. Also, if the high frequency vibration (which is discussed further in Section 7.3.5) increased significantly, then the time step had to be reduced.

7.3.2 Effect of Inlet Pressure on Stability

A summary of the results gained in Series A, B and C is shown in Fig. 7.1. The behaviour of the membrane in each test is depicted by a different symbol according to whether it was found to be stable, unstable or to result in a limit cycle. The graph clearly shows that as the pressure drop is increased the tension exerted on the membrane has to be increased to maintain stability. The curve through the

three points at which the transition to stability occurs passes through zero tension at zero pressure drop (or zero flow). Thus, on the available evidence, any amount of flow, however small, requires a finite tension to maintain stability.

We shall now discuss the results of each series of tests individually.

i) Series A

Figs. 7.2a to 7.4 show results from Series A. The results in Fig. 7.2a show a typical linear system response to a perturbation from equilibrium and this response, in what is essentially a non-linear system, is due to a small initial perturbation combined with a low inlet pressure producing a quasi-linear system. Test A10 shows a case of overdamping, Test A9 shows critical damping and the remaining tests exhibit underdamping. The exponential decay in the underdamped cases is typical of a viscously damped system, the damping in this case being due to the viscous shear of the fluid dissipating membrane energy at a rate which is proportional to the fluid velocity. The membrane shapes on the final time step shown in Fig. 7.2b confirm that the plots of the centre node oscillation in Fig. 7.2a are representative of the membrane response. Fig. 7.2b also shows that the tests cannot be taken further since numerical instability is encroaching on the result.

Fig. 7.3a shows the unstable result of Test A2 and the membrane shape in Fig. 7.3b indicates that the increase in oscillation amplitude is due to physical instability rather than numerical instability. On the assumption that any test which results in an increase in oscillation amplitude will continue to increase, as in

Test A2, the transition from stable to unstable behaviour can be assumed to occur between Tests A5 and A4 as seen in Fig. 7.2a.

ii) Series B

Results from Series B are shown in Figs. 7.5 to 7.8. Fig. 7.5 contains results of tests in the transition region with the transition seen to occur between Tests B5 and B4. The distinctly unstable results of Tests B2 and B1 at lower tensions are shown in Figs. 7.7 and 7.8 respectively with the plots of membrane shape in Figs. 7.7b and 7.8b indicating that the results are numerically stable.

The alternating amplitude seen in the result of Test B3 in Fig. 7.5 is due to the natural frequencies of the membrane and air waves being nearly equal (this is discussed further in Section 7.3.5). The increase in disorder of the membrane which indicates instability in this test is shown in Fig. 7.6b.

The ragged shape of the time plot from Test B6 in Fig. 7.5 is due to a coarse sampling rate. This also occurred in Series C and is discussed below. The membrane shape variation in Test B6 can be seen in Fig. 7.6a in which an overall decrease in amplitude is in evidence, thus confirming physical stability.

iii) Series C

Results from Series C are shown in Figs. 7.9 to 7.11c. The ragged shape of the curves in this series of tests is the result of too coarse a sampling rate. An example of the actual waveform obtained from a finer sampling rate is shown in Fig. 7.11c where it can be seen in conjunction with the ragged waveform from a coarse

sampling rate. The high frequency wave which is superimposed on the lower frequency wave oscillates at 11.1 kHz and is the result of the squeeze film vibration predicted in Section 5.5. This higher frequency vibration was present in many results but was only visible depending on the graph scale.

Fig. 7.9 shows the stable result of Test C8 and the results of Tests C4 and C7 which would appear to be limit cycles. Fig. 7.10a shows the membrane flattening out in Test C8 while the overall disorder does not decrease in Test C7 in Fig. 7.10b. Figs. 7.11a and 7.11b show the unstable result of Test C1.

Limit cycles were typical of a range of tensions in Series C as shown in Fig. 7.1 and are a possible result of a non-conservative non-linear system. This would therefore suggest that the non-linear terms in the equations are of greater magnitude in Series C than in the other series.

7.3.3 Effect of Membrane Density on Stability

The membrane density in Series D was one tenth that in Series A to C and the results are shown in Figs. 7.12 to 7.14. Fig 7.12 shows three results from Series D, each of which appears to be asymptotically stable and the membrane shape variation in Fig. 7.13a confirms this for Test D4. Examination of Fig. 7.13b, however, shows that although the oscillation amplitude has decreased at $x/l = 0.5$ in Test D3 it has increased in the region $0.8 < x/l < 1.0$. This test was therefore taken to be unstable and was the largest tension at which instability was found. An example of an obviously unstable result is shown in Fig. 7.14.

The lowest dimensionless tension which was required to maintain

stability was 2.69×10^{-4} (Test D4) which is approximately one sixth that of the comparable test in Series A (1.75×10^{-3} in Test A5). This would appear to contradict the usual tendency that a structure with a lower mass ratio (structure density to fluid density) is more susceptible to flow-induced vibrations. In this case, though, the viscosity of the fluid plays an important part in the behaviour of the structure and as the density of the membrane is reduced the energy dissipation due to viscous shear is more able to reduce its kinetic energy.

The 36.2 kHz oscillation which is superimposed on each plot in Fig. 7.12 is due to the squeeze film vibration and is more noticeable here than in the results of Series A to C since the lower inertia of the membrane allows a larger oscillation amplitude.

7.3.4 Alternative Initial Conditions

The transition point in tests run with the same membrane density and inlet pressure as Series A, but with different initial conditions, was found to occur in the same tension range as in Series A. Fig 7.15 shows the results of Tests F10 and F11 which were run with identical tensions to Tests A4 and A5 respectively but with the parabolic mid-point starting at $h/H = 0.63$ instead of at $h/H = 0.5125$. The membrane behaviour in Tests F10 and F11 is seen to be identical to that of Tests A4 and A5 in Fig. 7.2a. Tests F12 and F13 were also undertaken with the same conditions as Tests A4 and A5 respectively but with a parabolic impulse function applied along the membrane. The results are shown in Figs. 7.19 and 7.20 and the double curves in the time plots show the vibration envelope of the squeeze film vibration. This is seen to decay with time and the

oscillation frequency which remains in each case is the same as that seen in Fig. 7.2a for Tests A4 and A5. Again, the lower tension test is unstable and the higher tension is stable.

Tests F1 to F9 were run with the initial parabolic mid-point at $h/H = 0.94$ and the results of Tests F5a to F9 are shown in Fig. 7.17. Only these stable plots are shown here since Tests F1 to F4, which were run at lower tensions, failed the CFL condition too early to produce a result. The shape of the membrane was found to become highly irregular in the lower tension tests and an example is shown in Fig. 7.18 which is the result from Test F5a. This test appeared to be stable in Fig. 7.17 but it eventually failed due to its inability to meet the CFL condition. Although it proved impossible in Tests F1 to F9 to define a transition point with these alternative initial conditions it can be seen that the behaviour at higher tensions is the same as that in Series A. For example, Tests F7 and F9 (c.f. Tests A9 and A10) produce a critically damped and overdamped response respectively.

Tests F14 and F15 were basically a rerun of Tests C1 and C7 with the mid-point of the parabola changed from $h/H = 0.5125$ to $h/H = 0.5012$. The aim of these tests was to avoid the numerical instability which had prevented the tests in Series C being taken further. As can be seen in Figs. 7.21 and 7.22, the results of Tests F14 and F15 are identical to those of Tests C1 and C7 in Figs. 7.9 to 7.11 and hence no benefit was gained by changing the initial conditions.

7.3.5 Oscillation Frequencies

There are two areas of discussion regarding frequencies in this system. The first is the natural frequencies of the membrane and the air waves and how these interact, and the second is the oscillation due to the squeeze film effect. In the study of the natural frequencies we first define the expression for frequency f as:

$$f = \frac{c}{\lambda} \tag{7.2}$$

where λ is the wavelength.

The wavespeed of a compressible fluid is generally taken as $\sqrt{\gamma RT}$ (where γ is the ratio of the specific heats) but this is on the assumption of adiabatic flow. In the derivation of the equations of fluid motion in Chapter 5 it was assumed that the flow is isothermal and, on the assumption of perfect heat transfer, the speed of sound is therefore $\sqrt{RT}$ = 290m/s. With the wavelength of the air waves in an open ended duct equal to twice the duct length, the natural frequency of the air waves is therefore 2.8 kHz.

Calculation of the natural frequency of the membrane waves is more difficult because, as can be seen in the plots of membrane shape, there is not a definite number of waves between the end-points. The method which was employed was to measure the wavelength of the membrane in the neighbourhood of the centre of the membrane. The wavespeed in the membrane, c_m, is given by the characteristic speed as defined by equation 6.13a, which gives us:

$$c_m = \left(\frac{T}{\rho}\right)^{1/2} \tag{7.3}$$

The natural frequency is then calculated using equation 7.2. Table 7.7 lists the natural frequency of the membrane against the

actual frequency measured on the time plots for certain tests. The table shows that the actual frequency of the membrane is always between the natural frequency of the membrane and the 2.8 kHz frequency of the air waves. It would therefore appear that the air waves shift the frequency of the membrane in such a way that the actual frequency takes a value somewhere between the two natural frequencies.

A most interesting result is that of Test B3 in which the membrane oscillation itself oscillates (see Fig. 7.5). Morse (1948) describes a similar plot which is due to the coupling of two oscillators having the same natural frequency. Table 7.7 shows that the actual frequency of the membrane oscillation in Test B3 was nearly the same as the frequency of a standing air wave, hence the secondary oscillation.

It is also interesting to note that in the experimental model of a single duct, a frequency of 1.4 kHz was measured at a pressure of 1.26 bar in experiment E10. A linear interpolation between the frequencies measured in Series A and B gives a frequency of 1.68 kHz at 1.26 bar. This close correlation of experimental and theoretical results provides some validation of the theoretical model.

The oscillation due to the squeeze film effect which was predicted in Section 5.5 was found to occur in all the results. Its dependence on the system parameters was given by:

$$f = \frac{1}{2\pi}\left(\frac{2p_a}{\rho h_a}\right)^{1/2} \qquad (5.42)$$

It was found to be a low amplitude, high frequency oscillation compared to the other system oscillations and is only visible in

graphs with suitable scales. In graphs where this oscillation can be seen, the frequency is found to be very close to that predicted by this equation. For example, the high frequency wave of Test C1a seen in Fig. 7.11c has a frequency of 14.8 kHz and the predicted frequency (using the pressure at the central node) is 13.7 kHz. Also, the frequency of the lower density membrane in Series D is seen in Fig. 7.12 to be 37.0 kHz and the predicted frequency is 36.2 kHz. Fig. 7.12 also confirms that the frequency does not vary with tension.

Table 7.1

Dimensionless Pressure Drop and Membrane Density in Each Series

Series	Pressure Drop	Membrane Density
A	1.53	0.4
B	7.65	0.4
C	15.30	0.4
D	1.53	0.04

Table 7.2

Series A : Pressure Drop = 1.53 ; Density = 0.4

Test No	*N*	Tension $x10^3$	Comments
A1	80	0.054	Unstable
A1a	80	0.054	A1 with time step halved
A1b	160	0.054	Same time step as A1
A2	80	1.23	Unstable
A3	80	1.57	Unstable
A4	80	1.66	Unstable
A5	80	1.75	Stable
A6	80	1.92	Stable
A6a	320	1.92	Confirmation of Test A6
A7	80	2.69	Stable
A8	80	4.61	Stable
A9	80	5.38	Stable
A9a	320	5.38	Confirmation of Test A9
A10	80	53.8	Stable
A11	80	538.0	Stable

Table 7.3

Series B : Pressure Drop = 7.65 ; Density = 0.4

Test No	*N*	Tension	Comments
B1	320	0.0054	CFL failure
B1a	80	0.0054	Numerically unstable
B2	320	0.0137	Unstable
B3	320	0.0220	Unstable
B3a	80	0.0220	Numerically unstable
B4	320	0.0241	Unstable
B5	320	0.0262	Stable
B6	320	0.0304	Stable
B6a	80	0.0387	Numerically unstable
B6b	80	0.0553	Numerically unstable
B7	80	0.0720	Stable
B8	80	0.105	Stable
B9	80	0.139	Stable
B10	80	0.205	Stable
B11	80	0.272	Stable
B12	80	0.538	Stable

Table 7.4

Series C : Pressure Drop = 15.3 ; Density = 0.4

Test No	*N*	Tension	Comments
C1	320	0.0538	Unstable
C1a	640	0.0538	Confirmation of Test C1
C2	320	0.0605	Limit cycle
C3	640	0.0614	Limit cycle
C4	320	0.0672	Limit cycle
C5	320	0.0690	Limit cycle
C5a	640	0.0690	Confirmation of Test C5
C6	320	0.0707	Limit cycle
C7	320	0.0774	Limit cycle
C8	320	0.0841	Stable
C9	320	0.114	Stable
C10	320	0.175	Stable
C11	320	0.296	Stable
C12	160	0.538	Stable

Table 7.5

Series D : Pressure Drop = 1.53 ; Density = 0.04

Test No	*N*	Tension $x10^3$	Comments
D1	640	0.166	Unstable
D2	640	0.175	Unstable
D3	320	0.222	Unstable
D4	640	0.269	Stable
D5	320	0.363	Stable
D6	320	0.458	Stable
D7	320	0.552	Stable
D8	320	1.17	Stable
D9	320	1.66	Stable
D10	320	1.75	Stable
D10a	80	1.75	Numerically unstable

Table 7.6

Series F : Alternative Initial Conditions*

Test No	*h/H* at *N/2*	*N*	Tension	Comments
F1	0.94	80	0.054	CFL failure
F2	0.94	80	0.538	CFL failure
F2a	0.94	320	0.538	CFL failure
F3	0.94	80	1.14	CFL failure
F3a	0.94	320	1.14	CFL failure
F4	0.94	320	1.45	CFL failure
F5	0.94	80	1.75	Numerically unstable
F5a	0.94	320	1.75	CFL failure
F6	0.94	80	2.96	Stable response
F7	0.94	80	5.38	Stable response
F8	0.94	80	53.8	Stable response
F9	0.94	80	538.0	Stable response
F10	0.63	80	1.66	Unstable response
F11	0.63	80	1.75	Stable response
F12**	0.50	320	1.66	Unstable response
F13**	0.50	320	1.75	Stable response
F14	0.5013	320	53.8	Repeat of Test C1
F15	0.5013	320	77.4	Repeat of Test C7

* The system parameters in each test were the same as those of Series A except Tests F14 and F15 in which the parameters were the same as those of Series C.

** The perturbation from equilibrium in these tests consisted of an impulse function imparted on the membrane.

Table 7.7

Comparison of Frequencies

Test No	Actual Frequency (kHz)	Membrane Natural Frequency (kHz)
A4	1.02	0.86
B5	2.56	2.42
B3	2.76	2.61
C1	3.87	4.16
D9	1.71	1.45

Table 7.8

Comparison of Test Tension and Shear Force Tension

Series	Pressure Drop	Minimum Test Tension $x10^3$	Estimated Shear Tension $x10^3$
A	1.53	0.054	0.032
B	7.65	5.38	0.116
C	15.30	53.80	0.240
D	1.53	0.17	0.032

CHAPTER 8

DISCUSSION

8.1 Introduction

Two experimental motors have been constructed during this feasibility study of the viscous shear pneumatic torque motor. The multiple-disc motor provided flowrate measurements and the single-disc motor provided torque and flowrate measurements over a range of pressures, rotational speeds and duct sizes. These results have confirmed that the theoretical approach described in Chapter 2 provides predictions which are of the correct order of magnitude. The single-disc motor also confirmed that, with its dimensions, both torque and flowrate are insensitive to rotational speed over the speed range used here.

These theoretical predictions have shown that, for a torque requirement of 1.5 Nm at 6 bar gauge, the gap between the discs has to be very small in order to limit the flowrate. The restrictor plates therefore have to be very thin and the 50 μm thick steel shim used for the restrictor plates in the experimental motor was the minimum thickness that could be used, given the available materials and workshop facilities. Likewise, it was considered that the 250 μm disc spacing was the minimum that could be used while still maintaining clearance. With the chosen disc outer radius and duct width, it was estimated that 16 ducts of these dimensions were needed to produce the required torque.

The air flowrate through the motor which was built with these dimensions was measured at 17.5 dm^3/s at a pressure of 0.87 bar gauge. Linear extrapolation of this to 6 bar gauge leads to

a flowrate of 120 dm^3/s and a power consumption of 72 kW which is very high. Since flowrate has a third order dependency on the disc spacing while torque is linearly dependent, it would therefore be beneficial to reduce the spacing even further and increase the number of ducts. This introduces the need for restrictor plates which are thinner than 50 μm and which will be flexible as a consequence.

The downstream edge of the plates in the experimental motor broke up during testing and the cause appeared to be vibration fatigue. It also appeared as if the plates had buckled and pushed the rotor against the casing. Flexible plate stability in a thin gap is therefore a major consideration in the design of the motor and the feasibility study has focussed on this topic. On the assumption that the plate is perfectly flexible, it has been referred to as a membrane in the theoretical analysis.

In Section 8.2 we shall consider the theoretical model of flexible plate motion in a thin duct and the method of characteristics which was used in the solution of the final set of equations will be discussed in Section 8.3. Results from the theoretical model will then be compared with experimental results in Section 8.4 and the implication of these on the feasibility of the viscous shear torque motor will be discussed in Section 8.5.

8.2 Theoretical Model of Membrane Motion in a Duct

Rather than attempt to model the complex three dimensional duct found in the motor, the theoretical analysis was eased by modelling a two-dimensional duct similar to the straight duct experiment described in Chapter 3. Simplifying the geometry of the duct in this way, allowed a general study of membrane behaviour in a thin duct to

be undertaken rather than limiting the results specifically to the motor which was built.

Development of the model progressed through several stages. This commenced with a typical qualitative approach to stability analysis. The membrane was perturbed from an equilibrium position and the pressure force distribution along the membrane was calculated with a steady flow through the channels. Several membrane shapes were tested but it was not possible to draw any general conclusions regarding its stability.

The second approach to the problem was a quasi-steady dynamic model in which the instantaneous position of the membrane determined the flow in the channels. The membrane motion was dependent on the pressure distribution and the tension. Results from this model were found to be physically unrealistic because the membrane motion was too rapid in relation to the fluid wave speed for the assumption of instantaneous flow to be correct.

The final theoretical model used the same membrane equation of motion as the quasi-steady model but included an unsteady flow analysis. This approach was successful and provided the results discussed in Chapter 7.

The simplification of the system from three dimensions to two, has introduced the need to define boundary conditions which are dissimilar to those found in the motor. This is a common requirement when modelling a system and can lead to conflicting opinions on the best approach. For example, theoretical models of flexible walls containing a flow show considerable variation of boundary conditions. Grotberg and Reiss (1984) assume the duct is infinite and hence has no boundaries whereas Matsusaki and Fung (1979) assume

that the region to be analysed consists of perfectly flexible walls, simply supported at both ends and connected to rigid entrance and exit channels which are infinitely long.

The boundaries of the membrane in the present model were defined by the restrictions imposed by the mathematical model as well as the requirement to be representative of the plates in the motor. In deference to the "real" situation, the membrane supports were held stationary at both ends at $h/H = 0.5$ on the assumption that a motor can be made accurately enough to position the plates in the centre of the disc spaces. The supports were pin-jointed, which is implicit in the assumption of a non-rigid structure, and were positioned in the inlet and exit planes of the duct.

Positioning the supports outwith the duct may appear to be more representative of the real situation but this was not possible in the model due to the difference in fluid and membrane wavespeeds. Tests were performed to investigate this with the supports positioned outside the duct by defining a region of constant pressure either side of the membrane at a few nodes near the boundaries. The membrane was perturbed from the centre line into a parabolic shape and the inlet and outlet of the duct were maintained at atmospheric pressure. The pressure waves set up in the duct as a consequence of the oscillation of the membrane were found to be the main driving force once the membrane was moving. Since the membrane wavespeed was less than the fluid wavespeed (e.g. half at the transition to stability in Series C and one fifteenth in Series A) the movement of the membrane due to the pressure waves inside the duct was not communicated outside the duct at the same speed. With no resistance to bending, the membrane underwent vast changes in slope at the duct

boundaries which were clearly unrealistic. A continuous membrane shape was only possible if the tension produced a membrane wavespeed comparable to the air wavespeed but since the required dimensionless tension was 0.38 and the yield point for the chosen thickness of steel membrane is 0.26, this was not feasible.

Although the bending forces in the plate have been assumed to be negligible in the theoretical model and intuitively the introduction of stiffness should reduce the tension required for stability, the behaviour of the membrane may be altered. Only flutter was present in the tests undertaken here but perhaps divergence such as that observed in the perspex duct experiment would be obtained on the addition of plate stiffness.

8.3 Numerical Solution by the Method of Characteristics

Prior to the use of the method of characteristics in the solution of the differential equations, a two-step Lax-Wendroff scheme was adopted which proved to be unsuccessful. The Lax-Wendroff method could model a pressure transient in a rigid walled duct of varying height and it could model transients along the membrane in a vacuum but the simultaneous solution of both sets of transients proved elusive due to numerical instability. The instability occurred as a sawtooth waveform in the membrane at both boundaries and it affected the complete length of the membrane before meaningful results could be obtained. This prompted the investigation of different methods of solution at the boundaries which included first and second order extrapolations, and the method of characteristics. The characteristics were solved by a Hartree method in which both first and second order interpolations were used. None of these

methods cured the instability and an alternative means of solution was sought.

The method of characteristics used on a fixed rectangular grid (the Hartree method) is claimed by Zucrow and Hoffman (1976) to be the most accurate time-marching solution method available for hyperbolic equations. The Hartree-type method, which was used at the boundaries in the Lax-Wendroff method, was therefore extended to the solution at the interior nodes as well as at the boundaries. Unfortunately, numerical instability also appeared in this solution but it could be avoided by a combination of a greater number of elements and restricting the number of time steps. Although restricted in its performance, the method still gave adequate results to draw conclusions regarding the system's physical stability.

In the application of the Hartree solution method, interpolations are required to obtain values at the points where the characteristics intersect the spatial line. Although linear interpolation is the most common method, Wylie and Streeter (1978) claim that higher order interpolations generally produce improved results for smooth transients due to the reduction in numerical damping. A second order method was therefore used here in the interests of improved accuracy. For the solution at each interior node, i, this involved the values at i-1, i and i+1 on the previous time step and at the boundaries it involved the two nearest interior nodes and the boundary node.

In retrospect, the unstable behaviour of the membrane at the downstream boundary is probably due to the use of second order interpolations. Zucrow and Hoffman (1976) warn that the accuracy of the Hartree method is limited since the points used in the

interpolation are outwith the domain of dependence. It therefore follows that the accuracy will decrease as the ratio of the size of the domain of dependence to the numerical domain reduces and steeper characteristics will be at greatest risk of inaccuracy. Indeed, in the tests described here it was the steeper membrane characteristics which developed instability while the fluid transients remained stable. Vardy (1976) explains that the numerical dispersion, and hence the inaccuracy, caused by the interpolations can be reduced by using a finer grid size and it was found that numerical instability in the present tests reduced as the grid was refined. An increase in membrane tension which results in a reduced characteristic slope, also reduced numerical instability.

If test runs longer than those undertaken here are required, then some means of avoiding the numerical instability will be necessary. The simplest method is to refine the grid size even further. This leads to an increased time penalty and since the average computer time per test was 4 hours, it is not very practical. Alternatively, the use of linear interpolations at the boundaries may give improved accuracy and allow longer test runs with the same number of elements. Failing this, the time-line interpolation method described by Wylie (1980) may provide improved accuracy but would require substantial reprogramming. Finally, the best solution is to employ the natural grid of characteristics which eliminates all interpolation error.

8.4 Comparison of Results on Membrane Stability

Experimental results on the stability of a flexible plate in a thin duct were obtained from the perspex and straight duct experiments which were described in Chapter 3. These experiments were simple in concept and the results somewhat limited. They can therefore only serve as an indication of the type of behaviour to be expected. Theoretical predictions of stability, assuming a perfectly flexible plate (or membrane), were discussed in Chapter 7.

Flutter of the membrane occurred in both experiments and was also predicted theoretically. The frequency of the vibration could be measured in the perspex duct and was found to be 1.4 kHz at an inlet pressure of 0.26 bar gauge. This compares very well with a theoretical prediction of 1.68 kHz at the same pressure and provides some validation of the theoretical model.

A critical pressure, above which flutter occurred, could be defined in most tests in both experiments and it was found that the plate in the perspex duct fractured at the downstream end concomitant with this vibration. In the straight duct some variation in tension was possible and it was noted that the critical pressure increased with increasing tension. Below the critical pressure the plate was found to straighten out and did not vibrate. It is therefore not unreasonable to assume that the flutter of the plate in the perspex duct could be prevented with adequate tension.

Tests performed with the plate initially positioned off-centre in the two experiments produced markedly different results. The plate in the perspex model was found to diverge rapidly to the farthest wall. The same result was obtained by Thorpe et al (1971) with a rigid plate supported at its downstream end in a duct

containing an incompressible turbulent flow of air. With the plate positioned off-centre, parallel to the walls, it was found to rotate in a divergent motion until it contacted the farthest wall. He concludes that this is due to lower dynamic pressure and hence higher static pressure in the smaller channel. In the perspex duct tests, the Reynolds number of the flow in the larger channel was approximately 540, so it is unlikely that any dynamic pressure effects are responsible for a difference in static pressure. It is more likely that the divergence is simply due to the manner in which the flow negotiates the bend in the duct.

When the plate in the straight duct was positioned off-centre it was found to straighten out from an initially wavy shape into a straight line off-centre. In the theoretical model the membrane is also in equilibrium off-centre if it is parallel to the walls in a steady flow. The theory assumes that the flow is fully developed and laminar, but most importantly, entrance and exit effects are neglected. According to equation 4.8 the pressure distribution is therefore the same in any height of duct and there is no propulsive force perpendicular to the duct axis. This idealised case will be approached in reality as the duct height and membrane thickness are reduced and the losses at the entrance are minimised.

8.5 Feasibility of the Viscous Shear Pneumatic Torque Motor

It has been seen in both the theoretical and experimental work with a membrane (or flexible plate) in a thin duct that the membrane is prone to flow-induced vibration (or flutter). Proof that this was the cause of the plate breakage in the experimental motor was gained when the same breakage was observed in the perspex model of a duct in

the motor. In the preceding section it was concluded that the flutter could be prevented in the experiments by tensioning the plate. On the assumption that the results from these experiments are applicable to the motor, the application of adequate tension to the steel plates in the motor will therefore prevent the break-up of the downstream edge.

Theoretically it has been shown that, for a dimensionless density of 0.4, the critical dimensionless tension is 0.084 at a dimensionless pressure drop of 15.3. In a duct of length 0.052 m and height 250 μm - the height being the same as the disc spacing in the motor and the length an approximation of the arc length of the restricted section - these dimensionless values relate to actual values of 1 bar gauge inlet pressure, a membrane density of 400 g/m^2 (0.002 inch thick steel shim) and a tension of 7.3 kN/m. The maximum tensile strength for this thickness of steel plate is 23 kN/m, so the critical tension is achievable. On the assumption that the results from this idealised theoretical model are applicable to the motor, this indicates that, up to 1 bar gauge, adequate tension can be applied to maintain stability. Unfortunately, extrapolation of the theoretical critical pressure-tension relationship reveals that the critical tension will equal the maximum tensile strength of the material at an inlet pressure of only 1.9 bar gauge. The operating range of a motor with the present dimensions would therefore appear to be severely limited.

A common problem for both the single and multiple disc motors was that the rotor locked up when the air supply was turned on. It was originally assumed that the thin plates had buckled in the multiple-disc motor and acted as a brake by pressing against the

discs but this was clearly not the case in the single-disc motor. It was subsequently found that air leakage through the bearings caused the rotor in both motors to move axially and jam against the casing. This was remedied by incorporating adjustable bearing housings in the single-disc motor. The remedy for the multiple-disc motor was to push the rotor away from the casing with a pen nib pressed in the end of the shaft. Although rotation was achieved, the potential problem of plate buckling in the multiple-disc motor cannot be ruled out altogether, since the plate was found to diverge in the perspex duct experiment.

Construction of a second multiple-disc viscous shear torque motor of the same dimensions would necessitate some alterations in the design and construction. The flatness of the discs needs to be improved and could be achieved by either annealing the Duralumin discs after machining or by using another material. Tension needs to be applied to the restrictor plates to prevent breakage and the bearings would need to be leak tight. In the initial design specification of the motor in Section 1.3, it was proposed that air bearings are used to minimise friction. Since the bearing pressure would be greater than the pressure in the motor, leakage would be prevented and a small flow would actually pass into the motor. It may even be possible to "fine tune" the position of the rotor with alterations in bearing pressure.

The inertia of the rotor in the multiple-disc motor was 3.10^{-3} kg m^2 which is ten times greater than a typical DC motor of the same torque. Low inertia allows faster and more easily controlled motion and, in order to compete, the air motor rotor inertia would therefore have to be reduced. Discs of the same

material cannot be made much thinner because rigidity would be lost, so the best route forward may be the use of one of the new generation of plastics in the construction of the rotor.

Even at an inlet pressure of 0.87 bar gauge, the air consumption in the multiple-disc motor was 17.5 dm^3/s. This is relatively high and a reduction would be beneficial. If the reduction is achieved by reduced disc spacing, the restrictor plates may also need to be thinner. Fortunately, the theory predicts that as the membrane density is reduced, the tension required to maintain stability also reduces. Unfortunately, the one theoretical result pertaining to a reduction in membrane density predicts that for a tenfold reduction in density the critical tension only reduces by a factor of seven. This would therefore limit the upper pressure at which a thinner plate could operate.

Throughout this discussion the problems incurred due to the flexible restrictor plates have been explained. If 1.9 bar gauge, as predicted by theory, is indeed the maximum pressure at which the present multiple-disc motor could operate, then the potential performance is seriously restricted. This limits its applicability for position control but with the advantages of insensitivity to velocity transients, a linear torque-pressure relationship and low friction, the viscous shear torque motor could still find applications in other areas.

If the duct height could be increased then rigid restrictor plates could be used. This is a possibility in a larger diameter rotor since, with annuli at a larger radius, the flow path would be increased and the flowrate would therefore be reduced. With a larger flow cross-sectional area at a larger radius, the viscous shear

torque motor therefore has potential as a high torque motor. At the other end of the scale, a small motor may be feasible. The flow may be relatively large but the potential advantages could outweigh this.

CHAPTER 9

CONCLUSIONS

1. Equations have been derived for steady compressible flow through a viscous shear pneumatic torque motor. These equations have provided predictions of torque and flowrate which have shown that, for the envisaged position control application, the disc spacing has to be very small to limit flowrate.

2. The small disc spacing has led to the requirement for flexible restrictor plates.

3. An experimental viscous shear pneumatic torque motor has been constructed. Flowrate was measured over a range of pressures but the lack of rotor rotation precluded torque measurement. Several restrictor plates fractured at the downstream edge.

4. A single-disc motor has been constructed with variable duct height. Torque and flowrate measurements agree reasonably well with theory.

5. The flexible restrictor plates have been highlighted as the area of greatest concern and a theoretical and experimental investigation has been undertaken into flexible plate behaviour in thin ducts.

6. Equations have been derived for unsteady compressible flow through a high aspect ratio rectangular duct containing a membrane. The Navier-Stokes momentum equation and the continuity equation are integrated across the duct to give partial differential equations in x and t with the conserved quantities, mass and momentum, as the

dependent variables. An equation of motion for the membrane has also been derived.

7. Numerical methods have been developed for the solution of the equations. The first, a two-step Lax-Wendroff method, has not provided a numerically stable solution. The second, a Hartree type method, is used to solve the characteristics on a fixed rectangular grid and this has proved successful.

8. A computer program using the numerical methods described has been written to simulate the membrane motion in the duct.

9. A theoretical survey of membrane behaviour has been presented. A critical membrane tension has been defined at each of three inlet pressures and at a second membrane density at the lowest pressure. Below the critical tension an unstable flutter has been found to develop.

10. Two experiments have been performed to examine flexible plate behaviour in a thin duct. The first was a perspex copy of a duct in the experimental motor in which the plate support position could be varied. The second was a straight, high aspect ratio duct in which the plate end positions and the tension were varied.

11. Flutter occurred above a critical pressure in both experiments. The critical pressure increased with increased tension.

12. The flutter frequency in the perspex duct and the theoretically predicted frequency agree well.

13. Flutter was the cause of the breakage of the downstream edge of the plate in the perspex duct experiment. This damage is identical to the damage to plates in the motor. It is argued that flutter caused the damage to the motor plates and that tensioning the plate would prevent it.

14. Extrapolation of the theoretical results has predicted that a viscous shear pneumatic torque motor will have a limited operating range with the present dimensions. The tension required to stabilise the plates is greater than the yield point of the material at pressures above 1.9 bar.

15. With the advantages offered by the viscous shear pneumatic torque motor, further study of its feasibility is warranted. Future work should also encompass areas of use where rigid restrictor plates could be used.

APPENDIX A

ESTIMATION OF LEAKAGE FROM THE SINGLE-DISC MOTOR

The leakage from the single-disc motor passes through regions *C* and *D* on both sides of the disc as shown in Fig. 2.5. For the purpose of calculation, the pressure round the periphery of region *C*, p_3, is assumed to be uniform and was taken to be the average of the inlet and outlet pressures. The pressure round the annulus at the entry to region *D*, p_4, is also assumed to be uniform and the flow in region *C* is purely radial with no tangential component. The annulus is of radius r_s and length l_D.

The estimation of the flow through both regions will be based on the flow through a straight, high aspect ratio, rectangular duct and since the duct spaces are small we shall assume that the flow is laminar. This results in the analysis of the flow through region *C* following similar lines to the analysis of radial flow in an externally pressurized gas bearing (see Barwell 1979).

The expression for laminar flowrate through a high aspect ratio rectangular duct was given by equation 2.15, which, with $\omega = 0$ and some rearrangement becomes:

$$\dot{m} = - \frac{bh^3}{24\mu R\theta} \frac{dp^2}{dx} \qquad \text{(A1)}$$

For region *C* we take an infinitesimal strip at radius *r* and assume that the flow through this strip is equivalent to the flow through a rectangular duct of width $2\pi r$. Substitution of the relevant parameters into equation A1 then gives the following expression for

the mass flowrate through region C, $\dot{m}_C$:

$$\dot{m}_C = - \frac{\pi r h_C^3}{12\mu R\theta} \frac{dp^2}{dr} \qquad (A2)$$

Integration of equation A2 with respect to r and substitution of the limits $p = p_3$ at $r = r_i$ and $p = p_4$ at $r = r_s$ then gives:

$$\dot{m}_C = \frac{\pi h_C^3 \left(p_3^2 - p_4^2 \right)}{12\mu R\theta . \ln\left(r_s / r_i \right)} \qquad (A3)$$

We shall assume that region D can be approximated by a rectangular duct of width $2\pi r_s$. With the substitution of the relevant parameters, equation A1 becomes:

$$\dot{m}_D = - \frac{\pi r_s h_D^3}{12\mu R\theta} \frac{dp^2}{dx} \qquad (A4)$$

If we now integrate equation A4 with respect to x and substitute the limits $p = p_4$ at $x = 0$ and $p = p_2$ at $x = l_D$ we obtain:

$$\dot{m}_D = \frac{\pi r_s h_D^3 \left(p_4^2 - p_2^2 \right)}{12\mu R\theta l_D} \qquad (A5)$$

Since $\dot{m}_C = \dot{m}_D$, then equations A3 and A5 can be solved simultaneously for p_4 and the leakage, $\dot{m}_C$.

APPENDIX B

ESTIMATION OF MEMBRANE BENDING FORCE MAGNITUDE

In the analysis of the foil bearing Wildmann (1965) employs the steady state form of equation 5.4 with an additional term for bending stiffness which is derived in most texts on shells and plates such as Flügge (1962). The addition of the bending term in equation 5.4 gives us:

$$\rho\frac{\partial^2 h}{\partial t^2} = T\frac{\partial^2 h}{\partial x^2} - \frac{Es^3}{12\left(1 - \nu^2\right)}\frac{\partial h^4}{\partial x^4} + \left(p_a - p_b\right) \qquad \text{(B1)}$$

where E is the modulus of elasticity and ν is Poisson's ratio. Following the same procedure as Wildmann, the ratio between the first two terms on the right hand side of equation B1 can be calculated if it is assumed that h is of the form $A\sin(\pi x/L)$ (where L is a half wavelength of the membrane). This ratio is then equal to $Es^3\pi^2/12L^2(1-\nu^2)T$ and is equal to unity when:

$$L = \left(\frac{Es^3\pi^2}{12\left(1-\nu^2\right)T}\right)^{1/2} \qquad \text{(B2)}$$

We can now use the length defined in equation B2 as an indicator of the magnitude of the bending term. If a half wave in the membrane is much greater than L, then the bending force can be assumed to be negligible compared to the tension force.

REFERENCES

ADAMS, R.G. and RICE, W. (1970). "Expermental investigation of the flow between co-rotating disks", *Trans. ASME: J. Appl. Mech.*, **92**, 844-849.

AMES, W.F. (1977). *Numerical Methods for Partial Differential Equations*, Academic Press, New York.

BALJE, O.E. (1956). "Accessory drive turbines for aircraft and missiles", *Aeronautical Eng. Rev.*, **15**, 60-67.

BALJE, O.E. (1957). "Drag turbine performance", *Trans ASME*, **79**, 1291-1304.

BALJE, O.E. (1965). "A study on the performance potential of conventional and shear force pumps", ARL Rep. No. 65-118.

BARWELL, (1979). *Bearing Systems - Principles and Practice*, Oxford University Press, Oxford.

BASSET, C.E.Jr. (1975). "An integral solution for compressible flow through disc turbines", *Intersoc. Energy Convers. Eng. Conf.*, Univ. of Del., Newark, 1098-1106.

BEANS, W.E. (1966). "Investigation into the performance characteristics of a friction turbine", *J. Spacecraft and Rockets*, **3**, 131-134.

BEAVERS, G.S, SPARROW, E.M. and LLOYD, J.R. (1971). "Low Reynolds number turbulent flow in large aspect ratio rectangular ducts", *Jnl. Basic Eng.*, **93**, 296-299.

BLAND, S.R., RHYNE, R.H. and PIERCE, H.B. (1967). "Study of flow-induced vibrations of a plate in narrow channels", *Trans. ASME: J. Eng. Ind.*, **89**, 824-830.

BLEVINS, R.D. (1977). *Flow-Induced Vibration*, Van Nostrand Reinhold Company, New York.

BLOK, H. and VAN ROSSUM, J.J. (1953). "The foil bearing - a new departure in hydrodynamic lubrication", *Lubrication Eng.*, **9**, 316-320.

BOYACK, B.E. and RICE, W. (1971). "Integral method for flow between co-rotating disks", *Trans. ASME: J. Basic Eng.*, **93**, 350-354.

BOYD, K.E. and RICE, W. (1968). "Laminar inward flow of an incompressible fluid between rotating discs with full peripheral admission", *Trans. ASME: J. Appl. Mech.*, **35**, 229-237.

BRIETER, M.C. and POLHAUSEN, K. (1962). "Laminar flow between two parallel rotating discs", ARL Rep. No. 62-318.

CHARTERS, W.W.S., LIM, T.M. and DUNKLE, R.V. (1973) "Heat and momentum transfers: multiple-disc rotor units", *Trans. ASME: J. Heat Transfer*, **95**, 390.

CHU, C.K. and SERENY, A. (1974). "Boundary conditions in finite difference fluid dynamic codes", *J. Comp. Phys.*, **15**, 476-491.

CRONJE, J.S., BISHNOI, P.R. and SVRCEK, W.Y. (1980). "The application of the characteristic method to shock-tube data that simulate a gas pipeline rupture", *Can. J. Chem. Eng.*, **58**, 289-294.

DEN HARTOG, J.P. (1956). *Mechanical Vibrations*, McGraw-Hill Book Co., Inc., New York.

DESAI, S.M. (1974). "On fluffing of cards", *Trans. ASME: J. Fluids Eng.*, **96**, 227.

DODGE, F.T. and MULLER, A.F. (1969). "Viscous flow-induced vibrations of a flat plate suspended in a narrow channel", *AIAA/ASME 10th Structures, Structural Dynamics & Matls. Conf.*, New Orleans, LA, Apr 14-16, 205-209.

DOWELL, E.E. (1967). "Nonlinear oscillations of a fluttering plate II", *AIAA J.*, **5**, 1856-1862.

DUNLOP, R.W. (1988). "Development of pneumatic devices to provide integrated control using oil-free air", *8th Int. Symp. on Fluid Power*, Birmingham, England, 19-21 April, 1988, 87-106.

EGLI, A. (1937). "The leakage of gases through narrow channels", *Trans. ASME: J. Appl. Mech.*, A-63.

ESHEL, A. and ELROD, H.G.Jr. (1965). "The theory of the infinitely wide, perfectly flexible, self-acting foil bearing.", *Trans. ASME: J. Basic Eng.*, 831-836.

FLÜGGE, W. (1962). *Handbook of Engineering Mechanics*, McGraw-Hill Book Company, New York.

GARRISON, P.W., HARVEY, D.W. and CATTON, I. (1976). "Laminar compressible flow between rotating disks", *Trans. ASME: J. Fluids Eng.*, **98**, 382-389.

GOLDBERG, D.E and WYLIE, E.B. (1983). "Characteristics method using time-line interpolations", *Trans. ASCE: J. Hydr. Eng*, **109**, 670-683.

GROSS, W.A. (1962). *Gas Film Lubrication*, John Wiley and Sons, Inc, New York.

GROTBERG, J.B. and DAVIS, S.H. (1980). "Fluid-dynamic flapping of a collapsible channel: Sound generation and flow limitation", *J. Biomech.*, **13**, 219-230.

GROTBERG, J.B. and REISS, E.L. (1984). "Subsonic flapping flutter", *J. Sound Vib.*, **92**, 349-361.

GROTBERG, J.B. and SHEE, T.R. (1985). "Compressible-flow channel flutter", *J. Fluid Mech.*, **159**, 175-193.

HARTREE, D.R. (1953). "Some practical methods of using characteristics in the calculation of non-steady compressible flow", Report No AECU-2713, US Atomic Energy Commision.

HASINGER, S.H. and KHERT, L.G. (1963). "Investigation of a shear force pump", *Trans. ASME: J. Eng. for Power*, **85**, 201.

HENSON, D.A. and FOX, J.A. (1974). "Transient flows in tunnel complexes of the type proposed for the Channel Tunnel", *Proc. I. Mech. E.*, **188**, 153-167.

HWANG, J.Y. and THORPE, J.F. (1973). "Further investigation of stability of a rectangular flow channel", *ASME Pap.* 73-DET-66 *for Meet. Sept.* 9-12.

IVERSEN, H.W. (1955). "Performance of the periphery pump", *Trans. ASME*, **77**, 19-28.

KREYSZIG, E. (1979). *Advanced Engineering Mathematics*, John Wiley and Sons, Inc., New York.

LAWN, M.J.Jr. and RICE, W. (1974). "Calculated design data for the multiple-disk turbine using incompressible fluid", *Trans. ASME: J. Fluid Eng.*, **96**, 252-258.

LICHT, L., FULLER, D.D. and STERNLICHT, B. (1958). "Self-excited vibrations of an air-lubricated thrust bearing", *Trans. ASME*, 411-414.

MARTIN, C.S., PADMANABHAN, M. and WIGGERT, D.C. (1977). "Pressure wave propagation in two-phase bubbly air-water mixtures", *Proc. of the 2nd Int. Conf. on Pressure Surges*, BHRA, Cranfield, England.

MATSCH, L. and RICE, W. (1967). "Potential flow between two parallel circular discs with partial admission", *Trans. ASME: J. Appl. Mech.*, **89**, 239-240.

MATSCH, L. and RICE, W. (1967) "Flow at low reynolds number with partial admission between rotating disks", *Trans. ASME: J. Appl. Mech*, **89**, 768-770.

MATSCH, L. and RICE, W. (1968). "An asymptotic solution for laminar flow of an incompressible fluid between rotating disks", *Trans. ASME: J. Appl. Mech*, **35**, 155-159.

MATSUZAKI, Y. and FUNG, Y.C. (1977). "Stability analysis of straight and buckled two-dimensional channels conveying an incompressible flow", *Trans. ASME: J. Appl. Mech.*, **44**, 548-552.

MATSUZAKI, Y. and FUNG, Y.C. (1979). "Nonlinear stability analysis of a two-dimensional model of an elastic tube conveying a compressible flow", *Trans. ASME: J. Appl. Mech.*, **46**, 31-36.

MEIROVITCH, L. (1975). *Elements of Vibration Analysis*, McGraw-Hill Book Company, New York.

MORSE, P.M. (1948). *Vibration and Sound*, McGraw-Hill Book Company, New York.

PARODI, R. (1981). "The shear torque turbine", *Turbomachinery Int.*, **22**, 30-32.

PATEL, B.J. and CAMERON, A. (1957). "The foil bearing", *Proc. I. Mech. E., London Conf. on Lub. and Wear*, 219-223.

PATER, L.L., CROWTHER, E. and RICE, W. (1974). "Flow regime definition for flow between corotating disks", *Trans. ASME: J Fluids Eng.*, **96**, 29-34.

RICE, W. (1963). "Analytical and experimental investigation of multiple disk pumps and compressors", *Trans. ASME: J. Eng. for Power*, **85**, 191.

RICE, W. (1965). "An analytical and experimental investigation of multiple-disk turbines", *Trans. ASME: J. Eng. for Power*, **87**, 29-36.

ROACHE, P.J. (1972). *Computational Fluid Dynamics*, Hermosa Publishers, Albuquerque, N.M.

RODDY, P.J., DARBY, R., MORRISON, G.L. and JENKINS, P.E. (1987). "Performance characteristics of a multiple-disk centrifugal pump", *Trans. ASME: J. Fluids Eng.*, **109**, 51-57.

RUBIN, E.L. and BURSTEIN, S.Z. (1967). "Difference methods for the inviscid and viscous equations of a compressible gas", *J. Comp. Phys.*, **2**, 178-196.

SCHLICHTING, H. (1968). *Boundary-Layer Theory*, McGraw-Hill Book Company, New York.

SCIENTIFIC AMERICAN (1911). "The Tesla Turbine", September, 296-297.

SENOO, Y. (1948). "Theoretical research on friction pumps", *Reports of the Res. Inst. for Fluid Eng., Japan*, **1**.

SHAPIRO, A.H. (1953). *The Dynamics and Thermodynamics of Compressible Fluid Flow*, Vols. I & II, Ronald Press, New York.

SMITH, G.D. (1978). *Numerical Solution of Partial Differential Equations*, Clarendon Press, Oxford.

SMITH, M.C. (1987). "The positioning of a low friction pneumatic actuator using on-off control", PhD thesis, University of Edinburgh.

SPENCE, R.W. (1968). "The Rover nuclear rocket program", *Science*, **160**, 953-959.

TAYLOR, G. and SAFFMAN, P.G. (1957). "Effects of compressibility at low Reynolds number", *J. Aero. Sci.*, **24**, 553-562.

THORPE, J.F. (1963). "Hydraulic flow in coupled parallel channels of varying cross sectional area", *Trans. ASME: J. Basic Eng.*, 417-423.

THORPE, J.F. (1964). "Boundary conditions for parallel channel flow", *Nuclear Science and Engineering*, **18**, 329-334.

THORPE, J.F., HWANG, J.Y. and SMALL, N.C. (1971). "Hydro-rotational stability of a slender plate in a rectangular flow channel", *ASME Pap.* 71-Vibr-37 *for Meet. Sept.* 8-10.

VARDY, A.E. (1976). "On the use of the method of characteristics for the solution of unsteady flows in networks", *Proc. of the 2nd Int. Conf. on Pressure Surges,* BHRA, Cranfield, England, 15-30.

WEAVER, D.S. and PAIDOUSSIS, M.P. (1977). "On collapse and flutter phenomena in thin tubes conveying fluid", *J. Sound Vib.*, **50**, 117-132.

WILDMANN, M. (1965). "Foil bearings - their general behaviour", *I. Mech. E. Elastohydrodynamic Lubrication Symp.*, Sept. 1965.

WILDMANN, M. and WRIGHT, A. (1964). "The effect of external pressurization on self-acting foil bearings", *Trans. ASME Paper No.*, 64-Lub-20.

WILSON, W.A., SANTALO, M.A. and OELRICH, J.A. (1955). "A theory of the fluid-dynamic mechanism of regenerative pumps", *Trans. ASME*, **77**, 1303-1316.

WYLIE, E.B. (1980). "Inaccuracies in the characteristics method", *ASCE Proceedings, Computer and Physical Modeling*, Aug, 165-176.

WYLIE, E.B and STREETER, V.L. (1978). *Fluid Transients*, McGraw-Hill Book Company, New york.

ZUCROW, M.J. and HOFFMAN, J.D. (1976). *Gas Dynamics,* Vols. I & II, John Wiley & Sons, Inc, New York.

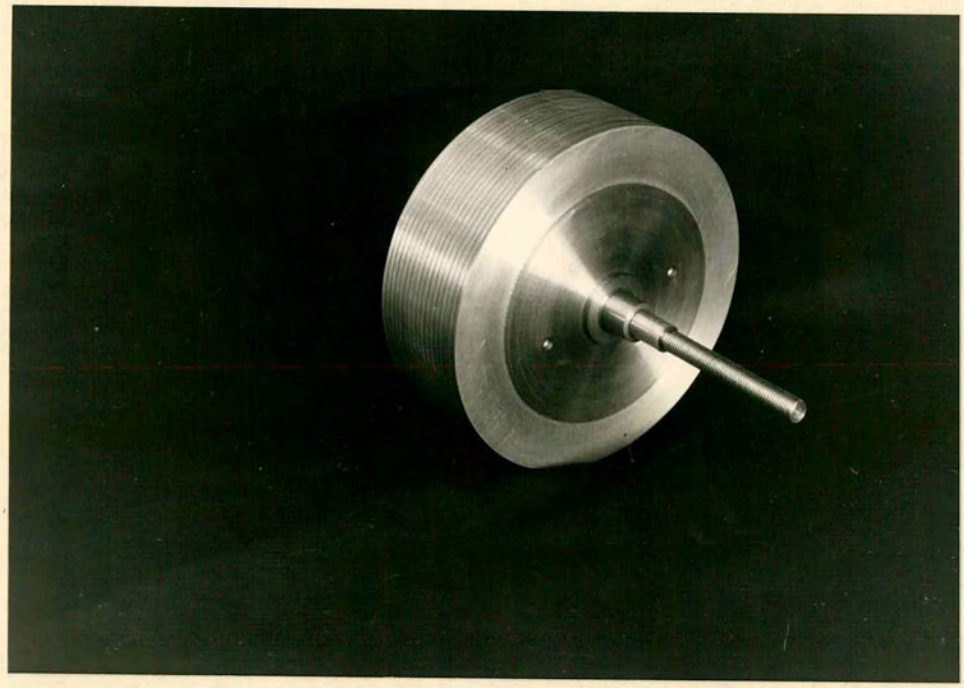

Plate 1

Plate 2

Multiple-disc
rotor assembly

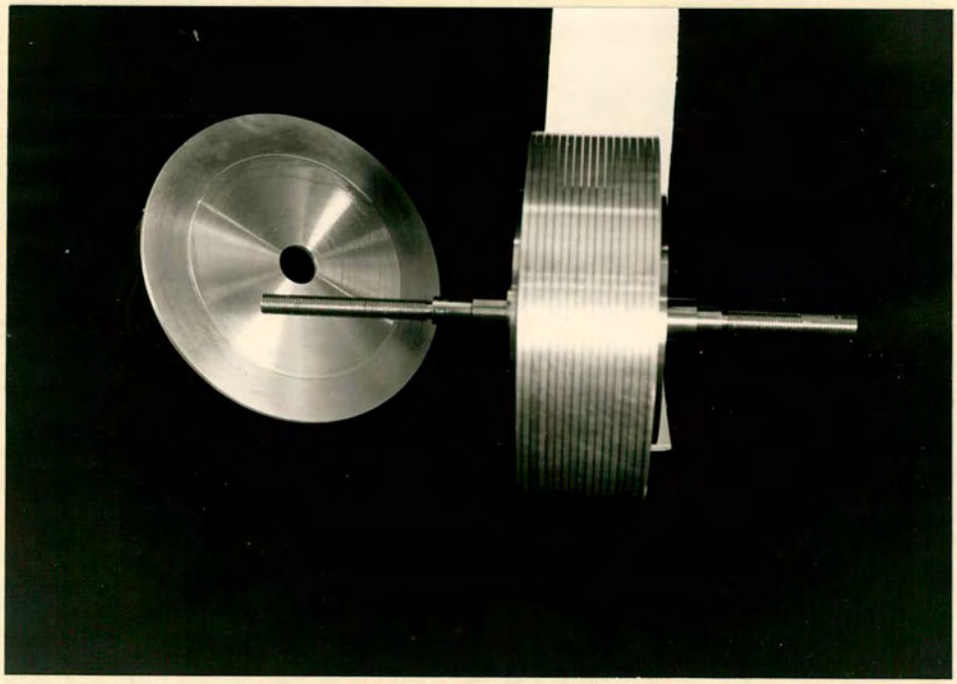

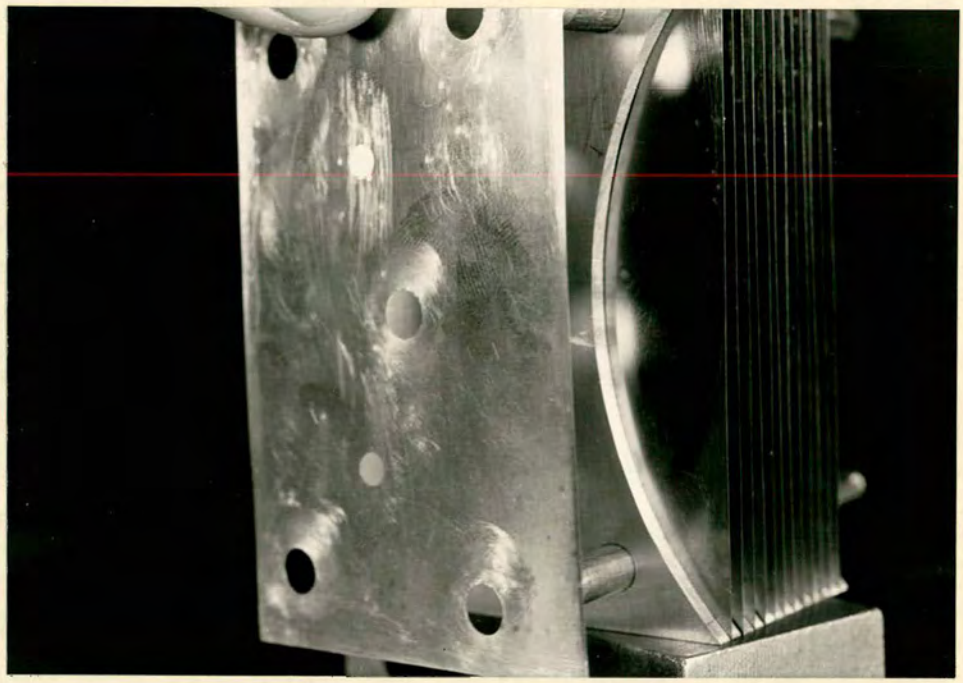

Plate 3

Plate 4

Preparation of restrictor plate assembly

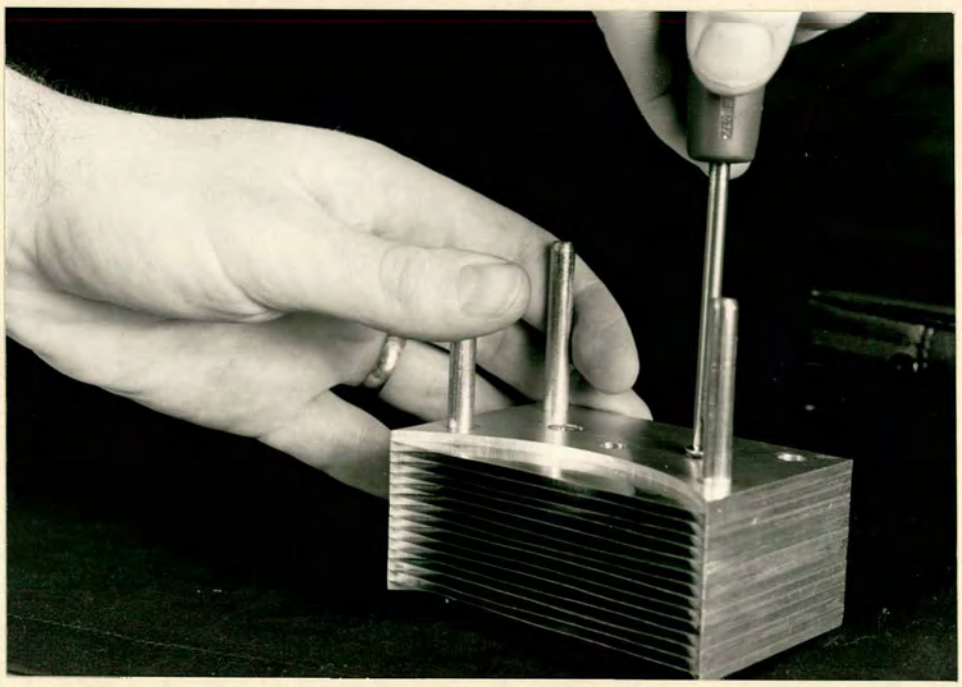

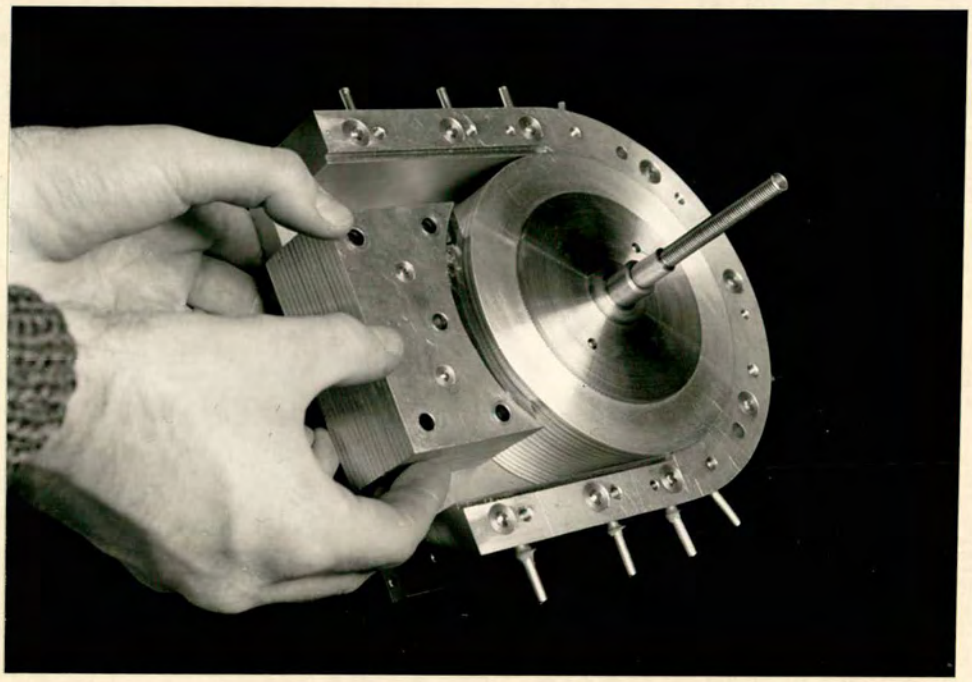

Plate 5 Plate assembly position in motor

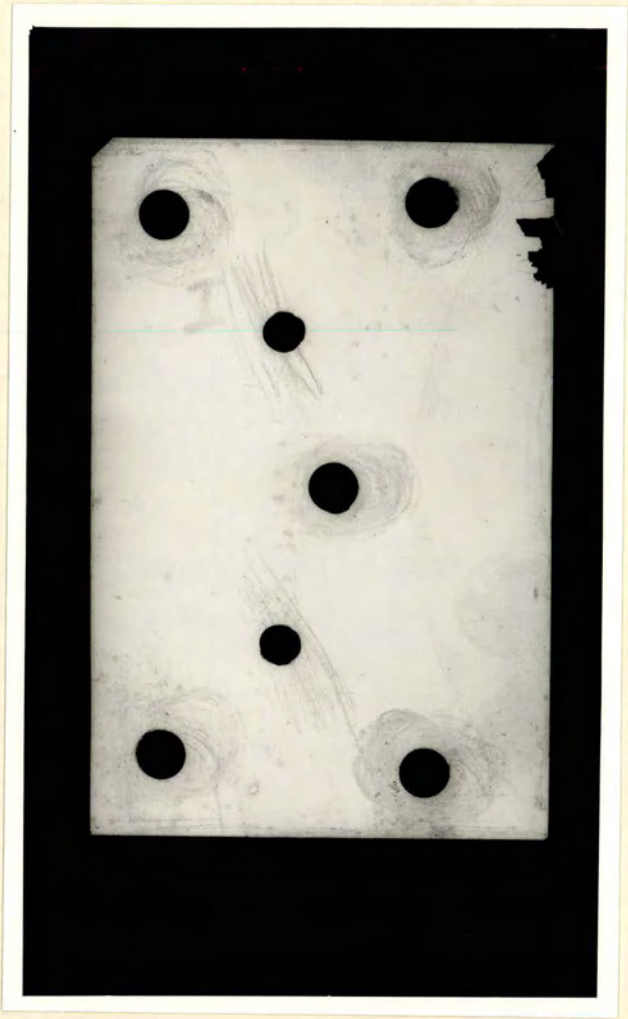

Plate 6 A damaged restrictor plate

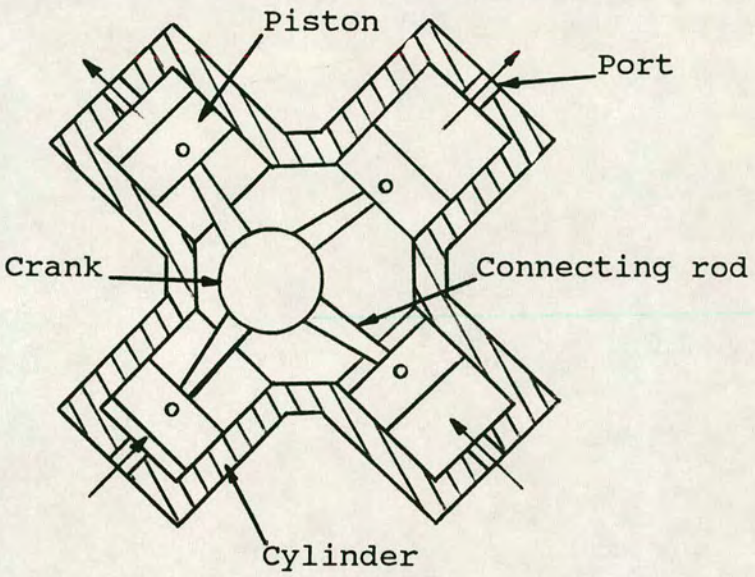

Fig.1.1 Radial piston motor

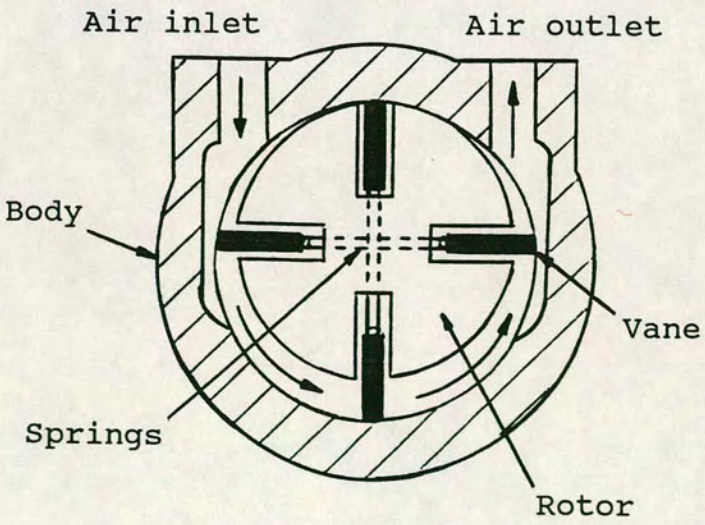

Fig.1.2 Vane motor

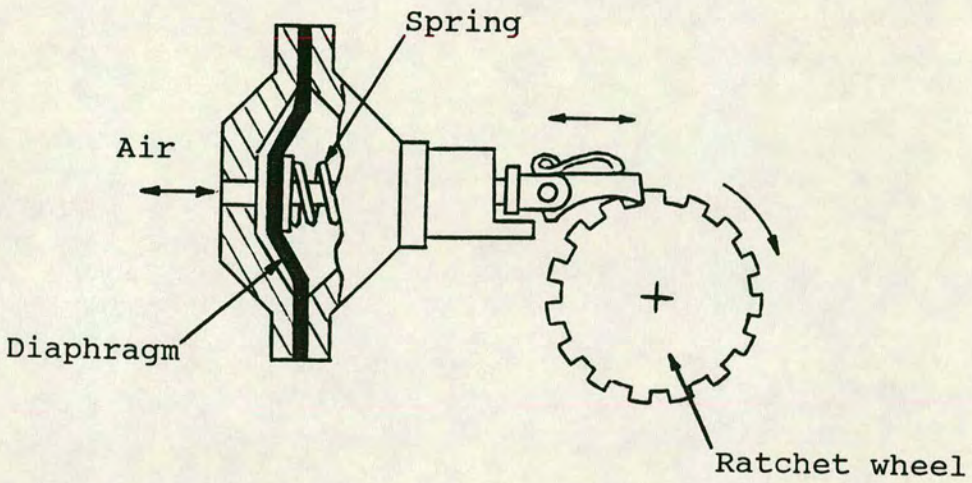

Fig.1.3 Diaphragm motor

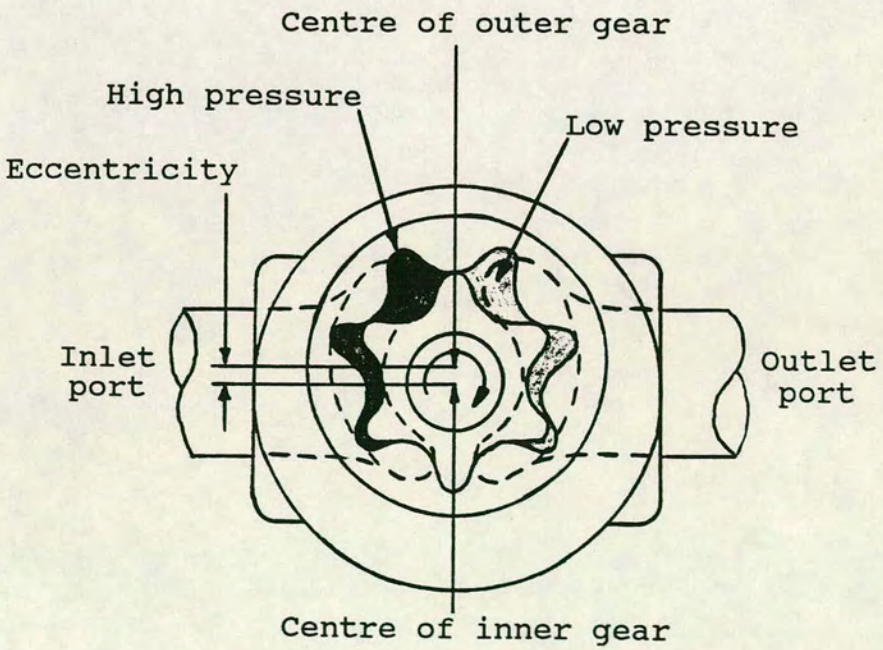

Fig.1.4 Gerotor motor

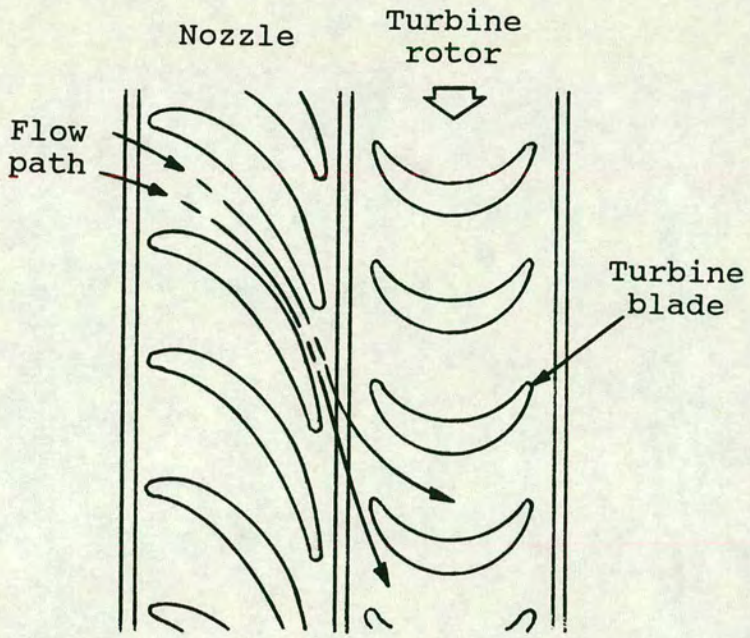

Fig.1.5 Impulse turbine concept

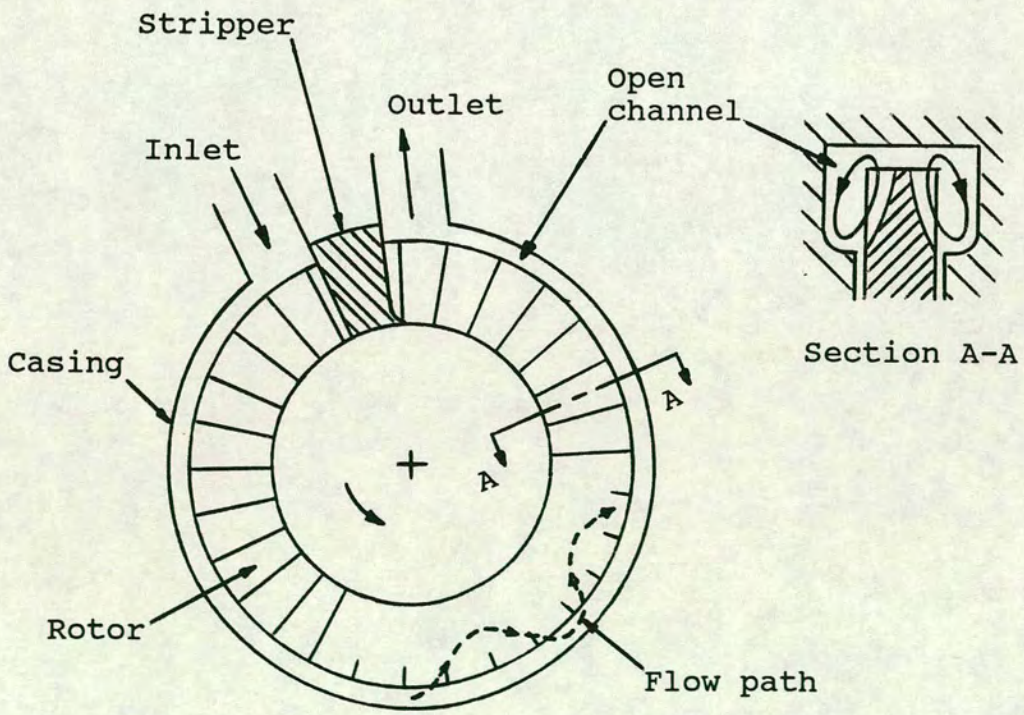

Fig.1.6 Drag turbine

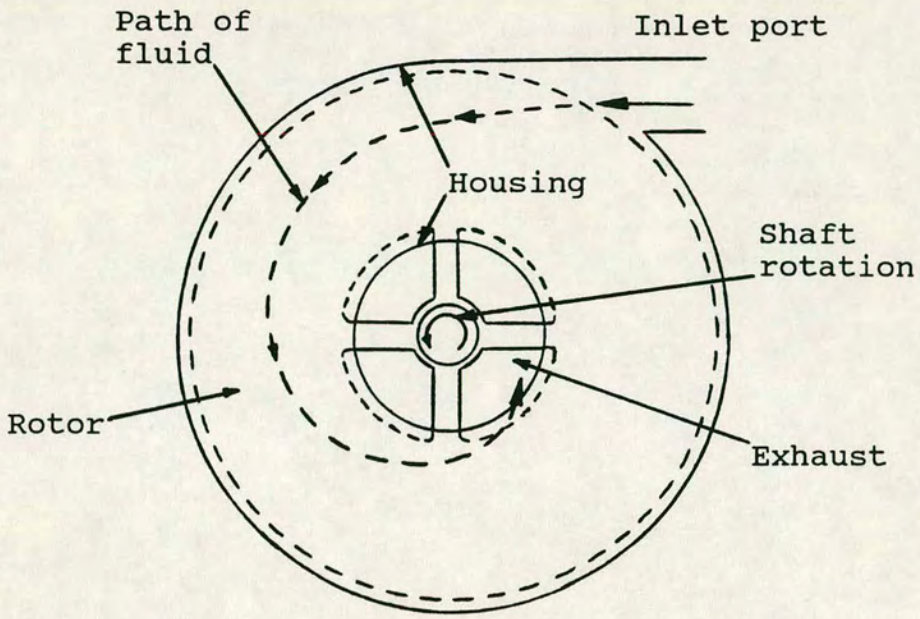

Fig.1.7 Tesla turbine

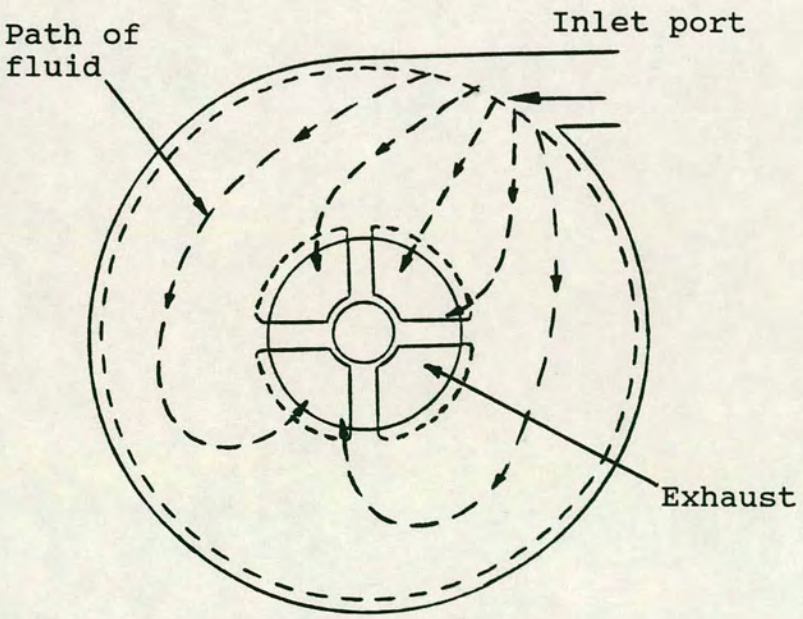

Fig.1.8 Flow through Tesla turbine
with negligible inertial force

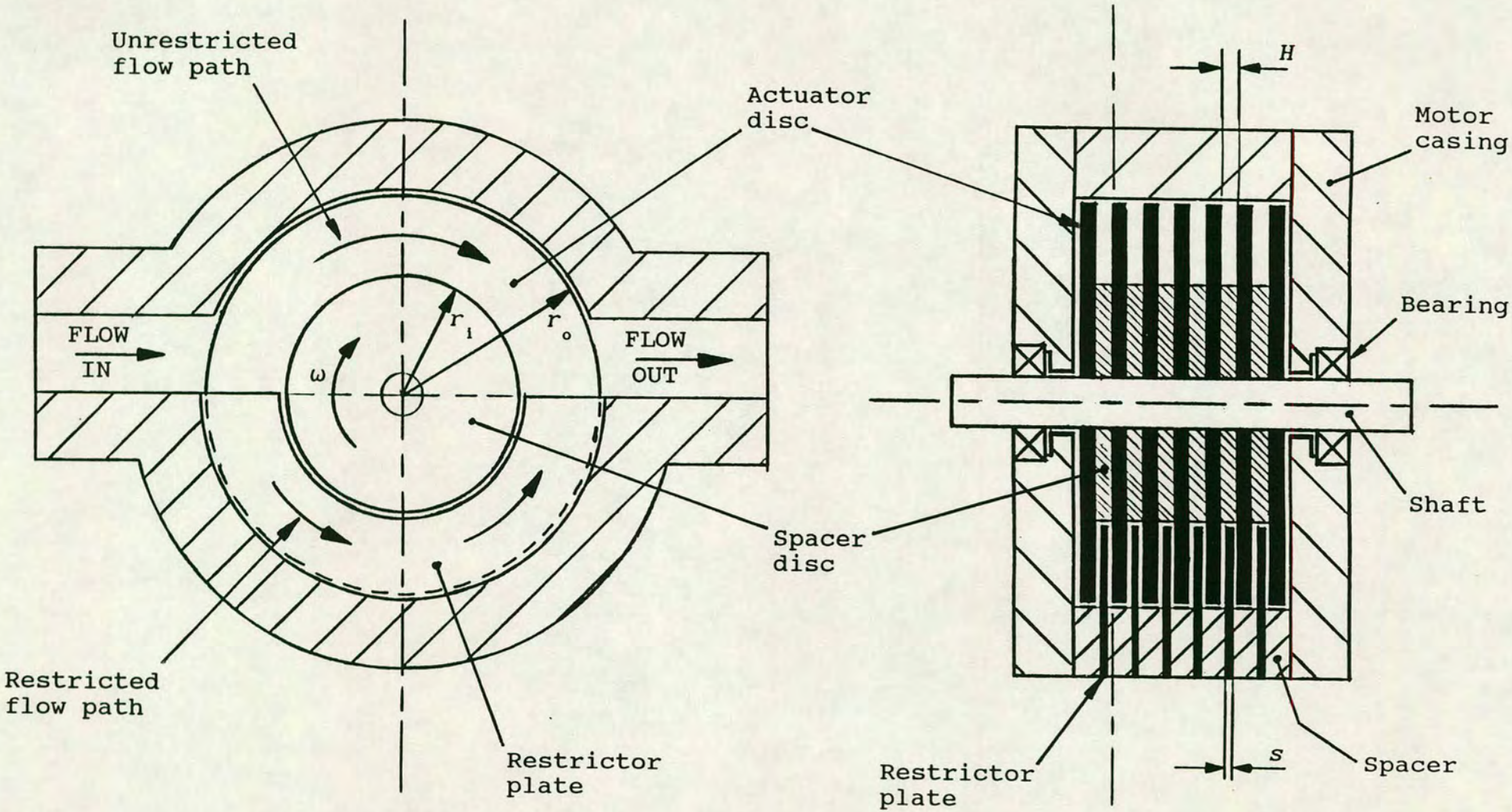

Fig.1.9 The viscous shear pneumatic torque motor

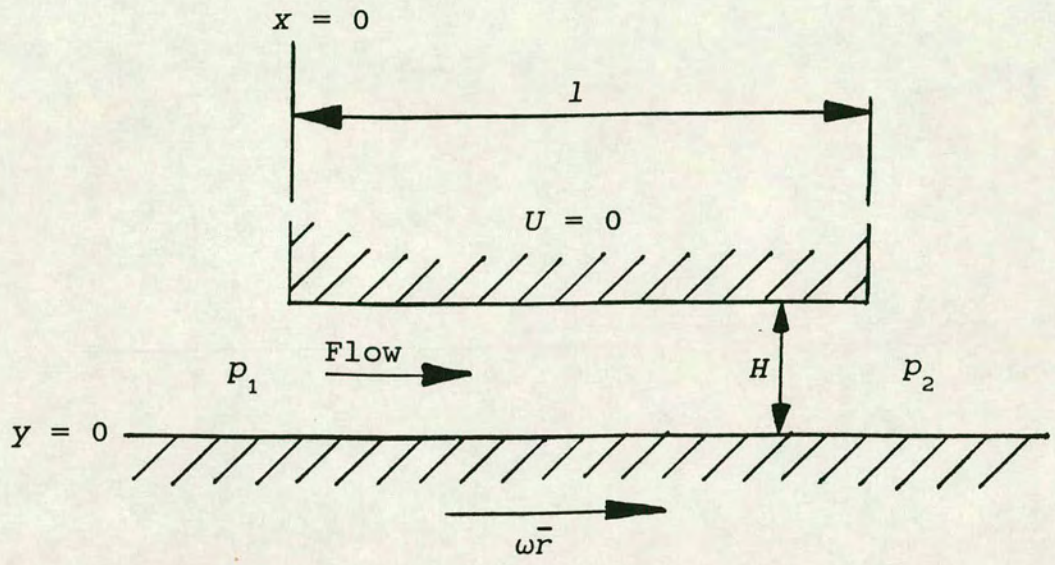

Fig.2.1 The straight duct configuration

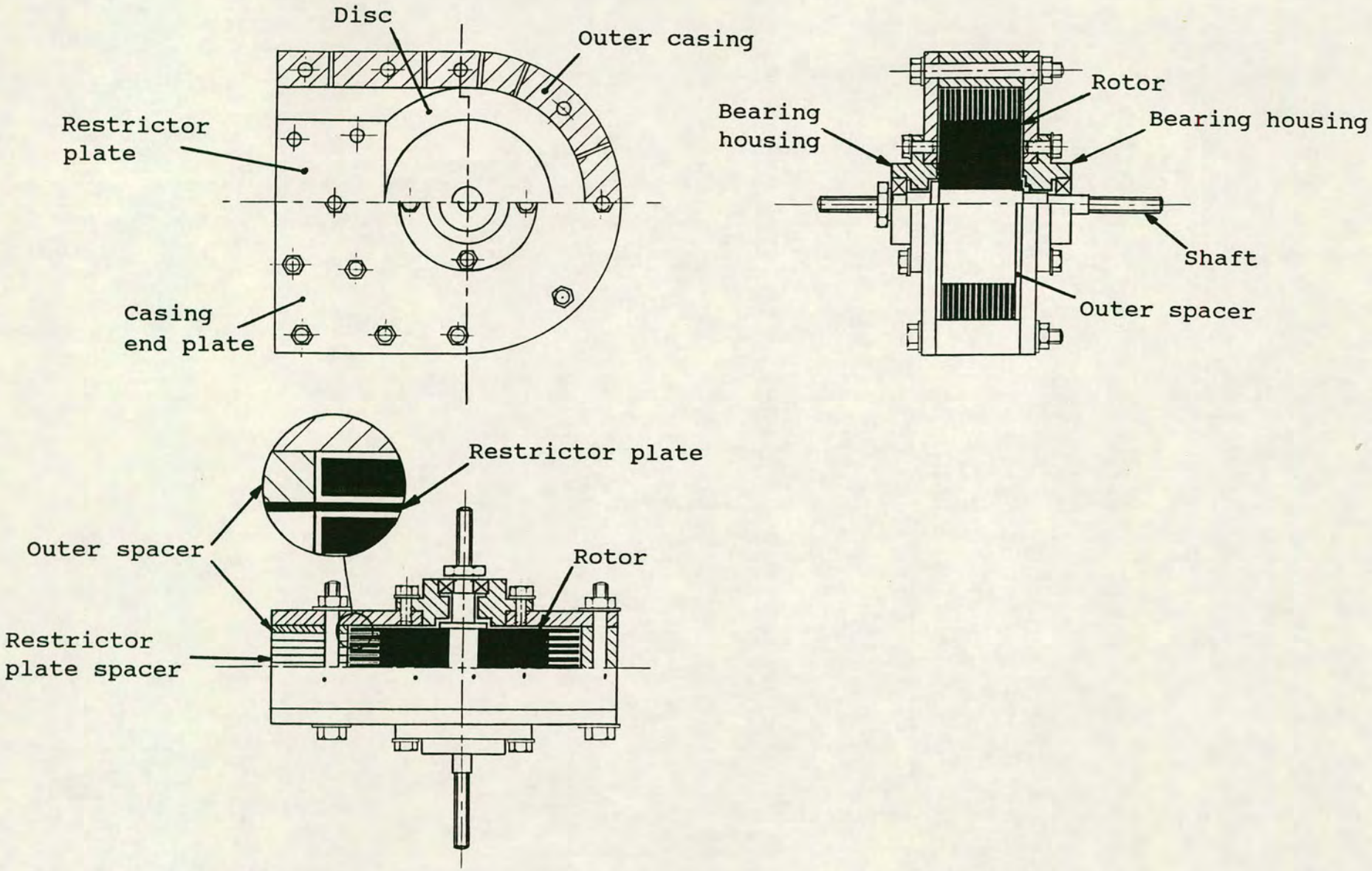

Fig.2.2 Assembly drawing of experimental motor

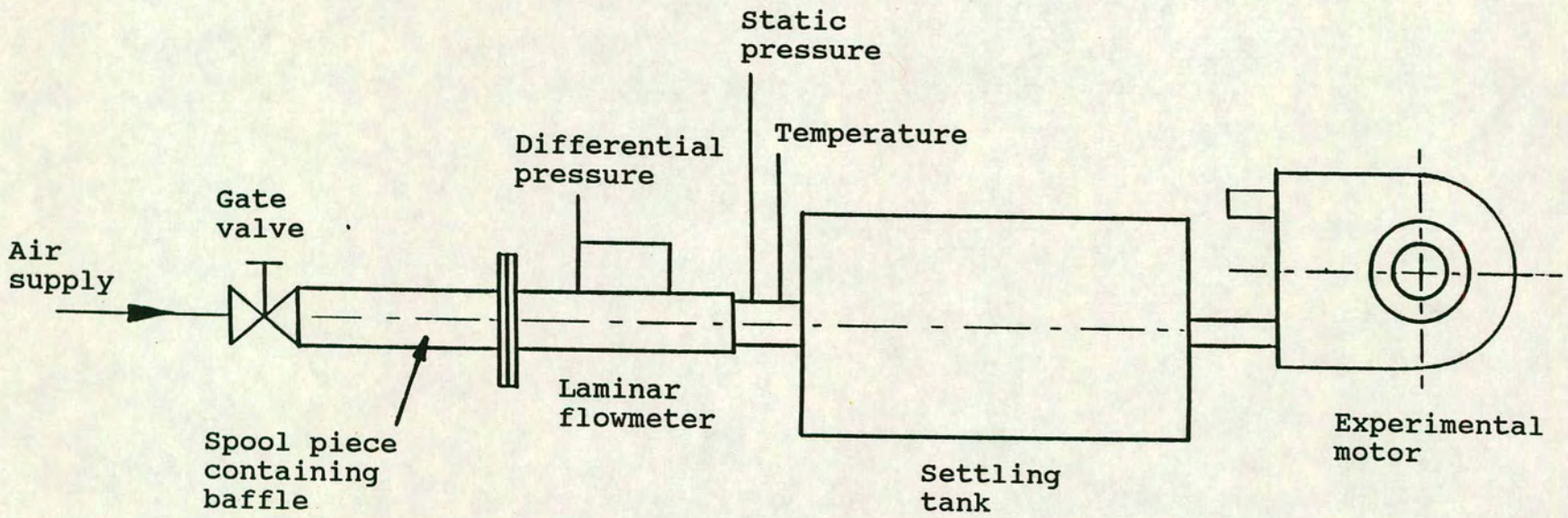

Fig.2.3 Diagram of experimental rig

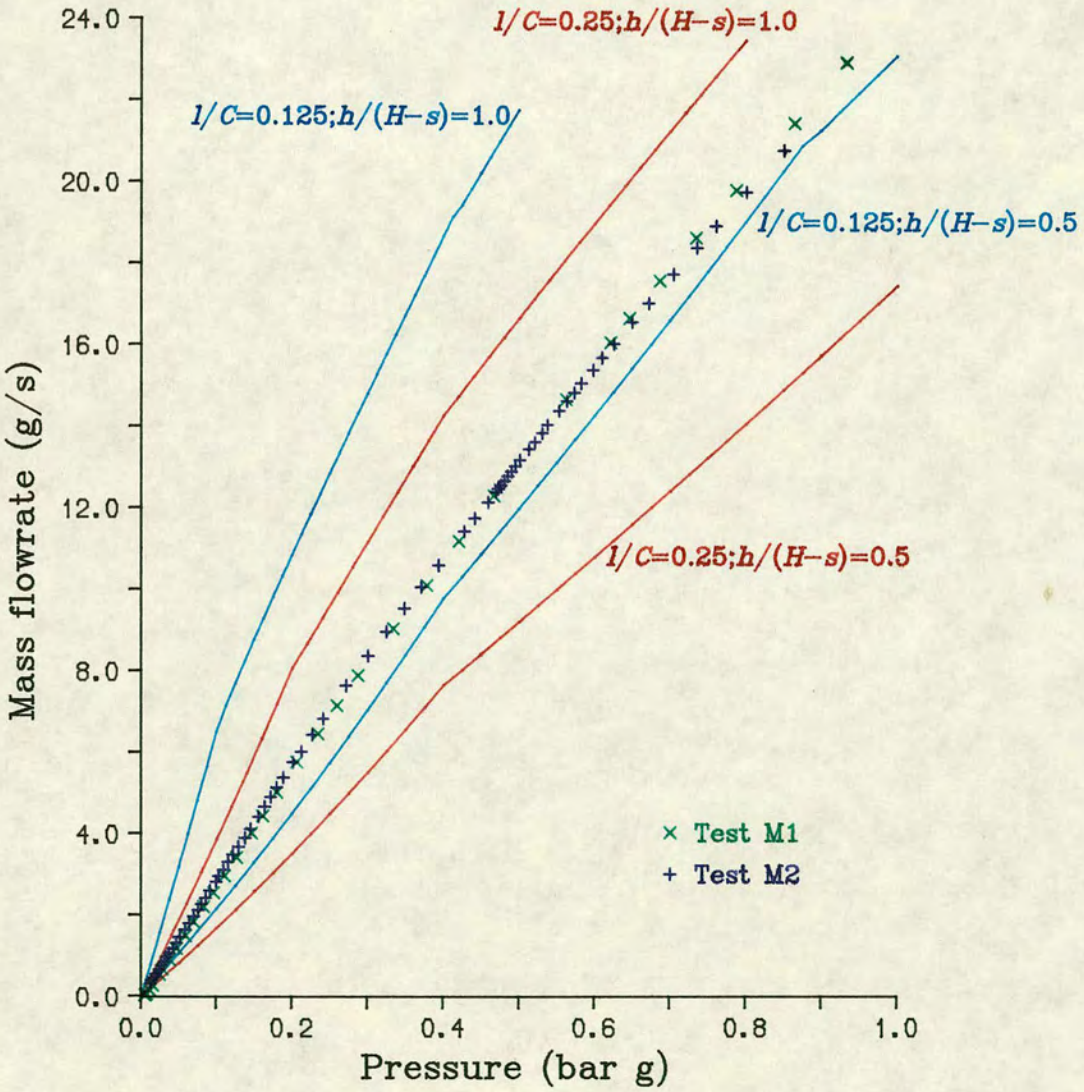

Fig.2.4 Tests M1 and M2
Compared with Theory

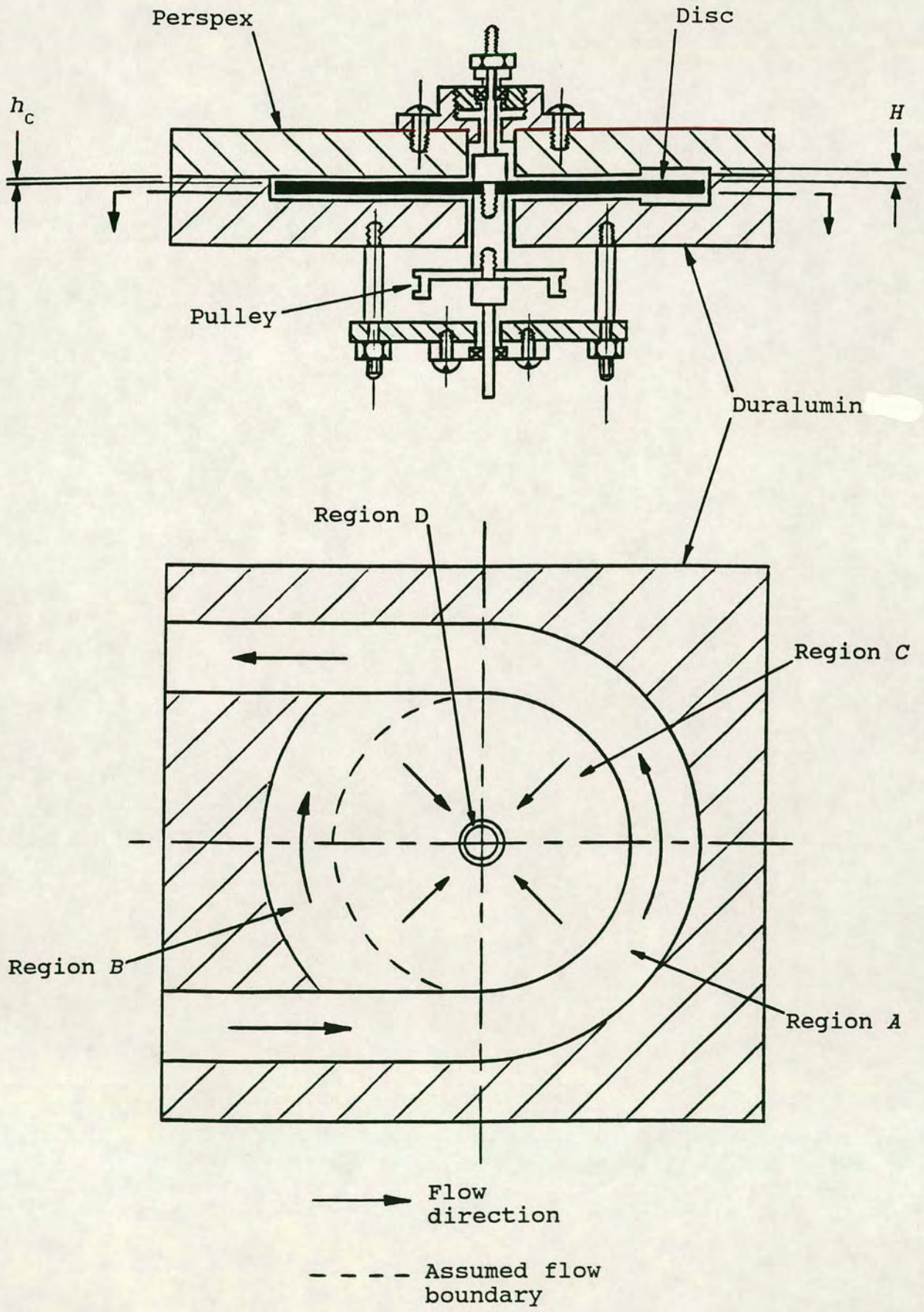

Fig.2.5 Diagram of the single disc motor

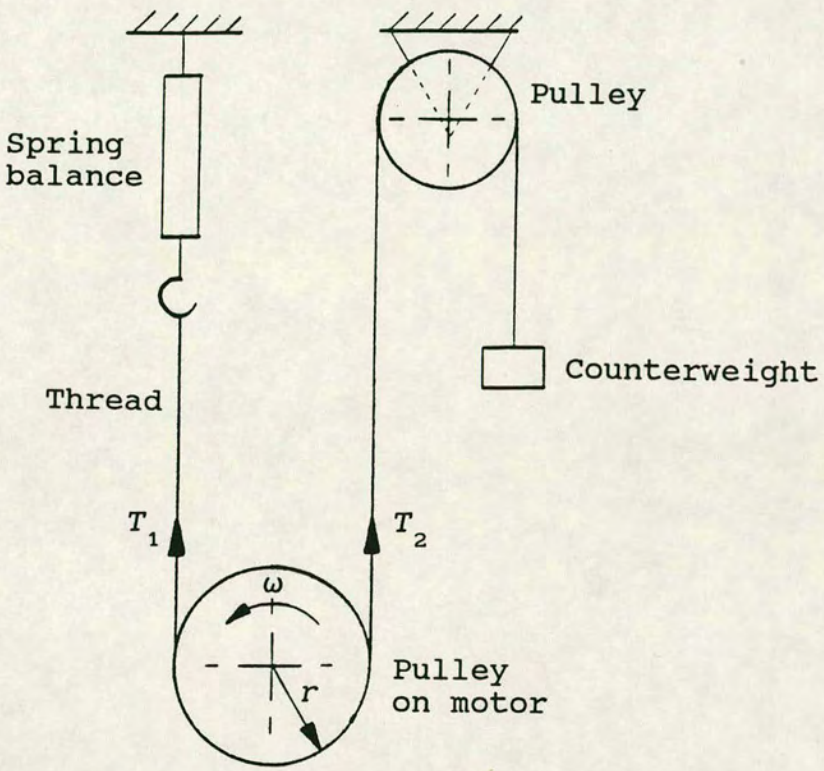

Fig.2.6 Apparatus for
torque measurement

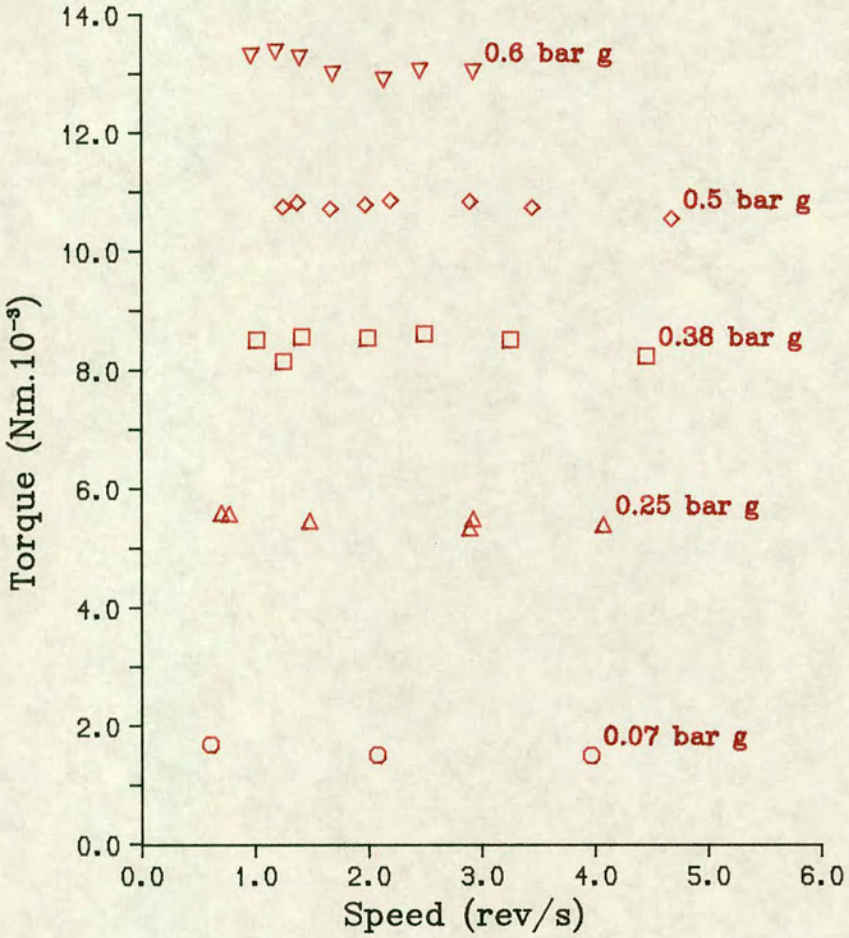

(a) Torque against speed

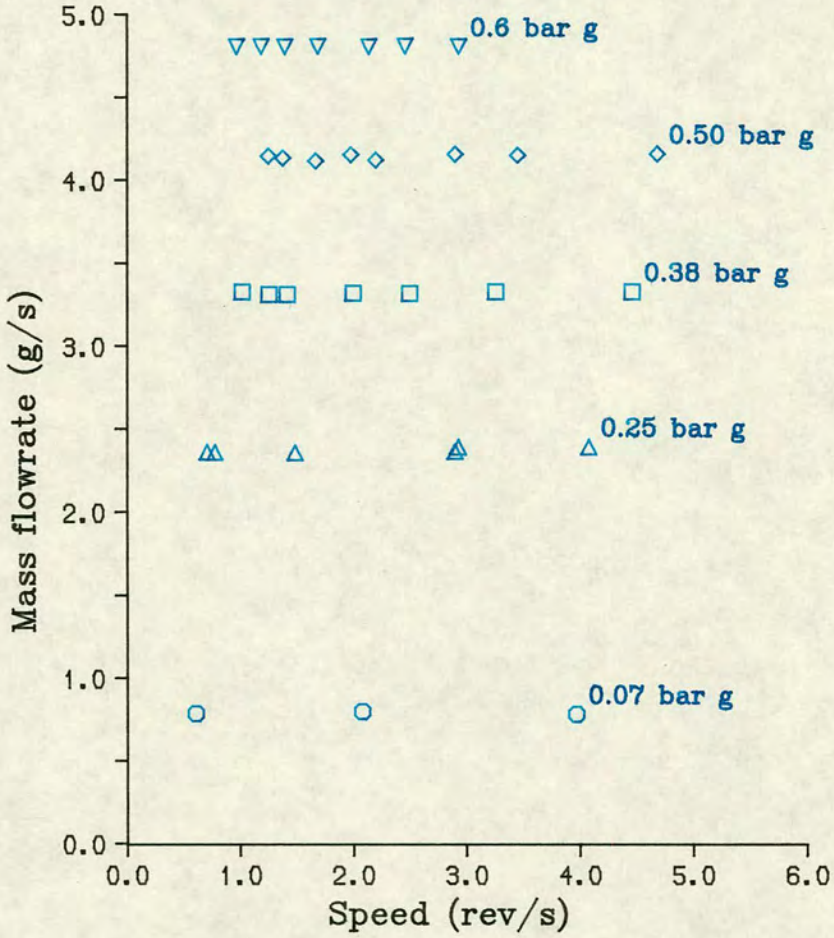

(b) Flowrate against speed

Fig.2.7 Single Disc Motor : Test S1 (H=360μm ; h_c=150μm)

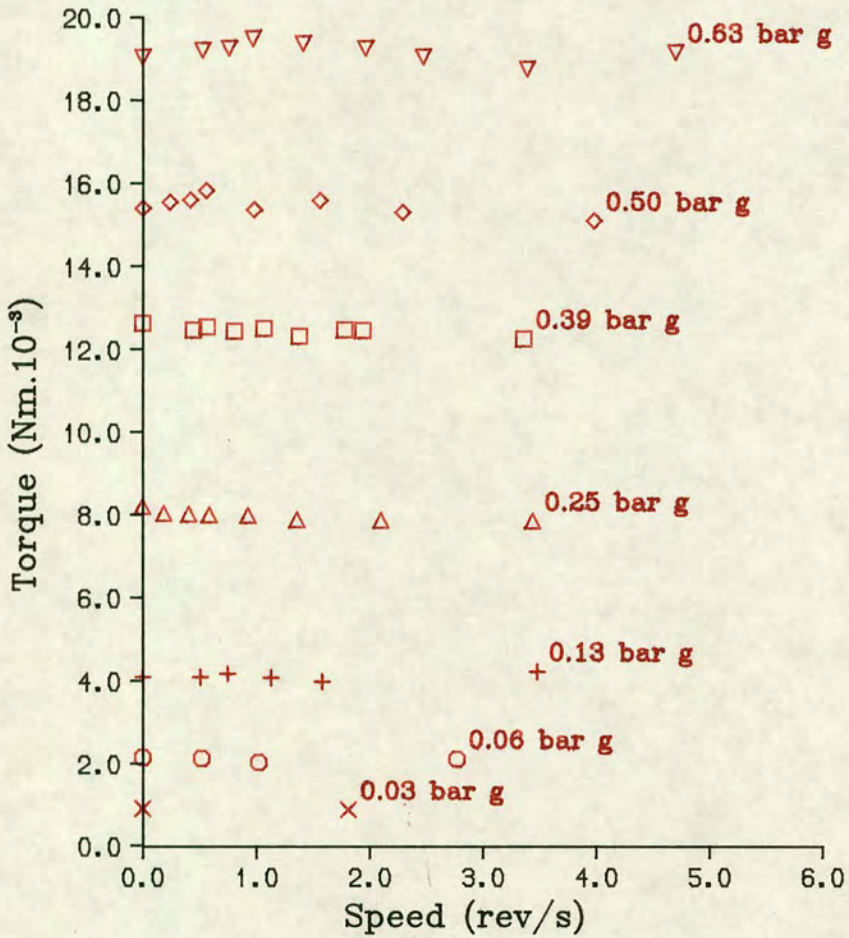

(a) Torque against speed

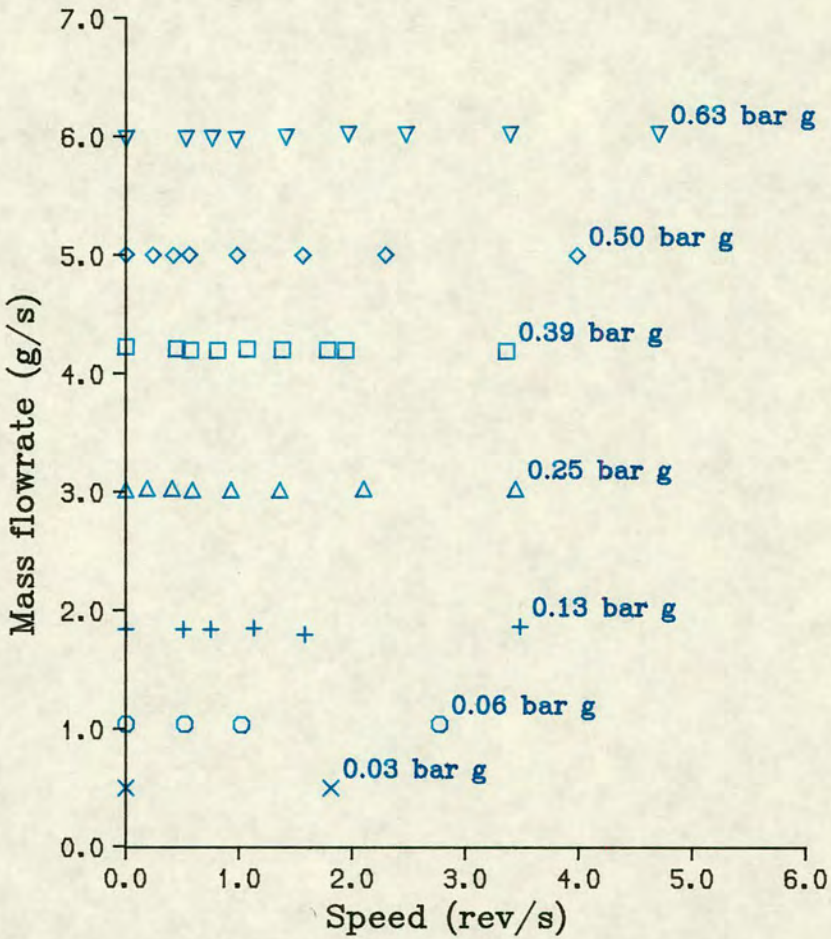

(b) Flowrate against speed

Fig.2.8 Single Disc Motor : Test S2 (H=440μm ; h_c=150μm)

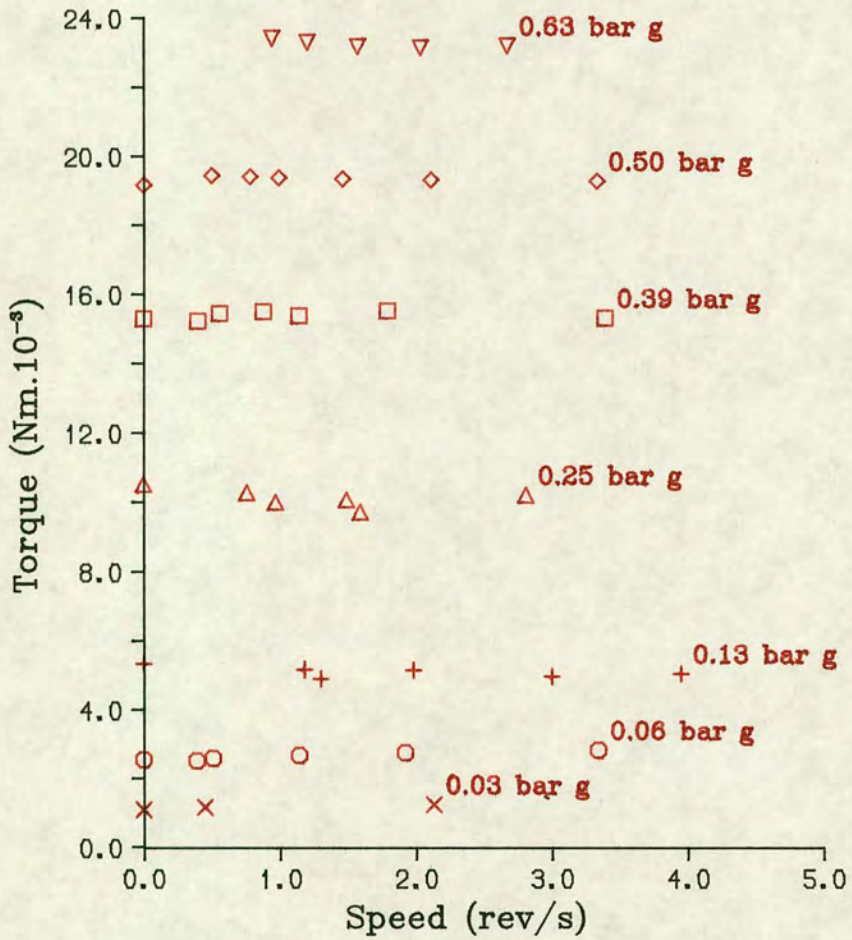

(a) Torque against speed

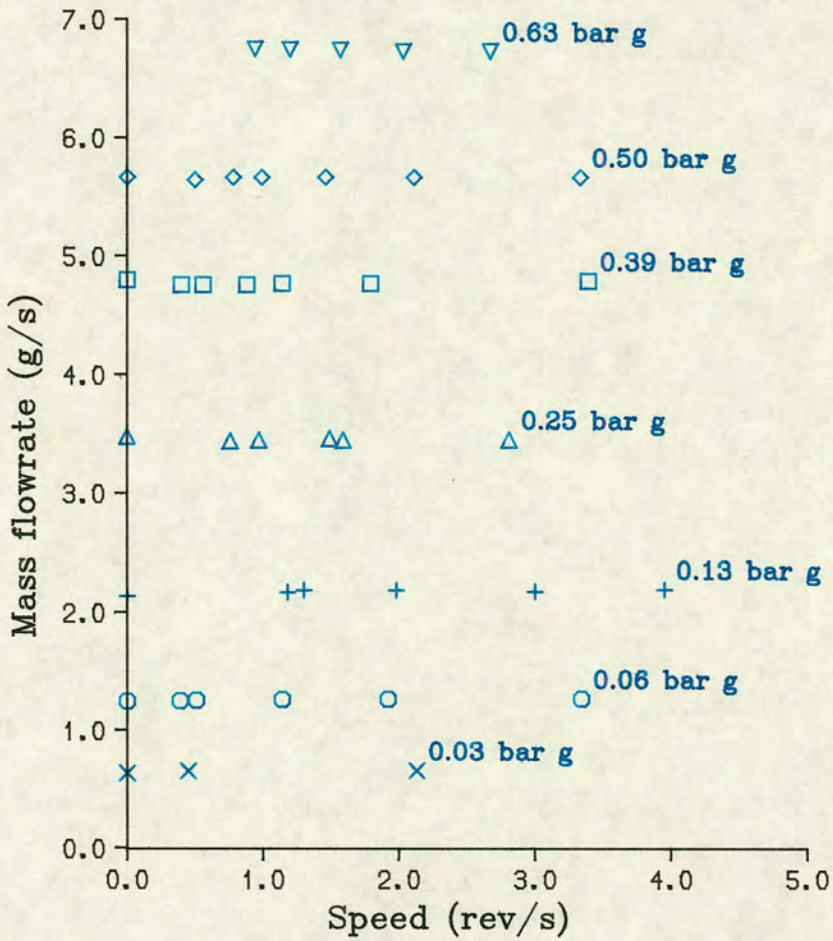

(b) Flowrate against speed

Fig.2.9 Single Disc Motor : Test S3 (H=550μm ; h_c=150μm)

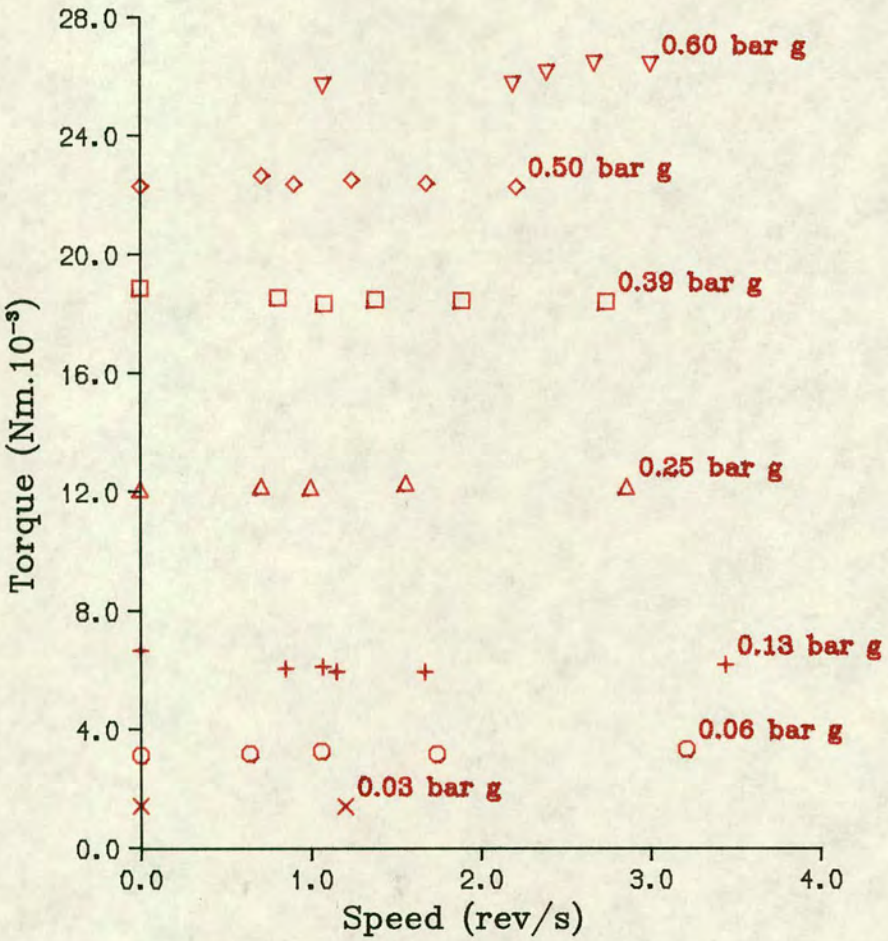

(a) Torque against speed

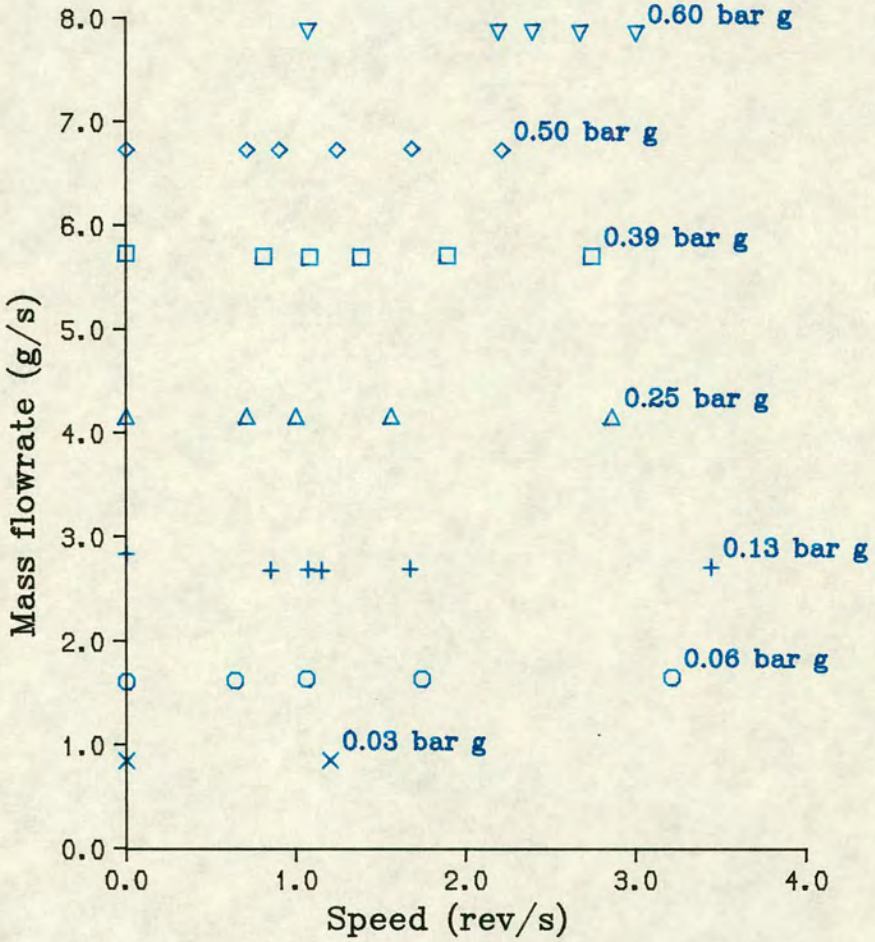

(b) Flowrate against speed

Fig.2.10 Single Disc Motor : Test S4 (H=670μm ; h_c=150μm)

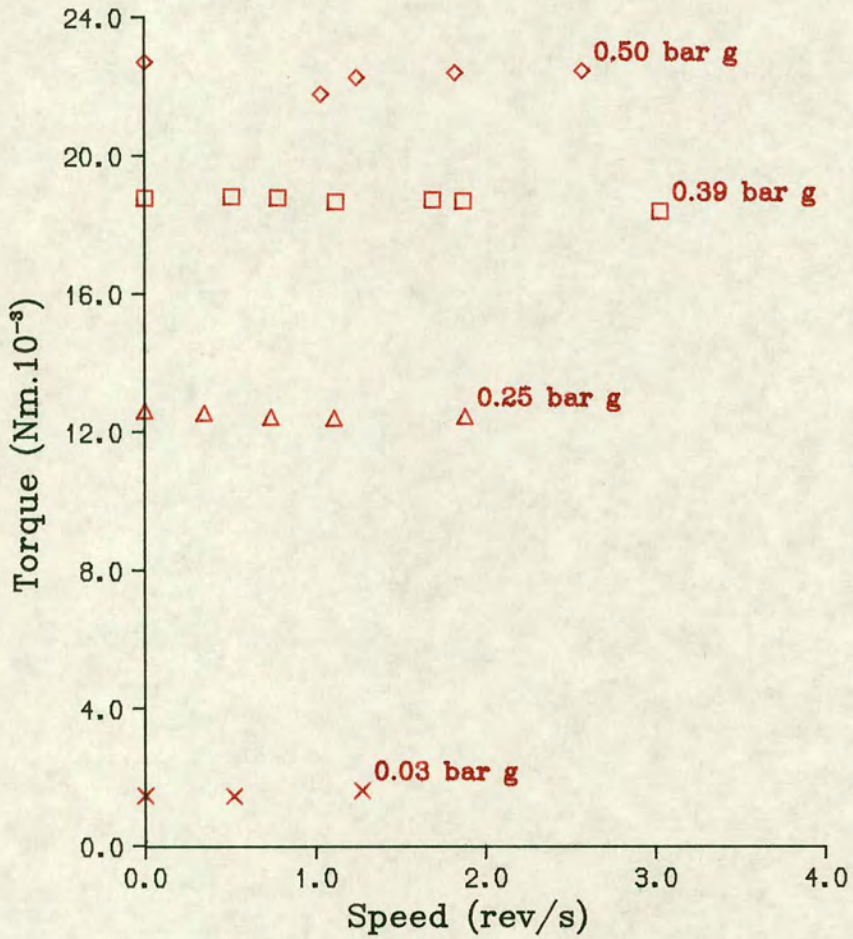

(a) Torque against speed

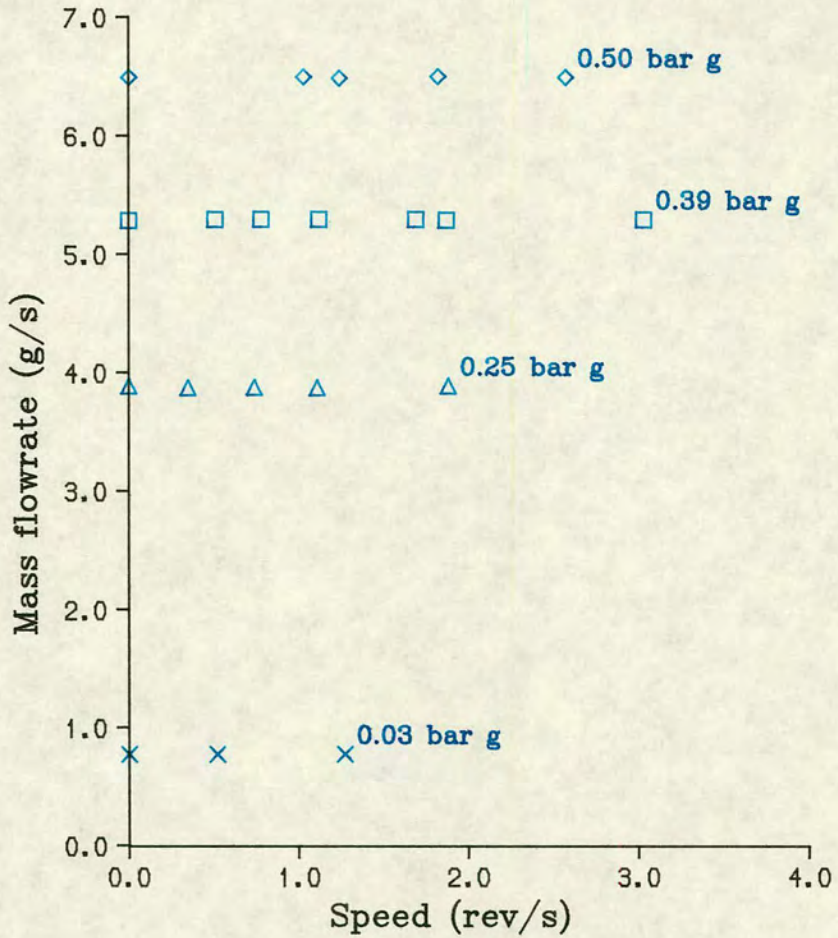

(b) Flowrate against speed

Fig.2.11 Single Disc Motor : Test S5 (H=645μm ; h_c=125μm)

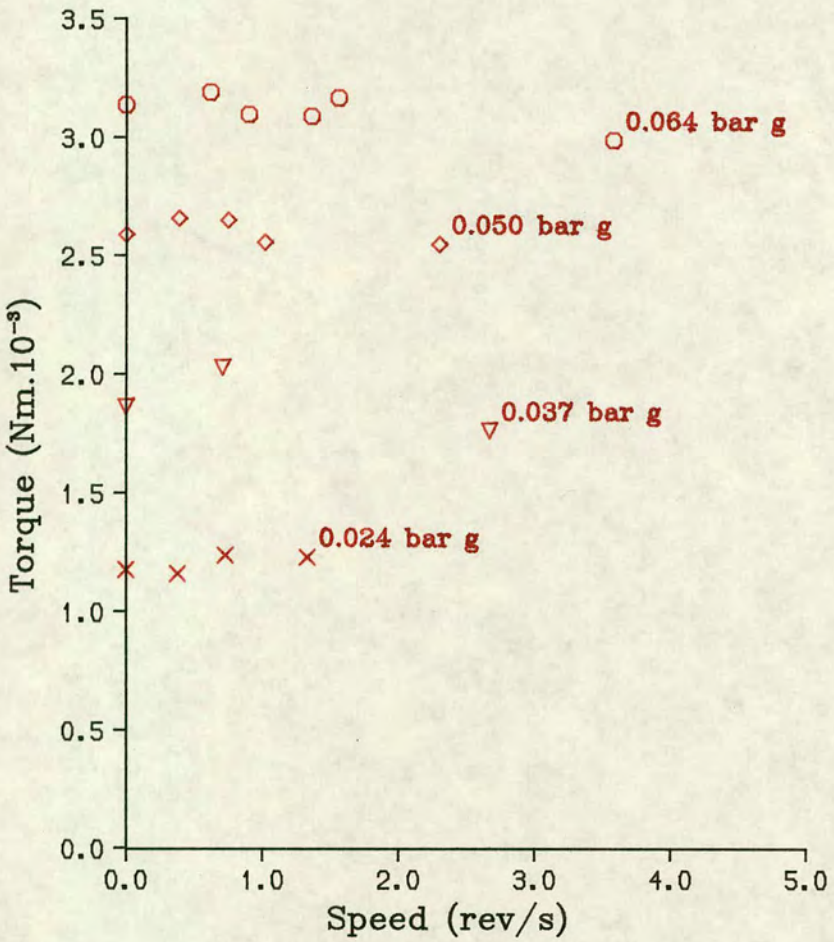

(a) Torque against speed

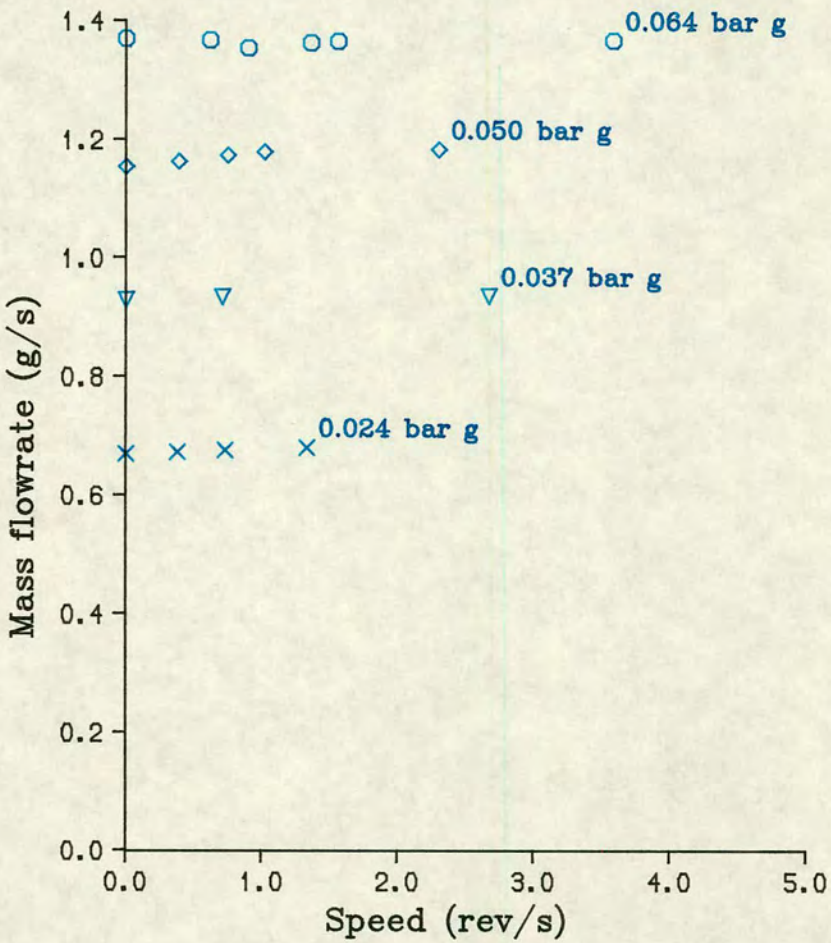

(b) Flowrate against speed

Fig.2.12 Single Disc Motor : Test S6 (H=620μm ; h_c=100μm)

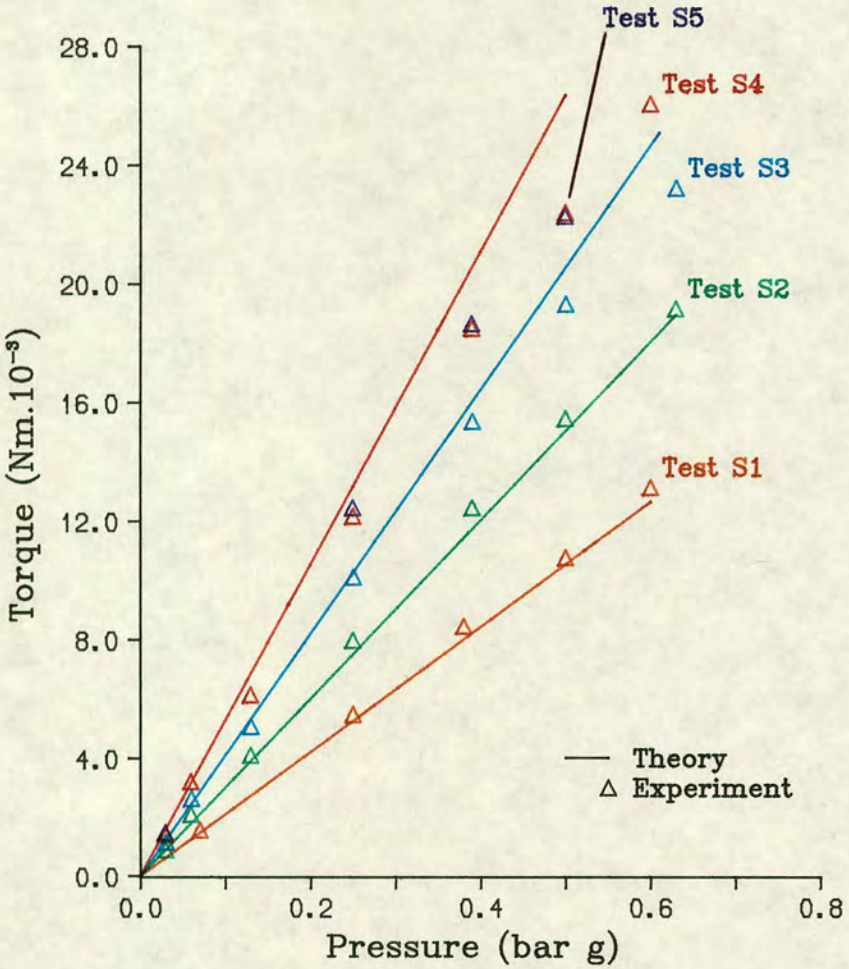

(a) Torque against pressure

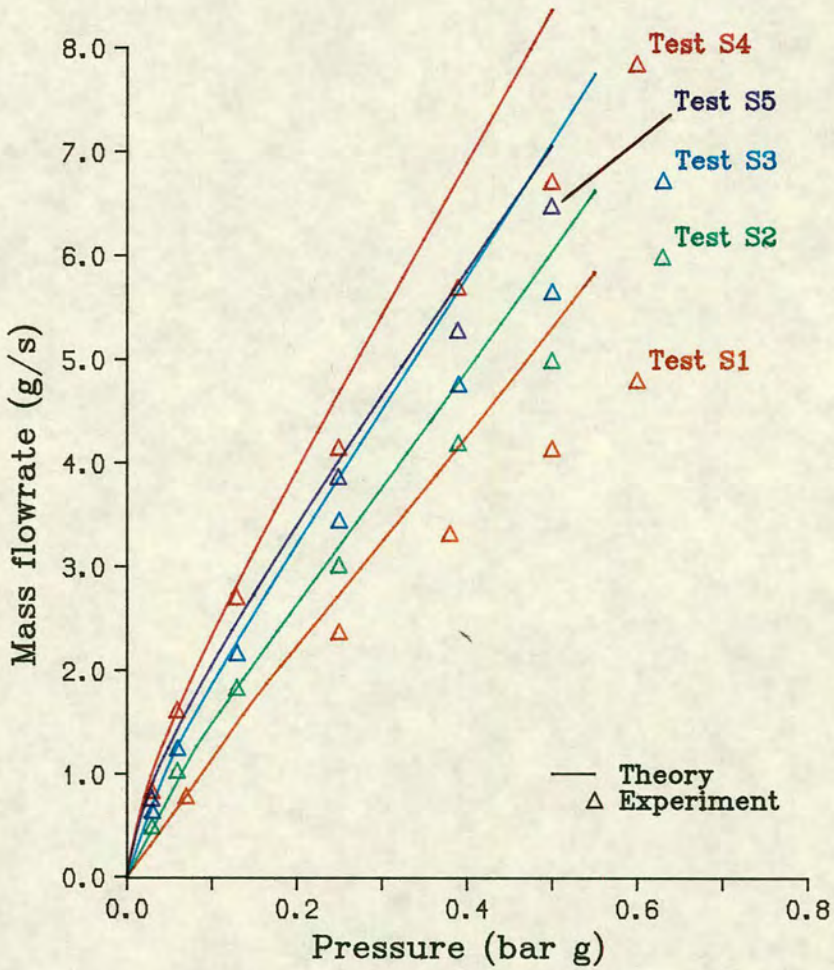

(b) Flowrate against pressure

Fig.2.13 Single disc motor results at zero or near zero speed

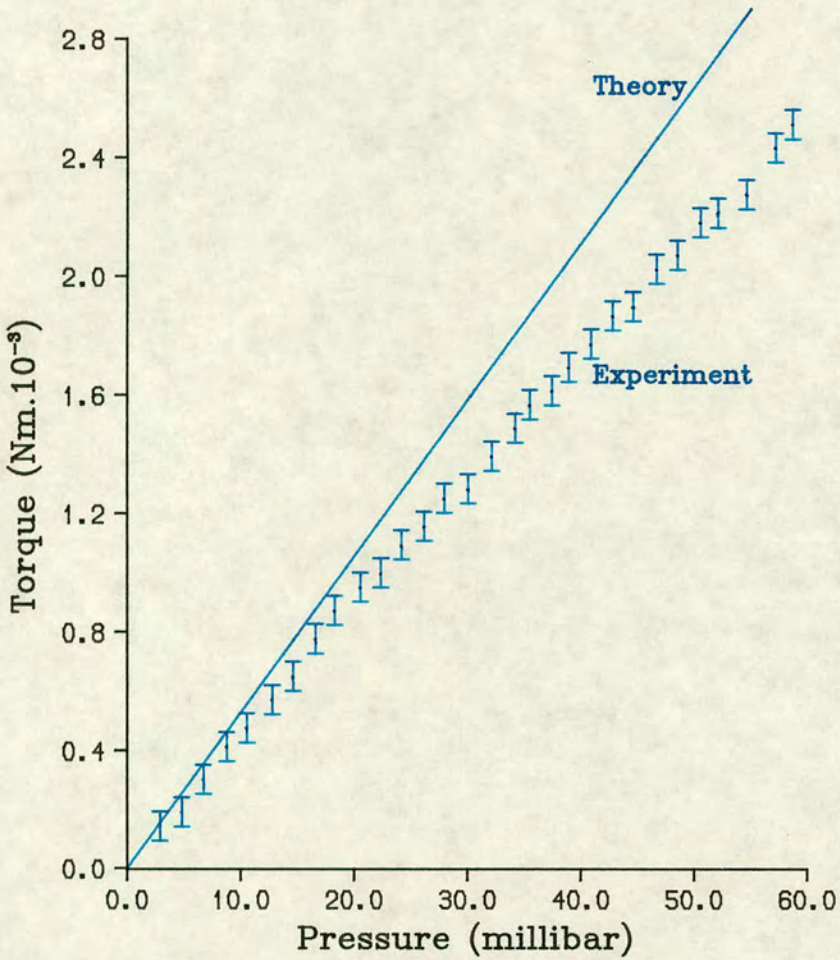

(a) Torque against pressure

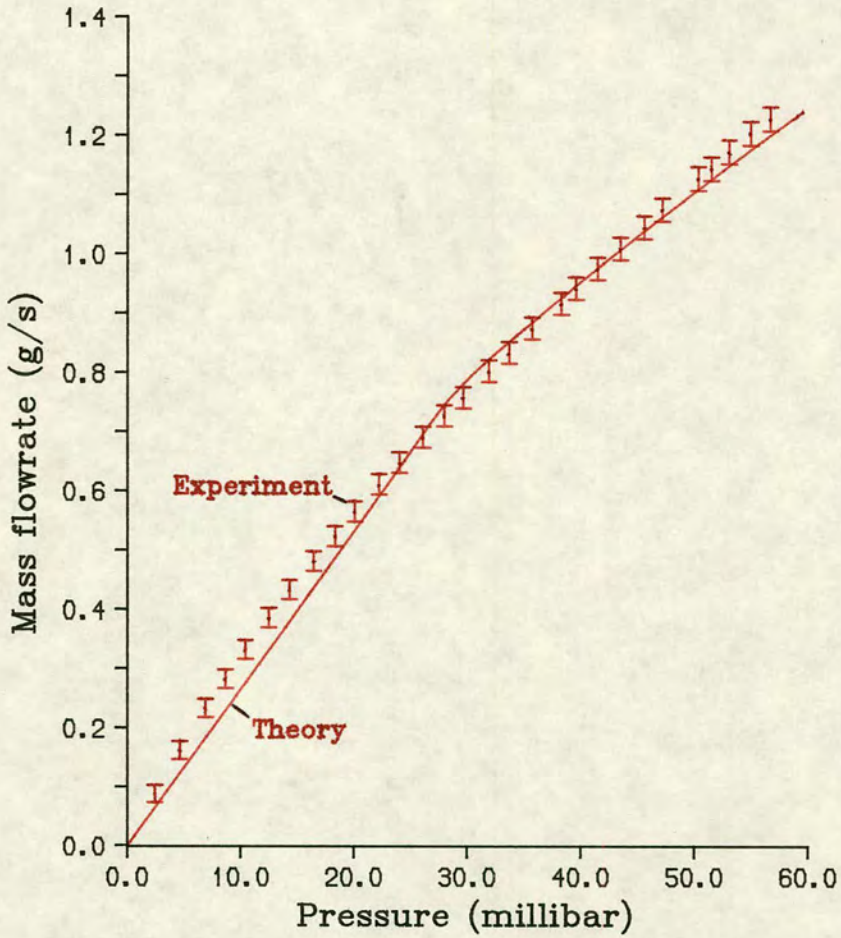

(b) Flowrate against pressure

Fig.2.14 Single Disc Motor : Test S6 (H=620μm ; h_c=100μm) : Rotor Stationary

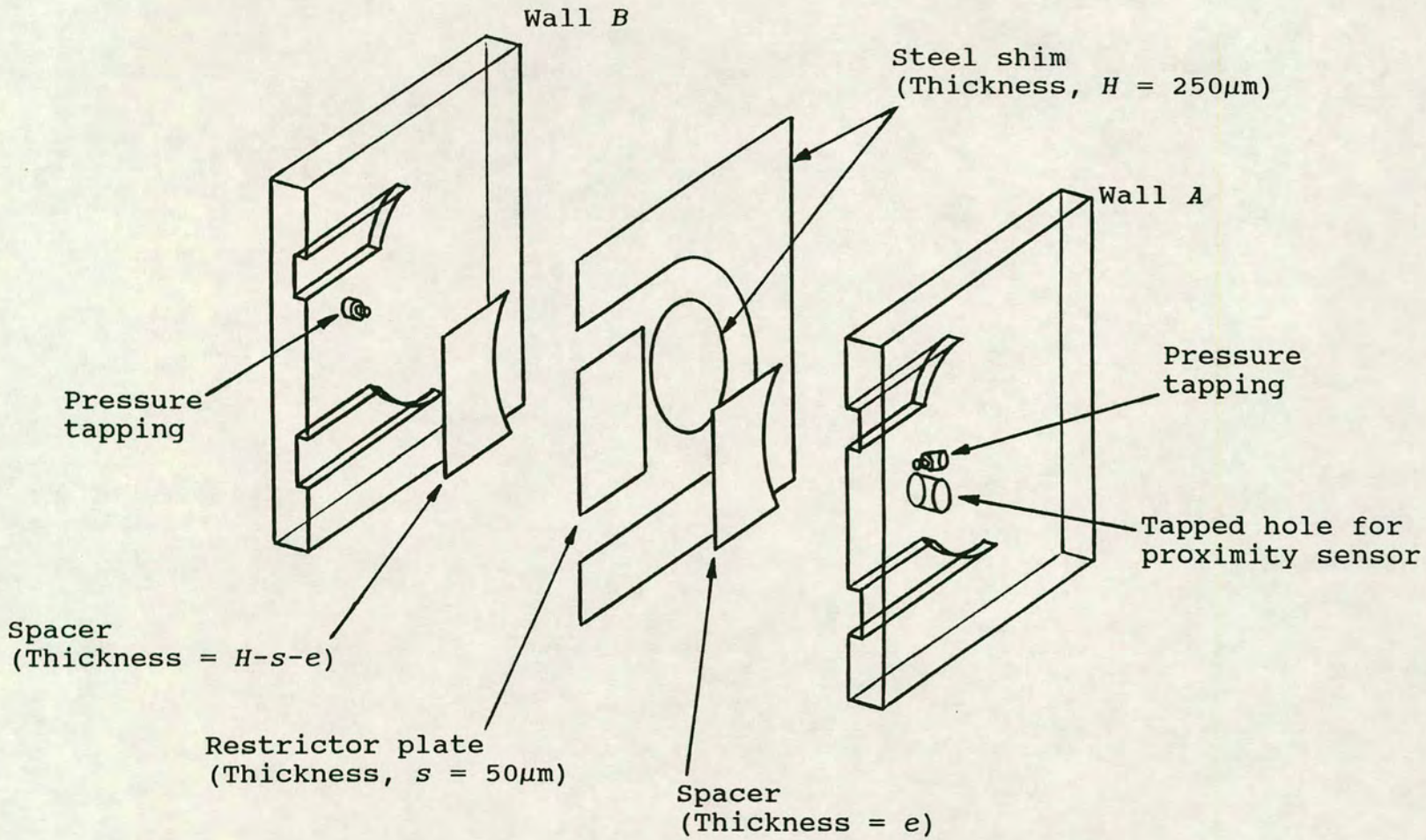

Fig.3.1 Exploded view of the perspex duct

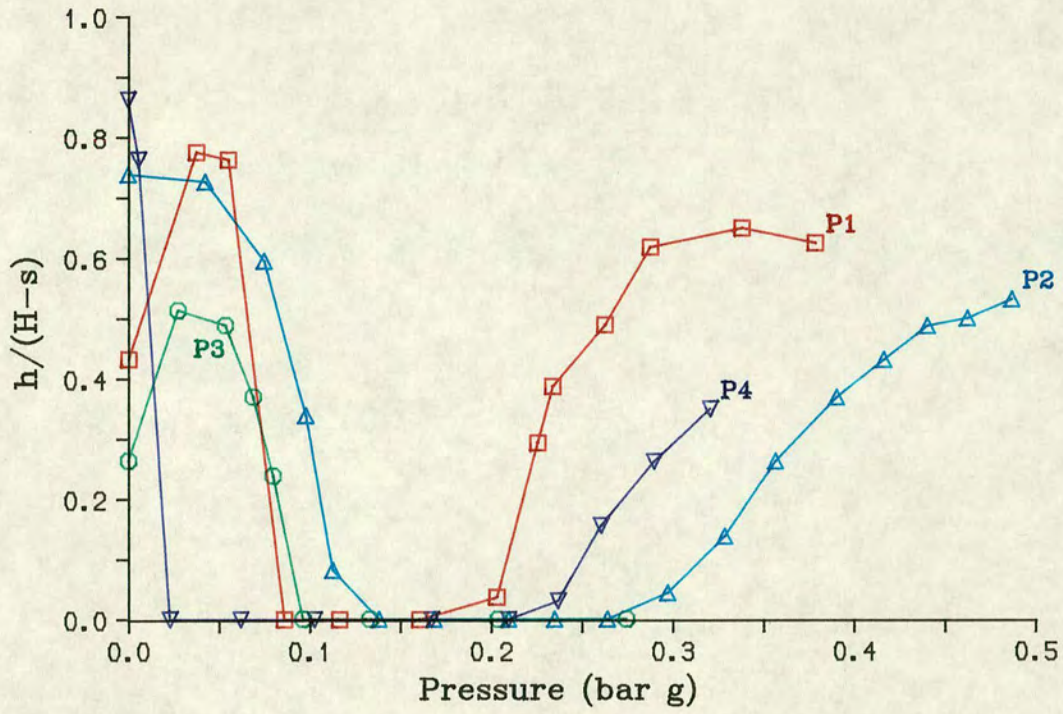

(a) Position of plate centre

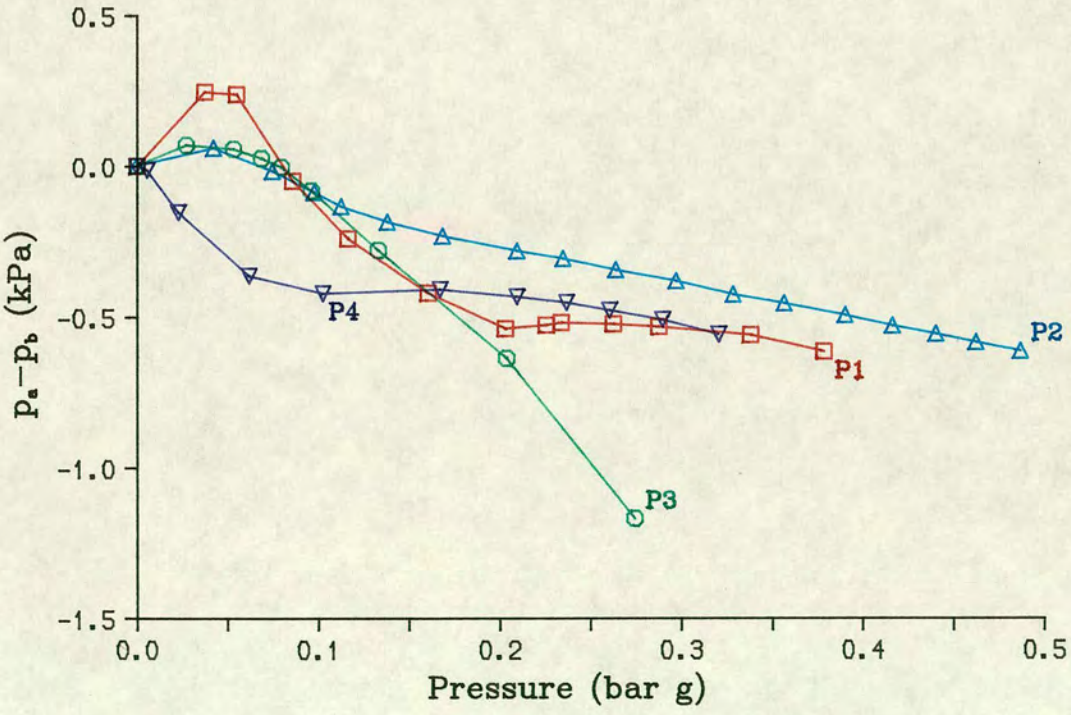

(b) Differential pressure at plate centre

Fig.3.2 Perspex Duct Tests P1 to P4

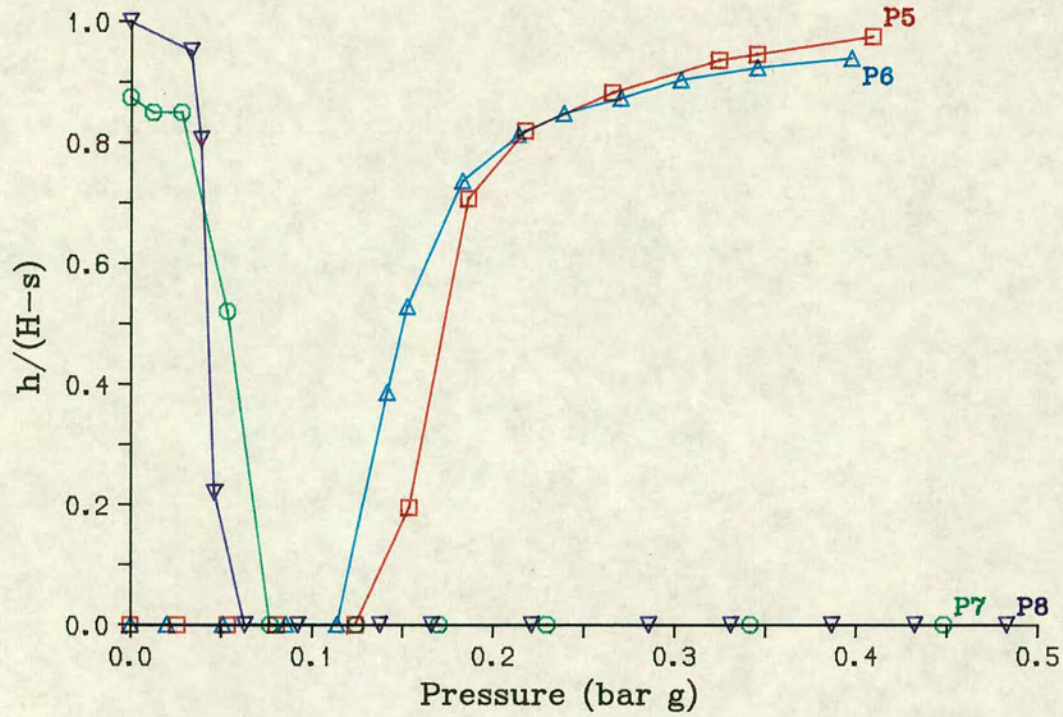

(a) Position of plate centre

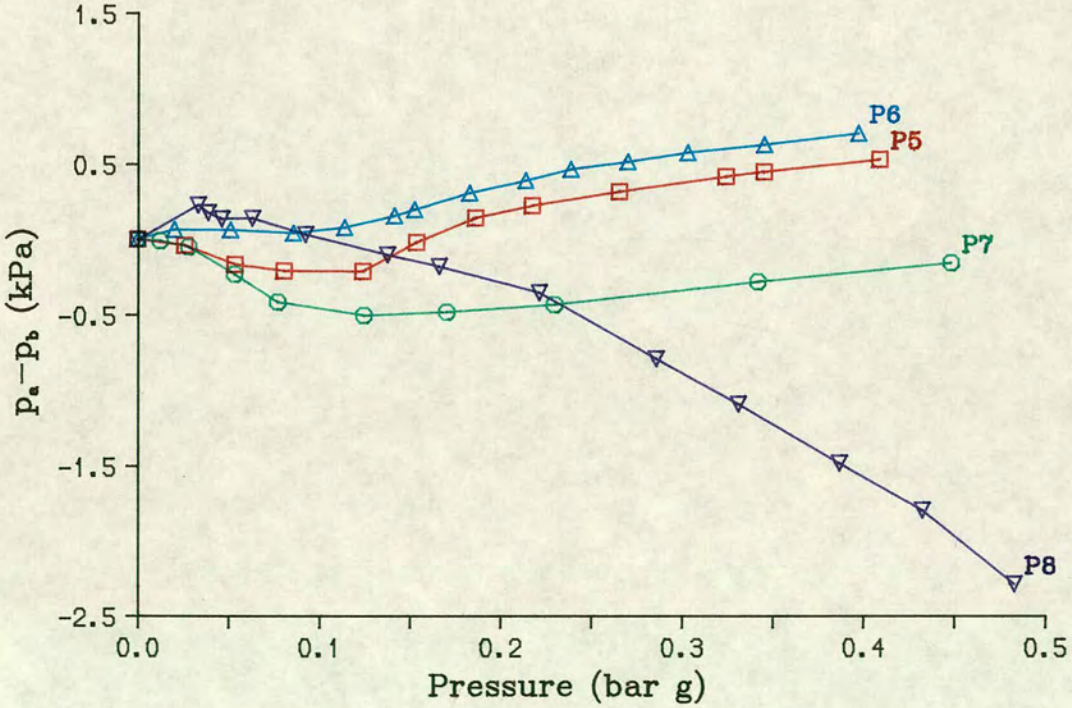

(b) Differential pressure at plate centre

Fig.3.3 Perspex Duct Tests P5 to P8

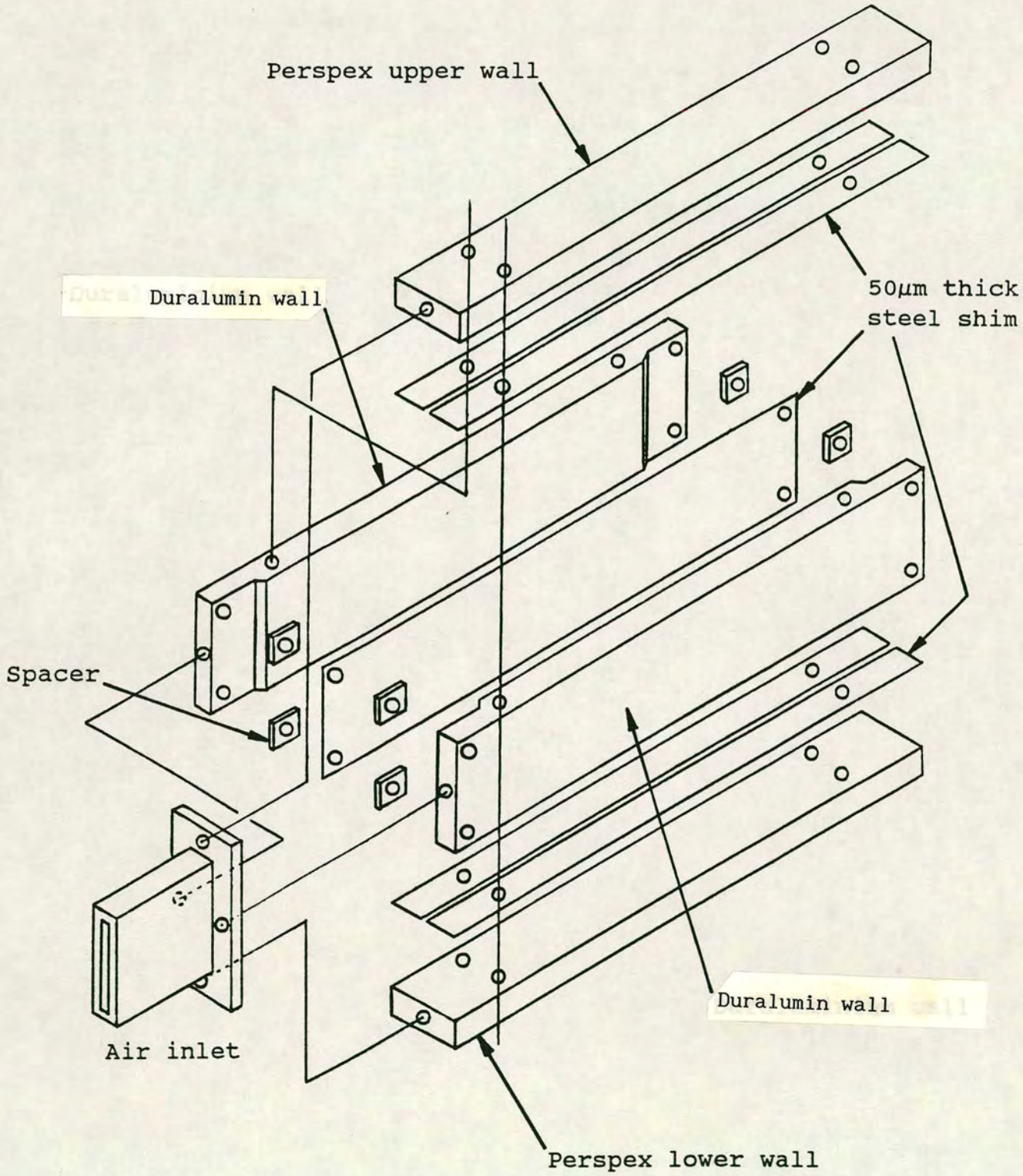

Fig.3.4 Exploded view of the straight duct

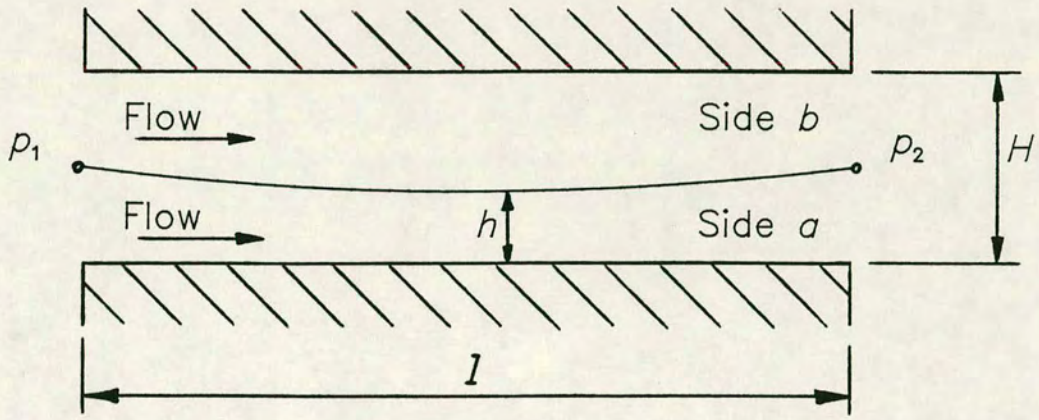

Fig.4.1 Membrane in parallel walled duct

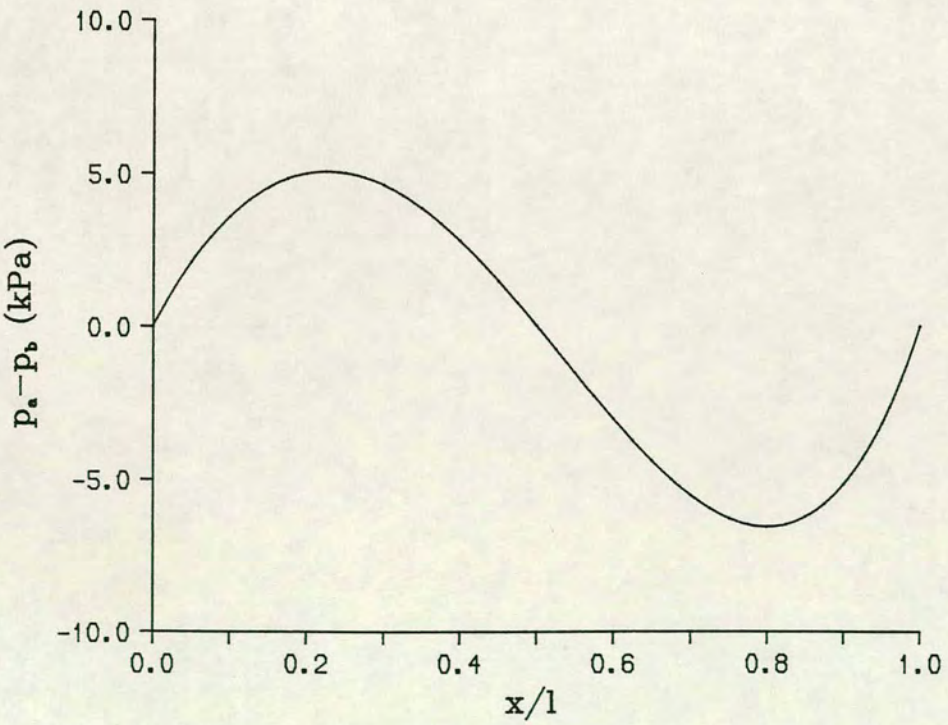

Fig.4.2 Pressure difference across membrane shown in Fig.4.1 ($p_1 - p_2 = 0.6$ bar)

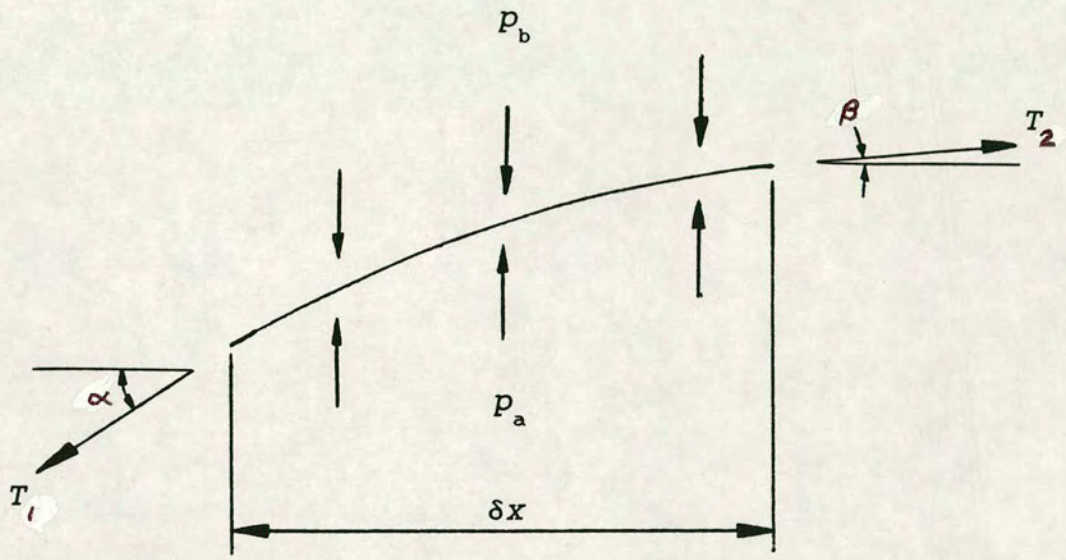

Fig.5.1 Force balance on a membrane element

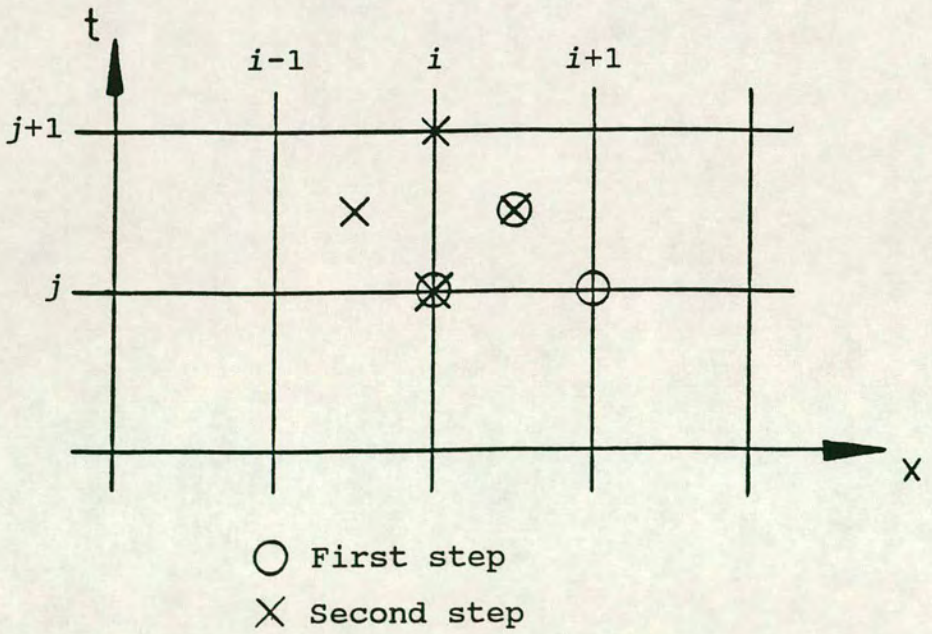

Fig.6.1 The Lax–Wendroff grid

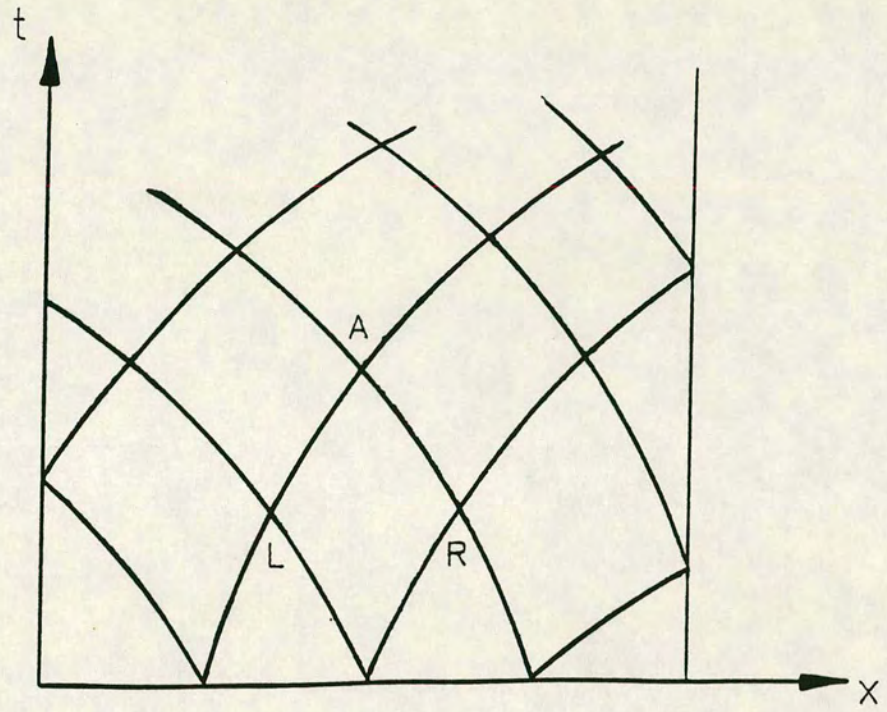

Fig.6.2 A typical characteristic grid

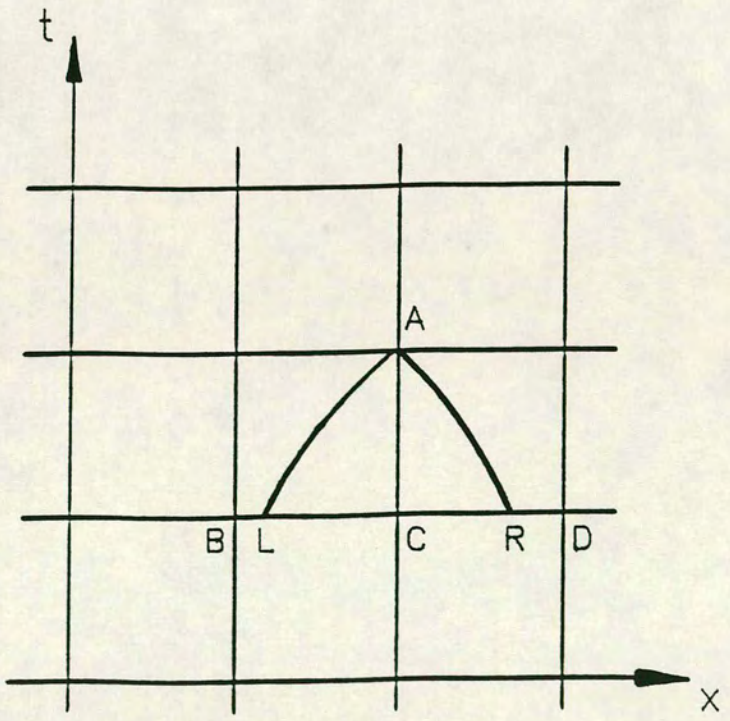

Fig.6.3 The Hartree method grid

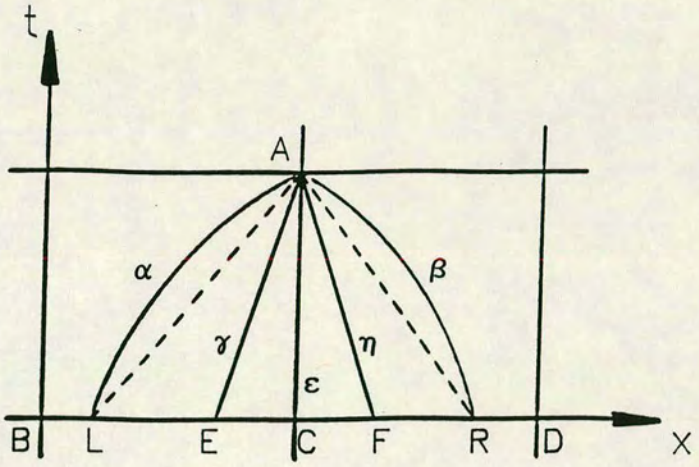

(a) An interior node

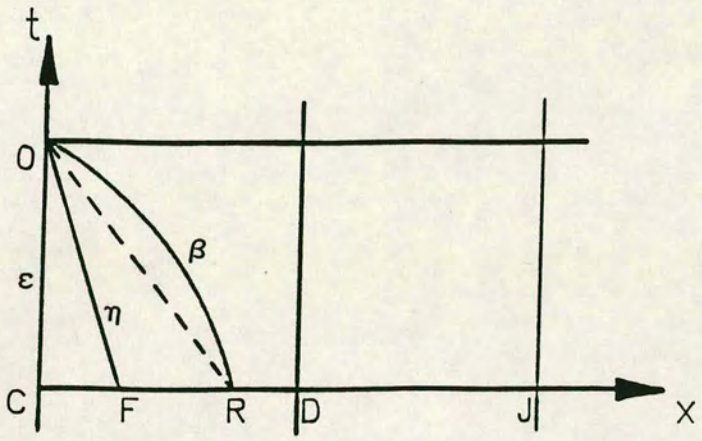

(b) The left hand boundary

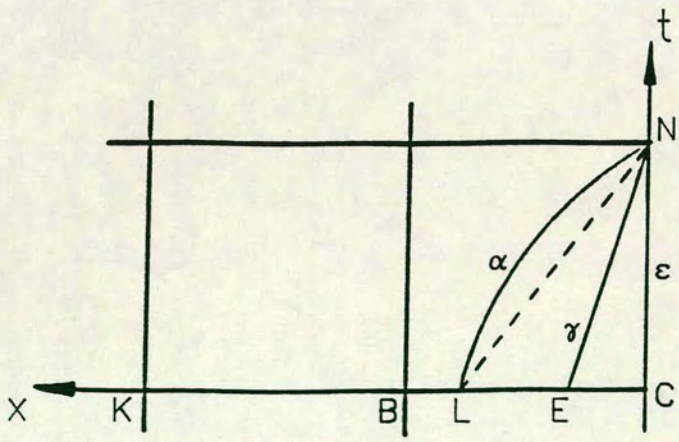

(c) The right hand boundary

Fig.6.4 The characteristics of the present problem

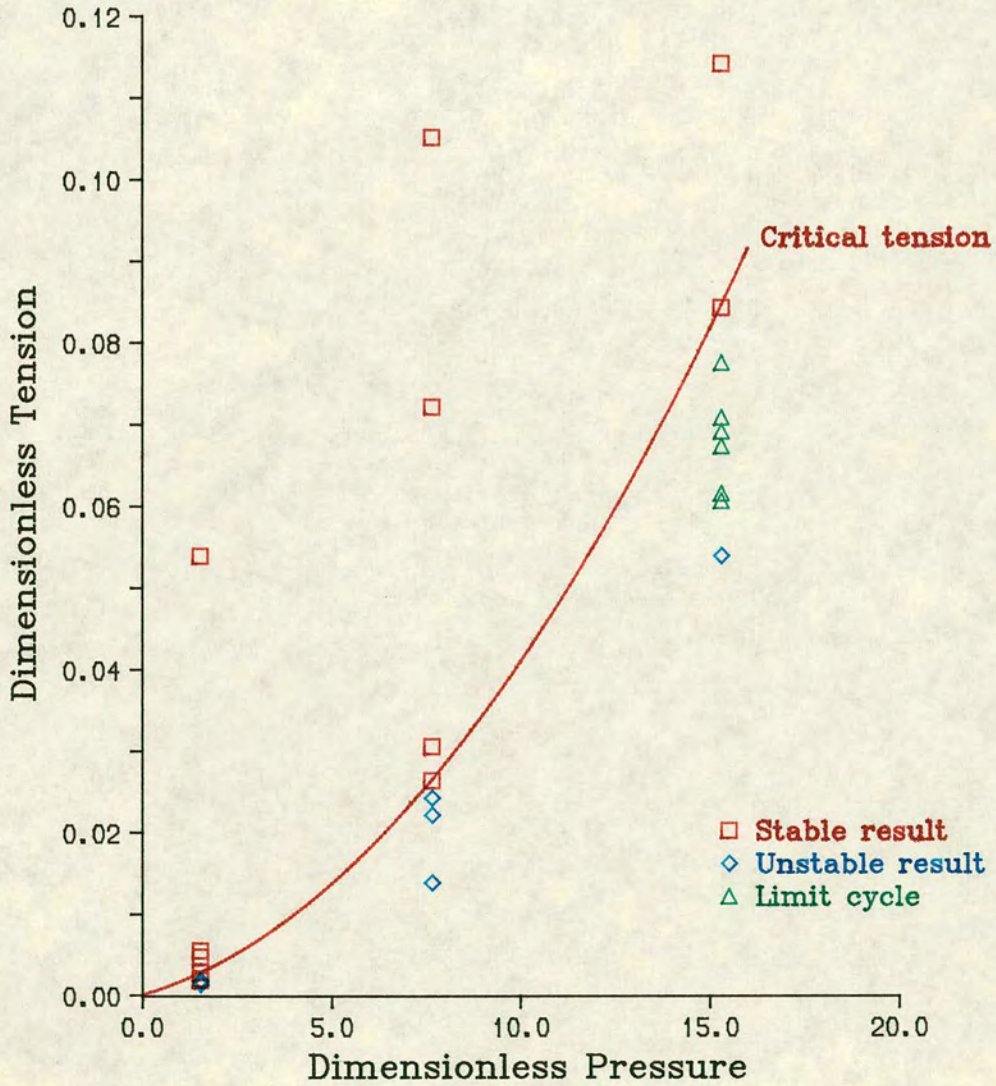

Fig.7.1 Stability map for Series A, B and C
(Dimensionless density = 0.4)

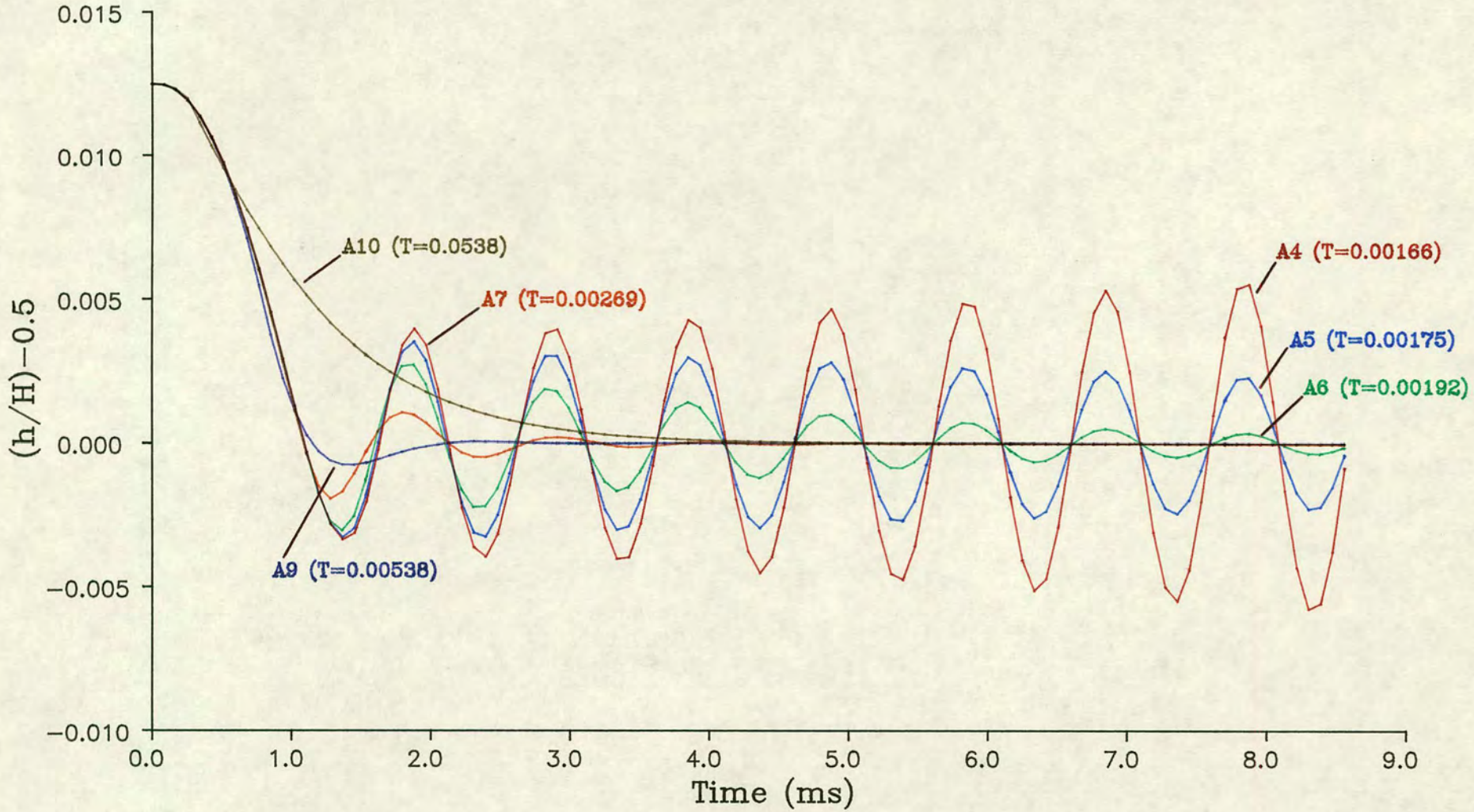

Fig.7.2a Motion of membrane mid−point in selected Series A tests

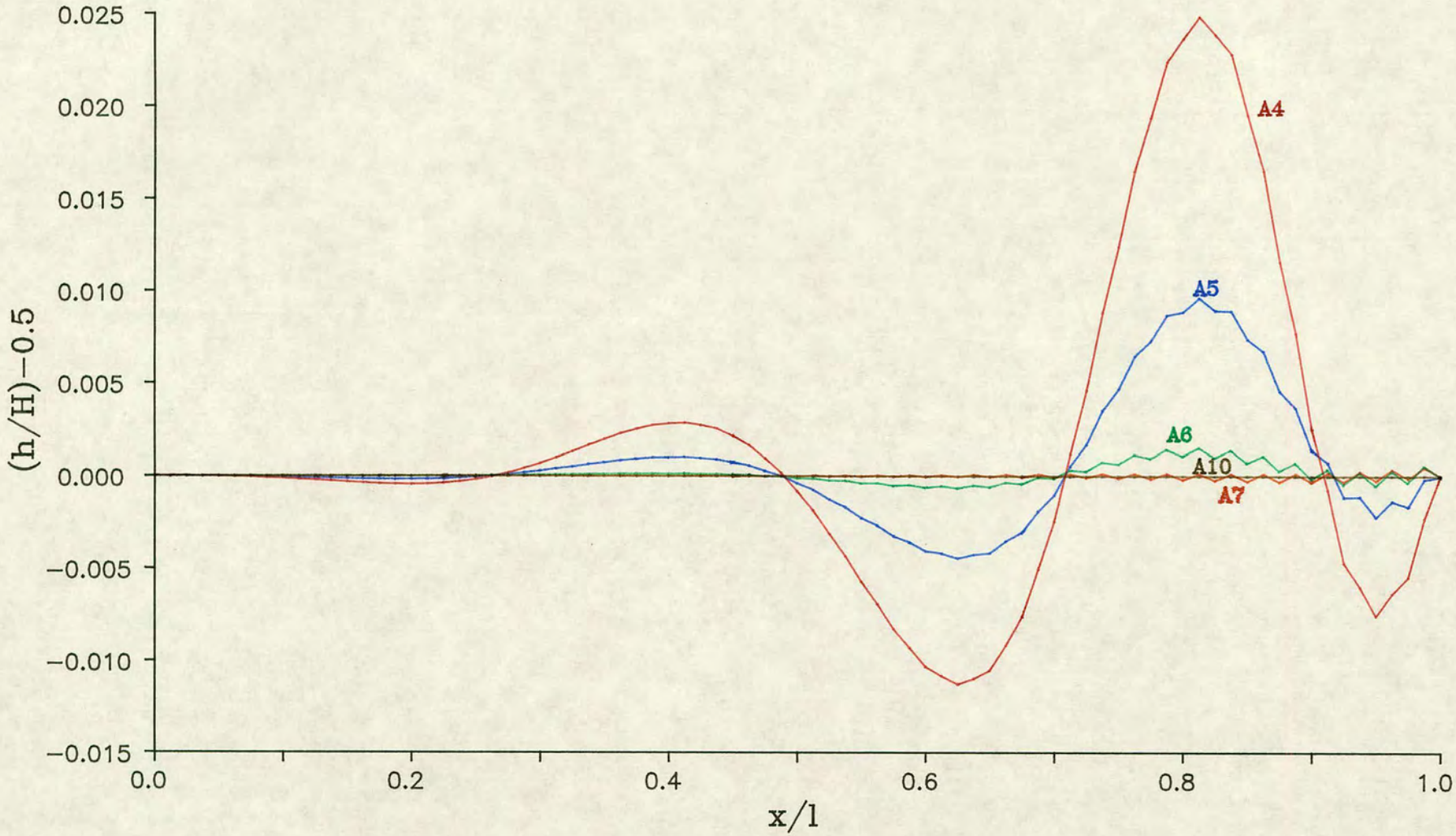

Fig.7.2b Membrane shape at 8.5 ms in selected Series A tests

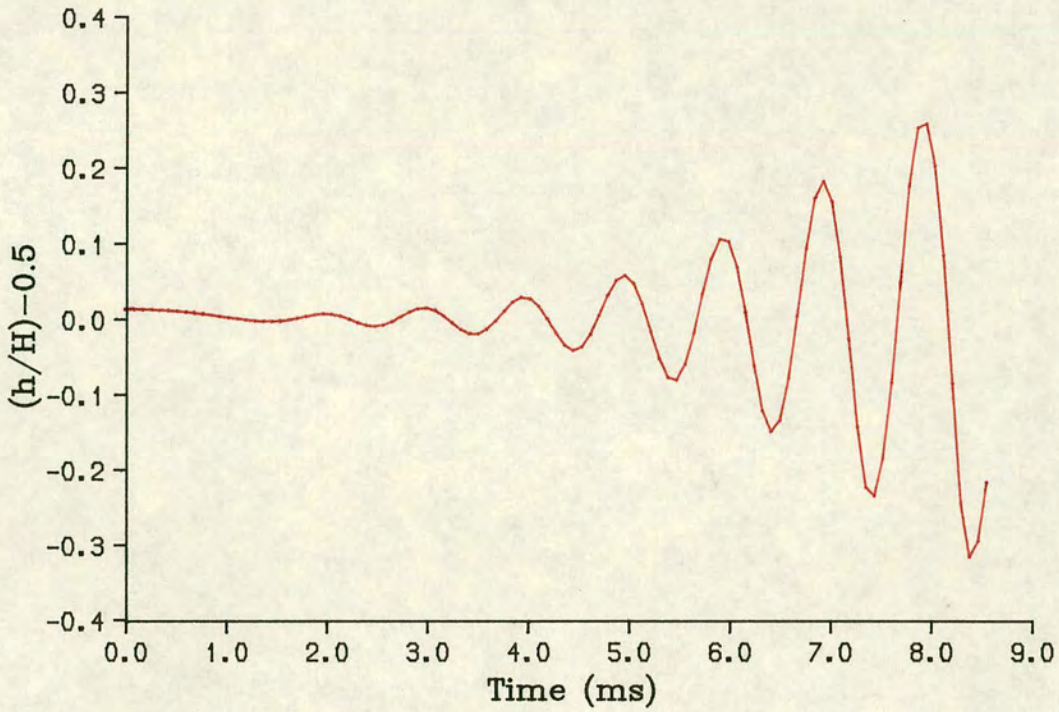

(a) Motion of membrane mid-point

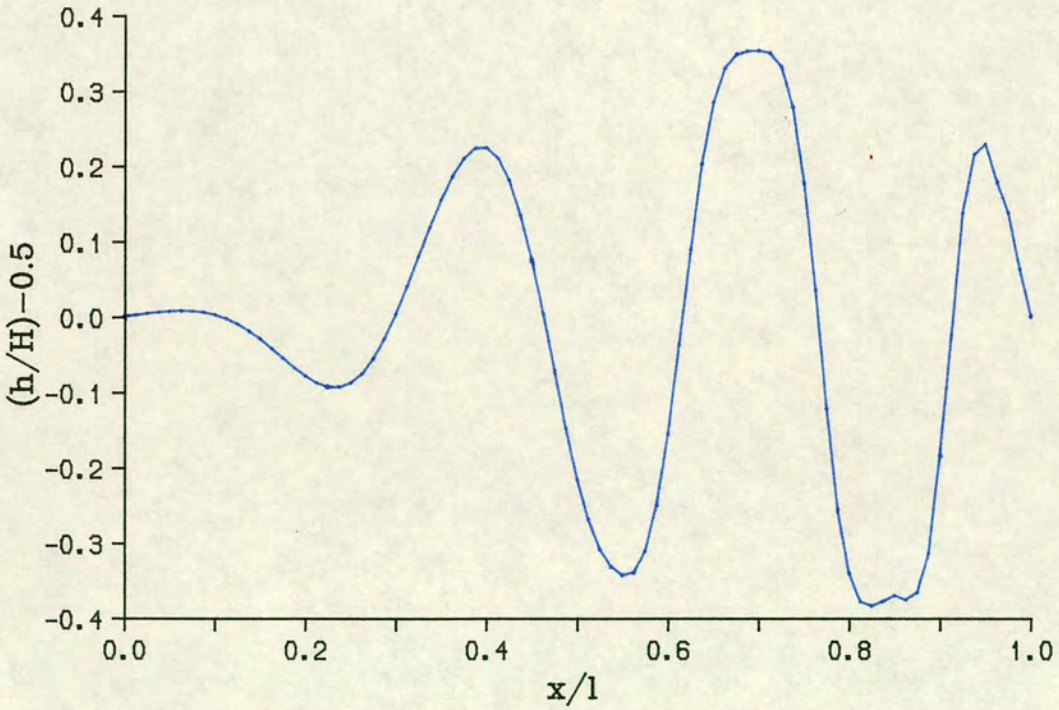

(b) Membrane shape at 8.5ms

Fig.7.3 Test A2 (T=0.00123)

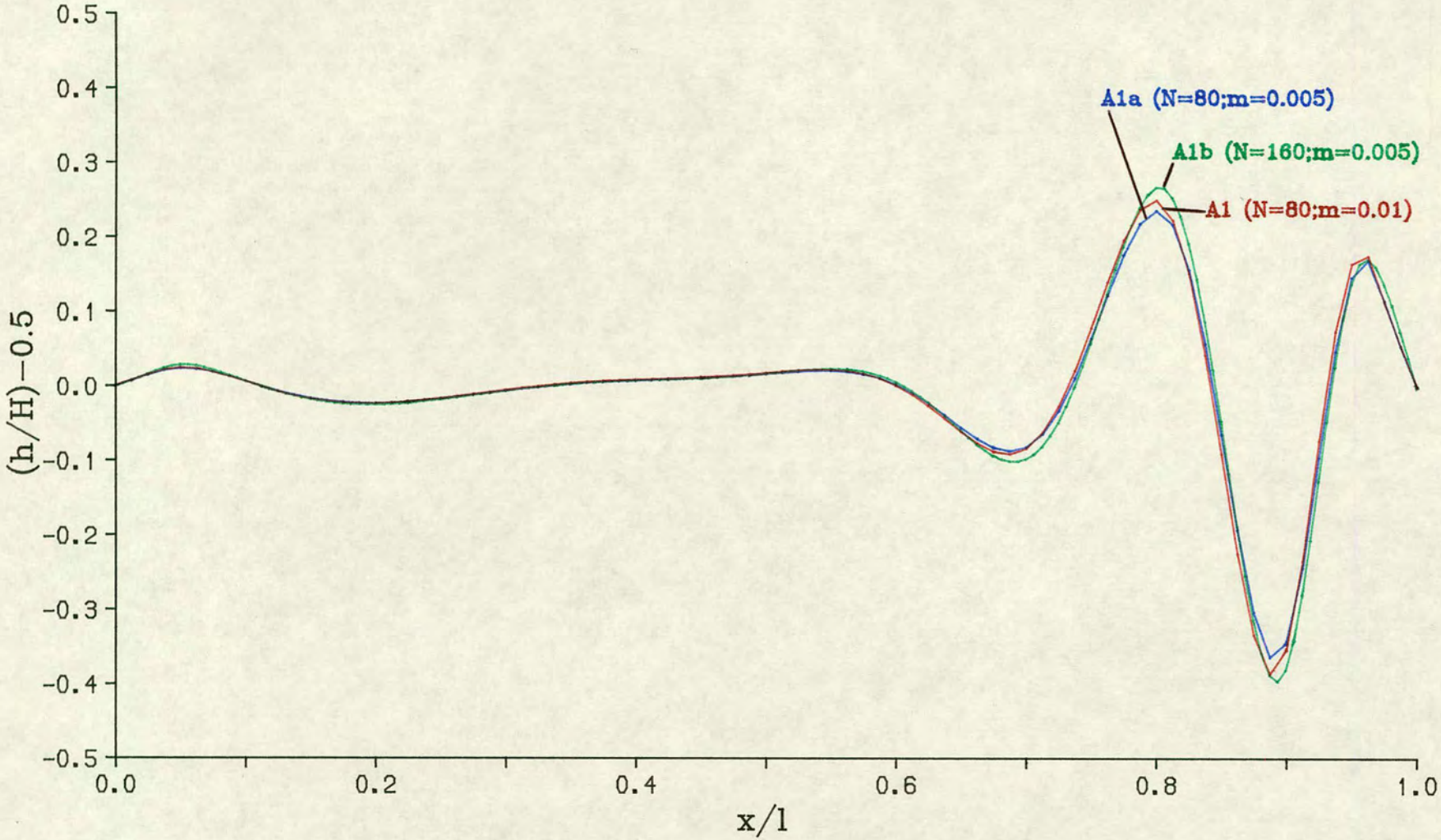

Fig.7.4 Membrane shape at 2.2ms in Test A1

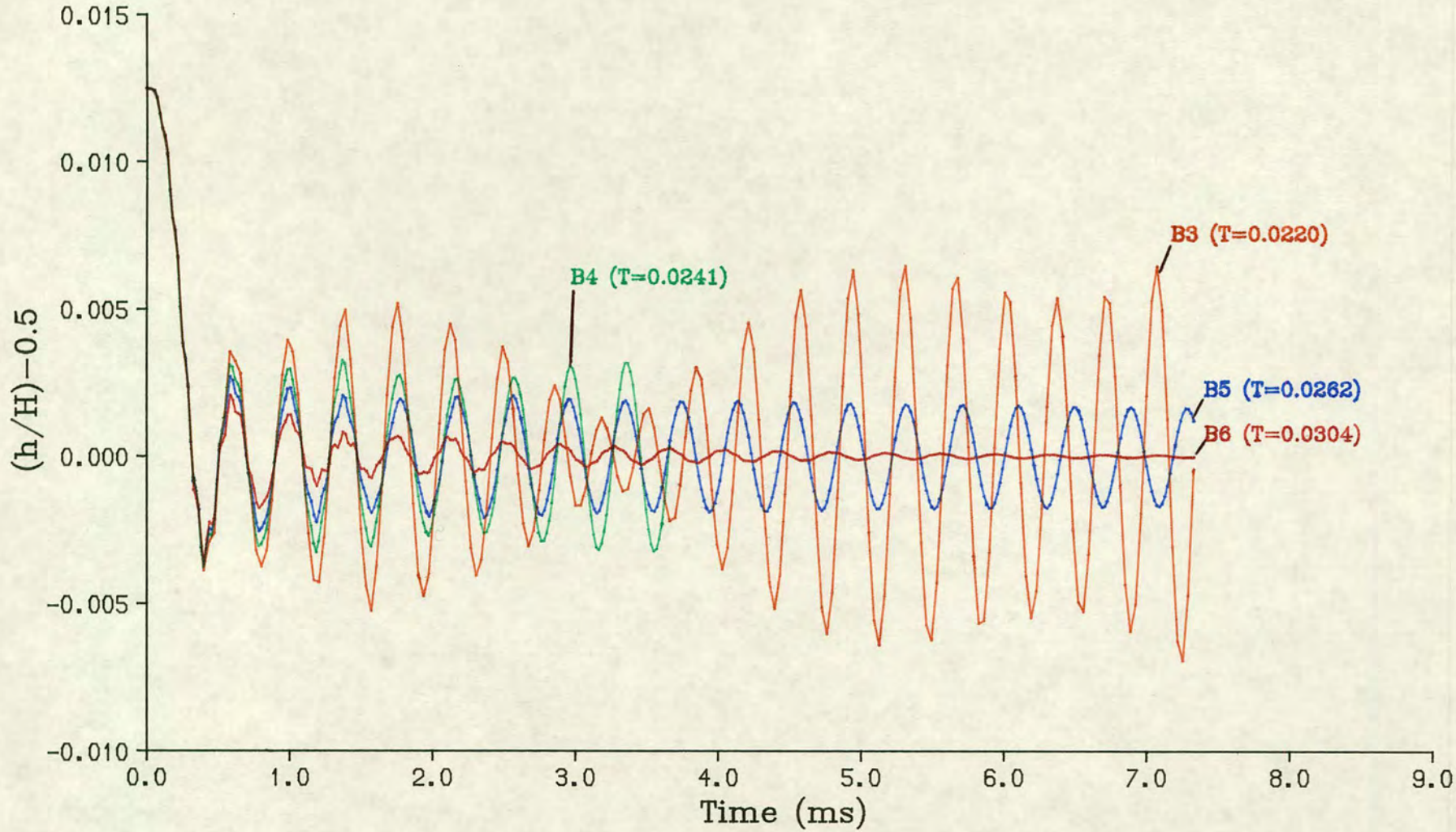

Fig.7.5 Motion of membrane mid-point in selected Series B tests

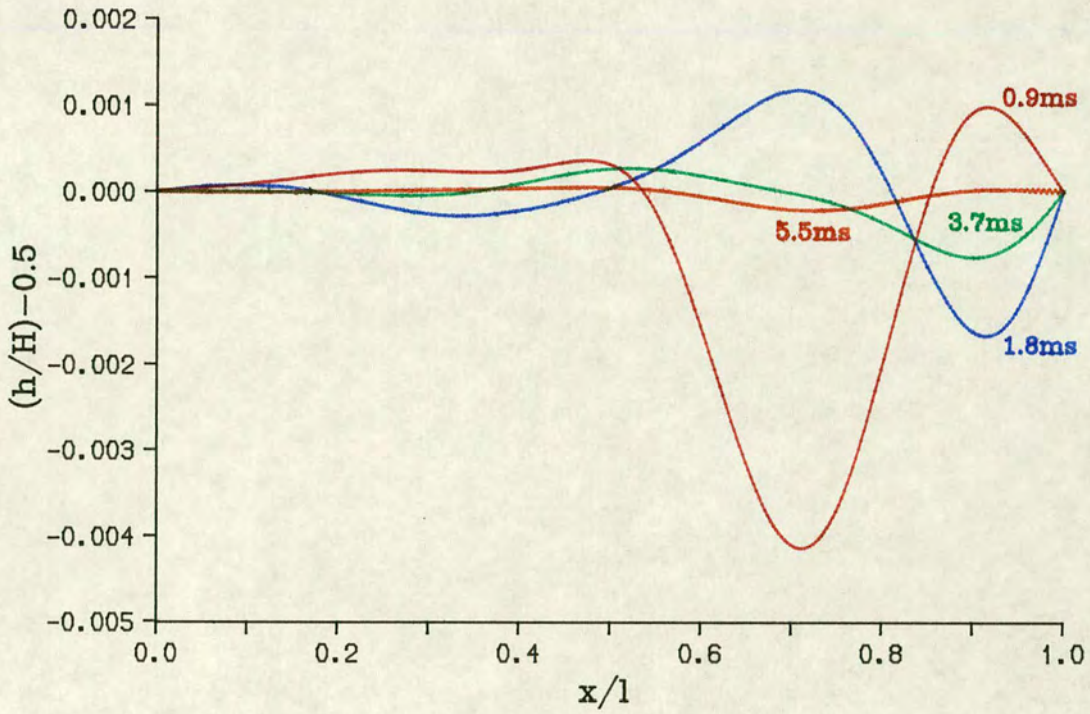

(a) Test B6 (T=0.0304)

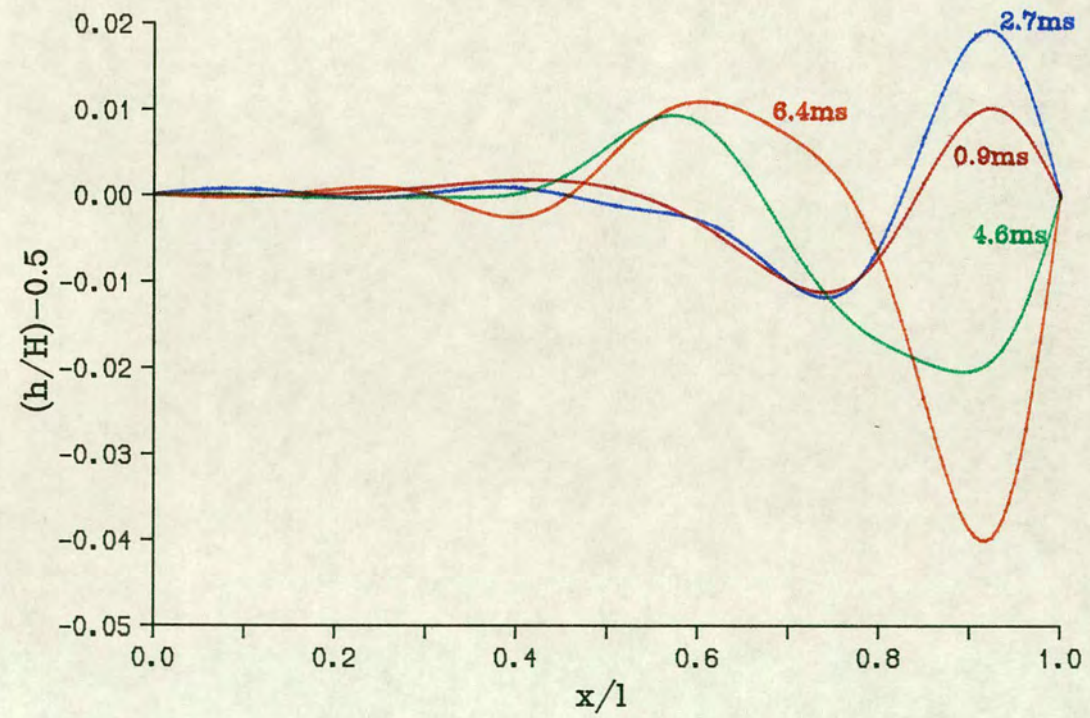

(b) Test B3 (T=0.0220)

Fig.7.6 Membrane shape variation with time

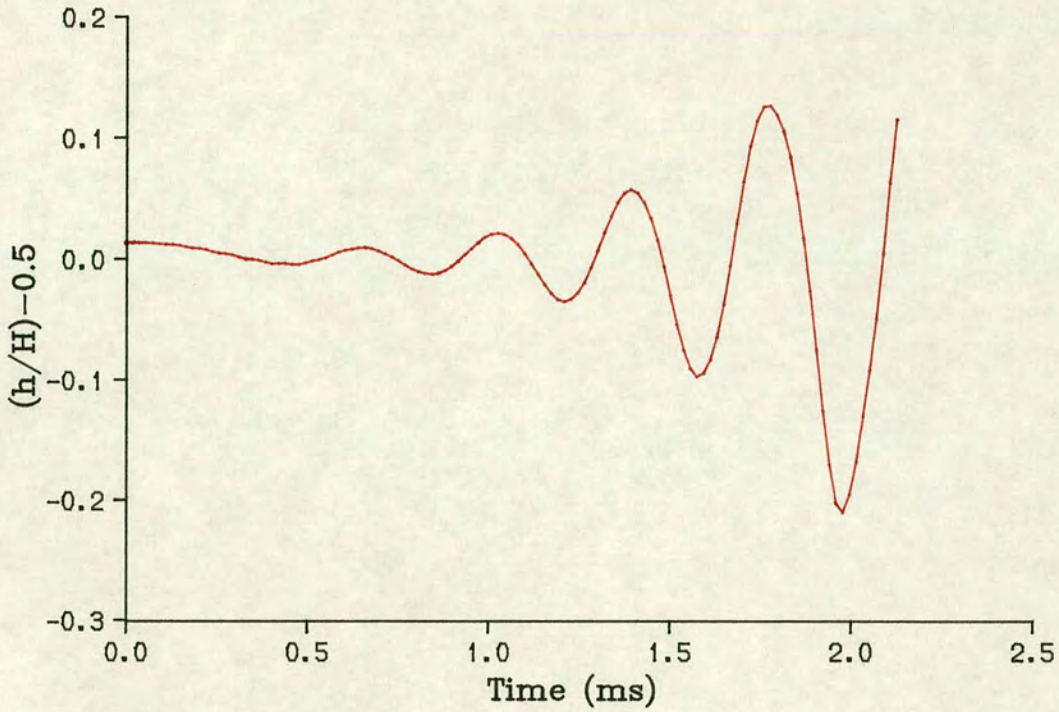

(a) Motion of membrane mid-point

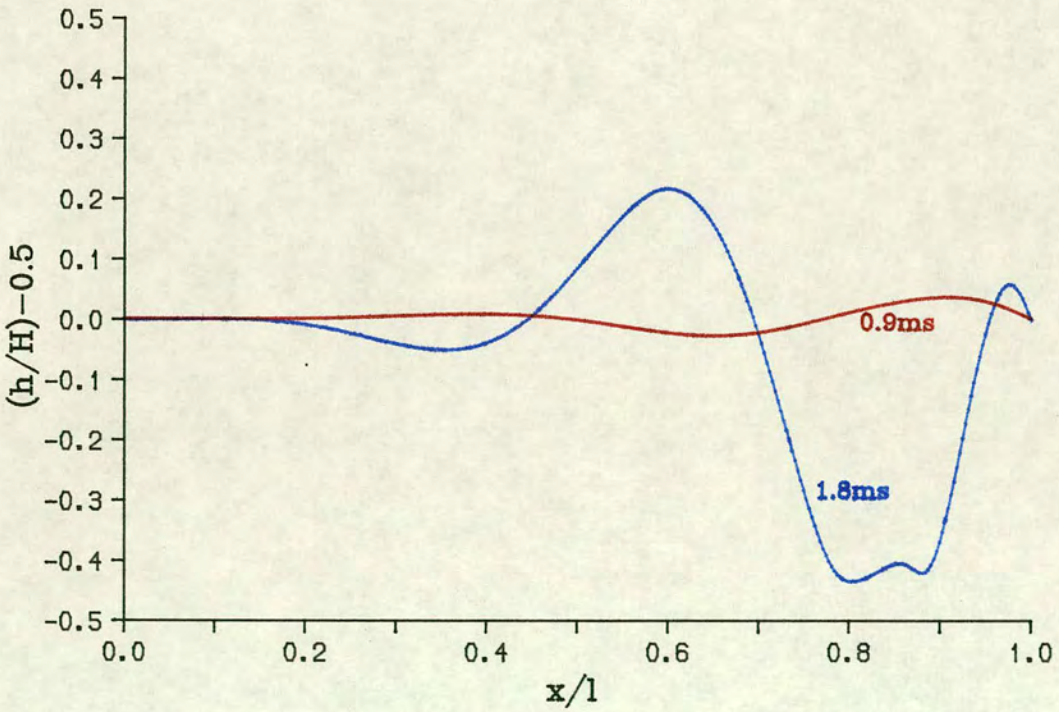

(b) Membrane shape variation with time

Fig.7.7 Test B2 (T=0.0137)

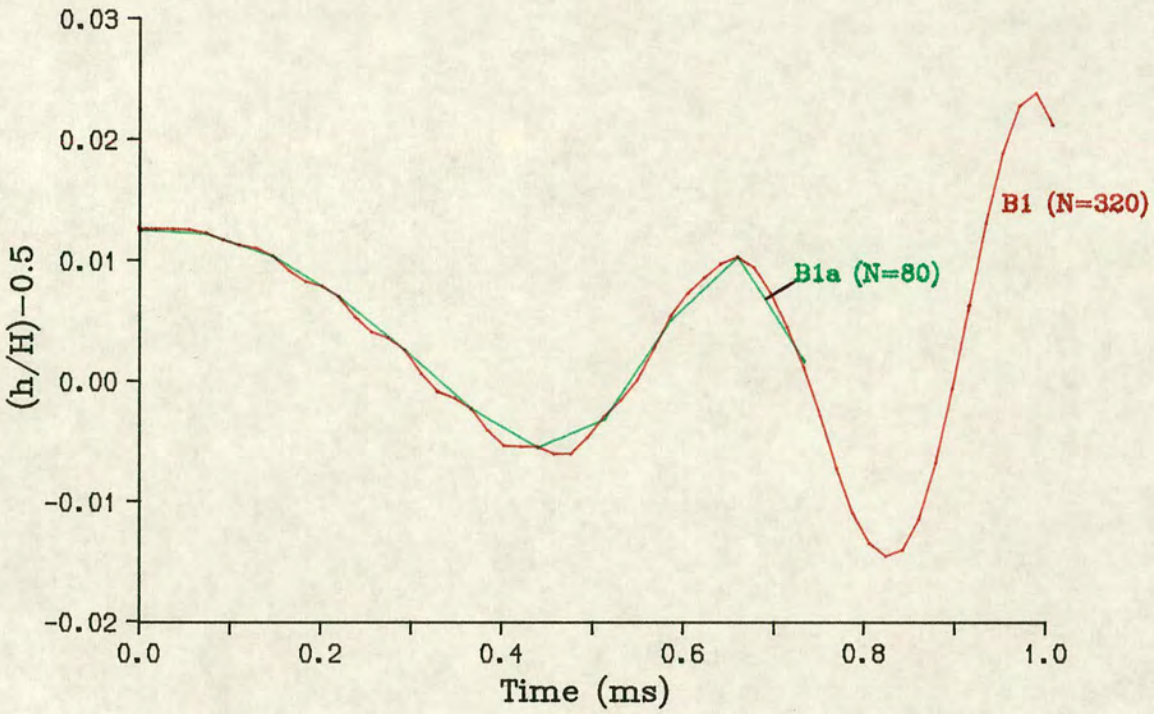

(a) Motion of membrane mid-point

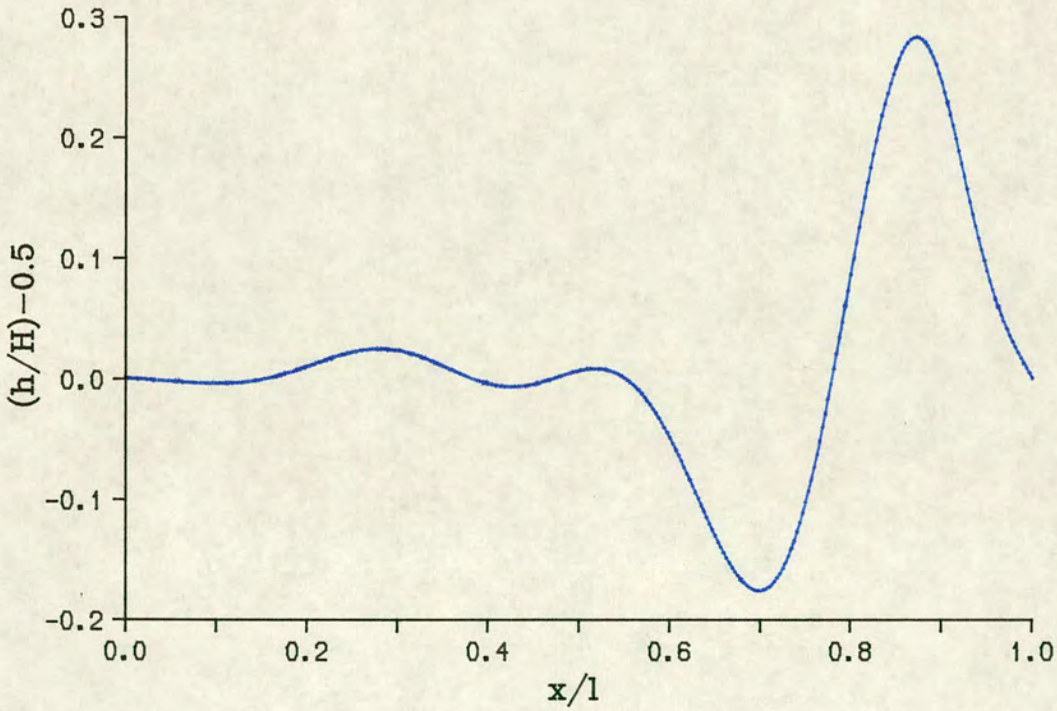

(b) Membrane shape at 1.0ms in Test B1

Fig.7.8 Test B1 (T=0.00538)

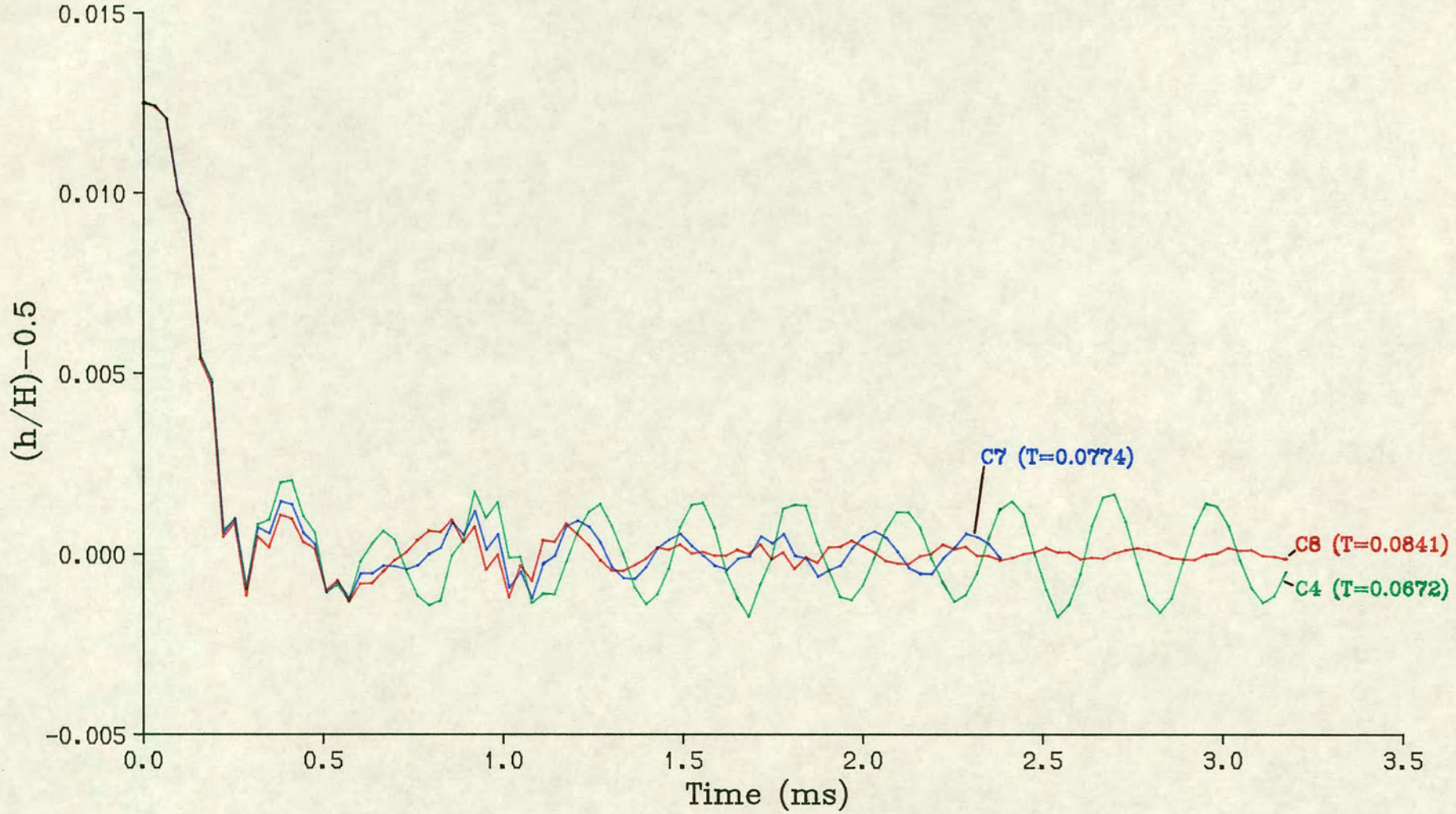

Fig.7.9 Motion of membrane mid−point in selected Series C tests

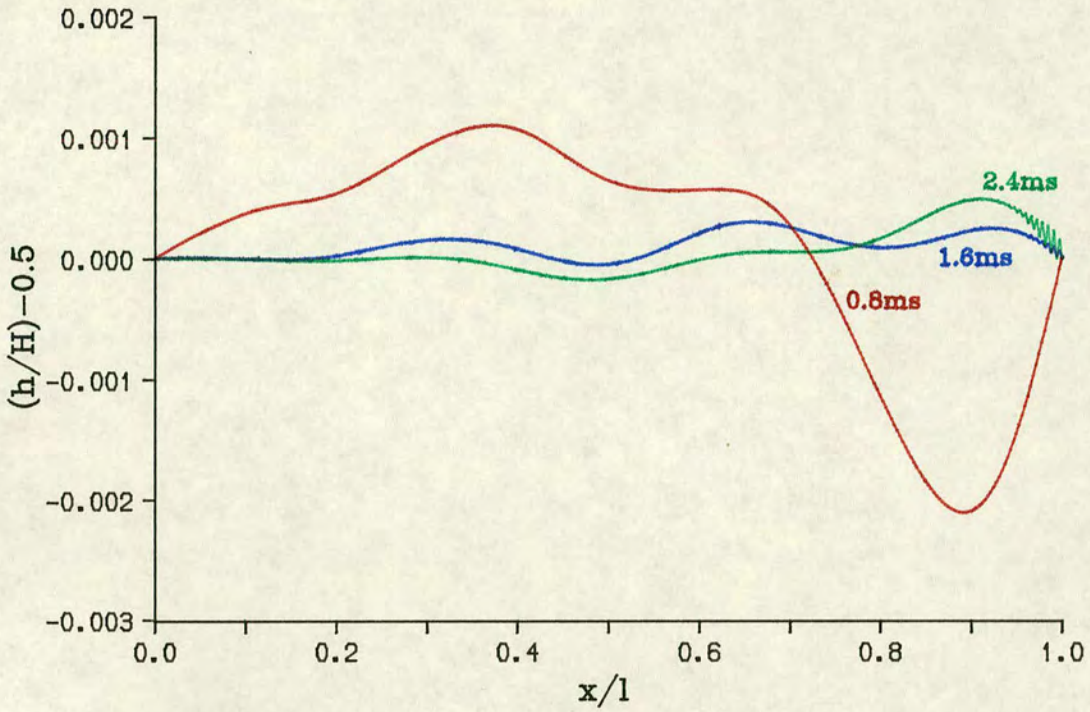

(a) Test C8 (T=0.0841)

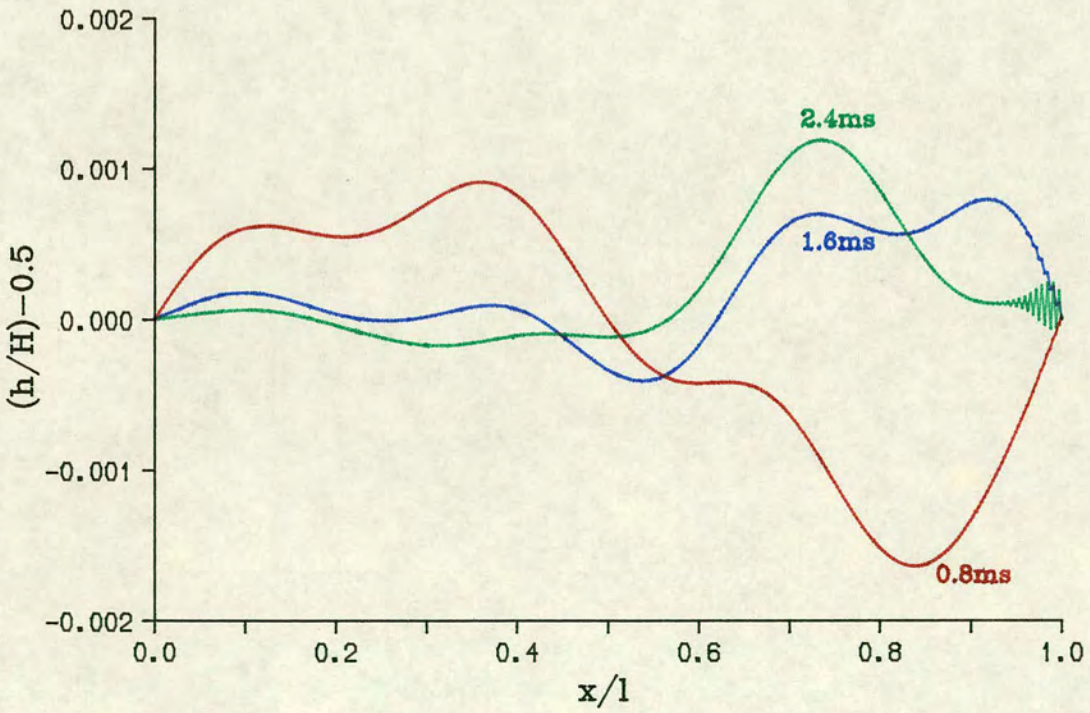

(b) Test C7 (T=0.0774)

Fig.7.10 Membrane shape variation with time

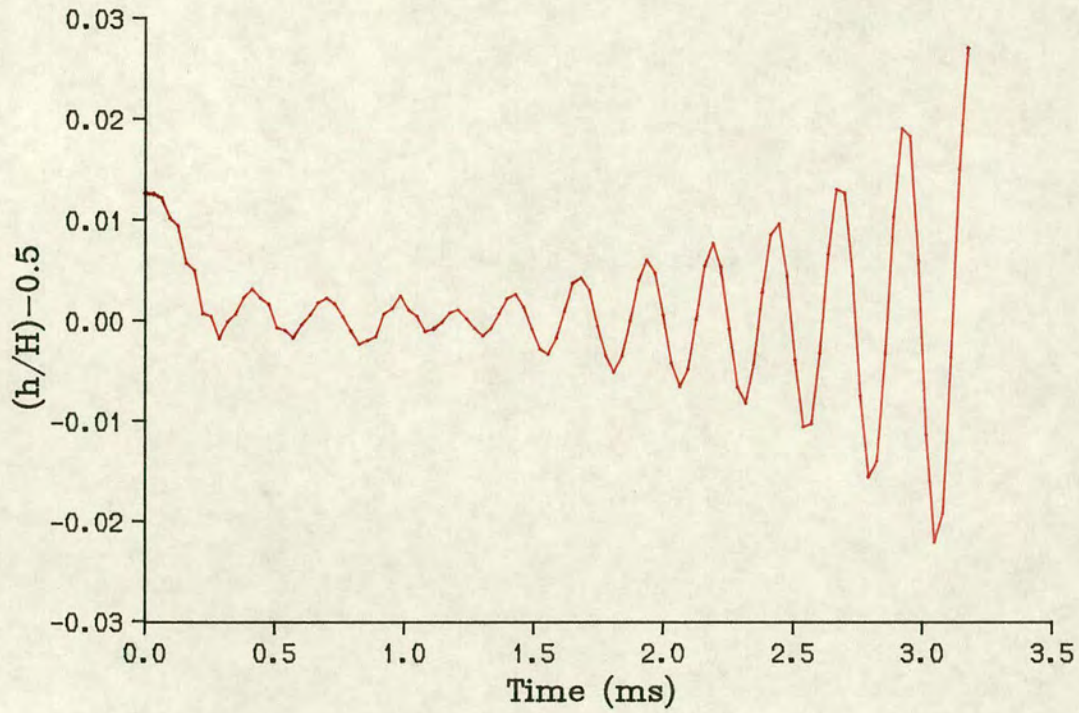

(a) Motion of membrane mid−point

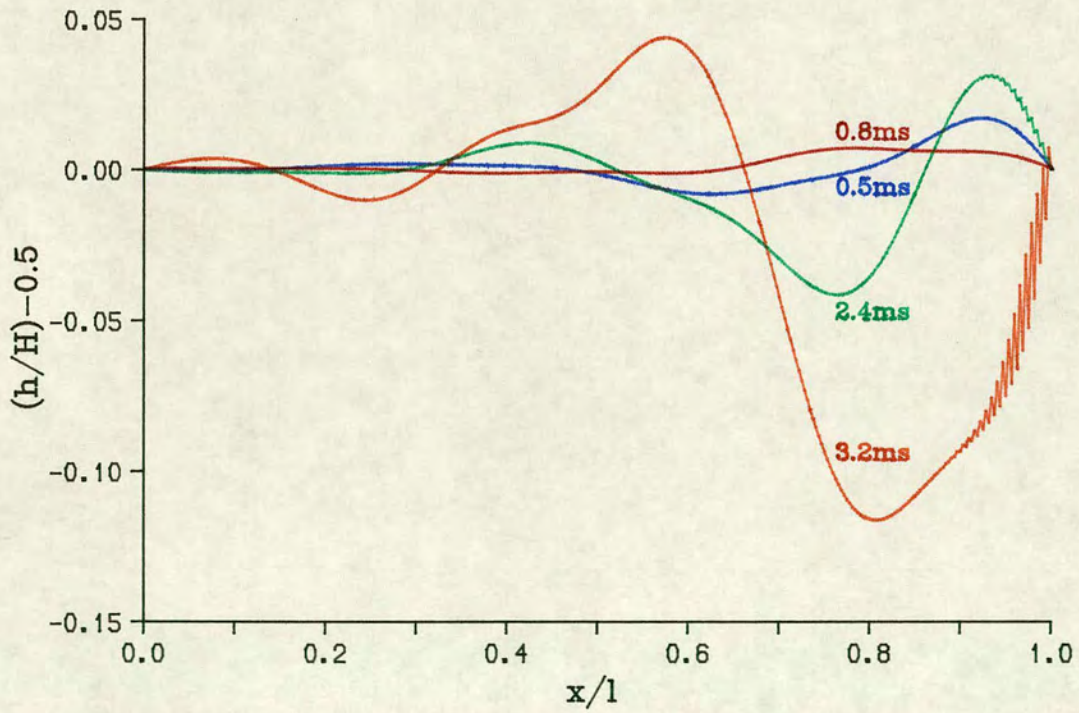

(b) Membrane shape variation with time

Fig.7.11 Test C1 (T=0.0538)

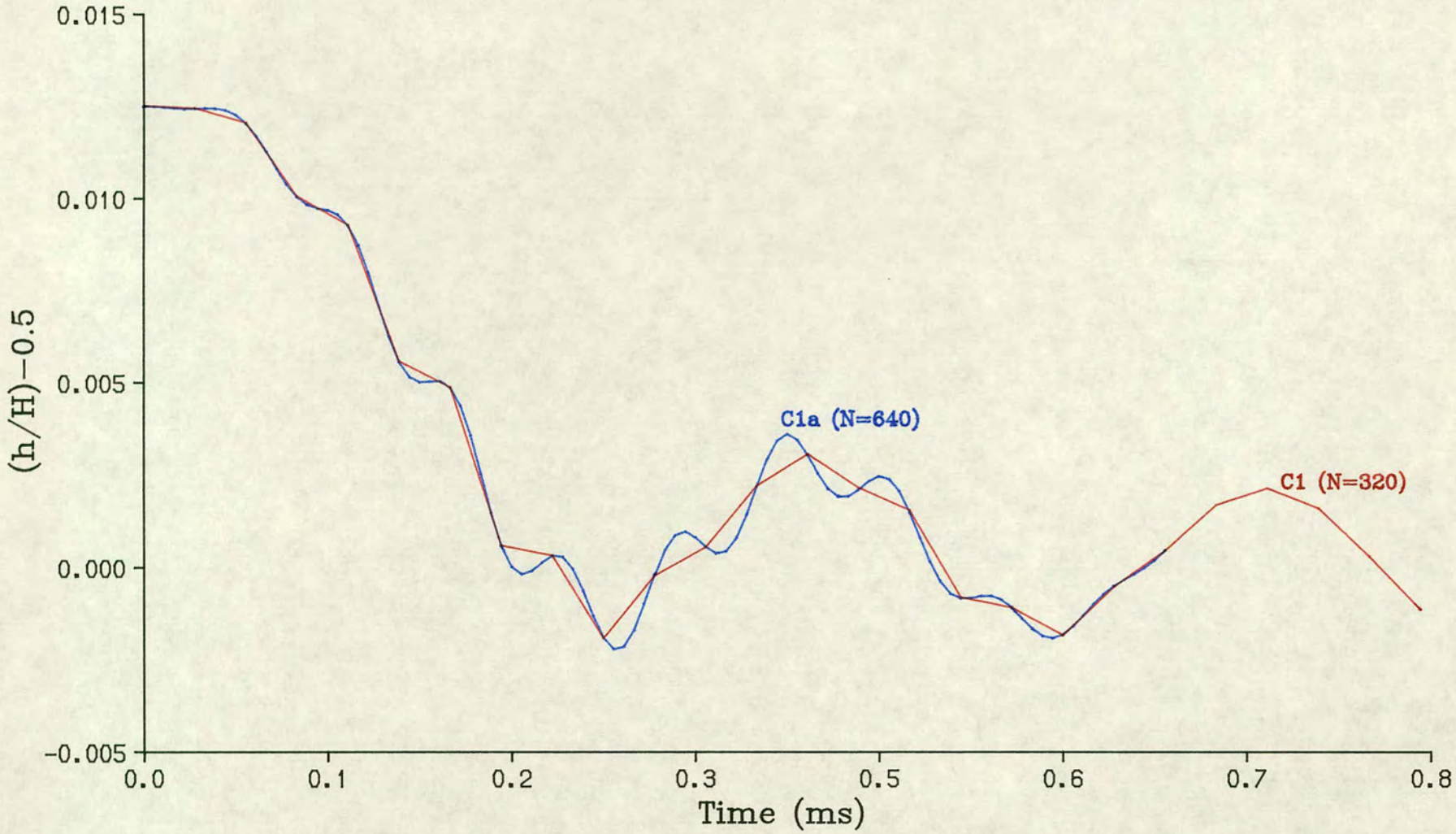

Fig.7.11c Coarse and fine sampling rates compared in Test C1

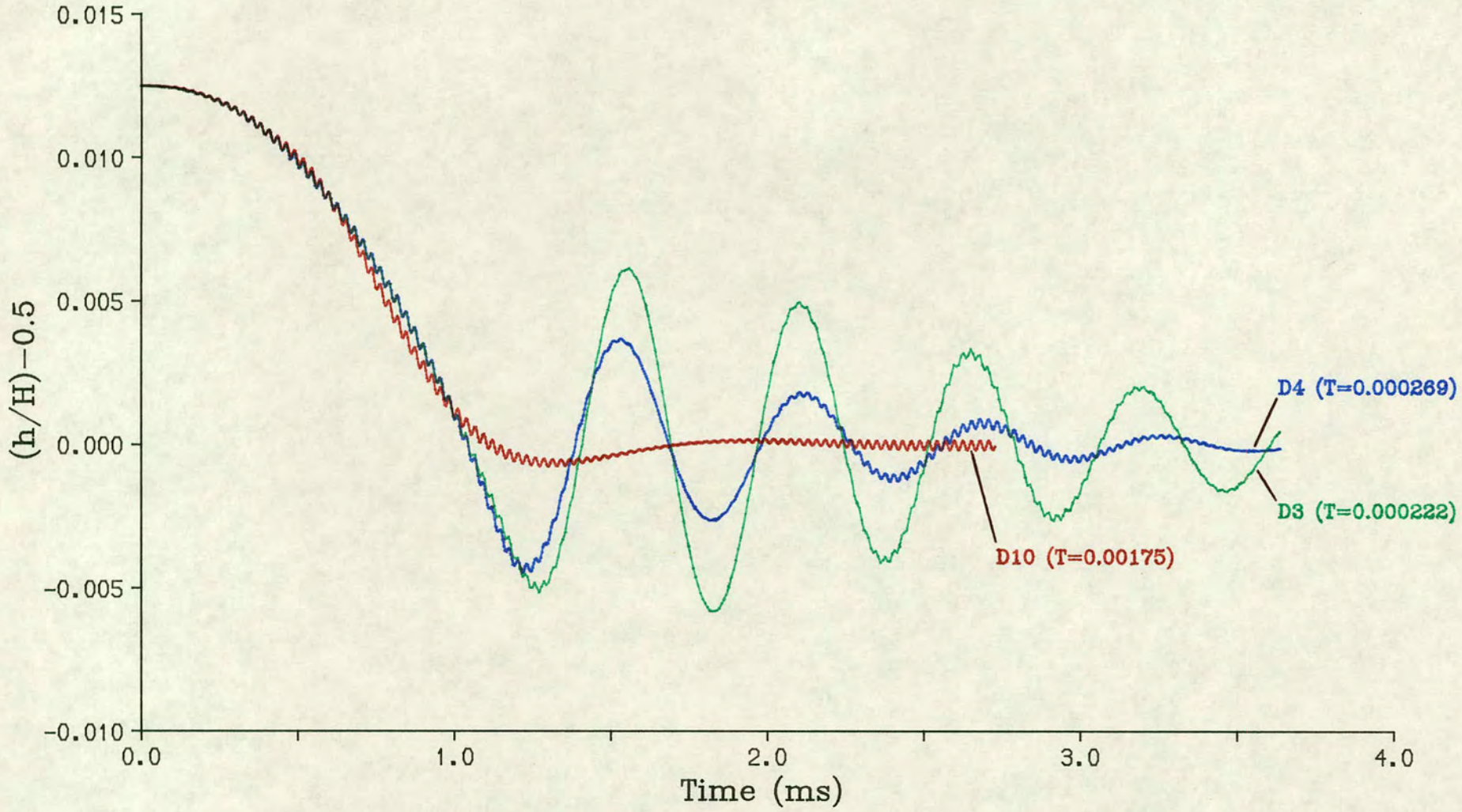

Fig.7.12 Motion of membrane mid-point in selected Series D tests

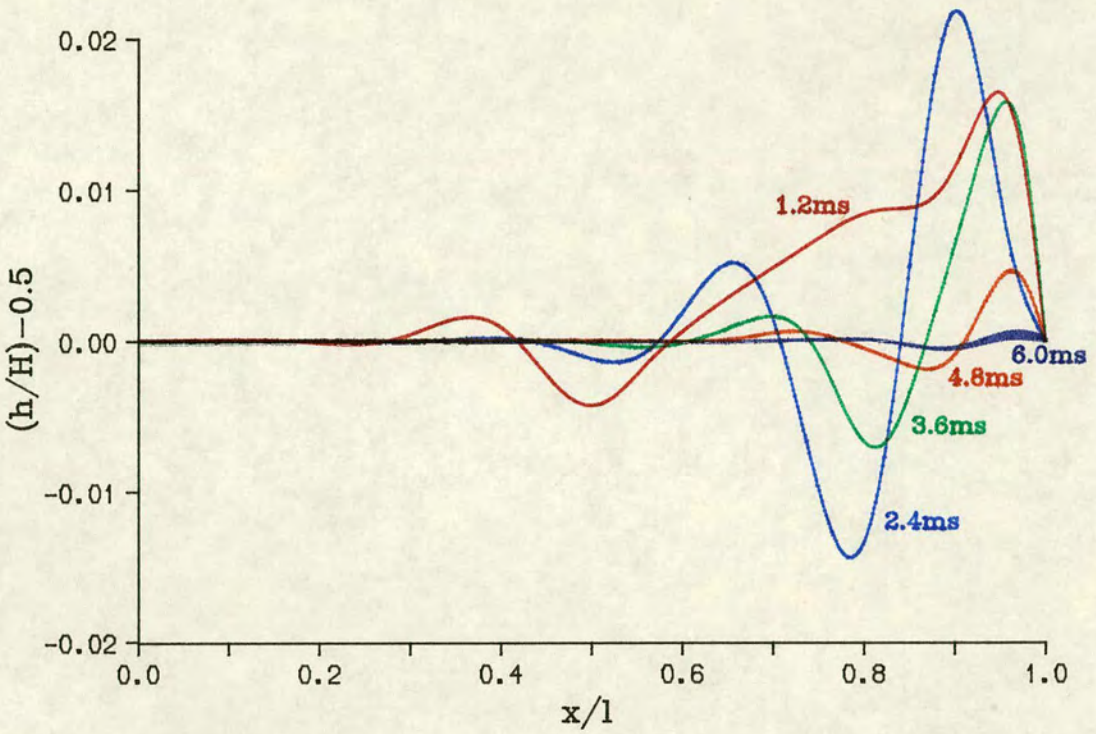

(a) Test D4 (T=0.000269)

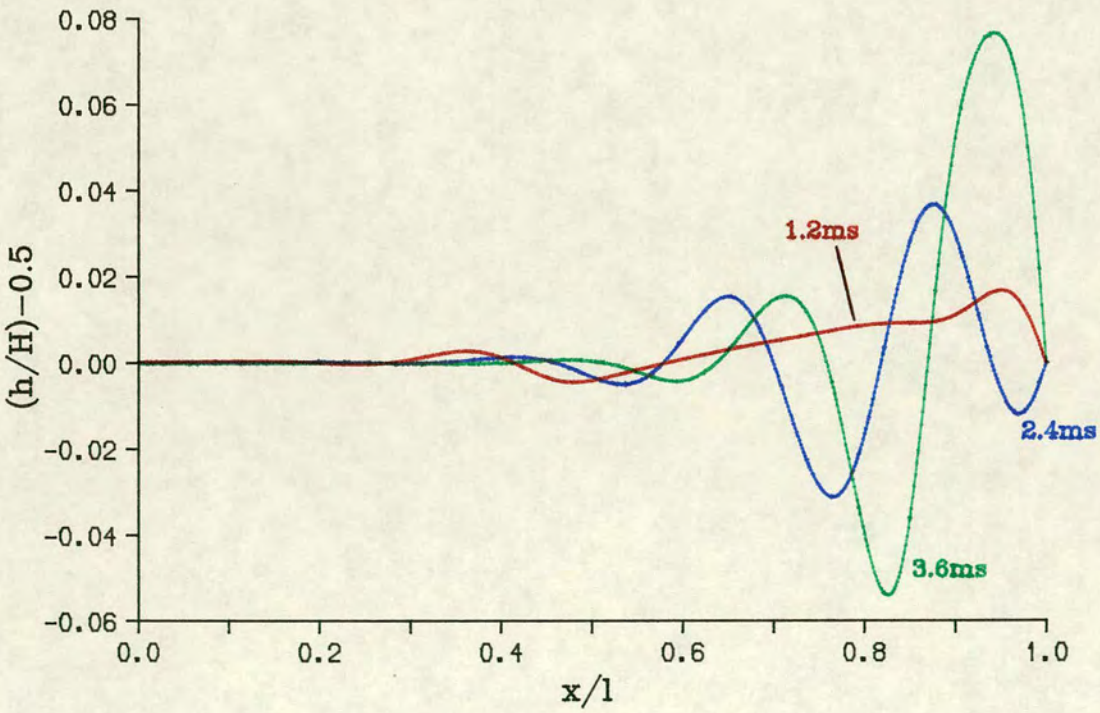

(b) Test D3 (T=0.000222)

Fig.7.13 Membrane shape variation with time

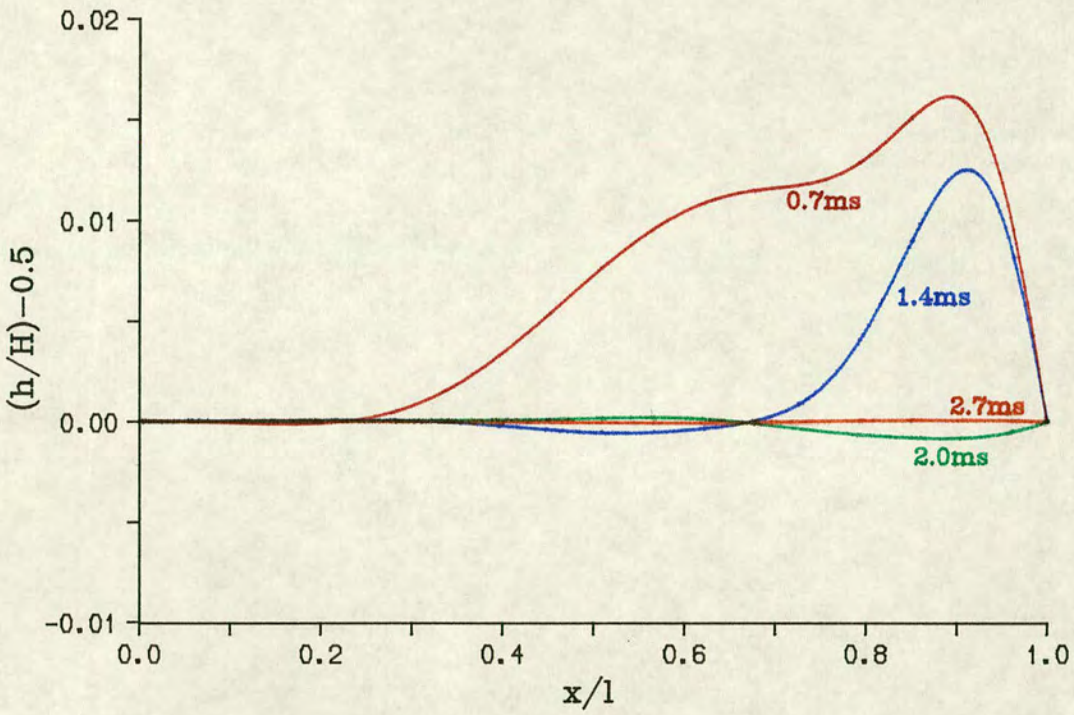

(c) Test D10 (T=0.00175) : N=320

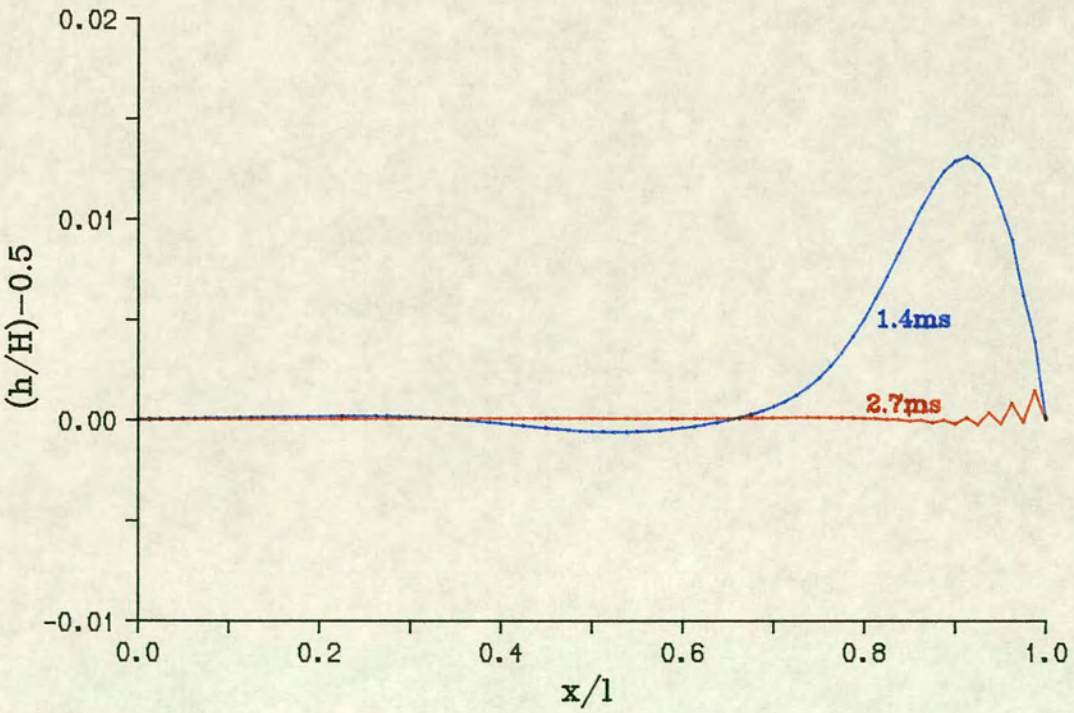

(d) Test D10a : N=80

Fig.7.13 (cont.)

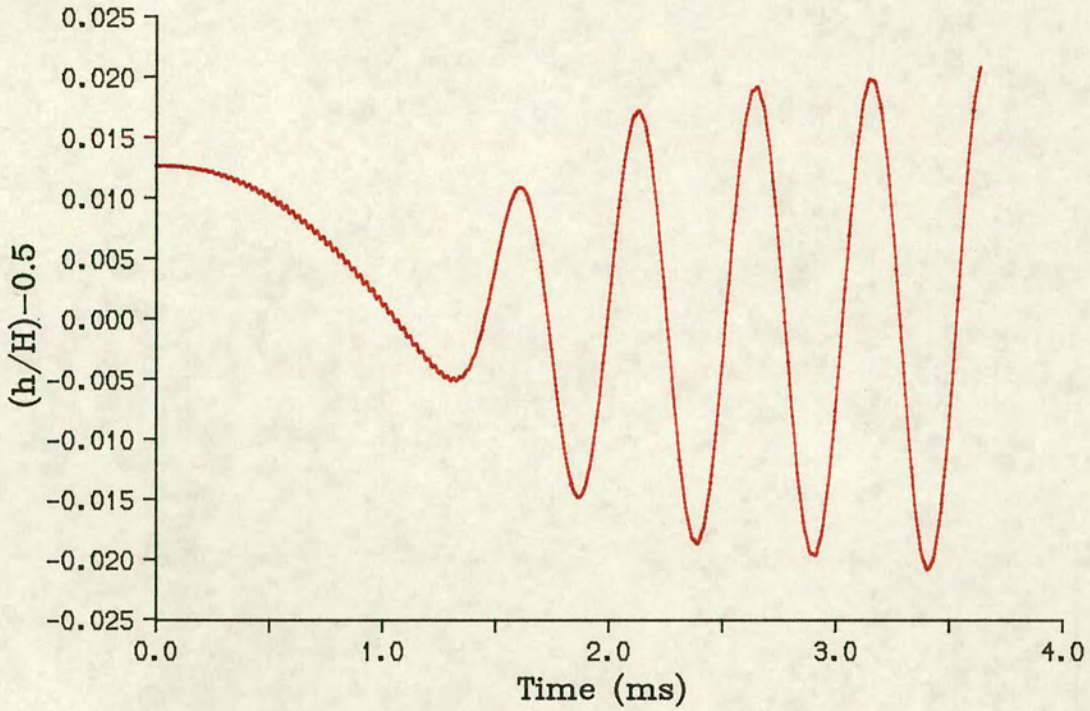

(a) Motion of membrane mid-point

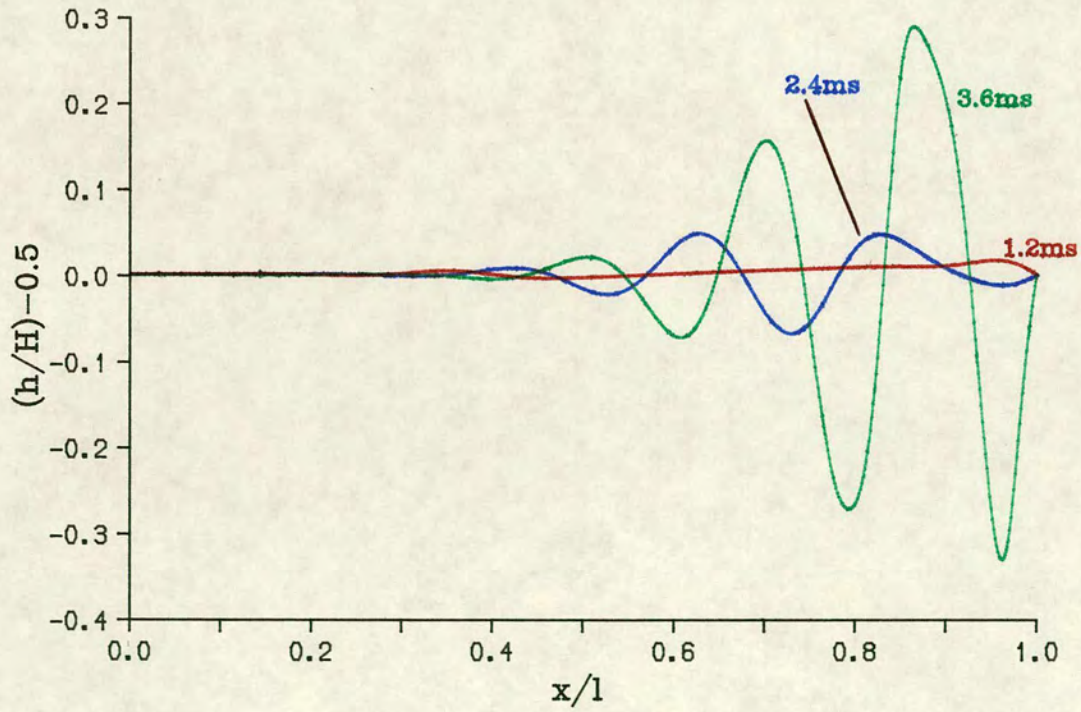

(b) Membrane shape variation with time

Fig.7.14 Test D2 (T=0.000175)

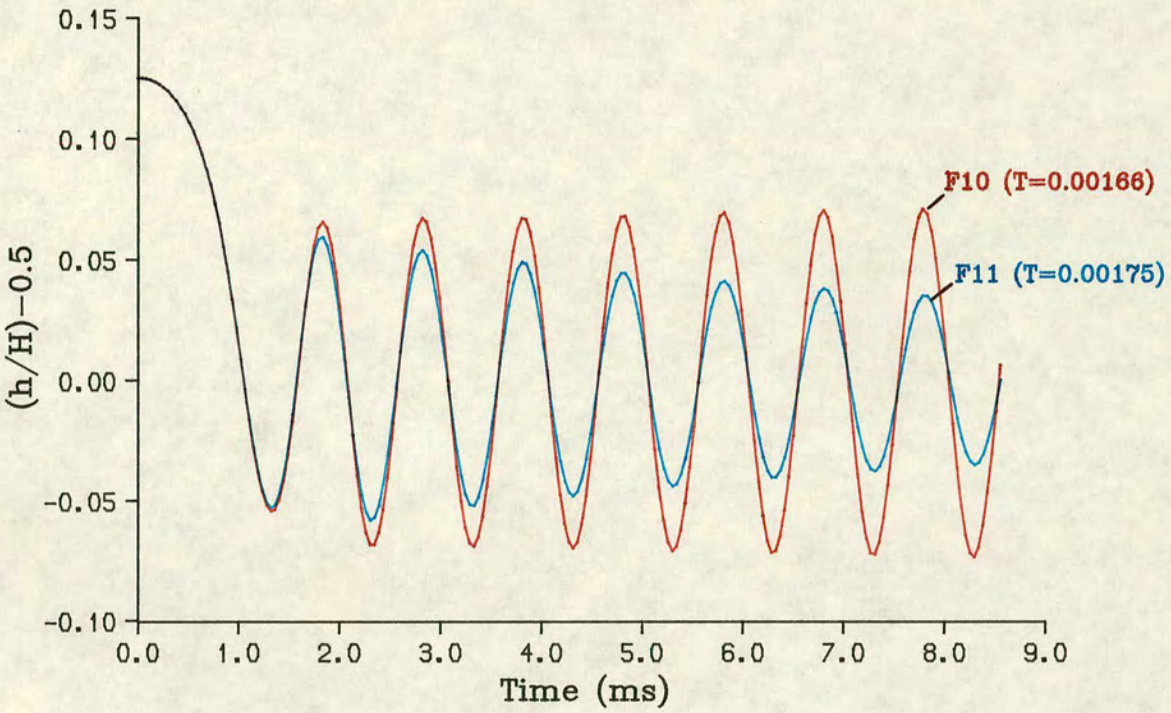

(a) Motion of membrane mid-point

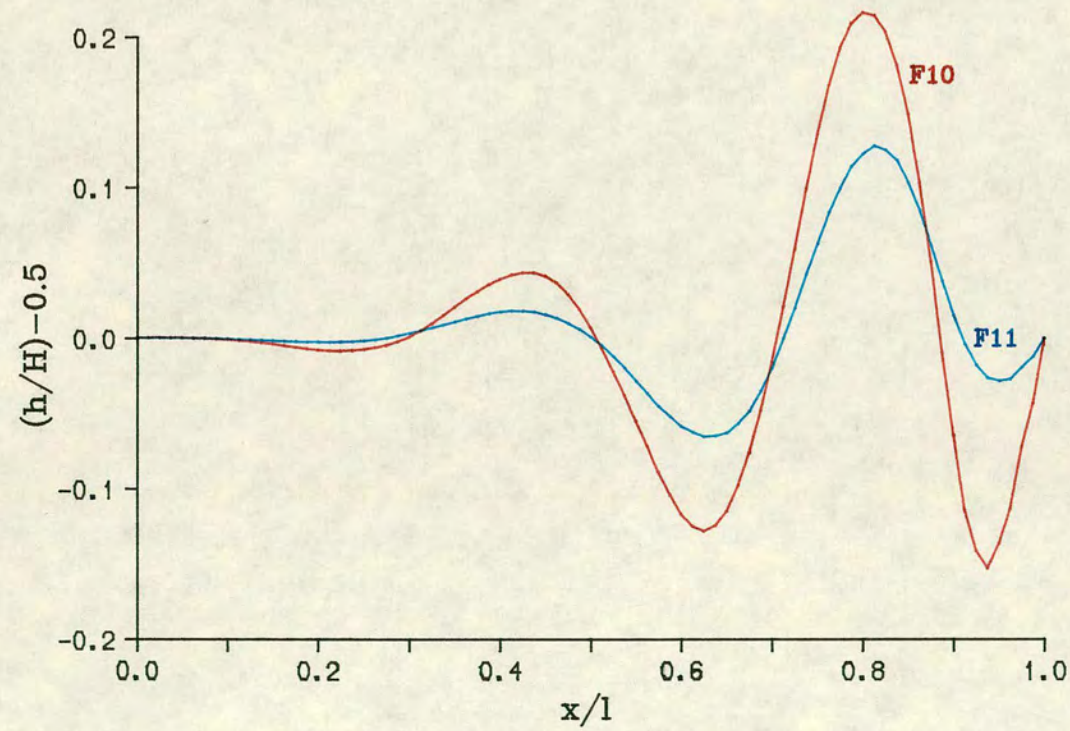

(b) Membrane shape at 8.6ms

Fig.7.15 Tests F10/F11 : h/H=0.63 at x/l=0.5, t=0

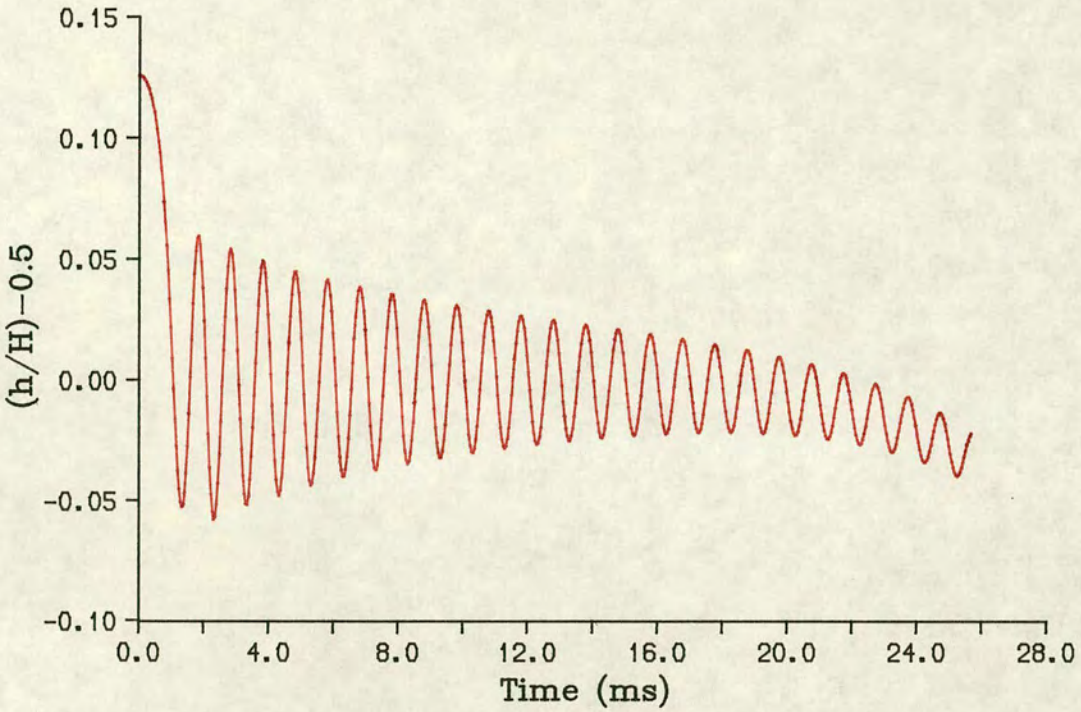

(a) Motion of membrane mid-point

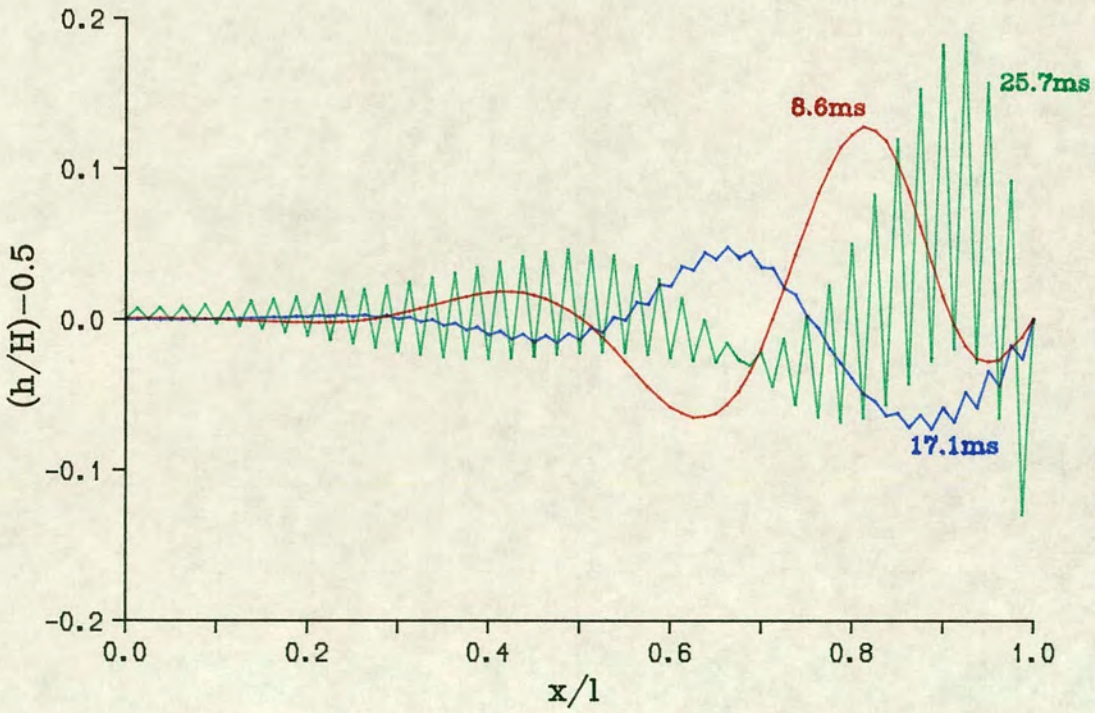

(b) Membrane shape variation with time

Fig.7.16 Test F11 (T=0.00175) : Extended run

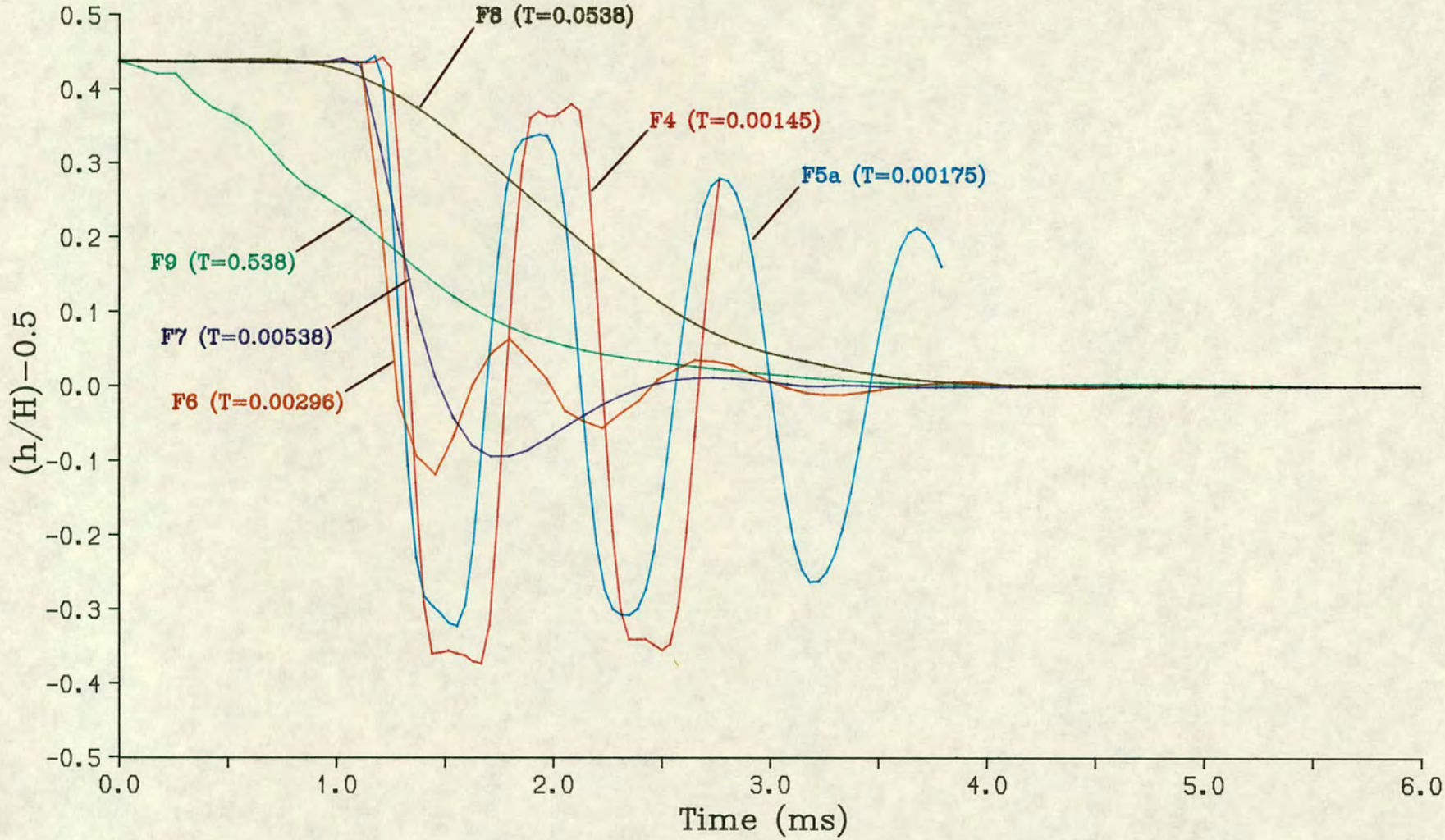

Fig.7.17 Motion of membrane mid−point : h/H=0.94 at x/l=0.5, t=0

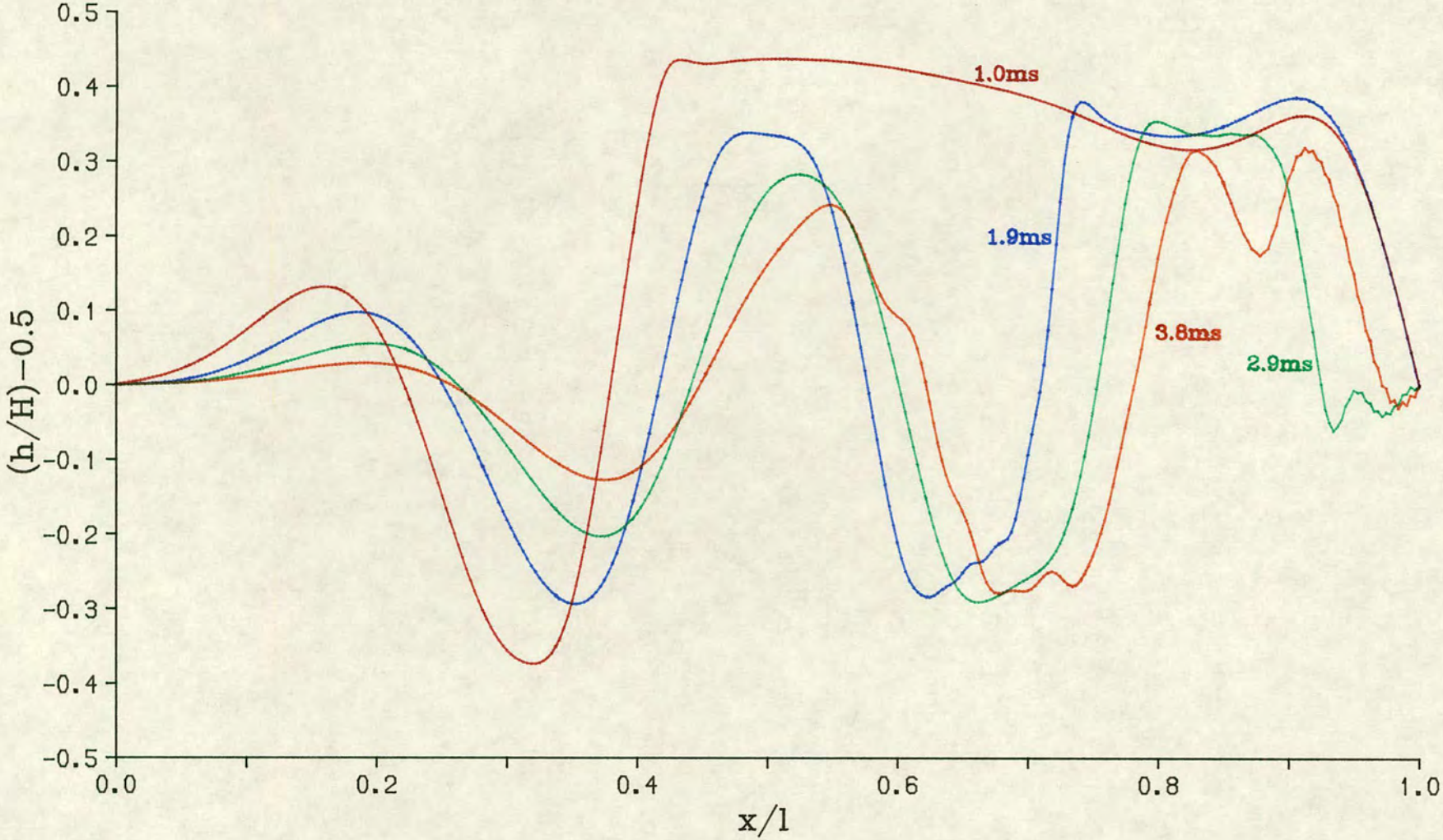

Fig.7.18 Test F5a (T=0.00175) : Membrane shape variation with time

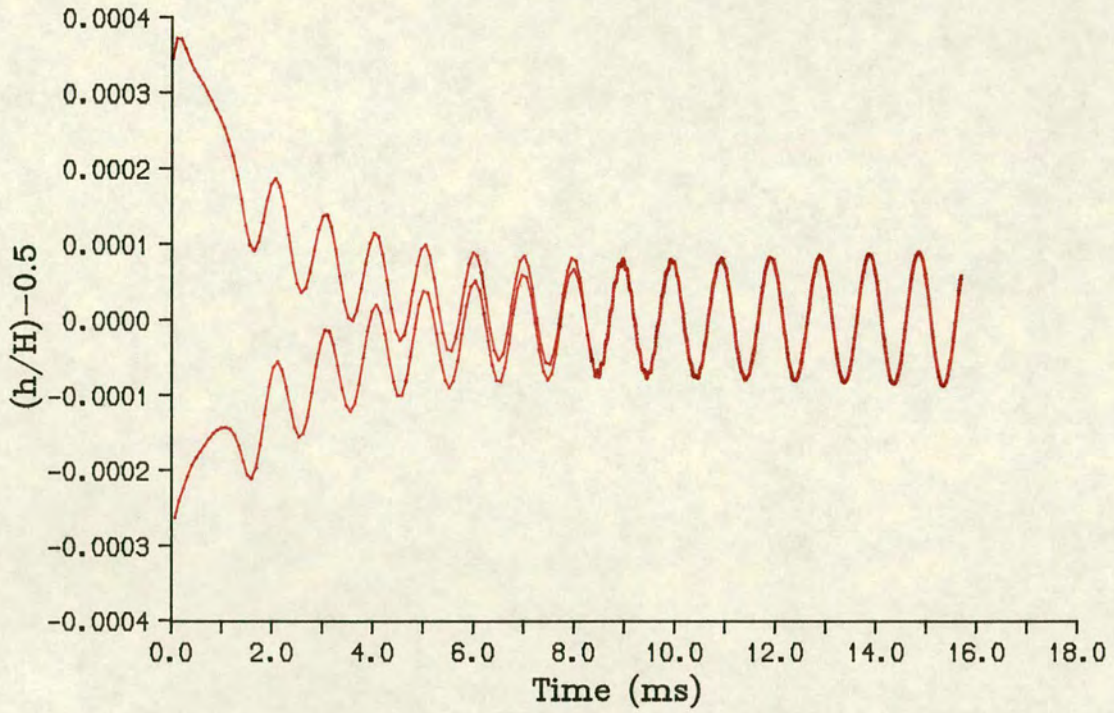

(a) Motion of membrane mid-point

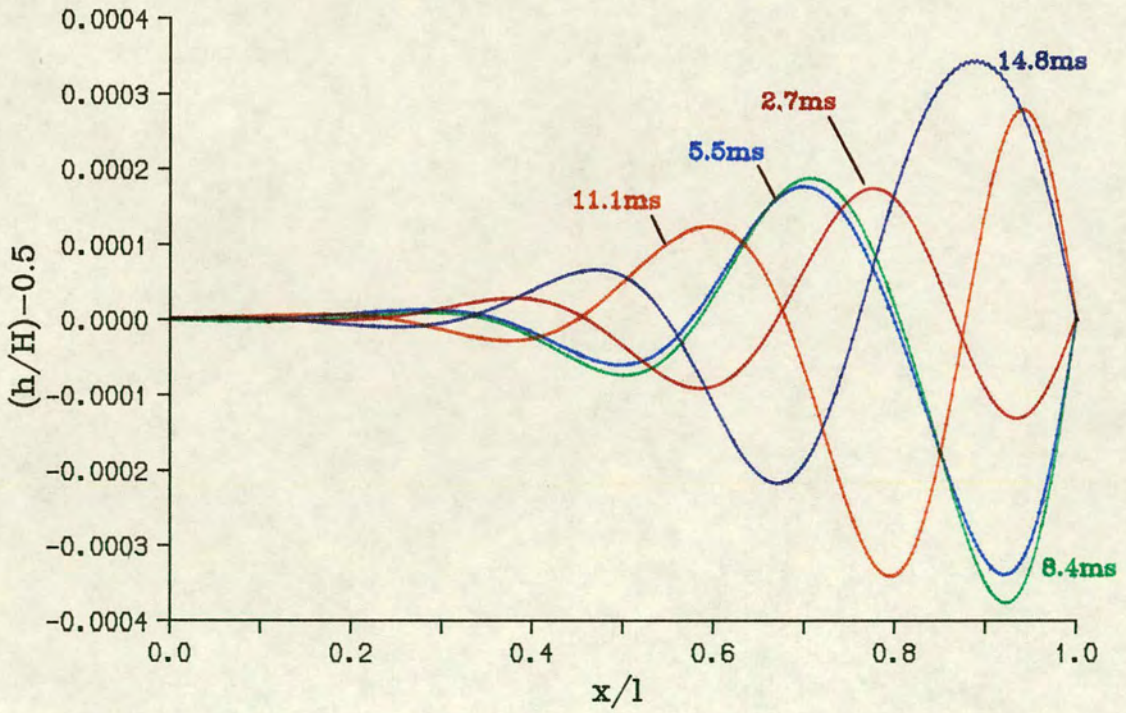

(b) Membrane shape variation with time

Fig.7.19 Test F12 (T=0.00166) : Impulse at t=0

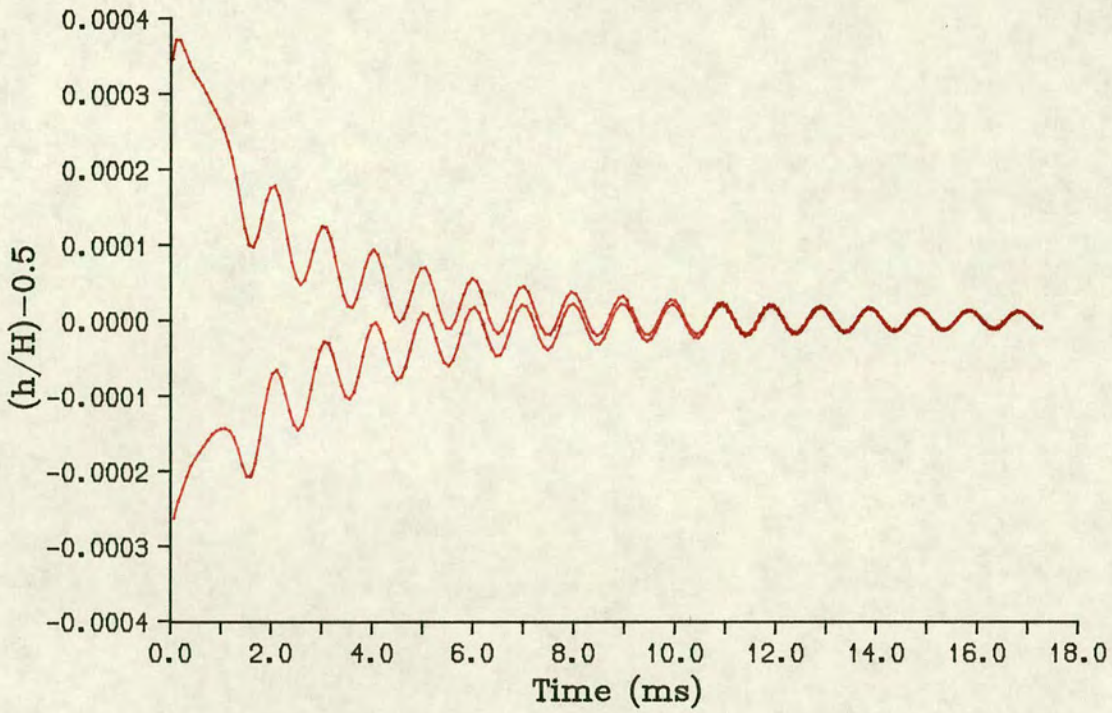

(a) Motion of membrane mid-point

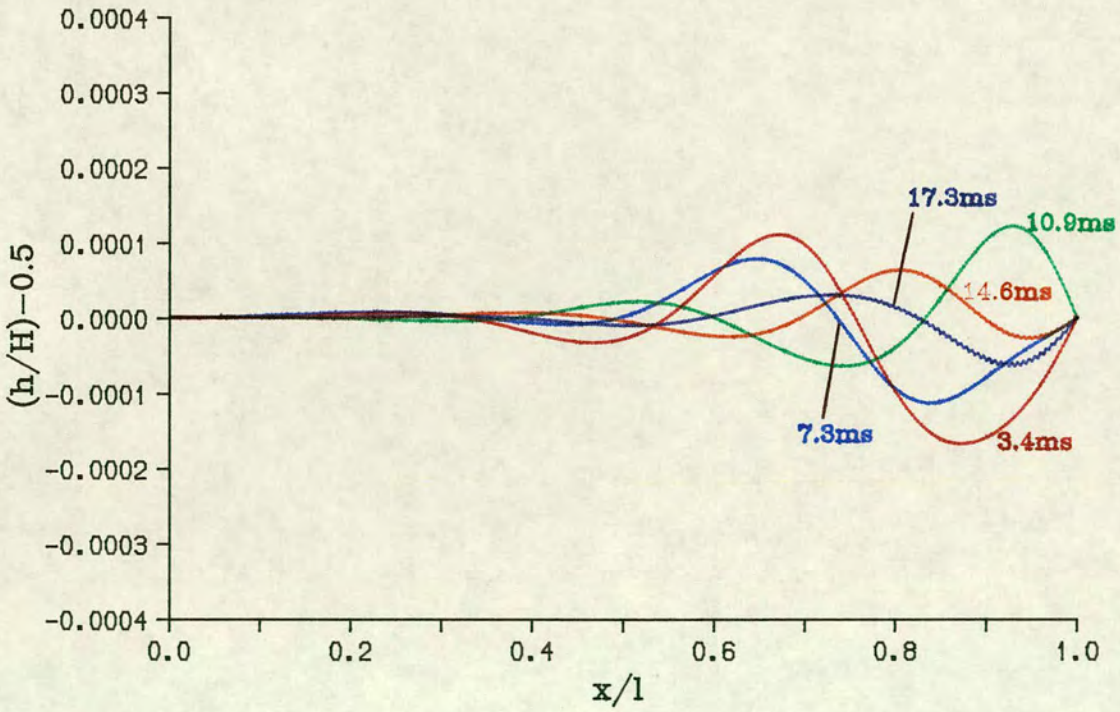

(b) Membrane shape variation with time

Fig.7.20 Test F13 (T=0.00175) : Impulse at t=0

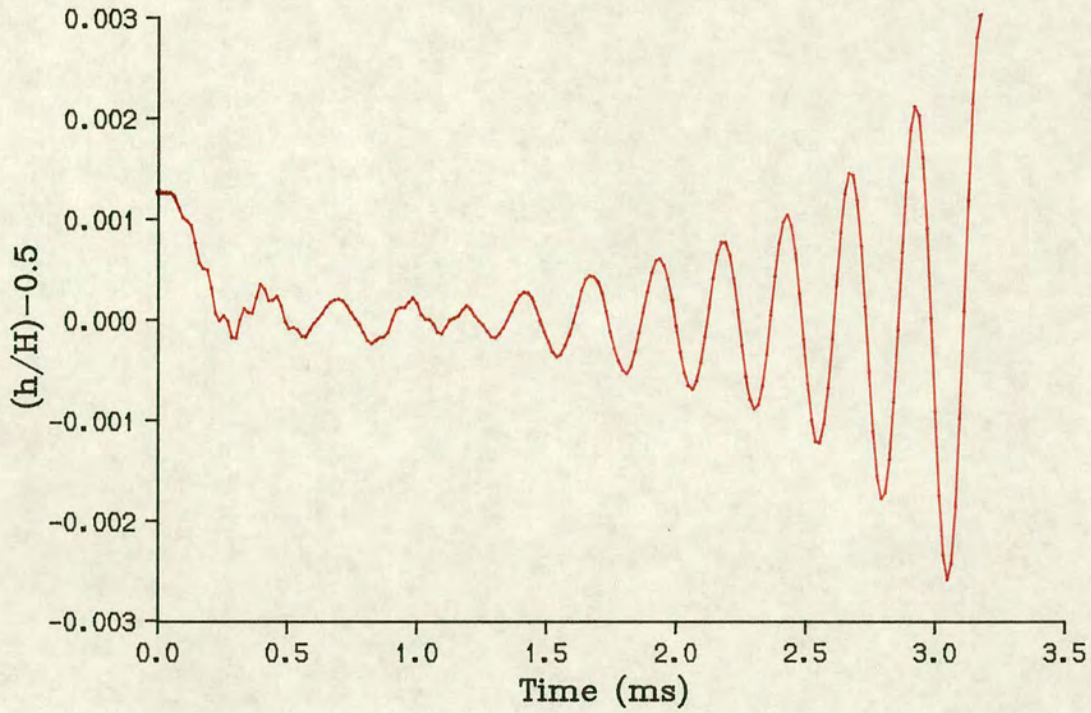

(a) Motion of membrane mid-point

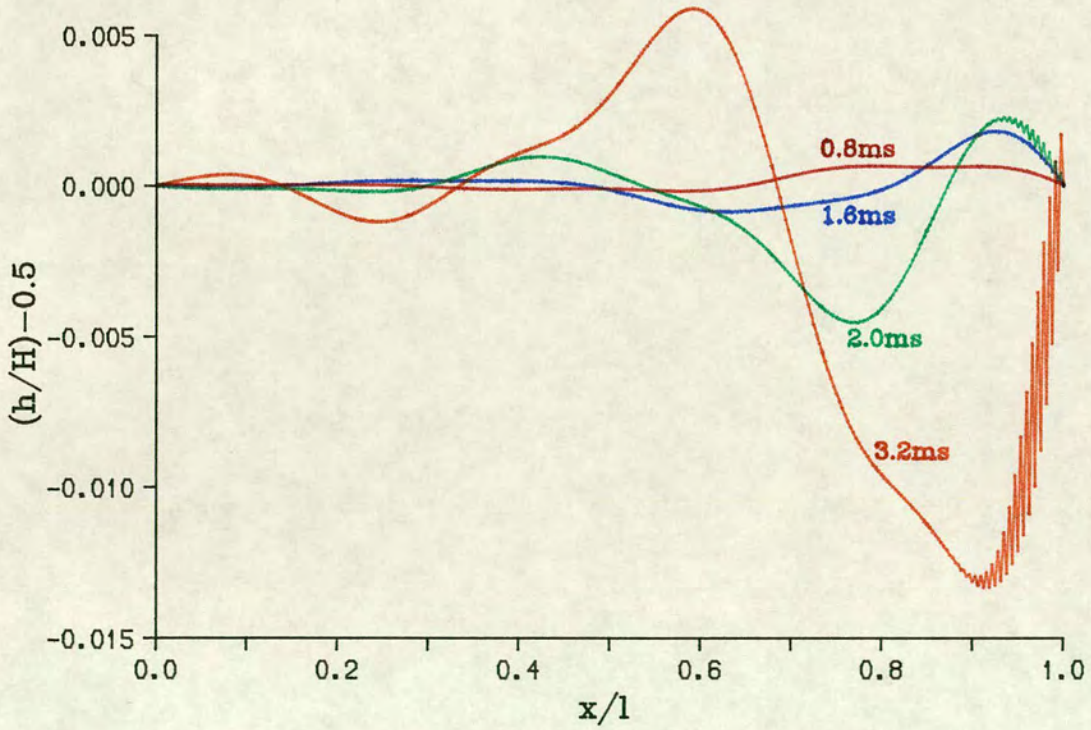

(b) Membrane shape variation with time

Fig.7.21 Test F14 (T=0.0538)

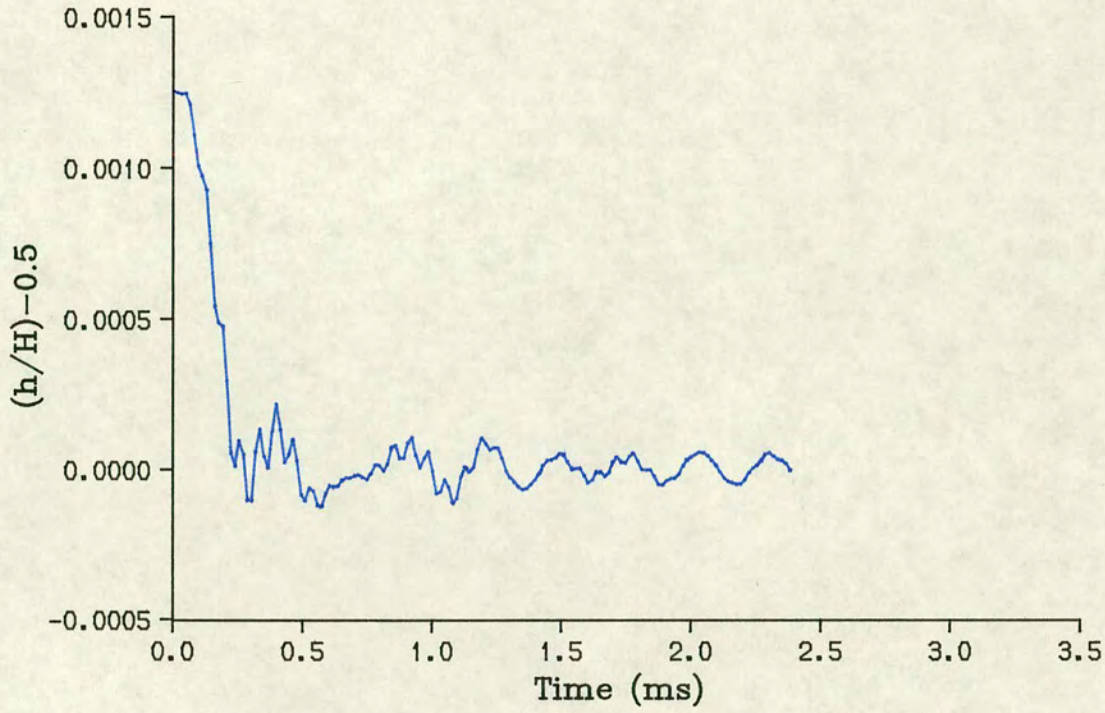

(a) Motion of membrane mid-point

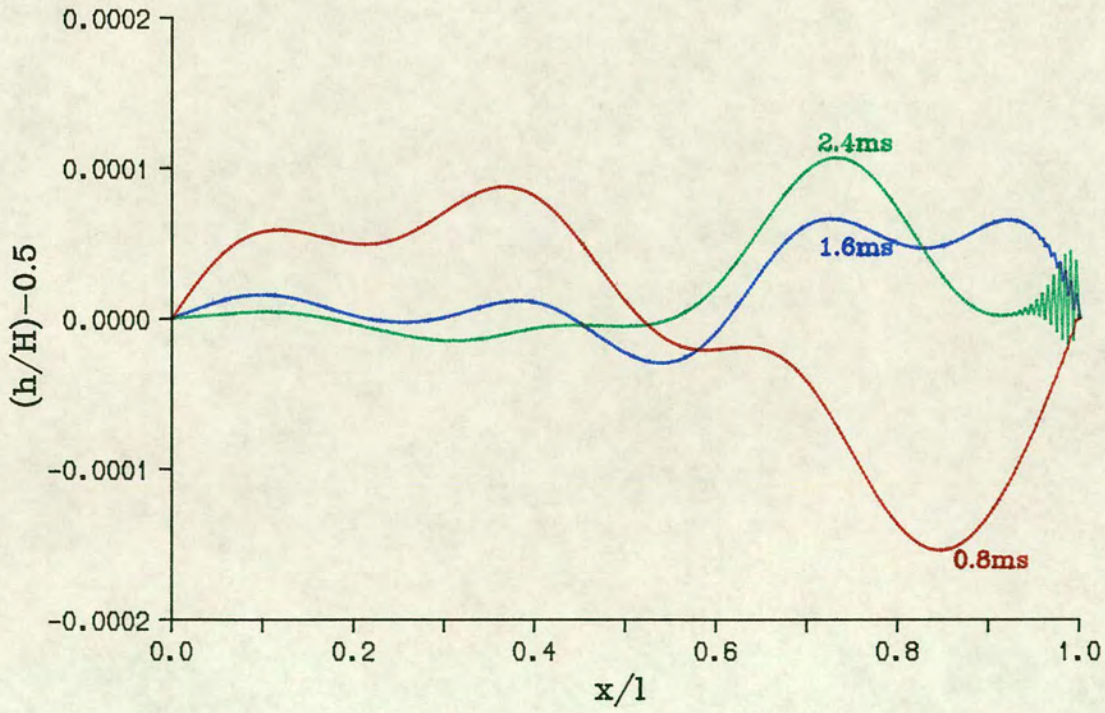

(b) Membrane shape variation with time

Fig.7.22 Test F15 (T=0.0774)